Inaugural – Dissertation

zur

Erlangung der Doktorwürde

der

Naturwissenschaftlich-Mathematischen Gesamtfakultät

der

Ruprecht – Karls – Universität

Heidelberg

vorgelegt von

Dipl.-Math. techn. Jonas Kratzke

aus Heidelberg

Tag der mündlichen Prüfung: .....

Uncertainty Quantification for Fluid-Structure Interaction: Application to Aortic Biomechanics

August 6, 2018

Advisors:

Prof. Dr. Vincent Heuveline

Prof. Dr. med. Carsten Beller

Abstract

Diseases of the cardiovascular system count to the most common causes of death in the developed countries. There are many open research questions with respect to a better understanding for example of the physiology of the heart and the main arteries or to the determination of the factors for aneurysm or stenosis development of the aorta. Furthermore, on a daily basis, a heart surgeon has to estimate the probability of success for different treatment scenarios as opposed to no intervention.

In recent decades, methods of investigation with living probands (in vivo) and artificial experiments (in vitro) have been complemented more and more by computational methods and simulation (in silico). In particular, numerical simulations have the capability to enhance medical imaging modalities with additional information. However, to date, the biomechanical simulation of aortic blood flow given an uncertain data situation represents a major challenge. So far, mostly deterministic models have been used, Yet, measurement data for the configuration of a simulation is subject to measurement inaccuracies. For the choice of model parameters, which are non-measurable in a living body, often imprecise information is available only.

In this work, novel development steps for a numerical framework are presented aiming for the simulation and evaluation of aortic biomechanics using methods of Uncertainty Quantification (UQ). The work includes the modelling of the aortic biomechanics as a fluid-structure interaction (FSI) problem with uncertain parameters. By means of a subject-specific workflow, the simulation of different probands, phantoms and, ultimately, patients is enabled. For the solution of the complex partial differential system of equations, they are discretised with the finite element method (FEM) and a novel, parallelly efficient and problem-specific solver is developed. To verify the numerical framework implemented in the course of this work, a novel analytically solvable benchmark for UQ-FSI problems is proposed. Furthermore, the numerical framework is validated by means of a prototypical aortic phantom experiment. Finally, the UQ-FSI simulation enables the evaluation of a stress overload probability. This novel parameter is exemplarily evaluated by means of the simulation of a human aortic bow.

Therewith, this work represents a new contribution to aspects of the development of simulation methods for the investigation of aortic biomechanics.

Zusammenfassung

Erkrankungen des Herz-Kreislauf-Systems zählen in den entwickelten Ländern zu den häufigsten Todesursachen. Eine Reihe an offenen Forschungsfragen adressiert das bessere Verständnis etwa der Physiologie des Herzens und der Hauptarterien oder die Bestimmung von Faktoren für die Aneurysma- oder Stenoseentwicklung der Aorta. Darüber hinaus zählt es zu den alltäglichen Aufgaben eines Herzchirurgen, die Erfolgswahrscheinlichkeit für verschiedene Operationsszenarien gegenüber keiner Intervention abzuschätzen.

In den letzten Jahrzehnten wurden die Untersuchungsmöglichkeiten an lebenden Probanden (in vivo) und künstlichen Experimenten (in vitro) zunehmend um computergestützte Methoden und Simulationen (in silico) erweitert. Insbesondere können numerische Simulationen ergänzend zu medizinischen Bildgebungsmodalitäten zusätzliche Informationen liefern. Bisher stellt die biomechanische Simulation des Aortenblutflusses bei unsicheren Datenlagen aber eine große Herausforderung dar. Es wurden bislang meist deterministische Modelle verwendet. Messdaten für die Konfiguration einer Simulation unterliegen jedoch Messungenauigkeiten. Für die Wahl von Modellparametern, die in einem lebenden Körper nicht messbar sind, liegen oft nur unzureichende Informationen vor.

In dieser Arbeit werden neue Entwicklungen eines numerisches Framework vorgestellt, welches auf die Simulation und Evaluierung der Aortenbiomechanik mit Methoden der Quantifizierung von Unsicherheiten (Uncertainty Quantification, UQ) abzielt. Die Arbeit umfasst die Modellierung der Aortenbiomechanik als ein Fluid-Struktur Interaktion (FSI) Problem mit unsicheren Parametern. Durch einen patientenspezifischen Workflow wird die Simulation verschiedener Probanden, Phantome und schließlich Patienten ermöglicht. Zur Lösung des komplexen partiellen Differentialgleichungssystems werden diese mit der Finite-Elemente-Methode (FEM) diskretisiert und ein neuartiger, parallel effizienter Löser wird entwickelt. Um das im Rahmen dieser Arbeit implementierte numerische Framework zu verifizieren wird ein neues, analytisch lösbares Benchmark für UQ-FSI-Probleme entwickelt. Darüber hinaus wird das numerische Framework mittels eines prototypischen Aortenphantom-Experiments validiert. Schließlich ermöglicht die UQ-FSI-Simulation die Auswertung einer Überlastungswahrscheinlichkeit der Gefäßwand. Dieser neuartige Parameter wird exemplarisch anhand der Simulation eines menschlichen Aortenbogens ausgewertet.

Damit leistet die Arbeit einen neuen Beitrag zur Entwicklung von Simulationsmethoden zur Untersuchung der Aortenbiomechanik.

Acknowledgements

Working on this thesis has been an exciting and eventful time at Heidelberg University for which I am very grateful. I would like to thank the Faculty of Mathematics and Computer Science and the Interdisciplinary Centre for Scientific Computing at Heidelberg University for their infrastructural and professional support. I am especially grateful to the HGS MathComp for the support and the organisation of great scientific workshops and social events.

Above all, my thanks go to Prof. Dr. Vincent Heuveline for the expert guidance and visionary discussions and for the inspiring research environment at the Engineering Mathematics and Computing Lab as well as for enabling my participation at various highly interesting research projects.

With respect to the latter, I am grateful to the BMBF for the funding via the project *Autostereoscopic Medical Visualization for Minimally Invasive Surgery* (AstemViz) and the project *An Integrated Heart Model* as well as to the DFG for the support via the collaborative research centre *Cognition-Guided Surgery* (SFB TRR 125).

My sincere thanks go to Prof. Dr. med. Beller for his valuable scientific advice on the medical part of my work. I also thank Fabian Rengier and Christian Weis for their medical advice and for providing me with experimental and clinical data.

A very big thank you is especially due to the current and former colleagues and students in the group, Nico, Chen, Fabian, Nils, Philipp L&G^2, Simon, Saskia, David, Sotirios, Mareike, Martin, Thomas, Eva, Teresa, Ina, Pia, Staffan, Ö, Maike, Jonathan, Katrin, Ellen and Linda with whom I've had a great time and lively discussions. A big help has been the advice and inspiration from Martin Baumann, Michael Schick and Peter Zaspel. I have to further thank Lydia Mehra for her awesome efforts on all kinds of organisational issues.

I would like to thank Theresa Jäckh for her encouragement in the beginning of this work.

My warmest heartfelt thanks go to all of my family and friends for sympathetic ears and loving support and these go in particular to Mara.

Und jedem Anfang wohnt ein Zauber inne,
Der uns beschützt und der uns hilft, zu leben.

Hermann Hesse: Stufen

Contents

1 Introduction

The worldwide percentage of cardiovascular diseases at causes of death has grown from 26.5 % in the year of 1990 to 32.3 % in 2016. More specifically, the global share of aortic aneurysms at causes of death has grown from 0.22 % to 0.3 % [44]. Despite a number of achievements in the understanding and treatment, there are still many open questions in the physiology and patophysiology of the cardiovascular system. What are the conditions for an optimal supply of the body organs with oxygen and nutrients via the bloodstream? Which factors have which share in the development of diseases? What is their influence on sudden failure of the system such as infarction or vessel rupture?

The cardiovascular network is a complex multi-scale system. A multi-disciplinary approach in research is necessary to gain a deeper insight into these questions. Basically, experiments on cardiovascular dynamics can be classified according to whether they are carried out on living humans (in vivo) or on artificial replicas (in vitro). As a supplementary column of investigation, computational methods (in silico) can also be utilised in the meanwhile. They enable, for example, a large number of virtual experiment runs with various settings or the calculation and simulation of inaccessible quantities.

For the examination of aneurysms, numerical simulations can provide additional information on risk parameters other than the vessel diameter [18]. Hereby, it is important to consider not only the blood flow but also the very important elastic movement of the aortic wall in the simulation. This leads to the mathematical formulation of complex fluid-structure interaction (FSI) problems. For a clinical application, it still represents a big challenge to carry out FSI simulations in an acceptable runtime.

In the development of simulation-based experiments, the verification and validation of the numerical framework is an essential preliminary step. Due to the detailed knowledge of their installation, in vitro experiments with vessel phantoms [138] can be used to calibrate and test numerical simulation frameworks.

As in non-medical areas, to date, numerical simulations are often based on deterministic models of reality. However, model and numerical errors, measurement noise and patient-specific parameters, that are not measurable non-invasively, all contribute to uncertainties. Their consideration in simulations can give the likelihood of possible results and a measure of reliability of the simulation outcomes, which is crucial, especially in medicine. Uncertainties can be propagated in a simulation by regarding the underlying model equations as a stochastical problem and by utilising the numerical methods of uncertainty quantification (UQ) [131]. As UQ typically increases the computational costs by a multiple of the the deterministic simulation, it remains challenging to derive efficient UQ schemes.

In this work, novel development steps for a numerical framework are presented aiming for

the simulation and evaluation of aortic biomechanics using methods of UQ. It is structured as follows:

Chapter 2 gives an overview on aortic blood flow, imaging modalities as well as diagnosis tools. The function of the aorta is depicted as a part of the cardiovascular system. Next, an aortic phantom experiment is described which serves as a validation instrument for the developed numerical framework.

Chapter 3 addresses the mathematical modelling of aortic blood flow under uncertainties. Firstly, the biomechanics of blood flow and vessel wall soft tissue are modelled. On a mathematical level a coupling method of the flow and tissue deformation dynamics by fluid-structure interaction is described. Methods for quantifying the uncertainty propagation in the developed framework are presented and potential parameters for risk assessment are discussed.

Chapter 4 goes into detail on the developed numerical framework. By means of a subject-specific workflow, the simulation of different probands, phantoms and, ultimately, patients is enabled. For the solution of the complex partial differential system of equations, they are discretised with the finite element method (FEM) and a novel, parallelly efficient and problem-specific solver is developed.

To verify the numerical framework implemented in the course of this work, the results for a well-established deterministic fluid-structure interaction benchmark are reproduced in chapter 5. Additionally, a novel analytically solvable benchmark for UQ-FSI problems is proposed in the section 5.2 of that chapter.

Chapter 6 shows validation results for the developed framework by means of an aortic phantom experiment. Finally, the UQ-FSI simulation enables the evaluation of a stress overload probability. This novel parameter is exemplarily evaluated by means of the simulation of a human aortic bow.

The conclusion in chapter 7 gives a summary, discussion and outlook on the simulation of aortic blood flow dynamics.

2 Aortic blood flow

This chapter gives an overview of the cardiovascular system. Details are given on the physiology as well as the pathology of the thoracic aorta. Furthermore, a study of blood flow by means of aortic phantom experiments is described. Then, medical imaging techniques for measuring aortic blood flow are explained. Finally, ways for transforming imaging data into discrete geometries for numerical simulations are depicted.

2.1 The cardiovascular system

The cardiovascular system is an organ system enabling the supply of the body cells with vital substances. It is also a mediator for several regulatory systems. The given information in the following sections is gathered from and more details can be found in [49, 45, 104].

Transporting breathing gases, the cardiovascular system brings oxygen from the lungs to the body cells. Also, carbon dioxide is brought from the body back to the lungs. Nutrients are transported via the cardiovascular system from the digestive tract to the organs. Amongst them are vitamins and minerals. Glucose is turned into energy generation by the target cells and lipids are used for the assembly of cell membranes. On the other hand, by-products are carried from the organs to the kidneys and the liver. For example cholesterol first has to be transformed in the liver before it can leave the body via the gall and the intestine.

The cardiovascular system also plays an important role in the immune regulation as it conveys leukocytes and hormones throughout the body. The various kinds of leukocytes protect the organism against many foreign substances and pathogens. Hormones get carried from the producing tissues to the respective organs. The cardiovascular system hence contributes to the function and regulation of the hormone balance. When injured, messenger substances are released, which activate coagulation. As a self-protection mechanism, coagulation counteracts blood loss and triggers wound healing.

Besides immune and hormone regulation, the cardiovascular system also ensures the homoeostasis of electrolytes and water providing a stable pH level. Furthermore, it regulates the body temperature to an almost constant temperature level.

2.1.1 The structure of the cardiovascular system

The cardiovascular system is a circulatory system with the heart being its central drive. Two vascular trees branch off of the heart: The low pressure pulmonary circulation through the lung and the high pressure systemic circulation through the rest of the body. The vascular trees begin with the arteries coming from the heart. The aorta, as the main artery of the

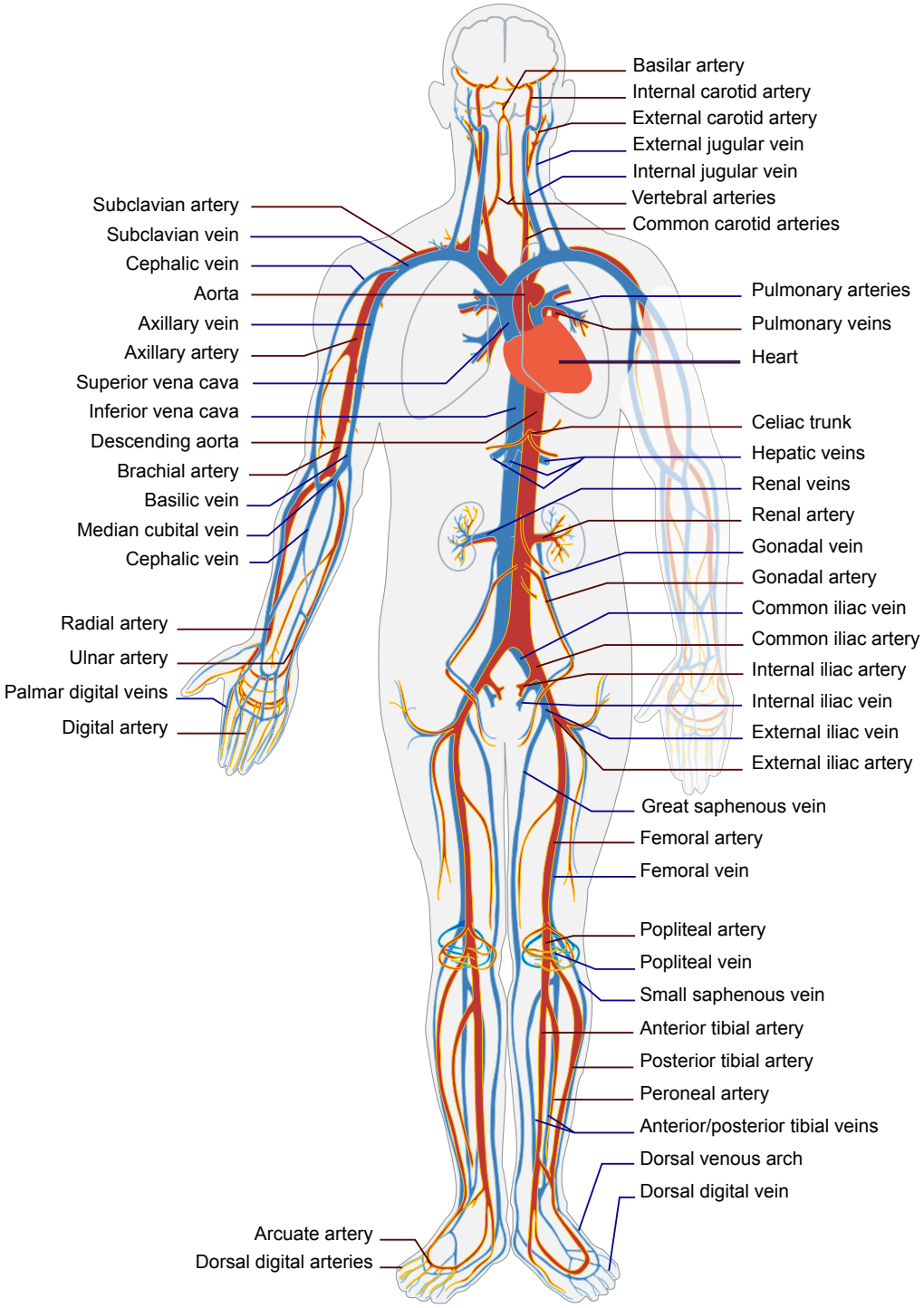

Figure 2.1: An overview on the human vascular tree [25]. Arteries are indicated by red. Blue colour indicates veins.

systemic circulation, has a diameter of about 25 mm and a wall thickness of approximately 2 mm. Both vascular trees branch mainly in bifurcations. As the arteries branch further to arterioles and capillaries, also anastomoses are present. In the fine network of the microcirculation, capillaries have a diameter of about 5 µm to 10 µm and a wall thickness of about 1 µm. With a diameter of roughly 7.5 µm, red blood cells can be bigger than capillary vessels. After exchanging breathing gases and nutrients with the respective body tissue, blood is led back to the heart through merging venules and veins. Unlike arteries, veins have valves preventing potential backflow of blood. The inferior vena cava approximatly has a diameter of 30 mm and a wall thickness of 1.5 mm. The estimations on the diameter and wall thickness are adopted from [16]. Figure 2.1 gives an overview on the various vessels of the cardiovascular circulatory.

2.1.2 Functioning of the heart

The heart is a muscular hollow organ that drives the blood through the vascular trees. It mainly consists of the myocardium with its specialised heart muscle cells. Heart muscle cells have a relatively low contractibility and a relatively high resistance to fatigue compared to other muscles in the human body.

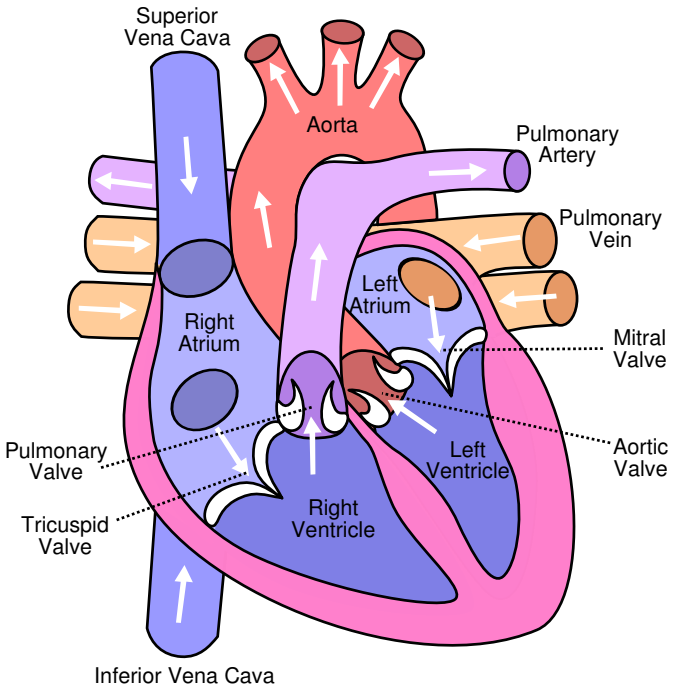

Figure 2.2: Illustration of the human heart with a denotion of the chambers, valves and the adjacent vessels [21]. Also, the direction of the respective blood flow in indicated.

The human heart is partitioned into two sides separated by the cardiac septum. Both, the right and the left side of the heart have two chambers, the atrium and the ventricle as it is shown in Figure 2.2. The atrium and the ventricle themselves are separated by the fibrous skeleton of the heart. The atrioventricular valves in this part of the skeleton, namely the

mitral valve on the left side and the tricuspid valve on the right side, ensure an unidirectional blood flow from the atrium to the ventricle. The semilunar valves control the flow direction from the ventricles to the subsequent arteries: The aortic valve on the left side and the pulmonary valve on the right side of the heart.

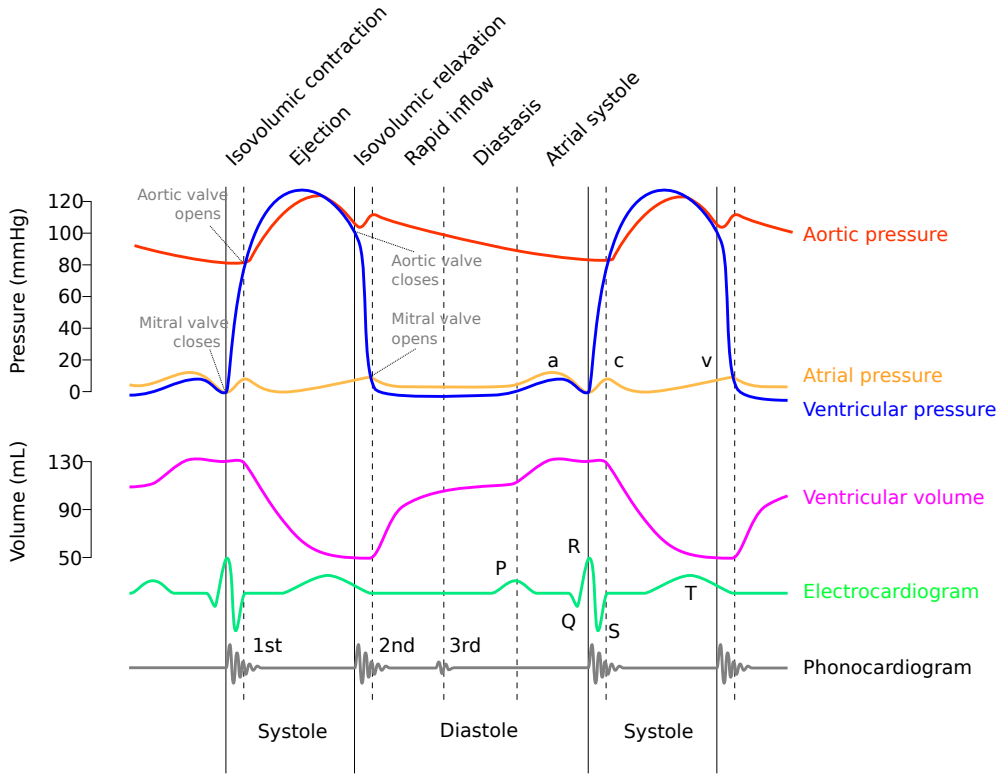

Figure 2.3: The Wiggers diagram [23], named after Dr. Carl J. Wiggers, plots the blood pressure in the aorta, the left atrial and the ventricular pressure as well as the ventricular volume over time. The electrocardiogram and the phonocardiogram (heart sounds) can also be included [99]. Important cardiac cycle events of the left side of the heart are also denoted in the figure. The atrial pressure shows three waves: a) atrial contraction, c) closing of the mitral valve bulging into the atrium, v) passive atrial filling. The waves in the electrocardiogram correspond to: P) atrial depolarisation, QRS) ventricular depolarisation and T) ventricular repolarisation. The 1st sound labelled in the phonocardiogram corresponds to the reverberation of blood from the sudden closure of the mitral valve and the 2nd originates from the reverberation of blood from the sudden closure of the aortic valve.

The heart works as a pressure pump by rhythmic contraction and relaxation. The contraction of the myocardium is triggered by pacemaker cells in the sinoatrial node by a progression of depolarisation. The electrical activity can be measured on the chest skin and shown in electrocardiograms as depicted in Figure 2.3. At the beginning of the systole (contraction phase), the pressure in the respective ventricle exceeds the pressure in the atrium such that the atrioventricular valves close. When in addition the arterial pressure is exceeded, the semilunar valves open and the blood is driven into the systemic and the pulmonary circu-

lation. In the diastole, the ventricles relax. Due to the reversed pressure differences, the semilunar valves close and shortly after, the atrioventricular valves open. The ventricles get filled again with blood from the atria until the beginning of the next systole. The periodical course of the pressure in the atrium, the ventricle and the aorta are part of the Wiggers diagram [99], see Figure 2.3.

2.1.3 Pulmonary circulation

The low-pressure pulmonary circulation comprises the exchange of gas in the lungs. Deoxygenated blood is pumped by the right ventricle of the heart through the pulmonary valve to the pulmonary artery. In the lung, the pulmonary arteries branch out into a fine network of thin-walled capillary blood vessels. They encounter the lung alveoli which can be seen as the end sections of the respiratory tree. Here, carbon dioxide gets released from the blood and blood is enriched with oxygen. The oxygenated blood is led by the pulmonary veins to the left atrium of the heart.

2.1.4 Systemic circulation

The systemic circulation supplies the body cells with oxigen and nutrients and carries off carbon dioxid and catabolites. At an average pressure of about 12.5 kPa blood is pumped by the left ventricle of the heart through the aortic valve into the aorta. In the ascending aorta, peak flow velocity can reach approximatly $1\,\mathrm{m\,s^{-1}}$ [104]. Especially the aorta, but also the subsequent arterial system damps out the pulsatile pressure waveforms coming from the heart. Blood flow volume is stored in the elastic, distensible vessels during systole and passed on during diastole. This can be compared to the effect of a Windkessel and leads to a more constant flow through the capillary network. In capillaries, blood flow reaches average values of approximately 3 kPa and $0.3\,\mathrm{mm\,s^{-1}}$. In contrast to large vessels capillary vessel walls have active muscles enabling a control of blood flow through the vessel network. Under lower pressure, the blood flows from the capillaries to the heart through a merging network of veins. It reaches the right atrium of the heart through the lower and upper vena cava at an average pressure of approximately 0.5 kPa.

2.1.5 Blood composition

Blood consists primarily of blood plasma (approximately 55 %) and blood cells (approximately 45 %). Approximately 92 % of the blood plasma volume is actually water. Furthermore it contains proteins such as fibrinogen and lipoproteins, small molecules like glucose and hormones as well as ions (e.g. Na^+, Cl^-). Red blood cells (RBCs, erythrocytes), white blood cells (leukocytes) and blood platelets (thrombocytes) belong to the cellular constituents of blood. The hematocrit, the volume percentage of erythrocytes in blood is approximately 45 % for men and 40 % for women under normal conditions. Erythrocytes have the shape of oval disks with concave sides. Their diameter is approximately 7.5 µm. In capillaries of smaller diameter the flexible cell membrane of erythrocytes can get highly deformed to pass the vessel.

2.2 The human aorta

Subsequent to the aortic root at the left ventricle of the heart, the human aorta leads upwards in the superior direction. Approximately at the fourth thoracic vertebra the aorta turns to the lateral left and posterior side. It continues in the inferior direction towards the pelvis where it bifurcates into the left and right common iliac artery.

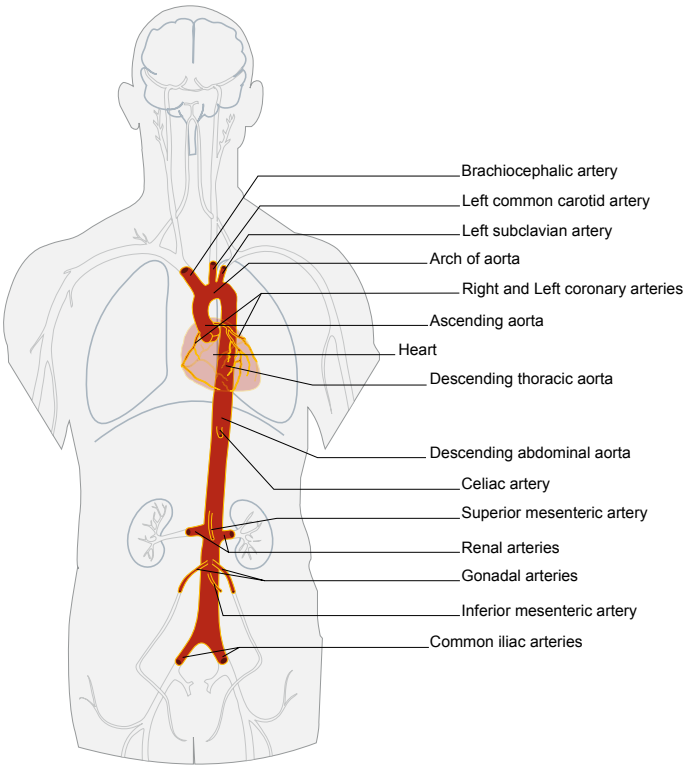

(a) The thoracic aorta from the heart to the abdominal aorta [20].

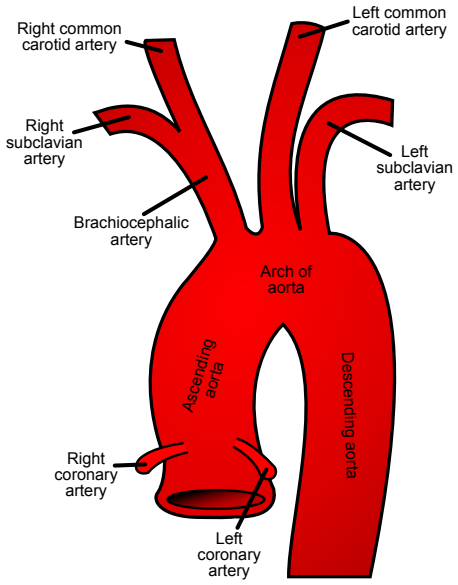

(b) The ascending aorta, the aortic bow and the beginning of the descending aorta [22].

Figure 2.4: Schematic overview of the aorta.

The major segments of the aorta are described in the following. An overview is given in Figure 2.4.

2.2.1 Overview on the anatomy

Ascending Aorta:

The ascending aorta begins with the widening of the aortic sinuses behind each of the three cusps of the aortic valve. The left and right aortic sinuses give rise to the left and right coronary artery. The posterior aortic sinus is usually not connected to a vessel. The coronary arteries provide the heart muscles with oxygenated blood. The sinotubular junction marks the end of the aortic sinuses where the aortic shape becomes tubular. From there, the ascending aorta leads a few centimetres in superior direction. Under healthy conditions, the diameter of the ascending aorta can reach 40 mm.

Aortic arch:

The aortic arch follows the ascending aorta and turns from the superior over the left posterior to the inferior direction. For most individuals, the aortic arch has three branches: Firstly, there is the brachiocephalic artery, which bifurcates into the right common carotid artery and the right subclavian artery. Secondly and thirdly, the left common carotid artery and the left subclavian artery branch off the aortic arch. There are also other branching variations of the carotid and subclavian arteries. The carotid arteries supply the head and neck with oxygenated blood and the subclavian arteries lead to the arms and parts of the upper body. The aortic arch can have a diameter of approximately 30 mm.

Descending Aorta:

The diameter of the descending aorta usually decreases to values below 25 mm. It leads in inferior direction to the pelvis and its branches supply the lower part of the body with oxygenated blood. One can distinguish between the thoracic aorta above the diaphragm and the abdominal aorta below the diaphragm. The abdominal aorta has several branches supplying the abdominal organs such as the stomach, the spleen, the pancreases, the liver and the intestine.

2.2.2 Vessel wall structure

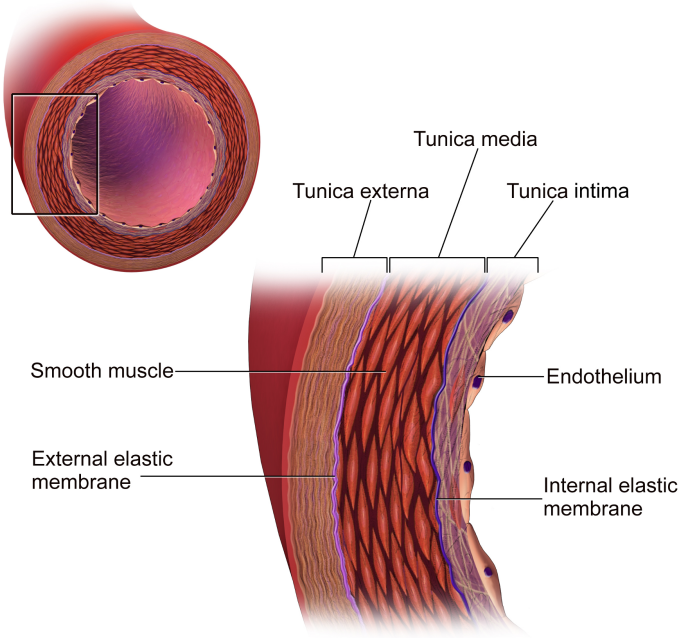

Figure 2.5: The main layers of an artery wall are given by the tunica intima, media and externa [24]. The three layers are complex composites of elastic fibers, smooth muscle cells and membranes. The innermost single-cell layer of the endothelium is in direct contact with the blood flow.

An early study on the mechanics of vessel wall soft tissue is given by [117]. Numerous investigations and experiments have led to a deeper understanding of the vessel wall structure. Recent reviews on the aortic vessel wall structure are given by [74, 53, 69].

As shown in Figure 2.5, an artery wall is composed of three layers, namely from inside to the outside: the intima (Tunica intima), the media (Tunica media) and the adventitia (Tunica externa). The intima consists of the endothelium, an innermost layer of endothelial cells, a subendothelial layer with connective tissue and a fenestrated membrane with an elastic fibre network. In the case of the aorta, the media consists of several layers of smooth muscle cells with elastic fibres. The layers of the media are separated by elastic laminae. The adventitia mainly consists of helical structured collagen fibres. Large arteries are additionally surrounded by an elastic lamina.

Overall, the aortic vessel wall can be seen as a complex system of layered elastic and viscoelastic soft tissue with anisotropic fibre networks and a non-linear stress-strain relation. The material is easily extensible at small dilatations and stiffens at higher pressure values [70].

Several methods have been used to examine the structure and mechanical behaviour of vessel wall soft tissue. To identify main orientations of the fibrous network structure, specimen of the different wall layers can be prepared. Histological microscopy images of the specimen provide information on the anisotropic structure. Stress-strain relations can be examined by uniaxial and biaxial extension tests. Hereby, the ends of a specimen are clamped in a strain- and stress-measuring device. Periodic loading and unloading of the material yields a respective stress-strain-curve [68]. Controlled peel testing can give further information on the mechanical material behaviour for example in the case of dissecting vessel wall layers [106].

The structure and mechanical behaviour of vessel wall soft tissue alters with ageing and disease. It could also be shown, that the mechanical properties of the wall have an influence on the blood flow dynamics and vice versa [4].

2.2.3 Aortic blood flow

On a macroscopic level blood flows through the aorta in a pulsatile way. Hereby, the flow is mostly laminar with the formation of helices in the ascending aorta and the aortic arch [100]. The average stroke volume of one heart beat which enters the aorta through the aortic valve has been measured in male and female to $95 \pm 14\,\mathrm{ml}$ [91]. Typical values of the left ventricular volume and the resulting aortic pressure are shown in Figure 2.3. One can speak of a flow and pressure wave generated with every heart beat that travels down the arterial tree and gets reflected at bifurcations. Measured waveforms are exemplarily shown in Figure 2.6. The distensibility of the aorta mainly influences the alteration of the waveforms along the vessel. Known as the Windkessel effect, flow volume is stored in the elastic vessel during systole and passed on during diastole. This way, the initial pressure gradient gets steeper along the aorta and the flow velocity flattens along the vessel tree [104]. The speed of the pressure and flow wave propagating down the arterial tree, namely the pulse wave velocity (PWV), has become an important biomarker to measure the vessel stiffness. PWV values higher than $10\,\mathrm{m\,s^{-1}}$ can be seen as critical in the case of hypertension [93]. Arterial stiffness along with the PWV increases with age [104].

On a microscopic level, blood is a suspension of cells in the blood plasma. Around 40 % to 45 % of the blood volume consists of RBCs. RBCs tend to aggregate to a three-dimensional

microstructure, mainly rouleaux, at low shear rates, which is dispersed at higher shear rates. Furthermore, RBCs tend to align with the flow field towards the centre of a vessel. Blood plasma behaves approximately like a Newtonian fluid with a linear stress-strain relation. The dynamics of aggregation and dispersion of blood cells leads to a shear thinning and thixotropic rheology [45]. This means, that the apparent viscosity decreases with increasing shear strain and with the duration of deformation. After a period of high shear strain, when the flow reaches an equilibrium state, the apparent viscosity increases again.

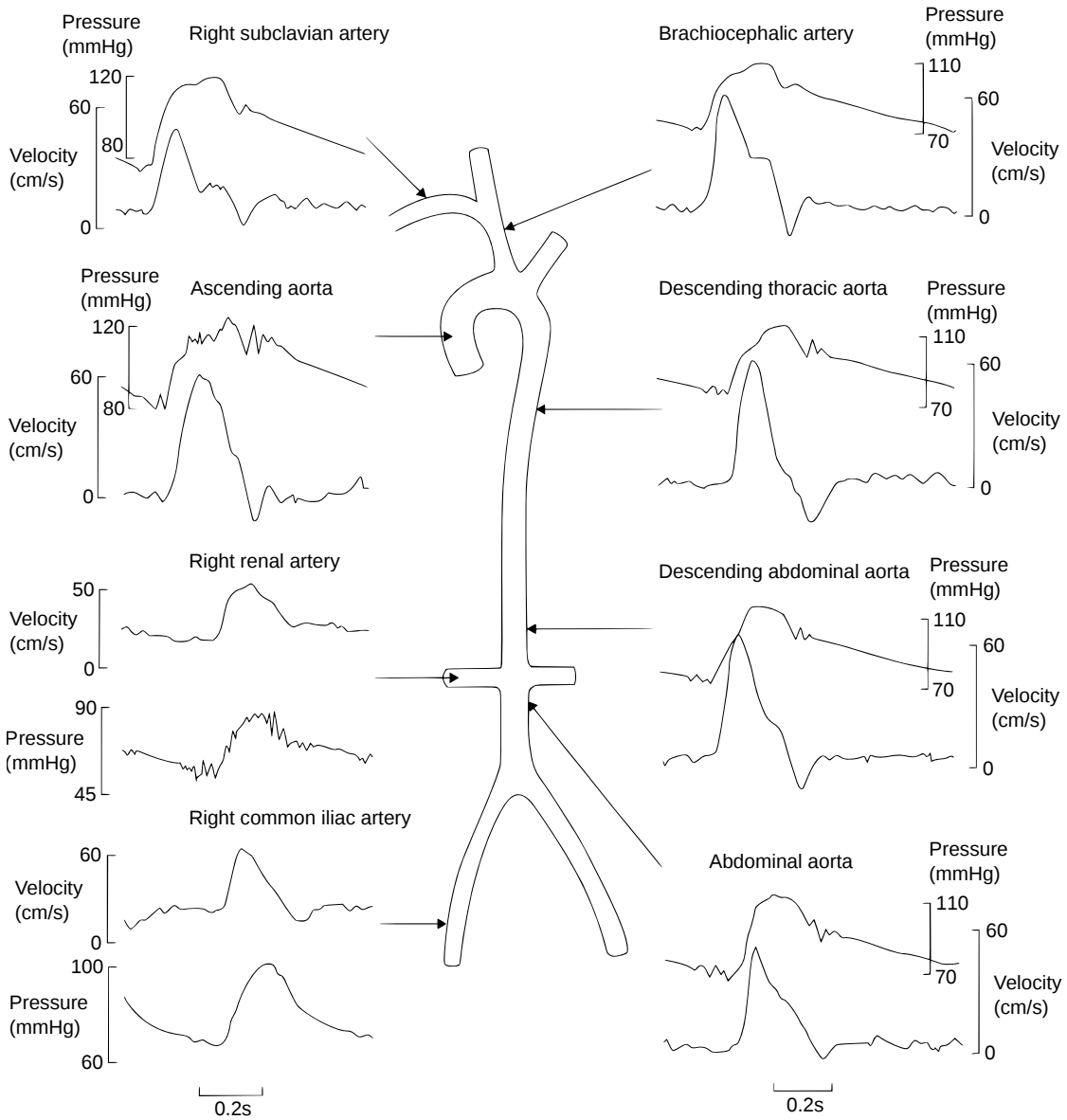

Figure 2.6: Waveforms of the pressure and the velocity in the main arteries of a human, adapted from [104]. The measurements were taken by diagnostic cardiac catheterisation.

2.2.4 Common aortic diseases

In the following a brief overview of most occurring forms of aortic disease is given. For detailed information the interested reader is referred to [104].

Atherosclerosis

A leading cause of cardiovascular disease is given by atherosclerosis. It typically emerges in the systemic circulation with a chronicle inflammation of vessel wall tissue. Usually initiated by a damage of endothelial cells, plaque gets deposited in the vessel wall. Besides the stiffening of the vessel wall it can lead to various complications. The plaque can either grow into the lumen of the vessel inducing a stenosis or it can weaken the connective vessel wall tissue with a dilatation to an aneurysm. In the case that the endothelium breaks open, a thrombus can be formed. If such a blood clot gets detached, it can lead to an embolisation of downstream arteriols. Depending on the location of an embolisation this can cause a heart attack or a stroke. Increased age, hypertension and cigarette smoking belong to the severest risk factors for atherosclerosis.

Marfan syndrome

A congenital defect of connective tissue, the Marfan syndrome can lead to cardiovascular abnormalities. With this condition, the aorta can degenerate due to a lack of aortic elastin. Vessel dilatation, aortic dissection and increased risk of vessel wall rupture belong to the effects.

Aortic aneurysms

60 % of thoracic aortic aneurysms appear in the ascending aorta. Normally, the aorta dilates at a low rate with ageing. Aneurysmatic vessels usually have much higher dilatation rates. Most often, it is caused by connective tissue weakness or high wall stress due to hypertension. The estimation of rupture risk is mainly based on the diameter of the vessel. A diameter over 5.5 cm is seen as critical [66], but discussed controversially [108]. Complementary biomarkers are needed to improve the risk stratification of aortic rupture. In most cases, a diseased vessel segment has to be replaced.

Aortic dissection

Along with the formation of an aneurysm in the ascending aorta, a dissection of the vessel wall can occur. The risk of aortic dissection is especially high for patients with Marfan syndrome. Hereby, vessel wall layers separate leading to blood entering a false lumen between the disrupted layers. This leads to a further weakening of the aorta and an increased risk of rupture. Surgery often includes the replacement of the ascending aorta and the aortic valve. Another method of treatment is endovascular repair with an expandable stent graft.

Aortic insufficiency

An insufficient function of the aortic valve is given if the valve leaflets don't close properly during diastole. This leads to a back-flow of blood from the ascending aorta to the left ventricle

of the heart. The most frequent causes for insufficiency of the aortic valve include dilatation of the aortic root and aortic dissection. In severe cases, symptomatic aortic insufficiency has to be treated with aortic valve replacement.

Aortic stenosis

With ageing and the permanent load on the aortic valve, fibrosis and calcification can occur in the aortic valve. A consequence is given in the hardening and the potential narrowing of the valve opening during systole. Increased risk for this condition is given in the case of rheumatic fever or if the valve is bicuspid. Usually, the aortic valve has three leaflets. Bicuspid valves congenitally have two leaflets resulting in a higher mechanical demand over time. For both, aortic insufficiency and aortic stenosis, the heart muscle tries to compensate the blood pressure in the aorta with a higher stroke volume. This leads to a thickening of the myocardium. Severe symptomatic valve stenosis can also be treated with the replacement of the valve.

2.2.5 Medical imaging for cardiovascular diagnosis

An overview on the assessment of the aorta by medical imaging techniques is given in [38]. Medical imaging provides information on the conditions of cardiovascular patients in a usually non-invasive way. It is an essential part of medical diagnosis for most cardiovascular diseases. Beyond that, numerical simulations can be calibrated patient-specifically by medical imaging data especially in terms of computational geometries and boundary conditions. In the following, three imaging modalities are briefly described, which are commonly used for the assessment of aortic disease.

Sonography / Ultrasound (US)

Ultrasound imaging devices utilise the reflection of sound waves at acoustic impedance transitions in the examined soft tissue. The strength of an echo response can be visualised in grey-scale images. Mainly two types of sonography are used for diagnosis of cardiovascular disease: Transthoracic echocardiography (TTE) and transoesophageal echocardiography (TOE). For TTE, the ultrasound transducer is applied to the chest. With TOE, the inner part of the organs can be examined by a transducer inserted through the oesophagus. Both of the techniques are suitable for displaying different parts of the heart and the aortic morphology and to assess heart valve insufficiency. TOE is more invasive than TTE but provides for some parts a better imaging view and resolution. Sonography is most frequently used for the initial imaging-based examination due to its ease of use and high availability compared to other imaging methods. After an initial assessment by sonography, the medical assessment often has to be complemented by CT or MRI [38].

Computed tomography (CT)

Computed tomography based on X-ray technology visualises the X-ray attenuation coefficient of the examined soft tissue material. Hereby, cross-sections of the body are scanned by X-rays from various encircling angles. Application of the inverse Radon transformation yields a grey-scale image of the respective tomographic slice. For angiography, a contrast agent can

be injected to the blood circulation to highlight vessels and blood flow. The resulting three-dimensional CT image enables the detection of most aortic diseases and related morphologic abnormalities. Image acquisition is usually achieved in a short time and CT has a high diagnostic accuracy for several aortic diseases [38]. Drawbacks are given with the applied ionising radiation and contrast agents can cause allergic reactions. A recent review on CT imaging is given by [58].

Magnetic resonance imaging (MRI)

The spin orientation of the bodies hydrogen protons can be modulated by an external magnetic field. The agglomeration of proton spin orientations itself induces a magnetic field that can be measured. Magnetic resonance imaging utilises these mechanisms by stimulating the spins and measuring the magnetic response signal. Applying a spatial gradient in the magnetic field enables the localisation of the field response, providing a grey-scale image with well distinguishable soft tissue structures. Additionally applying gradient pulses in the magnetic excitation allows for the reconstruction of proton movement. This enables the measurement of flow over time either unidirectionally in one cut plane (2D flow MRI) or fully resolved in all three spatial dimensions (4D flow MRI). MRI scans enable the diagnosis of most aortic diseases. In comparison to CT, MRI well visualises soft tissue structures and vessels usually without the need of contrast agents. The unique feature of non-invasive flow measurement enables the examination of blood flow patterns. Further biomarkers, such as the pulse wave velocity, wall shear stress, pressure gradients and flow kinetic energy can also be computed from 4D flow MRI measurements. As patients are not exposed to ionising radiation by MRI, it is suitable for series of follow-up examinations after cardiovascular surgery. A drawback of MRI is given by its relatively low availability and long measurement duration. Recent reviews on 4D flow MRI are given with [95, 37].

2.3 A prototypical aortic phantom

Aortic phantoms enable in vitro experiments for the investigation of blood flow under controllable conditions. With phantom experiments, new biomarkers for aortic blood flow based on modern imaging techniques can be examined and validated. The flow velocity, the pressure gradient, the pulse wave velocity and derived values can be studied for different cardiovascular disease conditions. Furthermore, the design of implants can be evaluated. Making use of rapid prototyping, implants and surgical procedures can be tested with aortic phantoms.

A range of aortic phantoms have been described in the literature for various purposes, see for example [138, 35]. Usually, aortic phantoms form a closed flow circuit representing the circulation. Artificial pumps can generate a physiologically realistic pulsatile flow and pressure profile. Silicone tubes of idealised or patient-specific shape represent vessel segments. Artificial valves can be used to either just control the direction of the flow or to themselves be investigated on. Mechanisms can be included to control peripheral flow resistance. To enable the usage in an MRI scanner, all of the components of a phantom experiment have to be non-metallic. With CT or MRI the geometry can be scanned and with 2D or 4D flow MRI, the velocity field can be observed, see section 2.2.5. The pressure profile at distinct positions can be measured by inserted catheters.

Aortic phantom experiments can be used to validate numerical frameworks for the simulation of aortic blood flow, as it is done for example in [86].

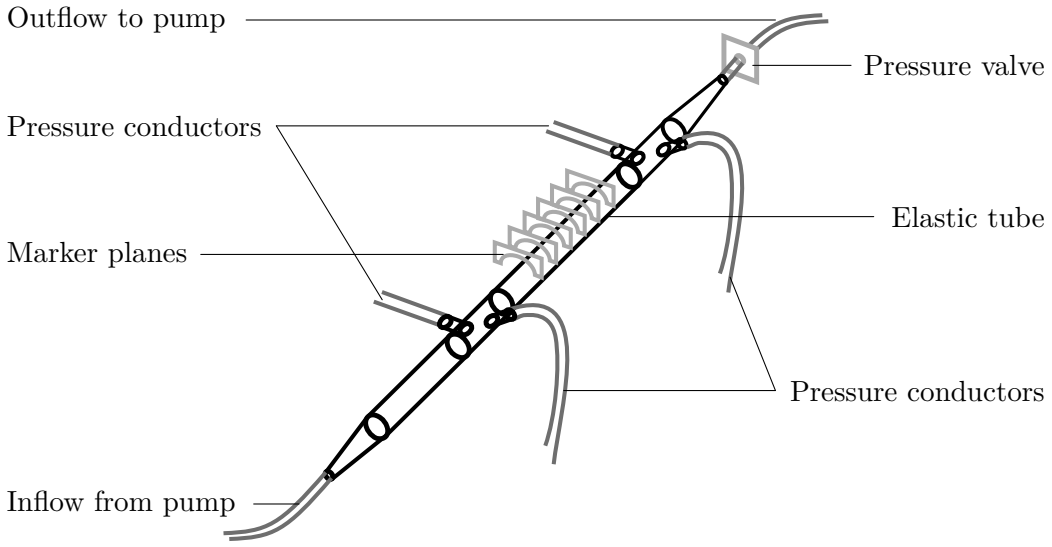

Figure 2.7: Experimental setup of a prototypical aortic phantom adopted from Delles et al. [31]. A pump drives a blood-like fluid through the elastic tube in a pulsatile way. After the elastic tube, a pressure valve acts as a resistor before the fluid flows back to the pump. The pressure conductors enable catheter-based pressure measurements in the elastic tube. The marker planes set the locations of 2D flow MRI measurements.

The numerical framework presented in this thesis is validated by means of a prototypical aortic phantom experiment described in [31]. For providing the measurement data of the in vitro experiment and the support in processing the data, the authors Michael Delles and

Fabian Rengier are to be acknowledged.

The setup of the phantom is shown in Figure 2.7. The utilised fluid consists to 60 % of water and 40 % glycerine resulting in a blood-like density of approximately $1101.45\,\mathrm{kg\,m^{-3}}$ and a dynamic viscosity of $4.545 \times 10^{-3}\,\mathrm{N\,s\,m^{-2}}$. To characterise the elasticity of the artificial vessel segment, the Young's modulus of the elastic tube material was measured to $642 \pm 193\,\mathrm{kPa}$. The pulsatile flow is driven by a pump and first passes a straight tube for full flow development. There are entry ports connected to pressure conductors before and after the elastic tube segment enabling catheter-based pressure measurements. A number of markers is located along the elastic tube. The markers define the location of the 2D flow MRI measurements and of the pressure measurements. The downstream resistance is controlled by a pressure valve after the elastic tube. The measured data includes the morphology and the time-resolved 2D flow MRI and the relative total pressure at the marker planes. The imaging techniques are further described in section 2.2.5. The measured data is compared to the simulation results of this work in section 6.1.2.

3 Mathematical modelling

This chapter introduces mathematical models of blood flow through the aorta and the modelling of occurring uncertainties. Basic information on the biomechanics is taken from the books [45, 49, 50, 104]. General flow problems in the vascular system are dealt with in [113]. An overview and review of rheology modelling in hemodynamical flow is given in [52]. [67] is a basis for elasticity modelling. Elasticity models for vessel soft tissue in particular are described in [71]. The cardiovascular system can be modelled on several scales and dimensions, on which an overview is given in [75, 47, 101]. Details on the coupling of blood flow and vessel wall elasticity with fluid-structure interaction are adopted from [51, 45]. Uncertainty modelling and methods for Uncertainty Quantification are described in [87, 131].

3.1 Biomechanical basics

On a microscopic level, as described in section 2.2, blood can be seen as a suspension of cells in the blood plasma and vessel wall soft tissue exhibits a cellular structure. To investigate the biomechanical dynamics on a macroscopic level, blood flow and soft tissue can be modelled as a continuum. The continuum is defined on the respective domain $\mathcal{D}_t$ of the considered geometry at time $t \in \mathbb{R}_+$.

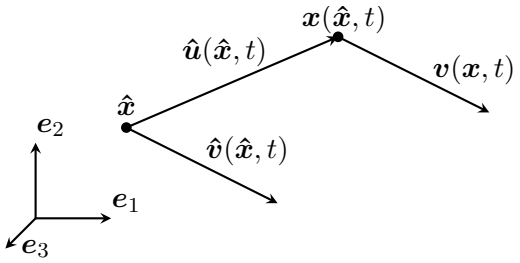

Figure 3.1: Displacement $\boldsymbol{u}$ and velocity $\boldsymbol{v}$ of a material point. The Cartesian coordinate system is indicated by the unit vectors $\boldsymbol{e}_i$, $i = 1, \ldots, d$.

Continuum mechanics describe the behaviour of mass points in space and time with respect to its coordinates $\boldsymbol{x} = (x_1, \ldots, x_d)$, where d is the dimension of the considered space. The coordinates can be designated by a reference position $\hat{\boldsymbol{x}} \in \hat{\mathcal{D}}$ and a point in time $t \in I$:

$$\boldsymbol{x} = \boldsymbol{x}(\hat{\boldsymbol{x}}, t) \in \mathcal{D}_t. \tag{3.1}$$

The displacement from the reference position can then be defined as

$$\hat{\boldsymbol{u}}(\hat{\boldsymbol{x}}, t) := \boldsymbol{x}(\hat{\boldsymbol{x}}, t) - \hat{\boldsymbol{x}}. \tag{3.2}$$

The velocity of the material point is given by the time derivative of its position:

$$\hat{\boldsymbol{v}}(\hat{\boldsymbol{x}}, t) := \frac{\mathrm{d}}{\mathrm{d}t}\boldsymbol{x}(\hat{\boldsymbol{x}}, t). \tag{3.3}$$

Observing a velocity field at a fixed position $\boldsymbol{x}$, it can be expressed via the inverse of the position mapping at a time $t \in I$:

$$\boldsymbol{v}(\boldsymbol{x}, t) := \hat{\boldsymbol{v}}(\boldsymbol{x}_t^{-1}(\boldsymbol{x}), t). \tag{3.4}$$

See Figure 3.1 for an illustration of the position, displacement and velocity of a material point.

3.1.1 Lagrangian and Eulerian specification

Quantities $\chi : \mathcal{D}_t \times I \to \mathbb{R}$ can be observed either from an associated material point $\boldsymbol{x}(\hat{\boldsymbol{x}}, t)$ (Lagrangian frame of reference) or from a fixed position $\boldsymbol{x}$ (Eulerian frame of reference). For example, the definition of the velocity of a material point (3.3) is given in the Lagrangian specification. Hereby, $\frac{\mathrm{d}}{\mathrm{d}t}$ is also called total time derivative. The rate of change of a quantity in the Eulerian frame of reference $\frac{\partial}{\partial t}$ can be derived with the multidimensional chain rule:

$$\frac{\mathrm{d}}{\mathrm{d}t}\chi(\boldsymbol{x}, t) = \frac{\partial}{\partial t}\chi(\boldsymbol{x}, t) + \nabla \cdot (\chi(\boldsymbol{x}, t)\boldsymbol{v}(\boldsymbol{x}, t)). \tag{3.5}$$

3.1.2 Conservation laws

In a continuum, several assumptions can be made on the conservation and change of mechanical quantities in arbitrary subdomains $V_t \subset \mathcal{D}_t$. Equations can be derived for the mass of a material volume, the momentum and angular momentum as well as the energy. With additional assumptions on the material laws the equations can be closed with respect to the number of unknowns. The obtained system of equations describe the considered mechanical behaviour of a material and can be formulated as an initial boundary value problem. For this work, the conservation of mass, momentum and angular momentum is considered in the following way.

Mass conservation

The mass of a material volume V_t is calculated by integrating the density ρ over V_t. The volume mass of is typically assumed to be constant in classical mechanics, hence

$$\frac{\mathrm{d}}{\mathrm{d}t}\int_{V_t} \rho \mathrm{d}\boldsymbol{x} = 0. \tag{3.6}$$

As equation (3.6) is stated for any volume V_t, the integral can be omitted and it is in the Lagrangian frame of reference

$$\frac{\mathrm{d}}{\mathrm{d}t}\rho = 0, \quad \text{in } \mathcal{D}_t \times I. \tag{3.7}$$

Momentum conservation

The momentum of a material volume

$$\frac{\mathrm{d}}{\mathrm{d}t}\int_{V_t}\rho\boldsymbol{v}\mathrm{d}\boldsymbol{x} \tag{3.8}$$

is typically assumed to change with a momentum flux given by a force on the surface of the volume and a force f acting on the volume. The surface force can be expressed by the Cauchy stress tensor $\boldsymbol{\sigma}$ along the surface normal $\boldsymbol{\eta}$. The volume force can be defined, for example, as gravity force. Hence, the equation for the balance of momentum reads

$$\frac{\mathrm{d}}{\mathrm{d}t}\int_{V_t}\rho\boldsymbol{v}\mathrm{d}\boldsymbol{x} = \int_{\partial V_t}\boldsymbol{\sigma}\cdot\boldsymbol{\eta}\mathrm{d}\boldsymbol{s} + \int_{V_t}\rho\boldsymbol{f}\mathrm{d}\boldsymbol{x}. \tag{3.9}$$

Applying Gauß' theorem on the boundary integral and again omitting the integrals over the arbitrary volume V_t, one obtains in the Lagrangian specification

$$\frac{\mathrm{d}}{\mathrm{d}t}\rho\boldsymbol{v} = \nabla\cdot\boldsymbol{\sigma} + \rho\boldsymbol{f}, \quad \text{in } \mathcal{D}_t\times I. \tag{3.10}$$

With the conservation of mass (3.7), equation (3.10) writes in non-conservative form

$$\rho\frac{\mathrm{d}}{\mathrm{d}t}\boldsymbol{v} = \nabla\cdot\boldsymbol{\sigma} + \rho\boldsymbol{f}, \quad \text{in } \mathcal{D}_t\times I. \tag{3.11}$$

Angular momentum conservation

The balance of angular momentum of a material volume

$$\frac{\mathrm{d}}{\mathrm{d}t}\int_{V_t}\boldsymbol{x}\otimes(\rho\boldsymbol{v})\mathrm{d}\boldsymbol{x} = \int_{\partial V_t}\boldsymbol{x}\otimes(\boldsymbol{\sigma}\cdot\boldsymbol{\eta})\mathrm{d}\boldsymbol{s} + \int_{V_t}\boldsymbol{x}\otimes(\rho\boldsymbol{f})\mathrm{d}\boldsymbol{x}. \tag{3.12}$$

together with the conservation of mass (3.7) and momentum (3.11) implies the symmetry of the stress tensor

$$\boldsymbol{\sigma} = \boldsymbol{\sigma}^T. \tag{3.13}$$

The basic conservation equations for modelling the blood flow and vessel wall motion in this work can be summarised written in the Lagrangian frame of reference as follows

$$\frac{\mathrm{d}}{\mathrm{d}t}\rho = 0, \qquad \text{in } \mathcal{D}_t\times I, \tag{3.14}$$

$$\rho\frac{\mathrm{d}}{\mathrm{d}t}\boldsymbol{v} = \nabla\cdot\boldsymbol{\sigma} + \rho\boldsymbol{f}, \quad \text{in } \mathcal{D}_t\times I, \tag{3.15}$$

$$\text{with } \boldsymbol{\sigma} = \boldsymbol{\sigma}^T.$$

In a three-dimensional space, (3.14) and (3.15) represent a system of four partial differential equations involving ten unknowns, namely the density and three velocity as well as six stress components. Hence, further material laws have to be taken into account in order to close the system and state a well-posed boundary value problem.

3.2 Fluid flow

For modelling fluid flow, the conservation equations (3.14) and (3.15) are typically considered in the Eulerian frame of reference. Applying the equation of the total time derivative (3.5) yields

$$\frac{\partial}{\partial t}\rho + \nabla \cdot (\rho \boldsymbol{v}) = 0, \qquad \text{in } \mathcal{D}_t \times I. \tag{3.16}$$

$$\rho \frac{\partial}{\partial t}\boldsymbol{v} + \rho(\boldsymbol{v} \cdot \nabla)\boldsymbol{v} = \nabla \cdot \boldsymbol{\sigma} + \rho \boldsymbol{f}, \quad \text{in } \mathcal{D}_t \times I. \tag{3.17}$$

The stress tensor $\boldsymbol{\sigma}$ can be specified by defining a constitutive material law, i.e. a relation to the symmetric strain rate tensor

$$\boldsymbol{S} := \frac{1}{2}\left(\nabla \boldsymbol{v} + (\nabla \boldsymbol{v})^T\right) \tag{3.18}$$

3.2.1 Blood flow models

The composition of blood is described in section 2.1.5 and it's physiological behaviour is delineated in section 2.2.3. For the flow through arterial vessels, the influence of volume forces, gravity in particular, can be neglected

$$\boldsymbol{f} = 0. \tag{3.19}$$

Furthermore, as blood mainly consists of water, it can be assumed to be incompressible. With that, the density becomes a material constant and equation (3.16) simplifies to the continuity equation

$$\nabla \cdot \boldsymbol{v} = 0. \tag{3.20}$$

To define a constitutive expression for the stress tensor $\boldsymbol{\sigma}$, assumptions can be made on the rheology of blood. According to [49], viscometer experiments showed that the viscosity of blood depends on the hematocrit value and temperature of blood and the shear rate of the flow. Generally speaking, blood viscosity increases along with the hematocrit and decreases at increasing temperature. Blood behaves shear-thinning in a range of small shear rates, whereas one observes an approximately linear dependency of viscosity to shear rate at higher shear rates. Standard rheology experiments where done in geometries much larger than the diameter of blood cells, where blood can be considered as a homogeneous fluid. However, capillaries have diameters in the scale of the blood cell size, wherein blood can be seen as a two-phase fluid.

For larger arteries such as the aorta, Fung [49] describes different constitutive laws of blood flow behaviour for resting blood, small shear rates and sufficiently high shear rates, namely a Hooke's law, Casson's equation and the Newtonian relation, respectively. Beyond that, dynamical experiments have shown, that blood also reveals viscoelastic and thixotropic behaviour with a dependency on the shear level and strain history [124]. It has also been observed that blood cells tend to migrate from a vessel wall towards its axis leaving a fluid layer of low hematocrit next to the wall [49].

Under the assumption of an incompressible fluid for which the stress tensor is spherically symmetric at rest and it only depends on the strain rate tensor, the most general form of $\boldsymbol{\sigma}$ can be shown to be

$$\boldsymbol{\sigma} = -p\boldsymbol{I} + \phi_1\boldsymbol{S} + \phi_2\boldsymbol{S}^2. \tag{3.21}$$

In this representation, the pressure p occurs as Lagrangian multiplier. ϕ_1 and ϕ_2 are functions of the second and third principal invariants of $\boldsymbol{S}$, namely $I\!I_{\boldsymbol{S}} = \frac{1}{2}((\mathrm{tr}\boldsymbol{S})^2 - \mathrm{tr}(\boldsymbol{S}^2))$ and $I\!I\!I_{\boldsymbol{S}} = \det(\boldsymbol{S})$. For blood flow, ϕ_2 and the dependence of ϕ_1 on $I\!I\!I_{\boldsymbol{S}}$ can be assumed to be negligible. One obtains the expression for generalised Newtonian fluids:

$$\boldsymbol{\sigma} = -p\boldsymbol{I} + 2\mu(\gamma)\boldsymbol{S}, \tag{3.22}$$

where the viscosity μ depends on the shear rate

$$\gamma := \sqrt{2\boldsymbol{S} : \boldsymbol{S}}. \tag{3.23}$$

More details and a discussion of various Generalised Newtonian models for blood can be found in [124]. The choice of a blood rheology model typically depends on the respective application scenario. Most models put an emphasis on specific physiological properties of blood flow but neglect others. For the flow of blood through large arteries such as the aorta, also a linear relation between stress and strain rate can be assumed. In this case, however, virtual experiments have shown significant discrepancies in the evaluation of specific flow parameters such as the wall shear stress [90].

Incompressible Navier-Stokes equations

This work considers the functional modelling of a prototypical aortic phantom as described in section 6.1. The fluid used for the phantom is a mixture of water and glycerine which behaves mainly Newtonian. Hence, a linear relation of stress and strain rate can be assumed and the viscosity does not depend on the shear rate. Accordingly, equation (3.22) simplifies to:

$$\boldsymbol{\sigma} = -p\boldsymbol{I} + 2\mu\boldsymbol{S}. \tag{3.24}$$

Insertion in the equations for mass and momentum conservation, (3.16) and (3.17) yields the incompressible Navier-Stokes equations (NSE) as stated in the following. Equation (3.17) is additionally divided by the density ρ and the kinematic viscosity $\nu = \mu/\rho$ is used in the notation. For the phantom, one can assume that external volume forces, especially the gravity can be neglected $f = 0$.

$$\begin{aligned} \nabla \cdot \boldsymbol{v} &= 0, \quad \text{in } \mathcal{D}_t \times I, \\ \frac{\partial}{\partial t}\boldsymbol{v} + (\boldsymbol{v}\cdot\nabla)\boldsymbol{v} - \nu\nabla\cdot\left(\nabla\boldsymbol{v} + (\nabla\boldsymbol{v})^T\right) + \frac{1}{\rho}\nabla p &= 0, \quad \text{in } \mathcal{D}_t \times I. \end{aligned} \tag{3.25}$$

The NSE are a system of partial differential equations, being non-linear in the velocity field $\boldsymbol{v}$. Due to the derivatives in space and time, the system is parabolic. An overview on the theory on existence and uniqueness of solutions of the NSE is given in [133].

3.2.2 Inflow and outflow boundary configuration

The measurement segment of the aortic phantom, which corresponds to the aorta, is modelled as three-dimensional geometry to enable the examination of the flow dynamics in all spatial dimensions. For the up- and downstream parts of the phantom, reduced models are used. They are coupled to the model of the main segment by boundary conditions for the in- and outflow. Standard fluid boundary conditions specify either velocity or pressure profiles at the in- and outflow planes.

Inflow boundary condition

As described in section 2.3, the velocity profile is measured over a periodic cycle at each measurement plane. This allows for setting the inflow boundary at the position of the first measurement plane and defining an inflow velocity boundary condition by means of the measured flow through the plane. The 2D flow MRI measurement provides flow values Q_i, $i = 0, \dots, N$ for the first plane at $N = 127$ points in time $t_i \in I$. In general, the time steps of the numerical simulation do not correspond to the measurement time stamps and the intervals are usually shorter. Hence, the flow values have to be interpolated. A periodic interpolation of the flow profile could be given by the trigonometric Fourier-Interpolation. Using Fourier-interpolation can however generate unphysiological oscillations between time stamps. For a smooth interpolation using only local information, it is suitable to use a cubic periodic spline-interpolation as described in [48]. A cubic spline fulfils

$$q \in C^2(I), \text{ with } q(t_i) = Q_i, \quad i = 0, \dots, N$$

and is piecewise defined by cubic polynomials

$$q|_{[t_i, t_{i+1}]}(t) = q_i(t) := a_i + b_i t + c_i t^2 + d_i t^3, \quad i = 0, \dots, N. \tag{3.26}$$

The following periodic smoothness conditions hold for the first and second derivative of the spline.

$$q_i'(t_{i+1 \bmod N+1}) = q_{i+1 \bmod N+1}'(t_{i+1 \bmod N+1}), \quad i = 0, \dots, N, \tag{3.27}$$

$$q_i''(t_{i+1 \bmod N+1}) = q_{i+1 \bmod N+1}''(t_{i+1 \bmod N+1}), \quad i = 0, \dots, N. \tag{3.28}$$

Based on these smoothness conditions, a linear system of equations can be derived from which the polynomial coefficients a_i, b_i, c_i, d_i can be calculated. Details can be found in [48].

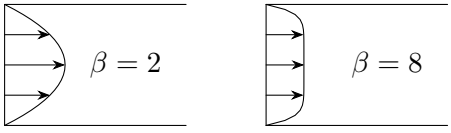

Figure 3.2: Illustration of two different parameter choices for β in the generalised Poisseuille inflow profile (3.29).

To obtain a smooth distribution of the flow velocity over the inflow boundary surface $\mathcal{B}_{\text{in}}$, the flow value q is mapped to a generalised Poisseuille profile [45]:

$$\boldsymbol{v}^{\text{in}}(r,t) := q(t)\frac{\beta+2}{\beta\pi R^2}\left(1 - \frac{r^\beta}{R^\beta}\right)\boldsymbol{\eta}, \quad t \in I, \text{ on } \mathcal{B}_{\text{in}}, \tag{3.29}$$

where r denotes the distance from the centre of the boundary surface and $\boldsymbol{\eta}$ is the normal vector that points to the inside of the geometry. As the measured spatial distribution of the velocity field shows a broader extension of the peak flow field in the centre of the vessel than a standard Poisseuille profile with $\beta = 2$, higher values for the parameter $\beta > 2$ should be chosen. The standard Poisseuille profile, $\beta = 2$, is compared to the case $\beta = 8$ in Figure 3.2.

Outflow boundary condition

For the outflow boundary conditions in aortic blood flow simulations, reduced models of the systemic circulation on different scales can be used [45]. A zero-dimensional approach is given by using the analogy to electrical circuits, where the flow can be seen as current and the pressure as voltage. In this scope, single vessel segments can be seen as resistors and the peripheral vascular tree can be modelled as a network of zero-dimensional elements of resistors, capacitors and inductors. A further model reduction leads to the so called Windkessel models, which account for the resistance of the capillary system and the temporal flow volume retention in distensible vessels. In the case of the aortic phantom, the downstream resistance is controlled by a pressure valve, see Figure 2.7. Its function can be modelled by a resistance boundary condition as described in [78]:

$$p^{\text{out}}(t) = \frac{\sqrt{\rho\beta}}{\sqrt{2}A^{5/4}} Q^{\text{out}}(t), \quad \beta := \frac{\sqrt{\pi}hY}{1-\gamma^2}. \tag{3.30}$$

The model relates the value for the pressure boundary condition p^{out} to the outflow value v^{out} by means of the surface area A, the vessel wall thickness h, and the elasticity material parameters Young's modulus Y and Poisson's ratio γ.

3.3 Vessel wall elasticity

In an analogues manner to fluid flow dynamics, elastic materials can be modelled on the basis of the conservation of mass and momentum. The equations for elastic deformations are typically considered in the Lagrangian frame of reference as they are stated in (3.14) and (3.15). The formulation considers the dynamics in the deformed state with respect to a reference configuration. In the following, variables defined with respect to the reference configuration are written with the hat symbol, i.e. for the conservation of momentum:

$$\hat{\rho}\frac{\mathrm{d}^2}{\mathrm{d}t^2}\hat{\boldsymbol{u}} = \hat{\nabla}\cdot\hat{\boldsymbol{\sigma}} + \hat{\rho}\hat{\boldsymbol{f}}, \quad \text{in } \hat{\mathcal{D}}\times I. \tag{3.31}$$

The mechanical behaviour of a specific solid material can be constituted by defining an expression for the stress tensor $\hat{\boldsymbol{\sigma}}$. First, basic definitions for deformation tensors and stress measures are given in the following.

Strain measures

Applying the gradient operator to the position of a material point $\boldsymbol{x}$ with respect to the reference configuration $\hat{\nabla} = \left[\frac{\partial}{\partial\hat{\boldsymbol{x}}_i}\right]_{i=1,\dots,d}$ one gets the deformation gradient tensor:

$$\hat{\boldsymbol{F}} := \hat{\nabla}\boldsymbol{x}, \text{ with } \hat{\boldsymbol{F}} = \hat{\nabla}\hat{\boldsymbol{u}} + \boldsymbol{I}. \tag{3.32}$$

In general, $\hat{\boldsymbol{F}}$ is an unsymmetrical tensor that describes the strain and the rotation of a solid material. We denote its determinant with

$$\hat{J} := \det(\hat{\boldsymbol{F}}). \tag{3.33}$$

A symmetric and rotational invariant measure for strain is given by the Green-Lagrange strain tensor:

$$\begin{aligned}\hat{\boldsymbol{E}} &= \frac{1}{2}\left(\hat{\boldsymbol{F}}^T\hat{\boldsymbol{F}} - \boldsymbol{I}\right) \\ &= \frac{1}{2}\left((\hat{\nabla}\hat{\boldsymbol{u}})^T\hat{\nabla}\hat{\boldsymbol{u}} + (\hat{\nabla}\hat{\boldsymbol{u}})^T + \hat{\nabla}\hat{\boldsymbol{u}}\right).\end{aligned} \tag{3.34}$$

For small displacements values $\boldsymbol{u}$, the second order term is negligibly small and $\boldsymbol{E}$ can be reduced to Cauchy's infinitesimal strain tensor

$$\hat{\boldsymbol{\epsilon}} = \frac{1}{2}\left((\hat{\nabla}\boldsymbol{u})^T + \hat{\nabla}\boldsymbol{u}\right). \tag{3.35}$$

Stress measures

In structural mechanics, the stress tensor $\boldsymbol{\sigma}$ as denoted in equation (3.15) is also called Cauchy stress tensor. The Cauchy stress tensor is a measure for the stresses in the deformed configuration related to the material's geometry in the deformed state. The reference system for the stress measure can be changed: The first Piola-Kirchhoff stress tensor $\hat{\boldsymbol{\sigma}}$ describes the stress in the deformed configuration related to the geometrical reference deformation.

$$\hat{\boldsymbol{\sigma}} = \hat{J}\boldsymbol{\sigma}\hat{\boldsymbol{F}}^{-T}. \tag{3.36}$$

The second Piola-Kirchhoff stress tensor $\hat{\boldsymbol{F}}^{-1}\hat{\boldsymbol{\sigma}}$ describes the stress in the reference configuration related to the geometrical reference deformation:

$$\hat{\boldsymbol{F}}^{-1}\hat{\boldsymbol{\sigma}} = \hat{J}\hat{\boldsymbol{F}}^{-1}\boldsymbol{\sigma}\hat{\boldsymbol{F}}^{-T}. \tag{3.37}$$

If known, a relation between stress and deformation can be derived from the energy functional for elastic deformation. It then holds for the first and second Piola-Kirchhoff stress tensor, respectively

$$\hat{\boldsymbol{\sigma}}^T = \frac{\partial \hat{W}}{\partial \hat{\boldsymbol{F}}}, \quad \hat{\boldsymbol{F}}^{-1}\hat{\boldsymbol{\sigma}} = \frac{\partial \hat{W}}{\partial \hat{\boldsymbol{E}}}. \tag{3.38}$$

3.3.1 Aortic wall soft tissue models

An overview on the structure of aortic wall soft tissue is given in section 2.2.2. The aortic vessel wall is composed of several soft tissue layers with different material behaviour. Through load tests one can try to determine models for the mechanical stress-strain relation of either the tissue composite or the different components. A comprehensive introduction to these investigations is given in [49]. Further constitutive equations and findings for biological soft tissue are described in [71]. In general, one can say, that the soft tissue layers of the aortic wall each show non-linear viscoelastic properties in the stress-strain relation. Oriented fibres lead to anisotropy. Through cyclically repeated loading the material can be preconditioned. At constant strain, stress relaxation can be observed as well as creep deformation at constant stress. Furthermore aortic wall tissue is constantly under stress, as the zero-stress state usually tends to be unfolded, if the wall is cut longitudinally. Alterations of mechanical behaviour can be caused by ageing or disease. The ageing aorta commonly stiffens and calcification can occur. Diseased vessel walls can also show weakened stiffness. Additionally, they can contain further materials such as deposits of lipids with their own biomechanics properties. An example for an anisotropic hyperelastic model of the aortic vessel wall is given in [53].

Saint Venant-Kirchhoff material

The prototypical phantom as considered in this work and described in section 2.3 is assumed to consist of a homogeneous rubber-like material. For the small range of occurring strain, the Saint Venant-Kirchhoff (STVK) model can be used for the definition of the stress-strain relation [67]. The strain energy function of the STVK model reads

$$\hat{W} = \frac{1}{2}\lambda_1(\mathrm{tr}\hat{\boldsymbol{E}})^2 + \lambda_2\hat{\boldsymbol{E}}^2. \tag{3.39}$$

Using equation (3.38), one gets an expression for the second Piola-Kirchhoff stress tensor, that is linear in $\hat{\boldsymbol{E}}$:

$$\hat{\boldsymbol{F}}^{-1}\hat{\boldsymbol{\sigma}} = \lambda_1(\mathrm{tr}\hat{\boldsymbol{E}})\boldsymbol{I} + 2\lambda_2\hat{\boldsymbol{E}}. \tag{3.40}$$

Hereby, the Lamé coefficients λ_1 and λ_2 relate to Young's modulus Y and Poisson's ratio γ as follows

$$\lambda_1 = \frac{Y\gamma}{(1+\gamma)(1-2\gamma)}, \quad \lambda_2 = \frac{Y}{2(1+\gamma)}. \tag{3.41}$$

The Young's modulus is a measure of the stiffness of a given material. The Poisson's ratio gives information on the compressibility. It can be set to nearly incompressible $\gamma = 0.45$ for the considered phantom.

Inserting the STVK model (3.40) in the equation for the balance of momentum (3.31) and omitting volume forces $\hat{f}$, one gets the following hyperbolic system of partial differential equations, which is non-linear in the displacement $\hat{\boldsymbol{u}}$.

$$\rho \frac{\mathrm{d}^2}{\mathrm{d}t^2} \hat{\boldsymbol{u}} = \hat{\nabla} \cdot \left(\hat{\boldsymbol{F}} \left(\lambda_1 \mathrm{tr}(\hat{\boldsymbol{E}}) \boldsymbol{I} + 2\lambda_2 \hat{\boldsymbol{E}} \right) \right), \quad \text{in } \hat{\mathcal{D}} \times I. \tag{3.42}$$

The density is considered to be a constant $\rho \in \mathbb{R}_+$ in the STVK model. On overview on the theory for existence and uniqueness of solutions can be found in [140].

3.3.2 Elasticity boundary conditions

The geometry of the vessel and with that it's boundaries are given by an MRI-Scan of the phantom. Typically, displacement and force boundary conditions can be defined to close the system of equations and to define a boundary value problem. By means of a zero-displacement boundary condition the computational model is constantly fixed at the boundary of the inflow $\mathcal{B}_{\text{in}}$ and the outflow $\mathcal{B}_{\text{out}}$.

$$\hat{\boldsymbol{u}}|_{\mathcal{B}_{\text{in}}} \equiv 0, \quad \hat{\boldsymbol{u}}|_{\mathcal{B}_{\text{out}}} \equiv 0. \tag{3.43}$$

The vessel segment is assumed to be able to move freely without any forces other than the fluid forces acting on it:

$$\hat{\boldsymbol{f}}|_{\mathcal{B}} \equiv 0. \tag{3.44}$$

3.4 Fluid-structure interaction

The biomechanics of blood flow through large arteries is mainly determined by the flow itself and by the elastic deformation of the vessel wall. As described in section 3.1, fluid flow dynamics and elastic material behaviour are based on the same conservation laws, but lead to a different system of partial differential equations. At the interface between the two phases, the model is supplemented with coupling conditions for the mathematical equations. We denote the time-dependent domains for the fluid flow and the solid material deformation with $\mathcal{D}_t^{\mathrm{f}}$ and $\mathcal{D}_t^{\mathrm{s}}$, respectively. On the common boundary of both domains $\mathcal{B}_t^{\mathrm{i}} := \mathcal{D}_t^{\mathrm{f}} \cap \mathcal{D}_t^{\mathrm{s}}$ it naturally holds, that the displacement of both domains is equal. This is given with respect to the reference coordinates by

$$\hat{\boldsymbol{u}}|_{\hat{\mathcal{D}}^{\mathrm{f}}} = \hat{\boldsymbol{u}}|_{\hat{\mathcal{D}}^{\mathrm{s}}}, \quad \text{on } \hat{\mathcal{B}}^{\mathrm{i}}, \quad \text{for } t \in I. \tag{3.45}$$

Additionally, the traction forces, which are defined by the respective stress tensor in normal direction $\boldsymbol{\eta}$, of both phases are equal at the interface:

$$\boldsymbol{\sigma}|_{\mathcal{D}_t^{\mathrm{f}}} \cdot \boldsymbol{\eta}_f = \boldsymbol{\sigma}|_{\mathcal{D}_t^{\mathrm{s}}} \cdot \boldsymbol{\eta}_s, \quad \text{on } \mathcal{B}_t^{\mathrm{i}}, \quad \text{for } t \in I. \tag{3.46}$$

In the following, methods for establishing the coupling equations (3.45), (3.46) are described. Further details can be found in [51].

Partitioned vs. implicit coupling

In principle, the coupling conditions (3.45) and (3.46) can be established in a partitioned way using two distinct solvers for the sub-problems of fluid flow and elasticity. Another approach is that of using implicit coupling in a single, monolithic solver for the full problem. Partitioned routines iteratively solve one sub-problem and set the result at the interface as a boundary condition for the other sub-problem. A weak coupling is given, if each sub-problem is only solved once per time step. A strongly coupled routine iterates several times between the two sup-problems until a requested accuracy is reached in each time-step. In monolithic approaches, the coupling conditions are often fulfilled implicitly. Usually the stability of partitioned routines with strong coupling is superior to weakly coupled routines and monolithic methods usually are more stable than partitioned methods. A numerical comparison of different coupling approaches is given, e.g. in [72].

3.4.1 Frame of reference handling

As described in section 3.1, fluid flow problems are typically formulated in the Eulerian frame of reference and structure deformation problems in the Lagrangian frame of reference. There are different approaches to combine the two perspectives. An overview is given in the review [72].

As for the immersed boundary [110, 12] and the fictitious domain methods [60, 114], the fluid and structure problems are kept in the Eulerian and Lagrangian frame of reference, respectively. Hereby, the solid domain typically lies in the fluid domain and the numerical mesh of the fluid domains overlays the solid domain. The boundary of the solid domain is incorporated in the fluid problem via interface tracking, for example by means of a level

set method or a Lagrangian multiplier. Immersed boundary and fictitious domain methods follow the partitioned approach with separate solvers for the fluid and the structure problem. The fictitious domain method has been used for FSI-simulations of the aortic valve in [62, 63].

By means of a deformation mapping between the perspectives, the Lagrangian and the Eulerian frame can be combined for the use in monolithic solvers. In the fully Eulerian approach [143], the structural domain is mapped to the Eulerian frame of reference in order to obtain a monolithically coupled FSI solver. In this case the solid boundary can be tracked by a level set method.

Methods incorporating the immersion of the solid structure in the fluid domain are especially suited for surround-flow problems. In case of distinct solid structures, also contact problems can be modelled.

Conforming mesh methods adapt the fluid domain to the Lagrangian perspective of the structure deformation. The fluid mesh is either explicitly moved in alignment with the structure or a deformation mapping from a reference domain to the current state is used. A standard method for the latter is given by the Arbitrary Lagrangian Eulerian (ALE) approach which is also utilised in this work. A description of the ALE method can be found for example in [73]. The ALE method is especially suited for FSI problems where the structure forms an outer boundary of the fluid domain as it is the case for elastic vessels. When contact of distinct structures occurs however, the fluid mesh or the deformation mapping can degenerate.

3.4.2 Arbitrary Lagrangian Eulerian formulation

The deformation of the structural domain can be described by means of its displacement vector field. The deformation of the adjacent fluid domain can be described by the displacement from a reference configuration, which is called ALE field. The ALE field is defined as

$$\begin{aligned} \hat{\mathcal{A}} : \hat{\mathcal{D}}^{\mathrm{f}} \times I &\to \mathcal{D}_t^{\mathrm{f}}, \\ (\hat{\boldsymbol{x}}, t) &\mapsto \boldsymbol{x}(\hat{\boldsymbol{x}}, t). \end{aligned} \tag{3.47}$$

Analogously to the deformation of the solid domain, the ALE field defines a displacement field

$$\hat{\boldsymbol{u}}(\hat{\boldsymbol{x}}, t) := \hat{\mathcal{A}}(\hat{\boldsymbol{x}}, t) - \hat{\boldsymbol{x}}, \quad \text{for } \hat{\boldsymbol{x}} \in \hat{\mathcal{D}}^{\mathrm{f}},\ t \in I. \tag{3.48}$$

An illustration of a displacement defined by an ALE field is given in Figure 3.3.

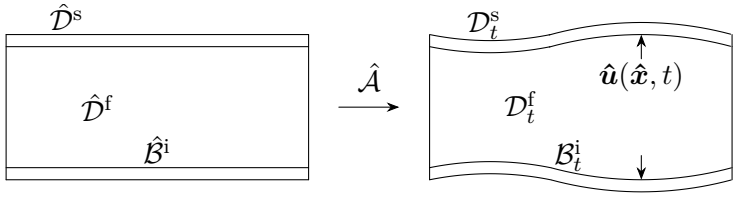

Figure 3.3: Deformation of a vessel geometry described by means of an ALE field $\mathcal{A}$.

The velocity of the domain is given as the time derivative of the ALE field:

$$\hat{\boldsymbol{w}}(\hat{\boldsymbol{x}}, t) := \frac{\partial}{\partial t} \hat{\mathcal{A}}(\hat{\boldsymbol{x}}, t) = \frac{\partial}{\partial t} \boldsymbol{x}(\hat{\boldsymbol{x}}, t). \tag{3.49}$$

In an analogous way to the total time derivative (3.5), the ALE time-derivative of a quantity $\frac{\hat{\partial}}{\hat{\partial}t}\chi$ can be defined and it holds

$$\frac{\hat{\partial}}{\hat{\partial}t}\chi := \frac{\partial}{\partial t}\chi(\hat{\mathcal{A}}(\hat{\boldsymbol{x}},t),t) = \frac{\partial}{\partial t}\chi + \hat{\boldsymbol{w}}\cdot\nabla\chi. \tag{3.50}$$

Inserting equation (3.50) into the Navier-Stokes equations (3.25) yields the Navier-Stokes equations in the ALE formulation:

$$\begin{aligned} \frac{\hat{\partial}}{\hat{\partial}t}\boldsymbol{v} + (\boldsymbol{v}-\hat{\boldsymbol{w}})\cdot\nabla\boldsymbol{v} - \nu\nabla\cdot\left(\nabla\boldsymbol{v} + (\nabla\boldsymbol{v})^T\right) + \frac{1}{\rho}\nabla p = 0, \quad &\text{in } \mathcal{D}_t^{\mathrm{f}}\times I,\\ \nabla\cdot\boldsymbol{v} = 0, \quad &\text{in } \mathcal{D}_t^{\mathrm{f}}\times I. \end{aligned} \tag{3.51}$$

The ALE displacement field (3.48) can be utilised to map the variables and spatial derivatives from a reference domain $\hat{\mathcal{D}}$ to the deformed configuration $\mathcal{D}_t$. Hereby, the multi-dimensional chain rule and the deformation gradient tensor (3.32) is used:

$$\begin{aligned} \nabla\chi &= \hat{\nabla}\hat{\chi}\hat{\boldsymbol{F}}^{-1},\\ \nabla\cdot\chi &= \mathrm{tr}(\nabla\chi) = \mathrm{tr}(\hat{\nabla}\hat{\chi}\hat{\boldsymbol{F}}^{-1}),\\ \boldsymbol{v}\cdot\nabla\chi &= \hat{\boldsymbol{F}}^{-1}\hat{\boldsymbol{v}}\cdot\hat{\nabla}\hat{\chi}. \end{aligned}$$

Analogously to equation 3.36, the fluid stress tensor specified in a reference configuration is given by

$$\hat{J}\hat{\boldsymbol{\sigma}}\hat{\boldsymbol{F}}^{-T}, \text{ with } \hat{\boldsymbol{\sigma}} = \rho\nu\left(\hat{\nabla}\hat{\boldsymbol{v}}\hat{\boldsymbol{F}}^{-1} + \left(\hat{\nabla}\hat{\boldsymbol{v}}\hat{\boldsymbol{F}}^{-1}\right)^T\right) - \hat{p}\boldsymbol{I}.$$

Furthermore, recapitulating the integral form 3.6 and 3.9 of the equations 3.51, respectively, we have

$$\int_{V_t}\chi(\boldsymbol{x})\mathrm{d}\boldsymbol{x} = \int_{\hat{V}}\hat{\chi}(\hat{\boldsymbol{x}})\hat{J}\mathrm{d}\hat{\boldsymbol{x}}. \tag{3.52}$$

With that, one obtains the incompressible NSE in the ALE formulation with respect to a reference domain $\hat{\mathcal{D}}$ in the so called conservative form:

$$\begin{aligned} \hat{J}\frac{\hat{\partial}}{\hat{\partial}t}\hat{\boldsymbol{v}} + \hat{J}\hat{\boldsymbol{F}}^{-1}(\hat{\boldsymbol{v}}-\hat{\boldsymbol{w}})\cdot\hat{\nabla}\hat{\boldsymbol{v}}&\\ -\nu\hat{\nabla}\cdot\hat{J}\left(\hat{\nabla}\hat{\boldsymbol{v}}\hat{\boldsymbol{F}}^{-1} + \left(\hat{\nabla}\hat{\boldsymbol{v}}\hat{\boldsymbol{F}}^{-1}\right)^T\right)\hat{\boldsymbol{F}}^{-T} + \frac{1}{\rho}\hat{\nabla}\cdot\left(\hat{J}\hat{p}\hat{\boldsymbol{F}}^{-T}\right) = 0, \quad &\text{in } \hat{\mathcal{D}}^{\mathrm{f}}\times I,\\ \hat{J}\mathrm{tr}(\hat{\nabla}\hat{\boldsymbol{v}}\hat{\boldsymbol{F}}^{-1}) = 0, \quad &\text{in } \hat{\mathcal{D}}^{\mathrm{f}}\times I. \end{aligned} \tag{3.53}$$

Mesh model

At the fluid-structure interface $\mathcal{B}_t^{\mathrm{i}}$, the ALE displacement field is specified by the displacement field of the solid domain. Through a smooth continuation of the displacement field from the interface to the fluid domain, the regularity of the finite element mesh movement is ensured

and degeneration of the transformed fluid mesh cells is prevented. A smooth continuation can be achieved for example by stating a Laplace problem for the ALE displacement field:

$$\begin{aligned} -\hat{\nabla} \cdot \left(\hat{J}^{-1} \hat{\nabla} \hat{\boldsymbol{u}} \right) &= 0, && \text{in } \hat{\mathcal{D}}^{\mathrm{f}} \times I, \\ \hat{\boldsymbol{u}} &= \hat{\boldsymbol{u}}|_{\hat{\mathcal{D}}^{\mathrm{s}}}, && \text{on } \hat{\mathcal{B}}^{\mathrm{i}} \times I, \\ \hat{\boldsymbol{u}} &= 0, && \text{on } \hat{\mathcal{B}} \setminus \hat{\mathcal{B}}^{\mathrm{i}} \times I. \end{aligned} \tag{3.54}$$

In the above equation (3.54), the diffusion parameter is given by the inverse of the determinant $\hat{J}$ of the deformation gradient tensor. This ensures a relatively high stiffness of mesh cells at large deformation with $\hat{J} \ll 1$ and a relatively low stiffness for distant cells with $\hat{J} \approx 1$.

Figure 3.4 illustrates an example of a resulting mesh deformation by means of an FSI benchmark problem. This example is taken from the benchmark simulation described in section 5.1. The mesh model described in equation (3.54) is used in all of the considered simulations in chapter 5 and 6.

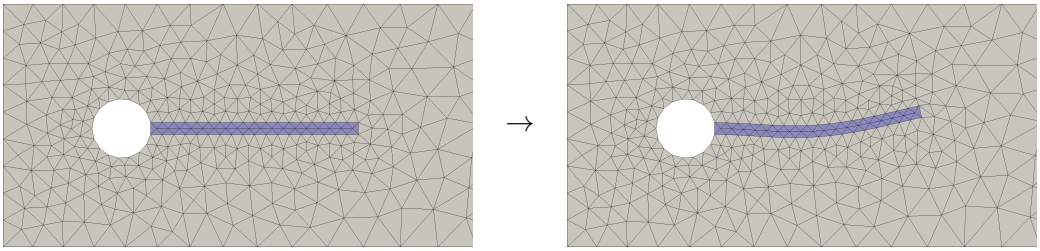

Figure 3.4: Exemplary illustration of the deformation of a finite element mesh by means of the utilised mesh model. The figure shows the displacement of an elastic bar in the FSI benchmark described in section 5.1.

Further models for the smooth continuation of the ALE field into the fluid domain are described in [130]. At large deformations towards complete rotation or contact of distinct structures, degeneration of the transformed fluid mesh can occur nevertheless. To simulate these cases, for example remeshing methods can be utilised.

3.4.3 Deterministic boundary value problem

The different parts of the mathematical modelling described in the previous sections of this chapter can be summarised to the following deterministic FSI boundary value problem. The elasticity STVK and the incompressible Navier-Stokes equations are formulated with respect to a reference domain. The interface coupling conditions are stated as well as the boundary conditions for the the displacement, velocity and pressure field.

$$
\begin{aligned}
\frac{\mathrm{d}^2}{\mathrm{d}t^2}\hat{\boldsymbol{u}} - \frac{1}{\rho}\hat{\nabla}\cdot\left(\hat{\boldsymbol{F}}\left(\lambda_1 \mathrm{tr}(\hat{\boldsymbol{E}})\boldsymbol{I} + 2\lambda_2\hat{\boldsymbol{E}}\right)\right) &= 0, && \text{in } \hat{\mathcal{D}}^{\mathrm{s}}\times I,\\
\hat{J}\frac{\hat{\partial}}{\hat{\partial}t}\hat{\boldsymbol{v}} + \hat{J}\hat{\boldsymbol{F}}^{-1}(\hat{\boldsymbol{v}}-\hat{\boldsymbol{w}})\cdot\hat{\nabla}\hat{\boldsymbol{v}} & \\
-\nu\hat{\nabla}\cdot\hat{J}\left(\hat{\nabla}\hat{\boldsymbol{v}}\hat{\boldsymbol{F}}^{-1} + \hat{\boldsymbol{F}}^{-T}\hat{\nabla}\hat{\boldsymbol{v}}^T\right)\hat{\boldsymbol{F}}^{-T} + \frac{1}{\rho}\hat{\nabla}\cdot\left(\hat{J}\hat{p}\hat{\boldsymbol{F}}^{-T}\right) &= 0, && \text{in } \hat{\mathcal{D}}^{\mathrm{f}}\times I,\\
\hat{J}\mathrm{tr}(\hat{\nabla}\hat{\boldsymbol{v}}\hat{\boldsymbol{F}}^{-1}) &= 0, && \text{in } \hat{\mathcal{D}}^{\mathrm{f}}\times I,\\
-\hat{\nabla}\cdot(\hat{J}^{-1}\hat{\nabla}\hat{\boldsymbol{u}}) &= 0, && \text{in } \hat{\mathcal{D}}^{\mathrm{f}}\times I,\\
\hat{\boldsymbol{u}}|_{\hat{\mathcal{D}}^{\mathrm{f}}} &= \hat{\boldsymbol{u}}|_{\hat{\mathcal{D}}^{\mathrm{s}}}, && \text{on } \hat{\mathcal{B}}^{\mathrm{i}}\times I,\\
\left(\nu\hat{J}\left(\hat{\nabla}\hat{\boldsymbol{v}}\hat{\boldsymbol{F}}^{-1} + \hat{\boldsymbol{F}}^{-T}\hat{\nabla}\hat{\boldsymbol{v}}^T\right)\hat{\boldsymbol{F}}^{-T} - \frac{1}{\rho}\hat{J}\hat{p}\hat{\boldsymbol{F}}^{-T}\right)\hat{\boldsymbol{\eta}}_f & \\
-\frac{1}{\rho}\left(\hat{\boldsymbol{F}}\left(\lambda_1\mathrm{tr}(\hat{\boldsymbol{E}})\boldsymbol{I} + 2\lambda_2\hat{\boldsymbol{E}}\right)\right)\hat{\boldsymbol{\eta}}_s &= 0, && \text{on } \hat{\mathcal{B}}^{\mathrm{i}}\times I,\\
\hat{\boldsymbol{u}} &= 0, && \text{on } \hat{\mathcal{B}}_{\mathrm{in}}\cup\hat{\mathcal{B}}_{\mathrm{out}}\times I,\\
\hat{\boldsymbol{v}} &= \boldsymbol{v}^{\mathrm{in}}, && \text{on } \hat{\mathcal{B}}_{\mathrm{in}}\times I,\\
-\nu\left(\hat{\nabla}\hat{\boldsymbol{v}}\hat{\boldsymbol{F}}^{-1}\right)\hat{\boldsymbol{\eta}} + \frac{1}{\rho}\hat{p}\hat{\boldsymbol{\eta}} &= p^{\mathrm{out}}\hat{\boldsymbol{\eta}}, && \text{on } \hat{\mathcal{B}}_{\mathrm{out}}\times I.
\end{aligned}
$$

In the following and for the rest of this work, the hat notation for indicating the referencing of the variables is omitted for better readability. The domains, variables and operators refer to the reference configuration if not specified different.

Variational formulation

The second time derivative of the solid displacement field can be replaced by the first time derivative of the solid velocity field. An additional equation can then be introduced equating the first displacement time derivative and the velocity of the solid domain:

$$
\frac{\mathrm{d}^2}{\mathrm{d}t^2}\boldsymbol{u} = \frac{\partial}{\partial t}\boldsymbol{v}, \quad \frac{\partial}{\partial t}\boldsymbol{u} = \boldsymbol{v}, \quad \text{on } \mathcal{D}^{\mathrm{s}}\times I. \tag{3.55}
$$

To obtain a variational formulation of the FSI boundary value problem, first, the following Sobolev spaces are defined for the test functions.

$$
\begin{aligned}
V &:= H^1(\mathcal{D},\mathbb{R}),\\
V_u^0 &:= \{u\in V : u = 0 \text{ on } \mathcal{B}_{\mathrm{in}}\cup\mathcal{B}_{\mathrm{out}}\}^d,\\
V_v^0 &:= \{v\in V : v = 0 \text{ on } \mathcal{B}_{\mathrm{in}}\}^d,\\
L &:= L^2(\mathcal{D}^{\mathrm{f}},\mathbb{R}).
\end{aligned} \tag{3.56}
$$

The Sobolev spaces for the ansatz functions include the time dimension:

$$\begin{aligned}
\mathcal{V} &:= H^1(\mathcal{D} \times I, \mathbb{R}), \\
\mathcal{V}_u^0 &:= \{u \in \mathcal{V} : u = 0 \text{ on } \mathcal{B}_{\text{in}} \cup \mathcal{B}_{\text{out}} \times I\}^d, \\
\mathcal{V}_v^0 &:= \{v \in \mathcal{V} : v = 0 \text{ on } \mathcal{B}_{\text{in}} \times I\}^d, \\
\mathcal{V}_v^D &:= \left\{v \in \mathcal{V} : v = v^{\text{in}} \text{ on } \mathcal{B}_{\text{in}} \times I\right\}^d, \\
\mathcal{L} &:= L^2(\mathcal{D}^{\text{f}} \times I, \mathbb{R}).
\end{aligned} \tag{3.57}$$

The equations of the boundary value problem are multiplied with the corresponding test functions and integrated over the respective domain. Integration by parts transfers the divergence operator from the solid and fluid stress tensor to the respective test functions and enables the specification of force and pressure boundary conditions. For the STVK stress tensor it holds

$$\begin{aligned}
&\int_{\mathcal{D}^{\text{s}}} \nabla \cdot \left(\boldsymbol{F}\left(\lambda_1 \text{tr}(\boldsymbol{E})\boldsymbol{I} + 2\lambda_2 \boldsymbol{E}\right)\right) \cdot \psi \text{d}x \\
&= \int_{\partial\mathcal{D}^{\text{s}}} \left(\boldsymbol{F}\left(\lambda_1 \text{tr}(\boldsymbol{E})\boldsymbol{I} + 2\lambda_2 \boldsymbol{E}\right)\right) \boldsymbol{\eta} \cdot \psi \text{d}s \\
&- \int_{\mathcal{D}^{\text{s}}} \left(\boldsymbol{F}\left(\lambda_1 \text{tr}(\boldsymbol{E})\boldsymbol{I} + 2\lambda_2 \boldsymbol{E}\right)\right) : \nabla\psi \text{d}x \quad \forall \psi \in V_u^0.
\end{aligned}$$

In the case of the Navier-Stokes stress tensor one gets

$$\begin{aligned}
&\int_{\mathcal{D}^{\text{f}}} \nabla \cdot \left(-\nu J \left(\nabla \boldsymbol{v} \boldsymbol{F}^{-1} + (\nabla \boldsymbol{v} \boldsymbol{F}^{-1})^T\right) \boldsymbol{F}^{-T} + \frac{1}{\rho} J p \boldsymbol{F}^{-T}\right) \cdot \psi \text{d}x \\
&= \int_{\partial\mathcal{D}^{\text{f}}} \left(-\nu J \left(\nabla \boldsymbol{v} \boldsymbol{F}^{-1} + (\nabla \boldsymbol{v} \boldsymbol{F}^{-1})^T\right) \boldsymbol{F}^{-T} + \frac{1}{\rho} J p \boldsymbol{F}^{-T}\right) \boldsymbol{\eta} \cdot \psi \text{d}s \\
&+ \int_{\mathcal{D}^{\text{f}}} \left(\nu J \left(\nabla \boldsymbol{v} \boldsymbol{F}^{-1} + (\nabla \boldsymbol{v} \boldsymbol{F}^{-1})^T\right) \boldsymbol{F}^{-T} - \frac{1}{\rho} J p \boldsymbol{F}^{-T}\right) : \nabla\psi \text{d}x \quad \forall \psi \in V_v^0.
\end{aligned}$$

The handling of the boundary terms of the integration by parts defines the fluid-structure interface coupling condition, the pressure outflow condition and a force condition acting on the outer solid boundary.

In not taking the solid and fluid boundary integral terms at the coupling interface into the notation of the weak formulation, they are implicitly equated, such that the coupling condition (3.46) holds. Not including a boundary integral term for the outer solid domain boundary in the weak formulation implicitly sets potential external forces acting on the boundary to zero. This can be seen as a do-nothing boundary condition for the solid displacement. With regard to the boundary integral of the fluid domain, the following boundary integral at the outflow has to be included in the weak formulation in order to satisfy the pressure boundary condition:

$$\int_{\mathcal{B}_{\text{out}}} \left(-\nu J \left(\boldsymbol{F}^{-T} \nabla \boldsymbol{v}^T\right) \boldsymbol{F}^{-T} + \frac{1}{\rho} J p^{\text{out}} \boldsymbol{F}^{-T}\right) \boldsymbol{\eta} \cdot \psi \text{d}s \quad \forall \psi \in V_v^0. \tag{3.58}$$

The transposed velocity gradient term in (3.58) eliminates the corresponding boundary integral term from the integration by parts, whereas the non-transposed velocity gradient

term is left over together with the pressure term to match the formulation of the pressure outflow boundary condition.

With that the FSI boundary value problem can be stated in weak form with the notation $(\cdot,\cdot)_\chi := \int_{\mathcal{D}_\chi} \mathrm{d}x$:

Problem 1. *Find* $(\boldsymbol{u}, \boldsymbol{v}, p) \in \mathcal{V}_u^0 \times \mathcal{V}_v^D \times \mathcal{L}$*, such that for almost all time steps* $t \in I$ *and* $\forall(\psi_u, \psi_v, \psi_p) \in V_u^0 \times V_v^0 \times L$*:*

$$\begin{aligned}
&\left(\frac{\partial}{\partial t}\boldsymbol{v}, \psi_v\right)_s + \left(\frac{\partial}{\partial t}\boldsymbol{u} - \boldsymbol{v}, \psi_u\right)_s + \left(\frac{1}{\rho}\boldsymbol{F}\left(\lambda_1 tr(\boldsymbol{E})\boldsymbol{I} + 2\lambda_2\boldsymbol{E}\right), \nabla\psi_v\right)_s \\
&\qquad + \left(J\frac{\partial}{\partial t}\boldsymbol{v}, \psi_v\right)_f + \left(J\boldsymbol{F}^{-1}(\boldsymbol{v}-\boldsymbol{w})\cdot\nabla\boldsymbol{v}, \psi_v\right)_f \\
&\quad + \left(\nu J\left(\nabla\boldsymbol{v}\boldsymbol{F}^{-1} + \boldsymbol{F}^{-T}\nabla\boldsymbol{v}^T\right)\boldsymbol{F}^{-T}, \nabla\psi_v\right)_f - \left(\frac{1}{\rho}Jp\boldsymbol{F}^{-T}, \nabla\psi_v\right)_f \\
&\qquad + \left(Jtr(\nabla\boldsymbol{v}\boldsymbol{F}^{-1}), \psi_p\right)_f \\
&\qquad + \left(J^{-1}\nabla\boldsymbol{u}, \nabla\psi_u\right)_f \\
&\qquad - \left(\nu J\boldsymbol{F}^{-T}\nabla\boldsymbol{v}^T\boldsymbol{F}^{-T}\boldsymbol{\eta} - \frac{1}{\rho}Jp^{out}\boldsymbol{F}^{-T}\boldsymbol{\eta}, \psi_v\right)_{out} = 0.
\end{aligned} \tag{3.59}$$

An overview on the existence and uniqueness of solutions of the elasticity and the Navier-Stokes problem can be found in [140] and in [133], respectively. For the theoretical analysis of the coupled problem, the reader is referred to [27, 28].

3.5 Uncertainty quantification

Naturally, the mathematical modelling of physiological dynamics and the medical measurements for their calibration are subject to uncertainties. Especially in clinical examinations, it is to be questioned, whether physiological dynamics can be represented by deterministic simulations, or if uncertainties should be taken into account to get an information on the reliability of the simulation. In regarding parameters and variables of a simulation as random processes, uncertainties can by measured by methods of uncertainty quantification. For example, given uncertain input data, the probability can be computed, that threshold values are exceeded. As a measure for the certainty of a simulation result, its standard deviation can be evaluated.

Several factors of uncertainty can be taken into account in modelling cardiovascular dynamics. First, the configuration of a subject-specific simulation is partly attained by medical imaging and measurement data. CT and MRI images, which typically yield the geometry of the considered vessels, are limited by their resolution. Some parameters such as the blood flow through specific vessel sections can be measured up to a certain accuracy. Other parameters such as the blood viscosity are not assessed in clinical routine or are not measurable at an acceptable invasiveness. The Young's modulus for example, which gives information on the stiffness of vessel wall soft tissue, can be measured mechanically with extracted specimen of soft tissue [68]. However, such a tissue extraction is usually not done for living patients. As compared in [30] there are approaches for estimating aortic stiffness non-invasively by means of MR Elastography or measurement of the pulse wave velocity. The measurement accuracy nevertheless is limited for the specification of the Young's modulus for biomechanical simulations. A further factor of uncertainty is the model's deviation from patient-specific physiology. The vessel wall soft tissue exhibits a multi-layered anisotropic structure, which differs from patient to patient. Alterations can also occur with medical conditions and with ageing. Numerical discretisation errors and computational errors also add to the general uncertainty of numerical simulations.

This section shows, how model equations from the previous sections can be regarded as stochastical problem in order to enable the quantification of uncertainties. Firstly, the propagation of uncertainties is modelled by means of random processes in section 3.5.1. The parameters assumed to be uncertain are given in section 3.5.2. Section 3.5.3 finally states the stochastical version of the boundary value problem considered in this work.

3.5.1 Propagation of uncertainties

In stating the considered mathematical model as a set of random differential equations, the propagation of uncertainties can be modelled and taken into account in a numerical simulation. The quantification of uncertainty in the respective simulation results can provide information on the reliability of the simulation outcome. Furthermore, the stochastical distribution of unknown simulation input parameters can be closer specified by means of inverse UQ. This can yield information on where input data should preferably be measured more accurately for reliable simulation results [135].

A general introduction to UQ is given in [87, 129]. Various applications in fluid and structure mechanics are described in [119]. A UQ approach for cardiovascular simulations has been developed in [118]. In the latter, blood flow through aneurysms and bifurcations

were considered but with rigid vessel walls not including fluid-structure interaction.

A common basis for the quantification of uncertainties is the modelling of the uncertain simulation input, boundary condition parameters and resulting parameters as random processes $\chi : \mathcal{D} \times I \times \Omega \to \mathbb{R}$ from a probability space (Ω, Σ, P). Hereby, Ω denotes the sample space. As the set of events, $\Sigma \subset \mathcal{P}(\Omega)$ is a σ-algebra and a subset of the power set of Ω. $P : \Sigma \to [0, 1]$ defines a probability measure on Σ. Hence, for a given location $\boldsymbol{x} \in \mathcal{D}$ and time $t \in I$, $\chi(\boldsymbol{x}, t, \cdot)$ is a random variable and $\chi(\cdot, \cdot, \omega)$ is a realisation of the random process.

In this work, we consider second-order random variables $\chi \in L^2(\Omega, \mathbb{R})$. The probability distribution of χ under P is defined as

$$\begin{aligned} P^\chi : \mathcal{P}(\chi(\Omega)) &\to [0, 1], \\ B &\mapsto P(\chi^{-1}(B)). \end{aligned} \tag{3.60}$$

A random variable can be characterised by its moments

$$\mathbb{E}[\chi^m] := \int_\Omega \chi^m(\omega) P(\mathrm{d}\omega). \tag{3.61}$$

The first moment is the expected value E and the second central moment is the variance σ^2. The standard deviation σ is the square root of the variance.

$$E(\chi) := \mathbb{E}[\chi] = \int_\Omega \chi(\omega) P(\mathrm{d}\omega), \tag{3.62}$$

$$\sigma^2(\chi) := \mathbb{E}[(\chi - E)^2] = \int_\Omega (\chi(\omega) - E)^2 P(\mathrm{d}\omega). \tag{3.63}$$

3.5.2 Uncertain inflow velocity and elasticity modulus

The flowrate values for the inflow boundary condition was measured by 2D flow MRI as described in the sections 2.3 and 2.2.5. The flowrate is interpolated as outlined in section 3.2.2, giving a single flowrate curve over a time period with unknown stochastical deviation. In this case a uniform distribution as so called ignorance model can be assumed:

$$q(\omega) := \bar{q} + \omega_1 \tilde{q}, \quad \omega_1 \sim U(-1, 1). \tag{3.64}$$

Hereby, $\bar{q}$ and $\tilde{q}$ denote the mean value and the maximal deviation from the mean value, respectively.

The stiffness of the vessel wall, indicated as Young's modulus, is also modelled as uniformly distributed random variable due to its limited measurability (see section 2.3:

$$Y(\omega) := \bar{Y} + \omega_2 \tilde{Y}, \quad \omega_2 \sim U(-1, 1). \tag{3.65}$$

The two stochastic parameters of the Young's modulus and the boundary velocity can be assumed to be stochastically independent. The respectively utilised values for the mean and the range of the uniform distribution are given in chapter 5 and 6.

Taking the two random variables into account, the sample space becomes $\Omega = [-1, 1]^2$ and the probability distribution P has the probability density function for a two-dimensional

uniform distribution $f^P(\omega) = 1/|\Omega| = 1/4$. With that, the moment operator (3.61) gets the explicit form

$$\begin{aligned}\mathbb{E}[\chi] &= \int_\Omega \chi^m(\omega) f^P(\omega) \mathrm{d}\omega \\ &= \int_{-1}^{1}\int_{-1}^{1} \chi(\omega)\frac{1}{4}\mathrm{d}\omega_1\mathrm{d}\omega_2.\end{aligned} \tag{3.66}$$

3.5.3 Stochastical boundary value problem

To enable the quantification of uncertainties in the simulation, the variables of problem (1) are regarded as random processes. The underlying dimensions of the problem, space and time, are extended with the stochastic sample space Ω. The definitions of the function spaces (3.56) are extended with square integrable random processes on the sample space:

$$\begin{aligned}\tilde{V}_u^0 &:= \left\{u : \mathcal{D}\times\Omega\to\mathbb{R},\ \text{with } u(\cdot,\omega)\in V_u^0,\ u(\boldsymbol{x},\cdot)\in L^2(\Omega,\mathbb{R})\right\}^d, \\ \tilde{V}_v^0 &:= \left\{v : \mathcal{D}\times\Omega\to\mathbb{R},\ \text{with } v(\cdot,\omega)\in V_v^0,\ v(\boldsymbol{x},\cdot)\in L^2(\Omega,\mathbb{R})\right\}^d, \\ \tilde{L} &:= L^2(\mathcal{D}^\mathrm{f}\times\Omega,\mathbb{R}).\end{aligned} \tag{3.67}$$

And for the time dependent variables, c.f. (3.57):

$$\begin{aligned}\tilde{\mathcal{V}}_u^0 &:= \left\{u : \mathcal{D}\times I\times\Omega\to\mathbb{R},\ \text{with } u(\cdot,\cdot,\omega)\in \mathcal{V}_u^0,\ u(\boldsymbol{x},t,\cdot)\in L^2(\Omega,\mathbb{R})\right\}^d, \\ \tilde{\mathcal{V}}_v^0 &:= \left\{v : \mathcal{D}\times I\times\Omega\to\mathbb{R},\ \text{with } v(\cdot,\cdot,\omega)\in \mathcal{V}_v^0,\ v(\boldsymbol{x},t,\cdot)\in L^2(\Omega,\mathbb{R})\right\}^d, \\ \tilde{\mathcal{V}}_v^D &:= \left\{v : \mathcal{D}\times I\times\Omega\to\mathbb{R},\ \text{with } v(\cdot,\cdot,\omega)\in \mathcal{V}_v^D,\ v(\boldsymbol{x},t,\cdot)\in L^2(\Omega,\mathbb{R})\right\}^d, \\ \tilde{\mathcal{L}} &:= L^2(\mathcal{D}^\mathrm{f}\times I\times\Omega,\mathbb{R}).\end{aligned} \tag{3.68}$$

The attained problem of stochastic partial differential equations is defined on the function spaces (3.67) and (3.68). It is given by equation (3.59) with the usage of the following definition of the scalar product:

$$(\cdot,\cdot)_\chi := \int_{\mathcal{D}_\chi\times\Omega} \mathrm{d}x P(\mathrm{d}\omega). \tag{3.69}$$

Problem 2. *Find* $(\boldsymbol{u},\boldsymbol{v},p)\in\tilde{\mathcal{V}}_u^0\times\tilde{\mathcal{V}}_v^D\times\tilde{\mathcal{L}}$*, such that for almost all time steps* $t\in I$ *and* $\forall(\psi_u,\psi_v,\psi_p)\in\tilde{V}_u^0\times\tilde{V}_v^0\times\tilde{L}$ *equation* (3.59) *holds with the scalar product* (3.69)*.*

Problem (2) is applied in this work to a benchmark scenario in section 5.2 and to aortic blood flow scenarios in chapter 6. The specific scenarios are solved numerically, for which the numerical discretisation is presented in the the following chapter 4.

3.6 Risk parameters

In general, the respective severity of a patient's condition can be assessed by the available diagnostic methods. Medical treatment and therapy can be chosen on the basis of this diagnosis. Especially for decisions on surgical interventions, the risks of not intervening have to be weighed against the risks of the possible surgical procedures. Up-to-date advice and guidance for clinicians is given for example by the *guidelines on the diagnosis and treatment of aortic diseases* from the European Society of Cardiology [38]. These guidelines give recommendations, which medical measurement and imaging methods (cf. section 2.2.5) can be used for the diagnosis and differential diagnosis of the various types of aortic disease. As an example, the recommendation for surgical interventions for aortic aneurysms is mainly based on the diameter of the dilated vessel. Vessel diameter thresholds are given, for which the risk of rupture is usually too high for not operating if the diameter threshold is exceeded. However, there are cases of vessel rupture at smaller diameters, which is discussed in [108]. The examination of bio markers for a most accurate assessment of the rupture risk is still subject of ongoing research. Non-morphologic parameters such as flow- and simulation-based parameters are also discussed. An overview of flow-based parameters obtained from flow MRI images is given in [37]. Simulation-based parameters are reviewed in [18]. Hereby, it is also examined with respect to aortic disease in general, in which way the parameters can provide insight into the development of aortic disease and how risk assessment for surgeries can be improved.

In this work, two parameters are exemplarily evaluated for an healthy aortic bow: The wall shear stress and the structural stress in the vessel wall as further explained in the following sections 3.6.1 and 3.6.2, respectively. Further analysis capabilities are enabled by flow visualisations in terms of vector maps, stream- and pathlines, maximum intensity projections, isosurfaces and volume rendering [37].

The uncertainty of the considered parameters and simulation results in this work is quantified by means of the expected value E, the standard deviation and the probability of the overstepping of threshold values. By means of the standard deviation, it can be evaluated, whether simulation results are conclusive at relatively small values of the standard deviation or if they bear a high level of uncertainty in the case of relatively high standard deviation compared to the mean value. Furthermore, this work proposes in section 3.6.3 to take the probability into account, that stress thresholds are exceeded given the uncertainty in the input parameters of the respective simulation.

3.6.1 Wall shear stress

The wall shear stress is the shear stress in the boundary layer of the fluid flow. It can be seen as a tangential force due to friction at the vessel wall. As it has been shown in several studies (cf. [107] and the references therein), the wall shear stress has an effect on the orientation of endothelial cells and causes an elongation of the same. The cells get shaped in the direction of the flow. Furthermore a stiffening of the cytoskeletal structure can be observed. According to [107], however, the mechanoreceptors of the cellular response are still not fully understood. In medical treatment, it is common to reduce the wall shear stress by decreasing blood pressure and heart contractility [38].

The magnitude of the wall shear stress for the fluid flow equations (3.25) is given by

$$\tau_{\mathrm{W}} = \left| \rho\nu(\nabla \boldsymbol{v} + \nabla \boldsymbol{v}^T) \cdot \boldsymbol{\eta} \right| \quad \text{on } \mathcal{B}_t^{\mathrm{i}} \times I. \tag{3.70}$$

Hereby, $\mathcal{B}_t^{\mathrm{i}}$ denotes the interface between the fluid domain and the vessel wall. The spatial variables and the gradient operator refer to the deformed configuration (cf. section 3.4.2).

3.6.2 Von Mises stress distribution

The stresses within the vessel wall can be evaluated by means of the von Mises stress. This scalar-valued stress measure is calculated via the principal stress components and the shear stress components of the Cauchy stress tensor $\boldsymbol{\sigma}$:

$$\begin{aligned} \tau_{\mathrm{M}} = &\Big(\boldsymbol{\sigma}_{11}^2 + \boldsymbol{\sigma}_{22}^2 + \boldsymbol{\sigma}_{33}^2 - \boldsymbol{\sigma}_{11}\boldsymbol{\sigma}_{22} - \boldsymbol{\sigma}_{11}\boldsymbol{\sigma}_{33} - \boldsymbol{\sigma}_{22}\boldsymbol{\sigma}_{33} + 3(\boldsymbol{\sigma}_{12}^2 + \boldsymbol{\sigma}_{13}^2 + \boldsymbol{\sigma}_{23}^2)\Big)^{\frac{1}{2}} \\ &\text{in } \mathcal{D}^{\mathrm{s}} \times I. \end{aligned} \tag{3.71}$$

The von Mises stress is a measure of the distortion energy. For many elastic material structures it can be used to define a yield criterion at which the distortion energy reaches a critical value. To analyse the biomechanics of blood flow vessels, the von Mises stress has been examined in [139, 76]. A comparison of diameter, wall shear stress and wall stress parameters, especially involving von Mises stress, is given in [92]. As the von Mises stress has not been used in a broad range of studies yet, comprehensive validation studies have to investigate the significance of the parameter for aortic risk assessment in the future.

This work contributes to the discussion in using the von Mises stress to visualise the inner wall stress load in an aortic phantom and in an aortic bow. Additionally, a measure for a stress overload probability based on UQ is proposed as described in the following section.

3.6.3 Stress overload probability

As discussed in [18], too high or too low values of the wall shear stress can have an adverse influence on the aortic physiology. As outlined in section 3.5, the assessment of clinical values based on simulations can be affected by uncertainties. Hence, given the uncertainties in the considered models and parameters, it can evaluated, at which probability simulated values are higher than specific threshold values. This evaluation can be achieved by UQ methods. At this, the computed stress distribution τ is understood as a random process. Let $\tau^{\max}$ be a maximal threshold value for the wall shear stress or the von Mises stress. Then, the highest probability over a heart cycle, that $\tau^{\max}$ is exceeded is given by

$$\begin{aligned} P^{\tau,\max} &= \max_{t \in I} \left(P^{\tau} \left([\tau^{\max}, \infty) \right) \right) \\ &= \max_{t \in I} \left(P \left(\tau^{-1} \left([\tau^{\max}, \infty) \right) \right) \right) \\ &= \max_{t \in I} \left(\int_{\tau^{-1}([\tau^{\max}, \infty))} f^P(\omega) \mathrm{d}\omega \right). \end{aligned} \tag{3.72}$$

$P^{\tau,\max}$ is defined on $\mathcal{B}^{\mathrm{i}}$ for the wall shear stress or on $\mathcal{D}^{\mathrm{s}}$ for the von Mises stress.

For a proof of concept, the probability for reaching the threshold values is computed exemplarily for the aortic bow of a healthy proband in section 6.2.

4 A patient-specific numerical simulation

In the previous chapter, the general modelling of aortic blood flow under uncertainties was introduced. One of the objectives of this work is to show the feasibility of the evaluation of the risk parameters presented in section 3.6 in a patient-specific and computationally efficient way.

The first section 4.1 of this chapter describes a workflow to incorporate a range of specificities of a given proband or patient in the simulation and evaluation procedure. An introduction to various methods for the setup of subject-specific cardiovascular simulations is given for example in [2]. Quarteroni et al especially addresses the preprocessing of clinical data for numerical simulations in [113]. Methods for the generation of computational meshes for patient-specific blood vessels and also the geometrically similar lung bronchi are described in [94]. The workflow presented in this work focuses on the processing of 4D flow MRI images of the thoracic aorta. It calibrates the generic model introduced in chapter 3 with the available clinical data.

Furthermore, the linearisation and discretisation of the mathematical problem 1 leads to a complex linear system of equations. General linear solvers, which do not take the structure of the system into account, are usually not able to approximate the solution of the problem with acceptable computational costs. Therefore, in the second section 4.2 a discretisation approach of the problem and the derivation of a problem-specific solution algorithm is presented. In the literature, other numerical solver routines for FSI problems with an application to hemodynamics have been presented in [7, 29]. Approaches focusing the utilisation of the block structure of monolithic FSI systems are introduced in [79, 141]. FSI solvers based on the algebraic or the geometric multigrid method are described in [115, 55]. An approach to solve stochastical problems of saddle point structure is presented in [112].

The numerical solver introduced in this work utilises the block saddle point structure of the discretised system of linear equations and includes the propagation of uncertainties in the simulation.

In chapter 5, the presented solver is then verified and evaluated in numerical experiments with respect to its accuracy and parallel efficiency.

4.1 Subject-specific workflow

Medical imaging and measurement provides the basis for the subject-specific setup and calibration of numerical simulations. The raw measurement data is to be processed into a

computational model. Hereby, the geometry and the relevant physiological quantities are extracted and prepared for the consideration in a finite element simulation.

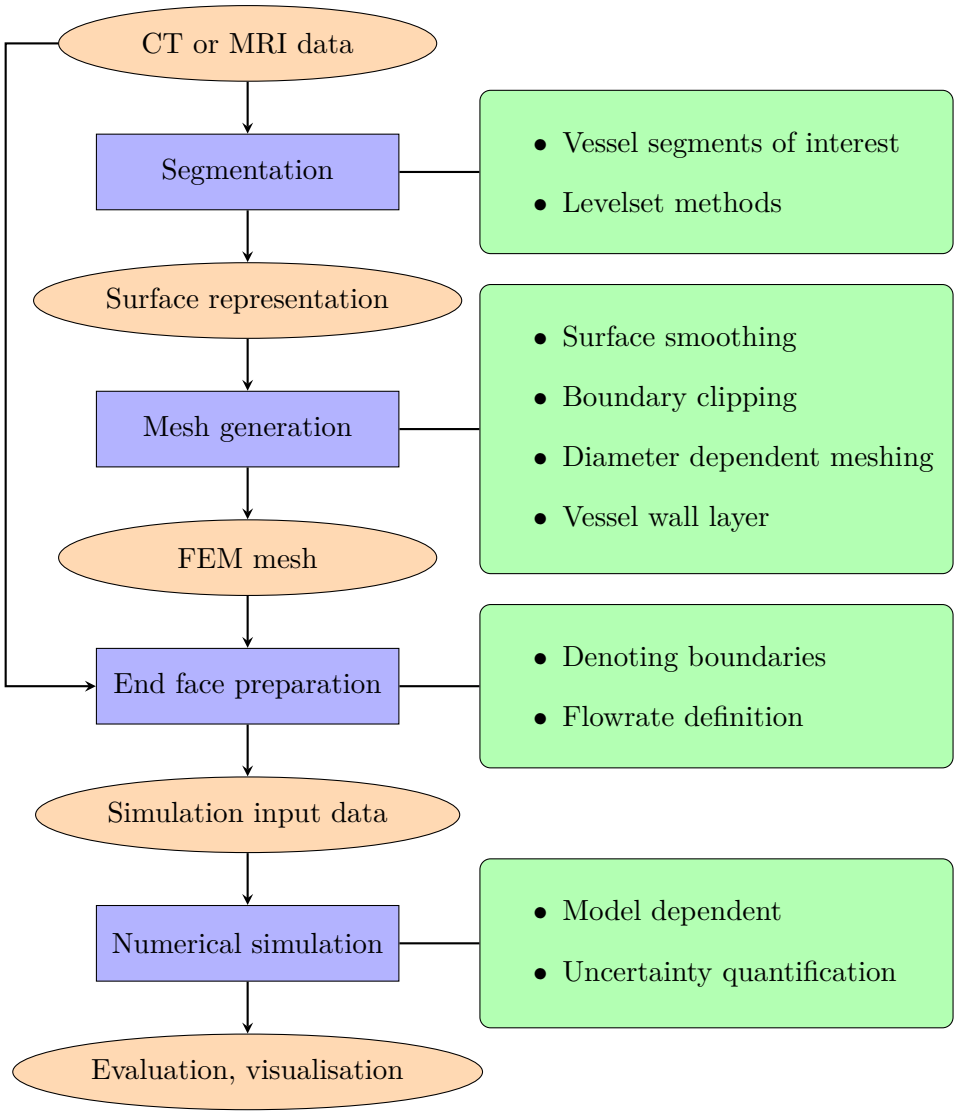

Figure 4.1: Medical data processing workflow for the patient-specific configuration of a numerical aortic blood flow simulation.

The generic mathematical model described in chapter 3 can be adapted and configured to subject-specific scenarios on various levels, namely on the level of the volumetric dynamics, on the level of the boundary dynamics and on the geometrical level. As for the level of volumetric dynamics, the constitutive material laws as stated in the equations (3.24) and (3.40) are suitable for the simulation of fluid and solid materials used in the aortic phantom experiment as introduced in section 2.3. In possible further developments of this work, they can be amended by more complex, but more realistic constitutive laws for blood flow and human vessel walls. In each case, material parameters, such as viscosity and stiffness, have to be

set. On the level of the boundary dynamics, the models for the in- and outflow of the considered vessel have to be configured on the basis of the available 4D flow MRI data. The geometry of the considered vessel can be virtually reconstructed from the MRI data, so it yields the individual definition of the fluid and solid domains $\mathcal{D}^{\mathrm{f}}$ and $\mathcal{D}^{\mathrm{s}}$. On all three levels the measurement input data bears uncertainties. The quality of the data is limited by its resolution and device-dependent measurement accuracy.

An overview on the processing steps is shown in Figure 4.1. Further details on the various data processing methods can be found in [2] and the references therein. A framework for formalising the simulation setup workflow is given with the *Medical Simulation Markup Language (MSML)*[1] [132], which is applied for example to patient specific mitral valve surgery scenarios in [122]. In the following, a closer look is taken at the processing methods relevant for this work.

4.1.1 Segmentation of the aorta

Segmentation is the virtual reconstruction of an organ's surface geometry from medical imaging data. The recognizability of a structure in a given image depends on its resolution and the distinguishable contrast of the structure. In the case of the aorta, the resulting geometry is typically tubular with a number of branches. Aneurysmatic dilatations can represent a significant deviation from a tubular geometry. Both have to be taken into account by the utilized segmentation method.

If an automatised segmentation is not applicable, surfaces can be delineated manually. Thresholding can be used, when the surface separates regions of interest at a well-distinguishable grey-scale value. A semi-automatic method is given by region growing [2]. Region growing typically starts with manually selected seed points. The therewith initialised region grows at a speed based on the intensity similarity to the neighbouring cells. At high intensity gradients the growing speed is typically chosen to be very small or zero. A variation of region growing especially suitable for vascular structures is given by the method of colliding fronts [2]. Hereby, the ends of a vascular network are used as seed points and the travelling time of the regions which expand along the vessels towards each other can be used as segmentation measure. Region growing segmentations can serve as an initialisation for levelset segmentation methods. Levelset methods use a potential field defined on the image. An isosurface of the potential field implicitly defines the segmented surface. For the aorta, it is suitable to use deformable shape models to define the levelset potential field [125]. The expansion of a deformable model can be controlled by the dependency of the inflation speed on image features and gradients. Also, smoothness constraints can be added. As opposed to the other methods mentioned in this section, deformable model levelset segmentation enables an accuracy beyond the pixel size.

For this work the Siemens software *Syngo.MR Cardiac Flow*[2] was used for the segmentation of vessel structures from MRI data.

[1] msml.readthedocs.io

[2] healthcare.siemens.com/magnetic-resonance-imaging/options-and-upgrades/clinical-applications/syngo-mr-cardiac-flow

4.1.2 Volumetric meshing

With the segmentation of a vessel segment a volumetric mesh can be generated for a finite element discretisation. To this end, the segmentation should be given by a smooth surface geometry without any irregular holes and a designation of the in- and outflow openings.

As an input for the finite element simulation, usually, the generation of a conforming mesh is needed. In a conforming finite element mesh, the mesh cells disjointedly cover the full domain of the geometry. Vertices, edges and faces that are shared by two cells fully belong to both of the cells. In other words, the mesh does not contain any hanging nodes. The quality of a finite element mesh can be characterised, amongst others, by the ratio of the inscribed circle diameter to the circumcircle diameter of each cell. A basic quality property is given by the Delaunay criterion which requires that the circumcircle of a tetrahedron does not contain any other node. For vessels, the cell size can be chosen depending on the diameter, such that each vessel segment approximately has the same number of cells in each cross section. To resolve the elastic vessel wall as a volumetric domain, the three-dimensional geometry can be extended with a layer of a specific thickness, e.g. 1mm in the case of the aorta.

For this work, the open source *Vascular Modeling Toolkit (vmtk)*[3] [3] is used and integrated into the workflow to generate subject-specific finite element geometries. The vascular modeling toolkit itself uses the open source software *Tetgen*[4] [126] for generating high-quality finite element meshes.

4.1.3 Treatment of the vessel segment boundaries

The different parts of the cardiovascular system can be modelled on several scales of complexity. Using a fully spatially and temporarily resolved model, the three-dimensional flow dynamics in time can be studied together with the movement and elasticity of the vessel wall. Depending on the given question, a fully resolved domain in three dimensions is usually only needed for a specific region of interest. The models of the subsequent parts of the cardiovascular tree can be reduced in dimensional complexity. Using, for example, symmetry assumptions on the tubular vessels yields a one-dimensional model of the segments. A further reduced model is given by zero-dimensional lumped parameter networks of the vascular tree.

When modelling vessel segments of interest in three dimensions, the end faces of the geometry have to be defined. For that, before meshing, the inlet and outlet cut planes of the considered aortic segment are denoted. The information about the location and shape of the cut planes and if available the respective flowrate is extracted from the medical measurement data and stored for the configuration of the numerical simulation.

Details on the modelling and the configuration of the boundaries are given in section 3.2.2, 6.1.1 and 6.2.1. For further reading, the reader is referred to [45].

4.1.4 Numerical simulation and evaluation

With the specification of the components and parameters on the three levels of the model and boundary dynamics as well as of the geometry, the respective numerical simulation can

[3] vmtk.org
[4] wias-berlin.de/software/tetgen

be set up. The simulation in this work is based on the mathematical models defined in chapter 3 and on their discretisation presented in the subsequent section. A summary of the most important discretisation parameters and additional information on the implementation and the utilized computing infrastructure is given in the appendix in section 8.2. As the considered hemodynamics are typically of the periodic form of a heart beat, the simulation results are evaluated over one period. Scalar valued results are plotted over one time period. For the discrete time steps, the simulated three dimensional dynamics are written out in the file format of the *Visualization Toolkit (VTK)*[5] [123]. In this work, they are visualised with *ParaView* [6] [6].

[5] vtk.org
[6] paraview.org

4.2 Problem-specific numerics

In this section, the discretisation of the mathematical model defined in chapter 3 is presented, as well as the numerical methods used to approximate solutions of problem (1). Literature references on problem-specific solvers for FSI-problems including uncertainties are given in the beginning of this chapter. A broad overview on the theory of partial differential equations is given in [40]. An introduction to the discretisation of partial differential equations is given e.g. in [80] and with a special focus on the finite element method in [9]. Numerical methods for FSI problems are described in [51]. The numerical quantification of uncertainties in the context of differential equations is introduced [87].

This section is structured as follows: Following the Rothe method, first, the discretisation of time is introduced in 4.2.1. After the description of the linearisation of the nonlinear equations in section 4.2.2, the discretisation in space is presented in section 4.2.3. Section 4.2.4 describes the numerical methods for UQ utilised in this work. Finally, section 4.2.5 presents a problem-specific linear solver.

The numerical framework, presented in this work, has been implemented by the author in the finite element software package *HiFlow*[7] [54]. The application is written in C++ and parallelised with the *Message Passing Interface (MPI)*[8] to allow for high performance computing.

4.2.1 Discretisation of time: One-step-θ scheme

The discretisation of partial differential equations aims at establishing stable and consistent numerical algorithms to approximate solutions of the equations. Together with the linearisation of nonlinear problems, the discretisation typically leads to systems of linear equations for a large number of discrete degrees of freedom which represent the solution variables. The time dimension can be discretised either solely on its own or in one approach together with the spatial dimensions, for example via a space-time finite element method [134]. Considering the time dimension on its own, general discretisation schemes for ordinary differential equations are applicable as for example the Runge-Kutta methods or backward differentiation formulae [34]. The methods can be categorised by their respective stability and convergence properties.

In this work, the one-step-θ scheme [65] is used. It is a one-step scheme with a parameter θ controlling the stability and consistency of the method. If a differential equation for the variable χ with a time-independent operator L can be expressed in the form

$$\frac{\partial}{\partial t}\chi + L(\chi) = 0, \tag{4.1}$$

the discrete values $\chi^l \approx \chi(t_l)$, $l = 0, \ldots, L$, approximate the solution of equation (4.1) in the time dimension with the following scheme:

$$\frac{1}{k}(\chi^l - \chi^{l-1}) + \theta L(\chi^l) + (1-\theta)L(\chi^{l-1}) = 0. \tag{4.2}$$

[7] hiflow3.org

[8] www.mcs.anl.gov/research/projects/mpi/index.htm

Choosing $\theta = 0$, one obtains the explicit Euler scheme. Choosing $\theta = 1$ leads to the implicit Euler scheme, which is strongly A-stable as opposed to the explicit version. Both of the Euler schemes are first order consistent. The Crank-Nicolson method with $\theta = 1/2$ is second order consistent and A-stable but not strongly A-stable. Strong A-stability of the Crank-Nicolson method can be obtained by shifting θ with the time step length k to $\theta = 1/2 + k$.

In the following, the one-step-θ scheme (4.2) is applied to the time derivatives of the displacement $\boldsymbol{u}$ and the velocity $\boldsymbol{v}$ of the FSI equations (3.59). The pressure and the divergence term of the velocity are handled fully implicitly. Also, the fluid mesh movement is treated fully implicitly with

$$\boldsymbol{w}(t_l) \approx \frac{1}{k}(\boldsymbol{u}^l - \boldsymbol{u}^{l-1}). \tag{4.3}$$

To obtain the time discrete version of equation (3.59), we first define

$$\begin{aligned}
L_T(\boldsymbol{u},\boldsymbol{v},\psi) :=& \left(\frac{\partial}{\partial t}\boldsymbol{v},\psi_v\right)_s + \left(\frac{\partial}{\partial t}\boldsymbol{u},\psi_u\right)_s \\
&+ \left(J\frac{\partial}{\partial t}\boldsymbol{v},\psi_v\right)_f - \left(J\boldsymbol{F}^{-1}\boldsymbol{w}\cdot\nabla\boldsymbol{v},\psi_v\right)_f, \\
L_D(\boldsymbol{u},\boldsymbol{v},\psi) :=& -(\boldsymbol{v},\psi_u)_s + \left(\frac{1}{\rho}\boldsymbol{F}\left(\lambda_1\mathrm{tr}(\boldsymbol{E})\boldsymbol{I} + 2\lambda_2\boldsymbol{E}\right),\nabla\psi_v\right)_s \\
&+ \left(J\boldsymbol{F}^{-1}\boldsymbol{v}\cdot\nabla\boldsymbol{v},\psi_v\right)_f + \left(\nu J\left(\nabla\boldsymbol{v}\boldsymbol{F}^{-1} + \boldsymbol{F}^{-T}\nabla\boldsymbol{v}^T\right)\boldsymbol{F}^{-T},\nabla\psi_v\right)_f \\
&- \left(\nu J\boldsymbol{F}^{-T}\nabla\boldsymbol{v}^T\boldsymbol{F}^{-T}\boldsymbol{\eta},\psi_v\right)_{\mathrm{out}}, \\
L_I(\boldsymbol{u},\boldsymbol{v},p,\psi) :=& -\left(\frac{1}{\rho}\left(Jp\boldsymbol{F}^{-T}\right),\nabla\psi_v\right)_f + \left(J\mathrm{tr}(\nabla\boldsymbol{v}\boldsymbol{F}^{-1}),\psi_p\right)_f \\
&+ \left(J^{-1}\nabla\boldsymbol{u},\nabla\psi_u\right)_f + \left(\frac{1}{\rho}Jp^{\mathrm{out}}\boldsymbol{F}^{-T}\boldsymbol{\eta},\psi_v\right)_{\mathrm{out}},
\end{aligned}$$

and then approximate $L_T(\boldsymbol{u}(t_l),\boldsymbol{v}(t_l),\psi) \approx L_T^k(\boldsymbol{u}^l,\boldsymbol{v}^l,\psi)$ with

$$\begin{aligned}
L_T^k(\boldsymbol{u}^l,\boldsymbol{v}^l,\psi) :=& \left(\frac{1}{k}(\boldsymbol{v}^l - \boldsymbol{v}^{l-1}),\psi_v\right)_s + \left(\frac{1}{k}(\boldsymbol{u}^l - \boldsymbol{u}^{l-1}),\psi_u\right)_s \\
&+ \left(J^{l,\theta}\frac{1}{k}(\boldsymbol{v}^l - \boldsymbol{v}^{l-1}),\psi_v\right)_f - \left(J\boldsymbol{F}^{-1}\frac{1}{k}(\boldsymbol{u}^l - \boldsymbol{u}^{l-1})\cdot\nabla\boldsymbol{v},\psi_v\right)_f, \\
J^{l,\theta} :=& \theta J^l + (1-\theta)J^{l-1}.
\end{aligned}$$

The resulting time discrete equation can be written as follows:

$$\begin{aligned}
0 = L^k(\psi) :=& L_T^k(\boldsymbol{u}^l,\boldsymbol{v}^l,\psi) \\
&+ \theta L_D(\boldsymbol{u}^l,\boldsymbol{v}^l,\psi) + (1-\theta)L_D(\boldsymbol{u}^{l-1},\boldsymbol{v}^{l-1},\psi) \\
&+ L_I(\boldsymbol{u}^l,\boldsymbol{v}^l,p^l,\psi).
\end{aligned} \tag{4.4}$$

Equation (4.4) gives a procedure to consecutively compute a time-discrete solution of problem (2) at the time steps t_l, $l = 1,\ldots,L$ starting from the initial condition for the variables given by $\{\boldsymbol{u}_0,\boldsymbol{v}_0,p_0\}$. An analysis of the stability of equation (4.4) is given in [142].

4.2.2 Analytical Jacobian for Newton iterations

The time stepping procedure (4.4) has the form of a nonlinear equation in the variable values of the next time step l. Almost all of the fluid flow terms are highly nonlinear due to the ALE mapping. Also, the elasticity terms have nonlinear parts.

A standard procedure to approximate solutions of nonlinear equations is given by the Newton method [43]. A similar approach to the one presented in the following is described in [142].

Let L be a nonlinear operator in the variable χ. A solution of the equation

$$L(\chi) = 0 \tag{4.5}$$

is iteratively approximated by the linear procedure for the Newton steps $n = 0, \ldots,$ with

$$L'[\chi^n](\delta\chi^n) = L(\chi^n), \tag{4.6}$$

$$\chi^{n+1} = \chi^n - \lambda\delta\chi^n, \tag{4.7}$$

$$\text{until} \quad \|L(\chi^{n+1}) - L(\chi^n)\|_2 < \epsilon,$$

where χ^0 should be close to the desired solution. In this work, χ^0 is chosen to be the solution of the previous time step. This way, the starting point is close enough to the solution of the next time step to observe quadratic convergence of the Newton method in the numerical experiments which are defined in chapter 5 and 6.

The first part (4.6) involves the directional derivative $L'[\chi^n]$ of the operator L in the direction of the preceding Newton approximation χ^n. It yields a new direction $\delta\chi^n$, which is used to update the Newton approximation in equation (4.7). With $\lambda \in (0, 1]$, the residual norm $\|L(\chi^{n+1}) - L(\chi^n)\|_2$ can be minimized via line search.

The directional derivative can be defined as Gâteaux derivative

$$L'[\chi](\delta\chi) := \lim_{\epsilon\to 0} \frac{1}{\epsilon} \left(L(\chi + \epsilon\delta\chi) - L(\chi)\right) = \frac{\mathrm{d}}{\mathrm{d}\epsilon} L(\chi + \epsilon\delta\chi)|_{\epsilon=0}. \tag{4.8}$$

To evaluate the directional derivative, automatic differentiation has been used in [36]. It is also possible to derive the directional derivative for equation (4.4) explicitly as shown in the following.

The main methods for the calculation of the directional derivative are given by the product and the chain rule. The directional derivatives for the strain tensors are

$$\boldsymbol{F}'[\boldsymbol{u}](\delta\boldsymbol{u}) = \nabla\delta\boldsymbol{u}, \tag{4.9}$$

$$(\boldsymbol{F}^{-1})'[\boldsymbol{u}](\delta\boldsymbol{u}) = -\boldsymbol{F}^{-1}\nabla\delta\boldsymbol{u}\boldsymbol{F}^{-1}, \tag{4.10}$$

$$J'[\boldsymbol{u}](\delta\boldsymbol{u}) = J\mathrm{tr}\left(\boldsymbol{F}^{-1}\nabla\delta\boldsymbol{u}\right), \tag{4.11}$$

$$\boldsymbol{E}'[\boldsymbol{u}](\delta\boldsymbol{u}) = \frac{1}{2}\left(\nabla\delta\boldsymbol{u}^T\boldsymbol{F} + \boldsymbol{F}^T\nabla\delta\boldsymbol{u}\right). \tag{4.12}$$

Applying the product rule and equations (4.9) - (4.12) to (4.4), one obtains for a time step l:

$$
\begin{aligned}
L_T^{k\,\prime}[\boldsymbol{u},\boldsymbol{v}](\delta\boldsymbol{u},\delta\boldsymbol{v},\psi) = &\frac{1}{k}\left(\delta\boldsymbol{v},\psi_v\right)_s + \frac{1}{k}\left(\delta\boldsymbol{u},\psi_u\right)_s \\
&+ \frac{\theta}{k}\left(J\mathrm{tr}(\boldsymbol{F}^{-1}\nabla\delta\boldsymbol{u})(\boldsymbol{v}-\boldsymbol{v}^{l-1}),\psi_v\right)_f \\
&+ \frac{1}{k}\left(J^{l,\theta}\delta\boldsymbol{v},\psi_v\right)_f \\
&- \frac{1}{k}\left(J\mathrm{tr}(\boldsymbol{F}^{-1}\nabla\delta\boldsymbol{u})\boldsymbol{F}^{-1}(\boldsymbol{u}-\boldsymbol{u}^{l-1})\cdot\nabla\boldsymbol{v},\psi_v\right)_f \\
&+ \frac{1}{k}\left(J\boldsymbol{F}^{-1}\nabla\delta\boldsymbol{u}\boldsymbol{F}^{-1}(\boldsymbol{u}-\boldsymbol{u}^{l-1})\cdot\nabla\boldsymbol{v},\psi_v\right)_f \\
&- \frac{1}{k}\left(J\boldsymbol{F}^{-1}\delta\boldsymbol{u}\cdot\nabla\boldsymbol{v},\psi_v\right)_f \\
&- \frac{1}{k}\left(J\boldsymbol{F}^{-1}(\boldsymbol{u}-\boldsymbol{u}^{l-1})\cdot\nabla\delta\boldsymbol{v},\psi_v\right)_f,
\end{aligned}
$$

$$
\begin{aligned}
L_D'[\boldsymbol{u},\boldsymbol{v}](\delta\boldsymbol{u},\delta\boldsymbol{v},\psi) = &-\left(\delta\boldsymbol{v},\psi_u\right)_s \\
&+ \frac{1}{\rho}\left(\nabla\delta\boldsymbol{u}(\lambda_1\mathrm{tr}(\boldsymbol{E})\boldsymbol{I}+2\lambda_2\boldsymbol{E}),\nabla\psi_v\right)_s \\
&+ \frac{1}{\rho}\left(\boldsymbol{F}(\frac{\lambda_1}{2}\mathrm{tr}(\nabla\delta\boldsymbol{u}^T\boldsymbol{F}+\boldsymbol{F}^T\nabla\delta\boldsymbol{u})\boldsymbol{I}+\lambda_2(\nabla\delta\boldsymbol{u}^T\boldsymbol{F}+\boldsymbol{F}^T\nabla\delta\boldsymbol{u})),\nabla\psi_v\right)_s \\
&+ \left(J\mathrm{tr}(\boldsymbol{F}^{-1}\nabla\delta\boldsymbol{u})\boldsymbol{F}^{-1}\boldsymbol{v}\cdot\nabla\boldsymbol{v},\psi_v\right)_f \\
&- \left(J\boldsymbol{F}^{-1}\nabla\delta\boldsymbol{u}\boldsymbol{F}^{-1}\boldsymbol{v}\cdot\nabla\boldsymbol{v},\psi_v\right)_f \\
&+ \left(J\boldsymbol{F}^{-1}\delta\boldsymbol{v}\cdot\nabla\boldsymbol{v},\psi_v\right)_f \\
&+ \left(J\boldsymbol{F}^{-1}\boldsymbol{v}\cdot\nabla\delta\boldsymbol{v},\psi_v\right)_f \\
&+ \nu\left(J\mathrm{tr}(\boldsymbol{F}^{-1}\nabla\delta\boldsymbol{u})(\nabla\boldsymbol{v}\boldsymbol{F}^{-1}+\boldsymbol{F}^{-T}\nabla\boldsymbol{v}^T)\boldsymbol{F}^{-T},\nabla\psi_v\right)_f \\
&+ \nu\left(J(\nabla\delta\boldsymbol{v}\boldsymbol{F}^{-1}+\boldsymbol{F}^{-T}\nabla\delta\boldsymbol{v}^T)\boldsymbol{F}^{-T},\nabla\psi_v\right)_f \\
&- \nu\left(J(\nabla\boldsymbol{v}\boldsymbol{F}^{-1}\nabla\delta\boldsymbol{u}\boldsymbol{F}^{-1}+\boldsymbol{F}^{-T}\nabla\delta\boldsymbol{u}^T\boldsymbol{F}^{-T}\nabla\boldsymbol{v}^T)\boldsymbol{F}^{-T},\nabla\psi_v\right)_f \\
&- \nu\left(J(\nabla\boldsymbol{v}\boldsymbol{F}^{-1}+\boldsymbol{F}^{-T}\nabla\boldsymbol{v}^T)\boldsymbol{F}^{-T}\nabla\delta\boldsymbol{u}^T\boldsymbol{F}^{-T},\nabla\psi_v\right)_f \\
&- \nu\left(J\mathrm{tr}(\boldsymbol{F}^{-1}\nabla\delta\boldsymbol{u})\boldsymbol{F}^{-T}\nabla\boldsymbol{v}^T\boldsymbol{F}^{-T}\boldsymbol{\eta},\psi_v\right)_{\mathrm{out}} \\
&+ \nu\left(J\boldsymbol{F}^{-T}\nabla\delta\boldsymbol{u}^T\boldsymbol{F}^{-T}\nabla\boldsymbol{v}^T\boldsymbol{F}^{-T}\boldsymbol{\eta},\psi_v\right)_{\mathrm{out}} \\
&- \nu\left(J\boldsymbol{F}^{-T}\nabla\delta\boldsymbol{v}^T\boldsymbol{F}^{-T}\boldsymbol{\eta},\psi_v\right)_{\mathrm{out}} \\
&+ \nu\left(J\boldsymbol{F}^{-T}\nabla\boldsymbol{v}^T\boldsymbol{F}^{-T}\nabla\delta\boldsymbol{u}^T\boldsymbol{F}^{-T}\boldsymbol{\eta},\psi_v\right)_{\mathrm{out}},
\end{aligned}
$$

$$
\begin{aligned}
L_I'[\boldsymbol{u},\boldsymbol{v},p](\delta\boldsymbol{u},\delta\boldsymbol{v},\delta p,\psi) = &-\frac{1}{\rho}\left(J\mathrm{tr}(\boldsymbol{F}^{-1}\nabla\delta\boldsymbol{u})p\boldsymbol{F}^{-T},\nabla\psi_v\right)_f \\
&-\frac{1}{\rho}\left(J\delta p\boldsymbol{F}^{-T},\nabla\psi_v\right)_f \\
&+\frac{1}{\rho}\left(Jp\boldsymbol{F}^{-T}\nabla\delta\boldsymbol{u}^T\boldsymbol{F}^{-T},\nabla\psi_v\right)_f \\
&+\left(J\mathrm{tr}(\boldsymbol{F}^{-1}\nabla\delta\boldsymbol{u})\mathrm{tr}(\nabla\boldsymbol{v}\boldsymbol{F}^{-1}),\psi_p\right)_f \\
&+\left(J\mathrm{tr}(\nabla\delta\boldsymbol{v}\boldsymbol{F}^{-1}),\psi_p\right)_f \\
&-\left(J\mathrm{tr}(\nabla\boldsymbol{v}\boldsymbol{F}^{-1}\nabla\delta\boldsymbol{u}\boldsymbol{F}^{-1}),\psi_p\right)_f \\
&-\left(J^{-1}\mathrm{tr}(\boldsymbol{F}^{-1}\nabla\delta\boldsymbol{u})\nabla\boldsymbol{u},\nabla\psi_u\right)_f \\
&+\left(J^{-1}\nabla\delta\boldsymbol{u},\nabla\psi_u\right)_f \\
&+\frac{1}{\rho}\left(J\mathrm{tr}(\boldsymbol{F}^{-1}\nabla\delta\boldsymbol{u})p^{\mathrm{out}}\boldsymbol{F}^{-T}\boldsymbol{\eta},\psi_v\right)_{\mathrm{out}} \\
&-\frac{1}{\rho}\left(Jp^{\mathrm{out}}\boldsymbol{F}^{-T}\nabla\delta\boldsymbol{u}^T\boldsymbol{F}^{-T}\boldsymbol{\eta},\psi_v\right)_{\mathrm{out}}.
\end{aligned}
$$

4.2.3 Spatial discretisation: Finite element method

With the linearisation of the time stepping procedure (4.4) as shown in the previous section 4.2.2, the linear equation (4.6) has to be solved in each Newton step. There are several methods for discretising a differential equation such as (4.6) in the spatial dimensions. Usually, they lead to a large system of linear equations for discrete degrees of freedom of the solution variables.

The integrals over the differential terms can be approximated by the finite volume method (FVM) [102]. Another approach is to approximate the derivatives by the finite differences method (FDM) [88]. Also, the Lattice Boltzmann method (LBM) [85] can be applied as a discretisation approach on a mesoscopic level between continuum mechanics and fluid particle movement. The FVM and LBM typically can be used for fluid flow problems not involving the dynamics of elastic structures. With the FDM, discrete solutions are only represented by nodal values. A discrete representation of the solution functions can be obtained by the finite element method (FEM) [13, 9, 59]. The FEM can be used to discretise a broad range of differential equations, especially for fluid flow and structural dynamics.

In this work, the FEM is utilised by means of a continuous Galerkin method based on the variational formulation as it is introduced in section 3.4.3.

In general, a finite element is given by the triple

$$(K,\Phi_K,\Xi_K).$$

$K\in\mathcal{T}_h$ is a finite convex element of a triangulation $\mathcal{T}_h$ of the domain $\mathcal{D}$.

$$\Phi_K=\{\psi:K\to\mathbb{R}\} \tag{4.13}$$

is a finite-dimensional space of shape functions on the cell K. Degrees of freedom are defined

as a set of linear independent functionals on the shape function space by

$$\Xi_K = \{\xi : \Phi_K \to \mathbb{R}\}. \tag{4.14}$$

In this work, triangulations are given by conforming meshes of triangles for two-dimensional geometries and tetrahedra for three-dimensional geometries (cf. section 4.1.2). Furthermore, Lagrange elements with polynomial shape functions

$$\Phi_K \subseteq \mathcal{P}_d(K),\ d = 1, 2 \tag{4.15}$$

are used, which are unisolvent, i.e.

$$\dim(\Phi_K) = \#\Xi_K. \tag{4.16}$$

The symbol # stands for the number of elements in a set. For Lagrange elements, the degrees of freedom are given by the evaluation of a shape function at a number of points $\boldsymbol{x}_j \in K$, $j = 1, \ldots, \#\Xi_K$:

$$\Xi_K = \{\xi_j : \Phi_K \to \mathbb{R}, \psi \mapsto \psi(\boldsymbol{x}_j)\}. \tag{4.17}$$

The evaluation points $\boldsymbol{x}_j$ for the degrees of freedom can be chosen in a way such that a shape function can be uniquely described by the set of degrees of freedom. For triangular cells, these points are indicated in Figure 4.2.

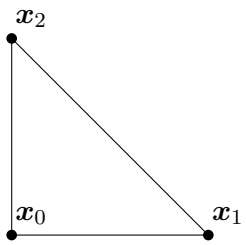

(a) Degrees of freedom for linear shape functions with $d = 1$ (P1).

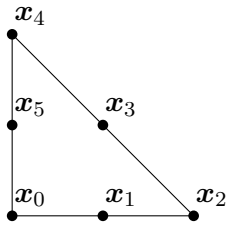

(b) Degrees of freedom for polynomial shape functions of degree $d = 2$ (P2).

Figure 4.2: Triangular Lagrange elements.

By means of the degrees of freedom, a basis of the shape function space can be defined:

$$\psi_j \in \Phi_K,\ \text{with } \psi_j(\boldsymbol{x}_i) = \delta_{ij},\ \text{for } j, i = 1, \ldots, \#\Xi_K. \tag{4.18}$$

Utilising the shape function basis (4.18), the solution functions can be approximated by a sum over a finite number of degrees of freedom $\chi_j^h \in \mathbb{R}$ of the function:

$$\chi(\boldsymbol{x}) \approx \sum_{K \in \mathcal{T}_h} \sum_{j=1}^{\#\Xi_K} \chi_j^h \psi_j(\boldsymbol{x}),\ \boldsymbol{x} \in \mathcal{D}. \tag{4.19}$$

In this work, the displacement and the velocity function is discretised with quadratic shape functions (P2) and the pressure with linear shape functions (P1). In the case of fluid

flow problems without elasticity, this combination is known as Taylor-Hood finite element. The P2-P2-P1 combination fulfils the inf-sup condition and is therefore stable [8]. The P1-ansatz is consistent of first order with respect to the H_1-norm and the P2-ansatz has second order consistency [13].

The finite element ansatz (4.19) can be inserted in the time-discrete and linearised weak formulation. For an exact integration over the polynomial shape functions, quadrature rules of corresponding order with quadrature points $q \in \mathcal{Q}$ and weights ζ_q can be used. For example, we have

$$(\boldsymbol{v}, \psi_i)_s \approx \sum_{K \in \mathcal{T}_h^s} \sum_{q \in \mathcal{Q}_K} \sum_{j=1}^{\#\Xi_K} \zeta_q \boldsymbol{v}_j^h \psi_j(q) \psi_i(q), \; i = 1, \ldots, \#\Xi_K. \tag{4.20}$$

This way, the Newton step (4.6) becomes a linear equation for each test shape function ψ_i, $i = 1, \ldots, \#\Xi_K$, $K \in \mathcal{T}_h$. The evaluation of the directional derivative can be written as a matrix-vector multiplication with the so-called Jacobian matrix J representing the directional derivative L' and the vector of degrees of freedom of the finite element ansatz function $(\boldsymbol{u}^h, \boldsymbol{v}^h, p^h)$. The discrete version of (4.6) reads:

$$\begin{bmatrix} J^{uu} & J^{uv} & J^{up} \\ J^{vu} & J^{vv} & J^{vp} \\ J^{pu} & J^{pv} & J^{pp} \end{bmatrix} \begin{bmatrix} \delta \boldsymbol{u}^h \\ \delta \boldsymbol{v}^h \\ \delta p^h \end{bmatrix} = \begin{bmatrix} L^{h,k}(\psi_u^h) \\ L^{h,k}(\psi_v^h) \\ L^{h,k}(\psi_p^h) \end{bmatrix}. \tag{4.21}$$

The superscripts at the Jacobian indicate the coupling of the ansatz and test functions. The detailed definition is given in the appendix, section 8.1.

4.2.4 Stochastical discretisation: Polynomial chaos

The modelling of uncertainties and the stochastical distribution of parameters and variables is described in section 3.5. It ends up in stating the stochastical boundary value problem (2) for FSI. In the previous sections of this chapter, the discretisation approaches for the time and spatial dimensions were presented. For the computation of the stochastical parameters of interest (cf. section 3.6), the discretisation of the stochastical dimensions is described in this section.

The stochastical space can be discretised in different ways. An overview of UQ-methods in computational fluid dynamics (CFD) is given in [87]. The UQ discretisation methods can be divided into two categories: intrusive and non-intrusive methods. Assuming the existence of an implemented deterministic solver for a given problem, the implementation has to be extended with the stochastical discretisation when following an intrusive UQ approach. In using non-intrusive methods, the deterministic solver usually can be reused as a part of the stochastical solution routine.

A family of non-intrusive techniques is given by Monte Carlo methods [77]. In Monte Carlo based methods, the simulation has to be carried out for a number of randomly chosen samples $\omega_i \in \Omega$, $i = 1, \ldots, N$ in order to approximate for example the stochastic moments by means of the sum

$$\mathbb{E}[\chi^m] \approx \mathbb{E}_N[\chi^m] := \frac{1}{N} \sum_{i=1}^{N} \chi^m(\omega_i). \tag{4.22}$$

The numerical convergence of standard Monte Carlo methods is independent of the dimension of the stochastic space. However, the number of necessary samples to achieve numerical convergence usually has to be large, because for standard Monte Carlo methods it typically holds

$$|\mathbb{E}[(\chi - E)^2] - \mathbb{E}_N[(\chi - E)^2]| = \mathcal{O}\left(\frac{1}{\sqrt{N}}\right).$$

Using modifications such as multilevel Monte Carlo methods, the numerical convergence can be improved [19].

Another approach for discretising the stochastic dimensions as used in this work is given by spectral methods. Hereby, a random variable χ is represented by an expansion series of functionals $\psi_j : \Omega \to \mathbb{R}$ with deterministic coefficients χ_j:

$$\chi(\omega) = \sum_{j=0}^{\infty} \chi_j \psi_j(\omega) \approx \sum_{j=0}^{M} \chi_j \psi_j(\omega), \quad \omega \in \Omega. \tag{4.23}$$

As opposed to point-wise sampling, the representation of the random variable as a sum of functionals over the full sample space allows for the definition of UQ methods of higher order convergence rates if the solution is smooth enough. In general, however, the convergence of spectral methods decreases with the dimension of the random variables, which is known as the curse of dimensions.

A specific spectral method is given by polynomial chaos (PC) [144, 145]. A review of PC-based UQ-methods in computational fluid dynamics is given in [103]. The ansatz of polynomial chaos is to choose orthogonal polynomials for the functionals ψ_j in the expansion (4.23). This approach requires a bounded variance and mutual independence of the random variables. The deterministic coefficients χ_j are also called modes of the respective PC expansion.

A classical PC expansion for Gaussian distributed random variables is given by Hermite polynomials. Other combinations of suitable stochastical distributions and types of polynomials can be determined via the Askey scheme of polynomials [5, 145]. This is known as generalised PC in the literature.

As motivated in section 3.5.2, the uncertain parameters considered in this work are uniformly distributed. According to the Askey scheme, it is suitable to use Legendre polynomials to construct the chaos polynomials for uniform parameter distributions:

$$\mathcal{L}_j(x) := \sum_{k=0}^{\lfloor j/2 \rfloor} (-1)^k \frac{(2j-2k)!}{(j-k)!(j-2k)!k!2^j} x^{j-2k}, \quad x \in [-1, 1], \tag{4.24}$$

with

$$\lfloor j/2 \rfloor := \begin{cases} \frac{j}{2}, & j \text{ even} \\ \frac{j-1}{2}, & j \text{ uneven} \end{cases}. \tag{4.25}$$

The first six Legendre polynomials are illustrated in Figure 4.3.

Integration over the interval $[-1, 1]$ gives

$$\int_{-1}^{1} \mathcal{L}_0(x) \mathrm{d}x = \int_{-1}^{1} 1 \mathrm{d}x = 2, \tag{4.26}$$

$$\int_{-1}^{1} \mathcal{L}_j(x) \mathrm{d}x = 0, \text{ for } j > 0, \tag{4.27}$$

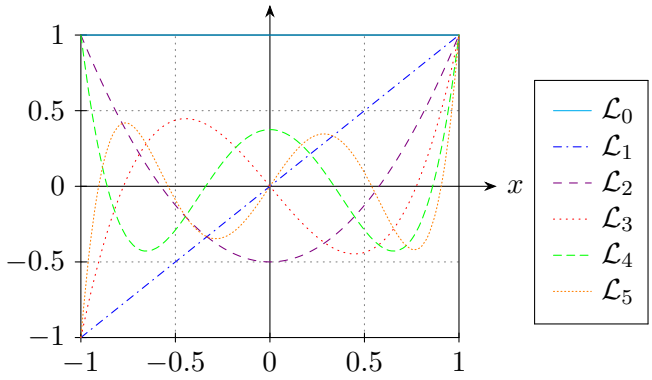

Figure 4.3: Legendre polynomials of degree $j = 0, \ldots, 5$.

and Legendre polynomials have the following orthogonality property:

$$\int_{-1}^{1} \mathcal{L}_j(x)\mathcal{L}_k(x)\mathrm{d}x = \frac{2}{2j+1}\delta_{jk}. \tag{4.28}$$

The chaos polynomials ψ_j in the expansion (4.23) are defined on an N-dimensional sample space Ω. They can be written as a tensor product of the one-dimensional Legendre polynomials. This involves the notation of a multi-index

$$\alpha^j = (\alpha_1^j, \ldots, \alpha_N^j) \in \mathbb{N}_0^N. \tag{4.29}$$

The tensor product reads

$$\psi_j(\omega) = \psi_{\alpha^j}(\omega) := \prod_{i=1}^{N} \mathcal{L}_{\alpha_i^j}(\omega_i), \quad \omega \in \Omega. \tag{4.30}$$

Given the number of stochastically independent parameters N and fixing the maximal degree of the Legendre polynomials P, the number of PC modes M can be calculated (cf. [57]) to:

$$M + 1 = \frac{(N+P)!}{N!P!}. \tag{4.31}$$

A mapping from the PC mode index $j = 0, \ldots, M$ to the multi-index α^j can be defined in the following way [87]:

1. Set $\alpha_i^0 = 0$, $i = 1, \ldots, N$.
2. For $P \geq 1$:
   (a) Set $\alpha_i^j = \delta_{ji}$, $j, i = 1, \ldots, N$.
3. For $\text{◊} \geq 2$:
   (a) Let $p \in \mathbb{N}_0^{N \times P}$ be a matrix of indices.
   (b) Set $p_{i,1} = 1$, $i = 1, \ldots, N$.

(c) Set $n = N$.

(d) For $k = 2, \ldots, P$:

i. Set $p_{i,k} = \sum_{m=i}^{N} p_{m,k-1}$, $i = 1, \ldots, N$.

ii. Set $l = n$.

iii. For $j = 1, \ldots, N$:
For $m = l - p_{j,k} + 1, \ldots, l$:

A. Set $n = n + 1$

B. Set $\alpha_i^n = \alpha_i^m$, $i = 1, \ldots, N$.

C. Set $\alpha_j^n = \alpha_j^n + 1$.

Let $\langle \phi, \psi \rangle := \int_\Omega \phi(\omega)\psi(\omega)\mathrm{d}\omega$ be the scalar product over the stochastic sample space. Then, the following orthogonality property holds for the chaos polynomials of two modes $j, k \in \mathbb{N}_0$ by the independence of the stochastical dimensions and with equation (4.28):

$$\begin{aligned}\langle \psi_j, \psi_k \rangle &= \int_\Omega \prod_{i=1}^{N} \mathcal{L}_{\alpha_i^j}(\omega_i) \prod_{l=1}^{N} \mathcal{L}_{\alpha_l^k}(\omega_l)\mathrm{d}\omega \\ &= \prod_{i=1}^{N} \delta_{\alpha_i^j \alpha_i^k} \int_{-1}^{1} \mathcal{L}_{\alpha_i^j}(\omega_i)\mathcal{L}_{\alpha_i^k}(\omega_i)\mathrm{d}\omega_i \\ &= \delta_{jk} \prod_{i=1}^{N} \frac{2}{2\alpha_i^j + 1}. \end{aligned} \tag{4.32}$$

Furthermore, integrating a PC polynomial results with (4.26) and (4.27) to

$$\int_\Omega \psi_j(\omega)\mathrm{d}\omega = \delta_{0j} 2^N, \text{ for } j \in \mathbb{N}_0. \tag{4.33}$$

By the orthogonality (4.32), the chaos polynomials ψ_j give a basis for the function space over Ω. The modes in equation (4.23) can be expressed as orthogonal projection:

$$\chi_j = \frac{\langle \chi, \psi_j \rangle}{\langle \psi_j, \psi_j \rangle}. \tag{4.34}$$

As an example, the random input parameters of the uncertain inflow velocity (3.64) and the Young's modulus (3.65) have the following PC expansion:

$$\begin{aligned} q(\omega) &= \bar{q} + \tilde{q}\omega_1 \\ &= \bar{q}\mathcal{L}_0(\omega_1)\mathcal{L}_0(\omega_2) + \tilde{q}\mathcal{L}_1(\omega_1)\mathcal{L}_0(\omega_2) \\ &= \bar{q}\psi_0(\omega) + \tilde{q}\psi_1(\omega), \end{aligned} \tag{4.35}$$

$$\begin{aligned} Y(\omega) &= \bar{Y} + \tilde{Y}\omega_2 \\ &= \bar{Y}\mathcal{L}_0(\omega_1)\mathcal{L}_0(\omega_2) + \tilde{Y}\mathcal{L}_0(\omega_1)\mathcal{L}_1(\omega_2) \\ &= \bar{Y}\psi_0(\omega) + \tilde{Y}\psi_2(\omega). \end{aligned} \tag{4.36}$$

The PC expansion of a solution variable χ (4.23) can be inserted in the definition of the stochastical moment operator (3.66). Using the equations (4.32) and (4.33), the expected value (3.62) and variance operator (3.63) then become

$$\begin{aligned}\mathbb{E}[\chi] &= \int_\Omega \sum_{j=0}^{\infty} \chi_j \psi_j(\omega) f^P(\omega) \mathrm{d}\omega \\ &= \int_\Omega \chi_0 \psi_0(\omega) \frac{1}{4} \mathrm{d}\omega \\ &= \chi_0, \end{aligned} \tag{4.37}$$

$$\begin{aligned}\sigma^2 &= \int_\Omega (\chi(\omega) - E)^2 P(\mathrm{d}\omega) \\ &= \int_\Omega \left(\sum_{j=1}^{\infty} \chi_j \psi_j(\omega) \right)^2 f^P(\omega) \mathrm{d}\omega \\ &= \sum_{j=1}^{\infty} \chi_j^2 \int_\Omega \psi_j^2(\omega) \frac{1}{4} \mathrm{d}\omega \\ &= \sum_{j=1}^{\infty} \chi_j^2 \prod_{i=1}^{2} \frac{1}{2\alpha_i^j + 1} \end{aligned} \tag{4.38}$$

In the following, both an intrusive and a non-intrusive method for UQ in FSI-simulations are presented based on the PC expansion method.

Intrusive Galerkin projection

Galerkin projection methods belong to the class of intrusive methods. Hereby, the random solution variables are projected onto a basis of the stochastical function space.

In the following, a Galerkin projection approach is described, which is used to approximate solutions of the benchmark problem presented in section 5.2. The benchmark problem is based on the stationary version of problem (2) with a linear elasticity equation. Furthermore, the benchmark does not include an outflow boundary. This way, it is possible to derive an analytical solution of the benchmark problem. The analytical solution is used to verify the correctness of the implemented numerical methods.

Following the Galerkin projection approach, the PC expansions (4.23) for the displacement, velocity and pressure fields are inserted in the variational stochastic FSI equation of problem 2. Hereby, the non-linearities induced by the ALE-mapping in the fluid domain lead to the occurrence of high order stochastic Galerkin tensors. However, the definition of the benchmark problem (cf. section 5.2) allows for a reduction of complexity in assuming that the ALE-displacement $\boldsymbol{u}_j|_{\mathcal{D}^\mathrm{f}}$ is not a PC coefficient, but a continuous continuation of the respective structural displacement PC mode $\boldsymbol{u}_j|_{\mathcal{D}^\mathrm{s}}$.

Insertion of the truncated PC expansions in the stationary version of the FSI equation (3.59) with the linear elasticity equations and applying the Galerkin projection on the

PC basis, the equation reads as follows

$$\begin{aligned}\left(\frac{1}{\rho}\sum_{j=0}^{M}\sum_{l=0}^{M}\left(\lambda_{1,j}(\nabla\cdot\boldsymbol{u}_l)\boldsymbol{I}+\lambda_{2,j}(\nabla\boldsymbol{u}_l+\nabla\boldsymbol{u}_l^T)\right)c_{jlk},\nabla\psi_v\right)_s \\ +\left(\sum_{j=0}^{M}\sum_{l=0}^{M}J_k\boldsymbol{F}_k^{-1}\boldsymbol{v}_j\cdot\nabla\boldsymbol{v}_l c_{jlk},\psi_v\right)_f \\ +\left(\nu J_k\left(\nabla\boldsymbol{v}_k\boldsymbol{F}_k^{-1}+\boldsymbol{F}_k^{-T}\nabla\boldsymbol{v}_k^T\right)\boldsymbol{F}_k^{-T},\nabla\psi_v\right)_f \\ -\left(\frac{1}{\rho}J_k p_k\boldsymbol{F}_k^{-T},\nabla\psi_v\right)_f+\left(J_k\mathrm{tr}(\nabla\boldsymbol{v}_k\boldsymbol{F}_k^{-1}),\psi_p\right)_f \\ +\left(J_k^{-1}\nabla\boldsymbol{u}_k,\nabla\psi_u\right)_f=0,\end{aligned} \tag{4.39}$$

for all modes $k=0,\dots,M$.

The indices j,l,k of the variables refer to the respective PC modes. As a result of the projection, the notation includes the third order stochastic Galerkin tensor

$$c_{jlk}:=\frac{\langle\psi_j\psi_l,\psi_k\rangle}{\langle\psi_k,\psi_k\rangle},\quad j,l,k=0,\dots,M. \tag{4.40}$$

The dependency of the PC modes of the Lamé coefficients λ_1 and λ_2 on the modes of the Young's modulus (3.65) is given by (3.41).

Details on the considered benchmark are given in section 5.2. The linear solver utilised for the benchmark is described in the last section 4.2.5 of this chapter.

Non-intrusive collocation

Collocation methods approximate solutions of random variables by means of point evaluations in the stochastic space. Thus, each collocation point is given by a deterministically computed value. In the case of a partial differential equation, each of these values is represented by a single deterministic simulation run. In this manner, one can speak of a non-intrusive method, as an already existing solver implementation can be used to calculate the collocation values. Various methods do exist to calculate the moments and probability distributions of random variable solutions based on a set of collocation points, such as the Monte Carlo method (4.22).

In this work, a PC-based collocation method is used to evaluate the three-dimensional numerical experiments given by the aortic phantom (section 6.1) and an aortic bow (6.2) with respect to the stochastical problem dimensions. For these scenarios, one cannot make the simplifying assumption used for the intrusive Galerkin projection, that the PC modes of ALE-displacement field do not couple with the different PC modes of the fluid velocity.

Instead, a collocation method based on chaos polynomials can be derived as illustrated in the following (cf. [105]).

By the orthogonal projection (4.34), the PC modes can be written as scalar products.

The integral of the scalar product can be approximated by a quadrature rule:

$$\begin{aligned}\chi_j &= \frac{1}{\langle \psi_j, \psi_j \rangle} \int_\Omega \chi(\omega)\psi_j(\omega)\mathrm{d}\omega \\ &\approx \frac{|\Omega|}{\langle \psi_j, \psi_j \rangle} \sum_{q \in \mathcal{Q}} \zeta_q \chi(q)\psi_j(q),\end{aligned} \tag{4.41}$$

with $\mathcal{Q} \subset \Omega$ denoting the set of quadrature points. The quadrature weights are given by

$$\zeta_q \in [0,1], \text{ for } q \in \mathcal{Q} \text{ with } \sum_{q \in \mathcal{Q}} \zeta_q = 1. \tag{4.42}$$

In this work, the Gauss-Legendre quadrature is used, which is optimal for integrating arbitrary polynomials. It is exact for polynomials of maximal degree $2\#\mathcal{Q} - 1$. As the random variable χ is approximated by a PC expansion of degree P, the maximal polynomial degree of the integrand in equation (4.41) can be approximated by $2P$. By this means, setting the quadrature order to $\#\mathcal{Q} = P + 1$ yields an exact integration rule. For the stochastical domain considered in this work $\Omega = [-1, 1]^2$, the quadrature points for a PC degree of $P = 4$ are illustrated in Figure 4.4.

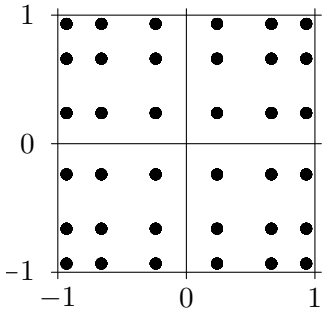

Figure 4.4: Gauss-Legendre quadrature points for a quadrature order of $\#\mathcal{Q} = 5$.

With the approximated PC modes, the mean value and the variance can be computed via (4.37), and (4.38), respectively. The stress overload probability (3.72), too, can be approximated with the help of the Gauss-Legendre quadrature rule:

$$\begin{aligned}P^\tau\left([\tau^{\max}, \infty)\right) &= \int_{\tau^{-1}([\tau^{\max}, \infty))} f^P(\omega)\mathrm{d}\omega \\ &\approx |\Omega| \sum_{q \in \mathcal{Q}, \tau(q) \geq \tau^{\max}} \zeta_q f^P(q) \\ &= 4 \sum_{q \in \mathcal{Q}, \tau(q) \geq \tau^{\max}} \zeta_q \frac{1}{4}.\end{aligned} \tag{4.43}$$

In the implementation for this work, the solver presented in the next section 4.2.5 is used to compute numerical solutions to the deterministic problem. The collocation method is executed via a Python script using the open source framework *ChaosPY*[9] for the UQ parts [42]. The essential functions of the script are listed in the appendix in section 8.2.

[9] github.com/jonathf/chaospy

4.2.5 Problem-specific linear solver

In the previous sections of this chapter, the discretisation methods utilised in this work have been presented. In the deterministic case as well as with the stochastic intrusive and non-intrusive approaches, the discretisation leads to liner systems of equations for the steps of the Newton method (4.21):

$$\mathcal{M}x = b. \tag{4.44}$$

In all scenarios considered in this work, the corresponding system matrix is unsymmetrical and of a sparse structure.

For the numerics on the solution of linear systems of equations in general, the reader is referred to [61]. In general, linear solvers can be classified in direct or iterative methods. Direct methods invert the system matrix at machine precision and therefore compute solutions accurately. The problem sizes considered in this work are too large for direct solvers in terms of computing demand. Suitable iterative solvers can approximate solutions much more efficiently to a required accuracy.

A family of standard iterative methods is given by Krylov subspace methods. A comprehensive introduction to Krylov subspace methods is given in [89]. Krylov subspace methods reduce the complexity of the given problem in determining an approximation to the solution in a subspace of a dimension significantly smaller than the dimension of the original problem. For the unsymmetrical system matrix and unsymmetrical submatrices, the flexible or the standard generalized minimal residual ((F)GMRES) method is used. The symmetric subproblems are solved with the conjugate gradients (CG) method. Assuming a rounding error free computation, both methods are capable of computing the exact solution after spanning the full Krylov subspace. Therefore, they can be seen as direct methods. However, a convergence of the approximation towards the solution can already be achieved at a much smaller number of iterations.

In general, the convergence of Krylov subspace methods depends on the condition number κ of the respective system matrix $\mathcal{M} \in \mathbb{R}^{d\times d}$. With respect to the Euclidean norm we have

$$\kappa_2(\mathcal{M}) := \|\mathcal{M}\|_2 \|\mathcal{M}^{-1}\|_2 = \frac{\sigma_{\max}(\mathcal{M})}{\sigma_{\min}(\mathcal{M})}. \tag{4.45}$$

Hereby, $\sigma_{\max}$ and $\sigma_{\min}$ denotes the maximal and minimal singular value, respectively. Analogously, the maximal and minimal eigenvalues are denoted by $\lambda_{\max}$ and $\lambda_{\min}$.

For the residual $r_n := \mathcal{M}x_n - b$ of the n-th iteration we have the following convergence estimation in the case of the GMRES method:

$$\|r_n\|_2 \leq \left(1 - \frac{\lambda_{\min}^2\left(\frac{1}{2}(\mathcal{M}^T + \mathcal{M})\right)}{\lambda_{\max}(\mathcal{M}^T\mathcal{M})}\right)^{n/2} \|r_0\|_2,$$

and for the CG method:

$$\|r_n\|_2 \leq 2\left(\frac{\sqrt{\kappa_2(\mathcal{M})} - 1}{\sqrt{\kappa_2(\mathcal{M})} + 1}\right)^n \|r_0\|_2.$$

Fluid flow and elasticity problems, respectively, and all the more a monolithically coupled FSI problem belong to the numerical class of stiff problems. Numerically stiff problems

possess a relatively broad distribution of eigenvalues and consequently a high condition number $\kappa \gg 1$. To nevertheless achieve convergence, equation (4.44) can be extended by means of a preconditioner $\mathcal{P} \in \mathbb{R}^{d \times d}$:

$$\mathcal{M}\mathcal{P}^{-1}\mathcal{P}x = b. \tag{4.46}$$

In the case of

$$1 \leq \kappa(\mathcal{M}\mathcal{P}^{-1}) \ll \kappa(\mathcal{M}),$$

the numerical convergence of a Krylov subspace method is usually considerably faster for

$$\mathcal{M}\mathcal{P}^{-1}y = b. \tag{4.47}$$

With the solution of

$$\mathcal{P}x = y, \tag{4.48}$$

the approximation to the solution of (4.44) can be obtained. Accordingly, the basic idea of preconditioning is to define an operator, which is similar to the system matrix in its principle effects $\mathcal{P} \approx \mathcal{M}$ reducing the spectrum with $\kappa(\mathcal{M}\mathcal{P}^{-1}) \approx 1$. The usage of a preconditioner is beneficial as soon as the costs for a repeated inversion of $\mathcal{P}$ is computationally cheaper than inverting $\mathcal{M}$ once without preconditioning.

There are problem-independent preconditioners, that can be used, if the system matrix has the required properties. However, often, a more efficient approach is to use a problem-specific preconditioner that exploits the given structure of the system matrix. Nevertheless, the development of efficient preconditioners for FSI problems is still a challenging effort.

A problem-independent, so-called black-box preconditioner is given by the incomplete LU decomposition [98], which has been applied to an FSI problem in [141]. Multigrid methods for preconditioning can be equipped with problem-specific smoothers as done in [116] for a geometric multigrid (GMG) and in [55] for an algebraic multigrid (AMG) approach. Ideas on utilising the block structure of the system matrix for a problem-specific preconditioner are given in [79]. A block-based preconditioner has been applied to hemodynamical problems in [32]. However, to the knowledge of the author, problem-specific solvers for FSI combined with UQ have not been published yet.

In the following, first, a solver for the intrusive approach (see equation (4.39)) is described. Subsequently, a preconditioner based on the Schur complement (SC) method is presented, which can be used for the computation of the collocation points $\chi(q)$ in (4.41).

An FSI solver for intrusive UQ

The system of equations (4.39) states a variational equation for each PC mode $k = 0, \ldots, M$. Each of the variational equations is similar to the deterministic counterpart. Linearisation (cf. section 4.2.2) and discretisation in the spatial dimensions by the FEM (cf. section 4.2.3) leads to a linear system of equations, which is $M + 1$ times larger than the deterministic system (4.21).

To create the Jacobian system matrix and right hand side of the linear system of equations for every Newton iteration, the FEM software package HiFlow^3 is used. In particular, HiFlow^3 has a UQ module providing the coefficients of the stochastic Galerkin tensor (4.40) as described in [54].

The linear system of equations is solved in parallel with the GMRES method implemented in HiFlow^3. To precondition the system matrix, a multilevel incomplete LU decomposition method in Crout's formulation [98] is applied with inverse-based dropping. For this, the software *ILU++* [97] is used.

A Schur complement solver for FSI problems

To compute both, the deterministic benchmark problem (see section 5.1) and the collocation points for the blood flow simulations under uncertainties (see chapter 6), this work includes the development of a problem-specific preconditioner. This preconditioner utilises the block structure of the Jacobian system matrix of equation (4.21). The block structure of the matrix is given as follows:

$$\begin{bmatrix} J^{uu} & J^{uv} & J^{up} \\ J^{vu} & J^{vv} & J^{vp} \\ J^{pu} & J^{pv} & J^{pp} \end{bmatrix} = \left[\begin{array}{ccc:ccc:cc} \frac{1}{k}\mathcal{M} & & 0 & & -\theta\mathcal{M} & & 0 & \\ & \frac{1}{k}\mathcal{M}+\mathcal{L} & & & & & 0 & 0 \\ 0 & & \mathcal{L} & 0 & 0 & & 0 & \\ \hdashline \mathcal{E} & & 0 & \frac{1}{k}\mathcal{M} & & & 0 & 0 \quad 0 \\ & \mathcal{E}+\mathcal{A}^v & & & \frac{1}{k}\mathcal{M}+\mathcal{N} & & \mathcal{D} & \\ 0 & & \mathcal{A}^v & 0 & & \mathcal{N} & & \\ \hdashline 0 & & & 0 & & & & \\ 0 & \mathcal{A}^p & & 0 & \tilde{\mathcal{D}} & & 0 & \\ 0 & & & 0 & & & & \end{array}\right]. \tag{4.49}$$

Hereby, the lines and rows are ordered by the degrees of freedom firstly of the variables and secondly of the domain, they belong to. The domain numbering respectively begins with the solid domain, then counts the degrees of freedom at the fluid-solid interface and ends with the fluid domain. Since the elasticity equation does not include the pressure as a variable on the solid domain, the degrees of freedom for the pressure only account for the interface and the fluid domain.

For the following definition of the submatrices, the scalar product notation is used, since the quadrature rule is chosen to be exact for the polynomial ansatz and test functions of the finite element discretisation. Here, j denotes the respective degree of freedom for the ansatz shape function and i denotes the respective degree of freedom for the test shape function. The variables and the strain tensors at the respective Newton iteration n are discretised as finite element functions, indicated by h. Variables of the previous time step are indicated with $l-1$.

The mass matrix occurs several times in the Jacobian matrix:

$$\mathcal{M}_{ij} = (\psi_j, \psi_i)_s .$$

The fluid mesh movement model results in the Laplace-like matrix

$$\mathcal{L}_{ij} = -\left(J^{-1}\mathrm{tr}(\boldsymbol{F}^{-1}\nabla\psi_j)\nabla\boldsymbol{u}^{h,n}, \nabla\psi_i\right)_f + \left(J^{-1}\nabla\psi_j, \nabla\psi_i\right)_f .$$

The matrix for the solid stress tensor has the form

$$\begin{aligned}\mathcal{E}_{ij} =& \frac{\theta}{\rho}\left(\nabla\psi_j(\lambda_1\mathrm{tr}(\boldsymbol{E})\boldsymbol{I} + 2\lambda_2\boldsymbol{E}), \nabla\psi_i\right)_s \\ &+ \frac{\theta}{\rho}\left(\boldsymbol{F}(\lambda_1\frac{1}{2}\mathrm{tr}(\nabla\psi_j^T\boldsymbol{F} + \boldsymbol{F}^T\nabla\psi_j)\boldsymbol{I} + \lambda_2(\nabla\psi_j^T\boldsymbol{F} + \boldsymbol{F}^T\nabla\psi_j)), \nabla\psi_i\right)_s .\end{aligned}$$

A large number of terms results from the linearised ALE-mapping of the fluid domain to the time-dependent configuration:

$$
\begin{aligned}
\mathcal{A}^v_{ij} =& \frac{\theta}{k}\left(J\mathrm{tr}(\boldsymbol{F}^{-1}\nabla\psi_j)(\boldsymbol{v}^{h,n}-\boldsymbol{v}^{h,l-1}),\psi_i\right)_f \\
&-\frac{1}{k}\left(J\mathrm{tr}(\boldsymbol{F}^{-1}\nabla\psi_j)\boldsymbol{F}^{-1}(\boldsymbol{u}^{h,n}-\boldsymbol{u}^{h,l-1})\cdot\nabla\boldsymbol{v}^{h,n},\psi_i\right)_f \\
&+\frac{1}{k}\left(J\boldsymbol{F}^{-1}\nabla\psi_j\boldsymbol{F}^{-1}(\boldsymbol{u}^{h,n}-\boldsymbol{u}^{h,l-1})\cdot\nabla\boldsymbol{v}^{h,n},\psi_i\right)_f \\
&-\frac{1}{k}\left(J\boldsymbol{F}^{-1}\psi_j\cdot\nabla\boldsymbol{v}^{h,n},\psi_i\right)_f \\
&+\theta\left(J\mathrm{tr}(\boldsymbol{F}^{-1}\nabla\psi_j)\boldsymbol{F}^{-1}\boldsymbol{v}^{h,n}\cdot\nabla\boldsymbol{v}^{h,n},\psi_i\right)_f-\theta\left(J\boldsymbol{F}^{-1}\nabla\psi_j\boldsymbol{F}^{-1}\boldsymbol{v}^{h,n}\cdot\nabla\boldsymbol{v}^{h,n},\psi_i\right)_f \\
&+\theta\nu\left(J\mathrm{tr}(\boldsymbol{F}^{-1}\nabla\psi_j)(\nabla\boldsymbol{v}^{h,n}\boldsymbol{F}^{-1}+\boldsymbol{F}^{-T}\nabla\boldsymbol{v}^{h,n^T})\boldsymbol{F}^{-T},\nabla\psi_i\right)_f \\
&-\theta\nu\left(J(\nabla\boldsymbol{v}^{h,n}\boldsymbol{F}^{-1}\nabla\psi_j\boldsymbol{F}^{-1}+\boldsymbol{F}^{-T}\nabla\psi_j^T\boldsymbol{F}^{-T}\nabla\boldsymbol{v}^{h,n^T})\boldsymbol{F}^{-T},\nabla\psi_i\right)_f \\
&-\theta\nu\left(J(\nabla\boldsymbol{v}^{h,n}\boldsymbol{F}^{-1}+\boldsymbol{F}^{-T}\nabla\boldsymbol{v}^{h,n^T})\boldsymbol{F}^{-T}\nabla\psi_j^T\boldsymbol{F}^{-T},\nabla\psi_i\right)_f \\
&-\frac{1}{\rho}\left(J\mathrm{tr}(\boldsymbol{F}^{-1}\nabla\psi_j)p^{h,n}\boldsymbol{F}^{-T},\nabla\psi_i\right)_f+\frac{1}{\rho}\left(Jp^{h,n}\boldsymbol{F}^{-T}\nabla\psi_j^T\boldsymbol{F}^{-T},\nabla\psi_i\right)_f \\
&-\theta\nu\left(J\mathrm{tr}(\boldsymbol{F}^{-1}\nabla\psi_j)\boldsymbol{F}^{-T}\nabla\boldsymbol{v}^{h,n^T}\boldsymbol{F}^{-T}\boldsymbol{\eta},\psi_i\right)_{\mathrm{out}} \\
&+\theta\nu\left(J\boldsymbol{F}^{-T}\nabla\psi_j^T\boldsymbol{F}^{-T}\nabla\boldsymbol{v}^{h,n^T}\boldsymbol{F}^{-T}\boldsymbol{\eta},\psi_i\right)_{\mathrm{out}} \\
&+\theta\nu\left(J\boldsymbol{F}^{-T}\nabla\boldsymbol{v}^{h,n^T}\boldsymbol{F}^{-T}\nabla\psi_j^T\boldsymbol{F}^{-T}\boldsymbol{\eta},\psi_i\right)_{\mathrm{out}} \\
&+\frac{1}{\rho}\left(J\mathrm{tr}(\boldsymbol{F}^{-1}\nabla\psi_j)p^{\mathrm{out}}\boldsymbol{F}^{-T}\boldsymbol{\eta},\psi_i\right)_{\mathrm{out}}-\frac{1}{\rho}\left(Jp^{\mathrm{out}}\boldsymbol{F}^{-T}\nabla\psi_j^T\boldsymbol{F}^{-T}\boldsymbol{\eta},\psi_i\right)_{\mathrm{out}}.
\end{aligned}
$$

The terms for the time derivative, convection and the fluid stress tensor of the Navier-Stokes equations yields the matrix

$$
\begin{aligned}
\mathcal{N}_{ij} =& \frac{1}{k}\left(J^{l,\theta}\psi_j,\psi_i\right)_f \\
&-\frac{1}{k}\left(J\boldsymbol{F}^{-1}(\boldsymbol{u}^{h,n}-\boldsymbol{u}^{h,l-1})\cdot\nabla\psi_j,\psi_i\right)_f \\
&+\theta\left(J\boldsymbol{F}^{-1}\psi_j\cdot\nabla\boldsymbol{v}^{h,n},\psi_i\right)_f+\theta\left(J\boldsymbol{F}^{-1}\boldsymbol{v}^{h,n}\cdot\nabla\psi_j,\psi_i\right)_f \\
&+\theta\nu\left(J(\nabla\psi_j\boldsymbol{F}^{-1}+\boldsymbol{F}^{-T}\nabla\psi_j^T)\boldsymbol{F}^{-T},\nabla\psi_i\right)_f \\
&-\theta\nu\left(J\boldsymbol{F}^{-T}\nabla\psi_j^T\boldsymbol{F}^{-T}\boldsymbol{\eta},\psi_i\right)_{\mathrm{out}}.
\end{aligned}
$$

The pressure term of the Navier-Stokes equations results in

$$
\mathcal{D}_{ij}=-\frac{1}{\rho}\left(J\psi_j\boldsymbol{F}^{-T},\nabla\psi_i\right)_f.
$$

The linearised ALE-mapping of the divergence term gives another part of the matrix

$$\begin{aligned}\mathcal{A}^p_{ij} = &\left(J\mathrm{tr}(\boldsymbol{F}^{-1}\nabla\psi_j)\mathrm{tr}(\nabla\boldsymbol{v}^{h,n}\boldsymbol{F}^{-1}), \psi_i\right)_f \\ &- \left(J\mathrm{tr}(\nabla\boldsymbol{v}^{h,n}\boldsymbol{F}^{-1}\nabla\psi_j\boldsymbol{F}^{-1}), \psi_i\right)_f .\end{aligned}$$

Finally, the divergence matrix of the Navier-Stokes equations reads

$$\tilde{\mathcal{D}}_{ij} = \left(J\mathrm{tr}(\nabla\psi_j\boldsymbol{F}^{-1}), \psi_i\right)_f .$$

A problem-specific preconditioner for the system matrix (4.49) can be developed by the SC method nested in two steps. The SC method is based on a block Gaussian elimination step on a 2×2 block system. It has been frequently used for example for solving the saddle point matrix resulting from incompressible Navier-Stokes problems [127, 33].

In general, a 2×2 block matrix can be decomposed in the product

$$\mathcal{M} = \begin{bmatrix}\mathcal{A} & \mathcal{B}\\ \mathcal{C} & \mathcal{D}\end{bmatrix} = \begin{bmatrix}\mathcal{A} & 0\\ \mathcal{C} & \boldsymbol{I}\end{bmatrix}\begin{bmatrix}\boldsymbol{I} & \mathcal{A}^{-1}\mathcal{B}\\ \mathcal{C} & \mathcal{S}\end{bmatrix},$$

with the SC matrix $\mathcal{S} := \mathcal{D} - \mathcal{C}\mathcal{A}^{-1}\mathcal{B}$. For the linear system of equations

$$\begin{bmatrix}\mathcal{A} & \mathcal{B}\\ \mathcal{C} & \mathcal{D}\end{bmatrix}\begin{bmatrix}x\\ y\end{bmatrix} = \begin{bmatrix}f\\ g\end{bmatrix},$$

the solution can then be obtained via successively solving

$$\begin{aligned}\mathcal{S}y &= g - \mathcal{C}\mathcal{A}^{-1}f,\\ \mathcal{A}x &= f - \mathcal{B}y.\end{aligned}$$

Applied to (4.21), the first part of the nested SC approach separates the computation of the displacement and the velocity-pressure field. With the solution of the SC equation

$$\mathcal{S}^u\begin{bmatrix}\delta\boldsymbol{v}^h\\ \delta p^h\end{bmatrix} = \begin{bmatrix}L^{h,k}(\psi^h_v)\\ L^{h,k}(\psi^h_p)\end{bmatrix} - \begin{bmatrix}J^{vu}\\ J^{pu}\end{bmatrix} J^{uu-1}L^{h,k}(\psi^h_u) \tag{4.50}$$

the velocity-pressure field is obtained. With

$$\delta\boldsymbol{u}^h = J^{uu-1}\left(L^{h,k}(\psi^h_u) - \begin{bmatrix}J^{uv}J^{up}\end{bmatrix}\begin{bmatrix}\delta\boldsymbol{v}^h\\ \delta p^h\end{bmatrix}\right)$$

the displacement field is computed. The SC matrix $\mathcal{S}^u$ is defined as follows

$$\mathcal{S}^u := \begin{bmatrix}J^{vv} & J^{vp}\\ J^{pv} & J^{pp}\end{bmatrix} - \begin{bmatrix}J^{vu}\\ J^{pu}\end{bmatrix} J^{uu-1}\begin{bmatrix}J^{uv}J^{up}\end{bmatrix}. \tag{4.51}$$

The SC equation (4.50) is a linear system of equations that can be seen as a discrete Navier-Stokes problem on the fluid domain and a mass operator with further terms in the system matrix on the solid domain. Since the method is meant to be used as a preconditioner,

it is sufficient to compute an approximation to the SC equation. The SC system matrix (4.51) can be approximated by exploiting the block structure of the matrix (4.49) and neglecting the fluid domain terms for the degrees of freedom on the fluid-structure interface:

$$\begin{aligned}
\mathcal{S}^u &= \begin{bmatrix} J^{vv} & J^{vp} \\ J^{pv} & J^{pp} \end{bmatrix} - \begin{bmatrix} \mathcal{E} & & & 0 \\ & \mathcal{E}+\mathcal{A}^v & & \\ 0 & & \mathcal{A}^v & \\ 0 & & & \mathcal{A}^p \\ 0 & & & \end{bmatrix} \begin{bmatrix} \frac{1}{k}\mathcal{M} & & & 0 \\ & \frac{1}{k}\mathcal{M}+\mathcal{L} & & \\ 0 & & & \mathcal{L} \end{bmatrix}^{-1} \begin{bmatrix} -\theta\mathcal{M} & & 0 & \\ & 0 & 0 & 0 \\ 0 & 0 & 0 & \end{bmatrix} \\
&\approx \begin{bmatrix} J^{vv} & J^{vp} \\ J^{pv} & J^{pp} \end{bmatrix} - \begin{bmatrix} \mathcal{E} & & 0 & \\ & 0 & & \\ 0 & 0 & \mathcal{A}^v & \\ 0 & & & \mathcal{A}^p \\ 0 & & & \end{bmatrix} \begin{bmatrix} k\mathcal{M}^{-1} & & 0 & \\ & 0 & & \\ 0 & 0 & \mathcal{L}^{-1} & \end{bmatrix} \begin{bmatrix} -\theta\mathcal{M} & & 0 & \\ & 0 & 0 & 0 \\ 0 & 0 & 0 & \end{bmatrix} \\
&= \begin{bmatrix} \frac{1}{k}\mathcal{M} & & & 0 & 0 & 0 \\ & \frac{1}{k}\mathcal{M}+\mathcal{N} & & \mathcal{N} & \mathcal{D} & \\ 0 & & & & & \\ 0 & & \tilde{\mathcal{D}} & & 0 & \\ 0 & & & & & \end{bmatrix} + \begin{bmatrix} \theta k\mathcal{E} & & 0 & & \\ & 0 & 0 & 0 & \\ 0 & 0 & 0 & & \\ & 0 & & 0 & \\ & & & & \end{bmatrix}.
\end{aligned}$$

With that, we set

$$\tilde{J^{vv}} := \begin{bmatrix} \frac{1}{k}\mathcal{M}+\theta k\mathcal{E} & & 0 \\ & \frac{1}{k}\mathcal{M}+\theta k\mathcal{E}+\mathcal{N} & \\ 0 & & \mathcal{N} \end{bmatrix}. \tag{4.52}$$

To solve the SC equation (4.50), the flexible GMRES method is used. Again, the SC method can be used for preconditioning in a second part of the nested method. This second part splits the computation of the velocity and the pressure field. The corresponding SC equation reads

$$\mathcal{S}^v \delta p^h = g - J^{pv} \tilde{J^{vv}}^{-1} f, \tag{4.53}$$

with the SC matrix

$$\mathcal{S}^v := -J^{pv} \tilde{J^{vv}}^{-1} J^{vp}, \tag{4.54}$$

and the right-hand side of equation (4.50)

$$\begin{bmatrix} f \\ g \end{bmatrix} := \begin{bmatrix} L^{h,k}(\psi_v^h) \\ L^{h,k}(\psi_p^h) \end{bmatrix} - \begin{bmatrix} J^{vu} \\ J^{pu} \end{bmatrix} J^{uu-1} L^{h,k}(\psi_u^h).$$

The velocity field is then updated via

$$\delta \boldsymbol{v}^h = \tilde{J^{vv}}^{-1} \left(f - J^{vp} \delta p^h \right).$$

Also the second SC equation (4.53) is solved with the flexible GMRES method. The second SC matrix (4.54) is preconditioned by the approximative inversion of the semi-implicit method for pressure-linked equations (SIMPLE) approximation [33] to $\mathcal{S}^v$

$$\mathcal{S}^v \approx \tilde{\mathcal{S}}^v := -J^{pv} \mathrm{diag}(\tilde{J^{vv}})^{-1} J^{vp}. \tag{4.55}$$

The matrix $\tilde{\mathcal{S}}^v$ can explicitly be computed by a matrix-matrix multiplication.

For the approximative inversion of the predominantly symmetric matrix J^{uu} the CG method is used and for the unsymmetric matrix $\tilde{J^{vv}}$ the GMRES method is used as the solver. All of the three matrices are preconditioned with the AMG method, available as *BoomerAMG* [64] in the open source software package *HYPRE*[10] [41], version 2.13.0. For the SC method, the implementation of the method in HiFlow[3], version 2.0, is used.

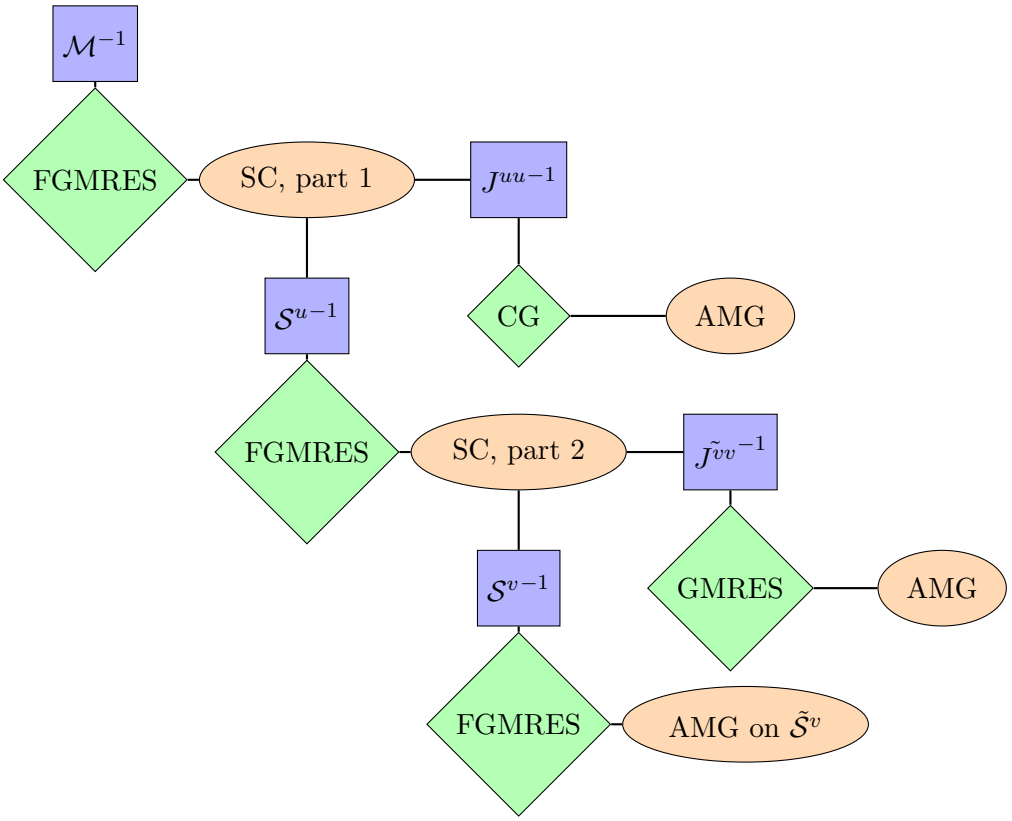

Figure 4.5: Linear solver routine with a nested Schur complement approach for preconditioning the linearised, discrete FSI problem. The blue rectangles indicate the respective linear operator that is to be inverted. The utilised linear solvers are named in the green diamonds. The orange ellipsis give the preconditioning methods of the linear subproblems.

A summary of the full linear solving algorithm is illustrated in Figure 4.5: In each Newton iteration (cf. section 4.2.2), the full linear system of equations is iteratively solved by the FGMRES method. It is preconditioned with a first application of the SC method, splitting the problem with respect to the displacement variables (system matrix J^{uu}) and the velocity and pressure variables (system matrix $\mathcal{S}^u$). Preconditioning the iterative inversion of $\mathcal{S}^u$ is achieved by a second application of the SC method. This leads to the subproblems for the velocity variables (system matrix $\tilde{J^{vv}}$) and for the pressure variables (system matrix $\tilde{\mathcal{S}}^v$).

[10] computation.llnl.gov/projects/hypre-scalable-linear-solvers-multigrid-methods

5 Numerical benchmarking

This chapter addresses the verification and benchmarking of the numerical solver presented in section 4.2. For the benchmarking of the deterministic FSI solver, a widely recognised benchmark, presented in [136], is used. The benchmark was run with various numerical solvers before, with a summary of the results in [137]. In section 5.1, a reproduction of the benchmark quantities with the numerical solver developed in this work is presented. Additionally, the implemented solver is examined with respect to its parallel scalability.

An overview on further benchmarks for different aspects of FSI problems is given in [10]. To the knowledge of the author, FSI benchmark problems with an analytical solution have not been published before. Therefore, a new benchmark for FSI problems with uncertain parameters is derived in section 5.2. The benchmark problem has an analytical solution, which enables the exact evaluation of the discretisation error.

5.1 Results for a deterministic FSI benchmark

For the verification and benchmarking of the FSI solver developed and implemented in the course of this work, a widely recognised benchmark problem is used. The benchmark is proposed in [136]. It can be seen as an extension of the laminar flow around a cylinder benchmark [121], whereby an elastic bar is attached downstream at the cylinder. A comparison of various solver implementations by means of this FSI benchmark is given in [137]. The FSI benchmark is based on a two-dimensional geometry and comprises three cases with different model parameters. In this work we focus on the FSI3 case, which has an instationary solution.

In the following section 5.1.1, a short description of the FSI benchmark is given. Section 5.1.2 presents the evaluation results for the benchmark quantities. Finally, results for the parallel scalability computing the benchmark are shown in section 5.1.3.

5.1.1 Flow around a cylinder with an elastic bar

The geometry of the benchmark is shown in Figure 5.1 and the specification of the geometrical parameters is given in Table 5.1. The geometry is based on the CFD benchmark of a laminar flow around a cylinder [121] with a rectangular channel and a circular obstacle at the beginning of the channel. The FSI benchmark extends the CFD benchmark with an elastic bar attached downstream to the obstacle.

In the FSI benchmark, the fluid flow is modelled as an incompressible Newtonian fluid and mathematically described by the incompressible Navier-Stokes equations. The model for the

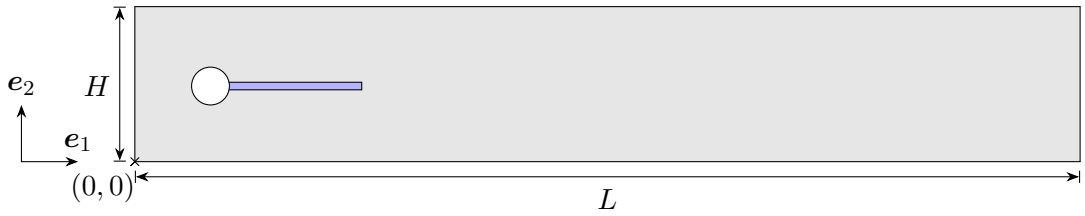

(a) Rectangular channel of the height H and the length L. Also, the orientation and the origin of the coordinate system are depicted.

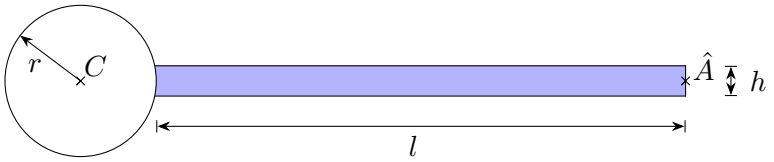

(b) Circular rigid obstacle around the centre point C with the radius r. The attached elastic bar has a length l and a width h. Additionally, the reference point $\hat{A}$ for measuring the displacement of the centred end point of the bar is marked.

Figure 5.1: Geometry of the FSI benchmark adopted from [136].

Parameter	Symbol	Value in [m]
Channel length	L	2.5
Channel height	H	0.41
Obstacle radius	r	0.05
Obstacle center	C	$(0.2, 0.2)$
Bar length	l	0.35
Bar height	h	0.02
Bar end point	$\hat{A}$	$(0.6, 0.2)$

Table 5.1: Geometrical parameters of the FSI benchmark.

Parameter	Symbol	Value
Density	ρ	$1 \times 10^3\,\mathrm{kg\,m^{-3}}$
Kinematic viscosity	ν	$1 \times 10^{-3}\,\mathrm{m^2\,s^{-1}}$
Poisson's ratio	γ	0.4
2nd Lamé coefficient	λ_2	$2 \times 10^6\,\mathrm{kg\,m^{-1}\,s^{-2}}$
Inflow speed	v^{in}	$2\,\mathrm{m\,s^{-1}}$

Table 5.2: Model parameters and their values.

elastic material is given by the STVK constitutive law. This modelling approach results in the two-dimensional version of the system of partial differential equations as stated in (3.59). The values for the model parameters are given in Table 5.2.

The obstacle as well as the upper and lower boundary of the channel are rigid and conform to a no-slip boundary condition for the fluid flow. The left side of the channel at the origin is the inflow with a prescribed inflow velocity profile. This profile corresponds to the two-dimensional version of the Poisseuille inflow boundary condition as defined in equation (3.29) with $\beta = 2$:

$$\boldsymbol{v}_1^{\text{in}}(0, y) = 1.5 v^{\text{in}} \frac{y(H-y)}{(H/2)^2}, \quad \boldsymbol{v}_2^{\text{in}}(0, y) = 0, \quad \text{for } 0 \leq y \leq H. \tag{5.1}$$

At the outflow boundary on the right side of the geometry, a pressure boundary condition is prescribed with a zero mean pressure $p^{\text{out}} = 0$ in equation (3.58). This corresponds to the do-nothing boundary condition for the incompressible Navier-Stokes equations.

The definition of the Reynolds number for this benchmark is given by the ratio of the effective inflow speed times the diameter of the circular obstacle to the kinematic viscosity:

$$\text{Re} = \frac{v^{\text{in}} 2r}{\nu} = 200.$$

The Reynolds number can be seen as a parameter for the ratio of inertial forces to viscous forces, and allows for the characterisation of a flow field with respect to its turbulence. At a value of $\text{Re} = 200$, a flow field is usually laminar with light vortex formation.

Similar to [136], the initial condition for the benchmark computation is chosen in a way such that the simulation can smoothly start with zero values in the variables:

$$\boldsymbol{v}_1^{\text{in}}(0, y, t) = \begin{cases} \boldsymbol{v}_1^{\text{in}}(0, y) \frac{1}{2}(1 - \cos(\pi \frac{t}{0.2})), & 0 \leq t < 0.2, \\ \boldsymbol{v}_1^{\text{in}}(0, y), & t \geq 0.2. \end{cases} \tag{5.2}$$

5.1.2 Benchmark results

The benchmark problem has been discretised and numerically solved as described in section 4.2. Hereby, *gmsh*[1] [56] has been used to create discrete FEM meshes of triangular cells at different refinement levels. The simulations for this work were carried out on the *BwForCluster MLS&WISO Production*[2] located at Heidelberg University. The computational costs ranged from 1 hour wall time on 2 CPU cores for the smallest mesh refinement R1 to 30 hours wall time on 64 CPU cores on the highest mesh refinement R4. The number of FEM degrees of freedom for the different mesh refinement levels is given in Table 5.3. A visualisation of the benchmark simulation is illustrated in Figure 5.2.

For the verification of a newly implemented FSI solver, ten values for comparison are defined for the FSI benchmark in [137]. The first four values are given by the mean and maximal displacement of the reference point $\hat{A}$ in horizontal $\boldsymbol{u}_1(\hat{A})$ and vertical direction $\boldsymbol{u}_2(\hat{A})$. Additionally, the frequencies of these periodical displacement values, f_1, f_2, respectively, can be compared. Furthermore, the mean values and amplitudes of the drag and lift forces on the obstacle together with the elastic bar are used. The drag force F_D and lift force F_L are

[1] gmsh.info

[2] www.bwhpc-c5.de/wiki/index.php/Category:BwForCluster_MLS%26WISO_Production

(a) The displacement in horizontal direction.

(b) The displacement in vertical direction. The elastic bar periodically flaps up and down.

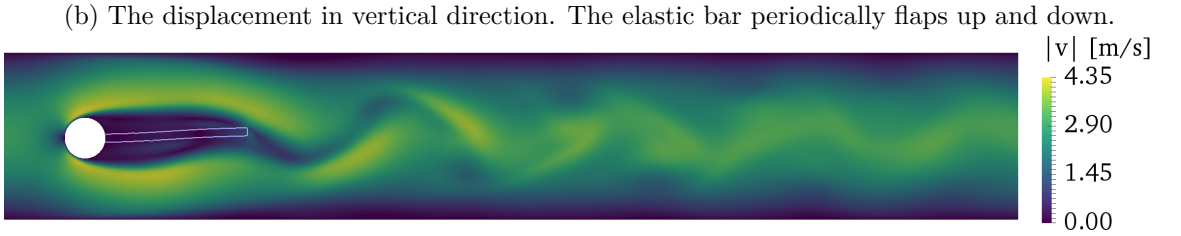

(c) The magnitude of the velocity field. The downstream flow shows vortices towards a Kármán vortex street.

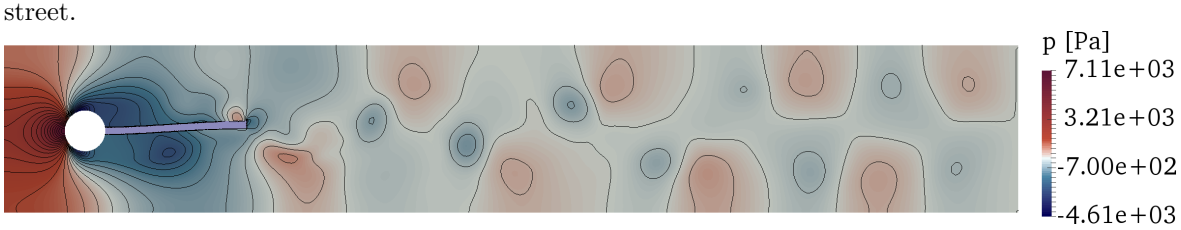

(d) The pressure field in the fluid domain with contour lines.

Figure 5.2: Visualisation of the FSI benchmark simulation at a time step of an instationary and fully developped downstream flow.

Mesh refinement	R1	R2	R3	R4
# dofs	9048	32,507	126,574	502,962
k	0.002	0.001	0.0005	0.001
$\boldsymbol{u}_1(\hat{A})$ $[10^{-3}\,\mathrm{m}]$	-1.87 ± 1.75	-2.70 ± 2.54	-2.94 ± 2.77	-2.94 ± 2.77
$\boldsymbol{u}_2(\hat{A})$ $[10^{-3}\,\mathrm{m}]$	2.58 ± 26.36	1.24 ± 33.70	1.45 ± 35.32	1.44 ± 35.33
f_1 $[\mathrm{s}^{-1}]$	10.73	10.83	10.94	10.96
f_2 $[\mathrm{s}^{-1}]$	5.36	5.42	5.47	5.48
F_D [N]	387.10 ± 12.72	422.10 ± 22.54	455.20 ± 27.06	459.20 ± 27.96
F_L [N]	-24.18 ± 139.30	5.45 ± 155.60	2.67 ± 159.30	2.69 ± 161.70

Table 5.3: Results for the computation of the benchmark values. The second row gives the number of degrees of freedom (dofs) for the respective mesh refinement level. The third row gives the respectively utilised discrete time step length k.

calculated by the boundary integral of the fluid stress tensor over the fluid-structure interface $\mathcal{B}^{\mathrm{i}}$ and the obstacle boundary $\mathcal{B}^{\mathrm{o}}$:

$$(F_D, F_L) = \int_{\mathcal{B}^{\mathrm{i}} \cup \mathcal{B}^{\mathrm{o}}} \left(\nu J \left(\nabla \boldsymbol{v} \boldsymbol{F}^{-1} + \boldsymbol{F}^{-T} \nabla \boldsymbol{v}^T \right) \boldsymbol{F}^{-T} + \frac{1}{\rho} J p \boldsymbol{F}^{-T} \right) \boldsymbol{\eta} \mathrm{d}s. \tag{5.3}$$

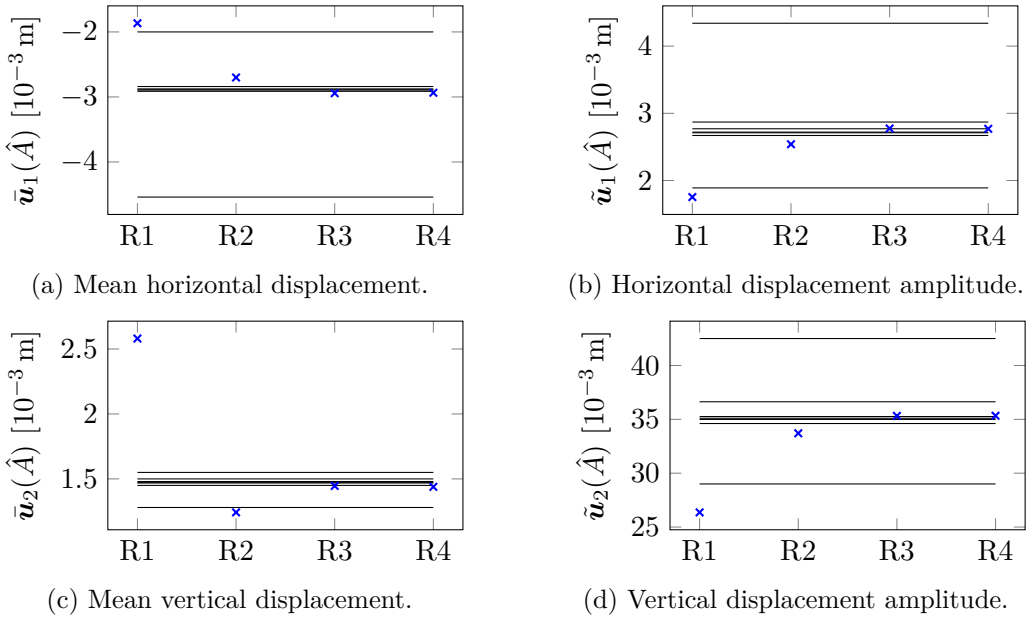

(a) Mean horizontal displacement.

(b) Horizontal displacement amplitude.

(c) Mean vertical displacement.

(d) Vertical displacement amplitude.

Figure 5.3: Benchmark results for the displacement of point $\hat{A}$ with respect to different mesh refinements. The values computed in this work are marked with blue crosses. The various reference values from [137] are delineated with black lines.

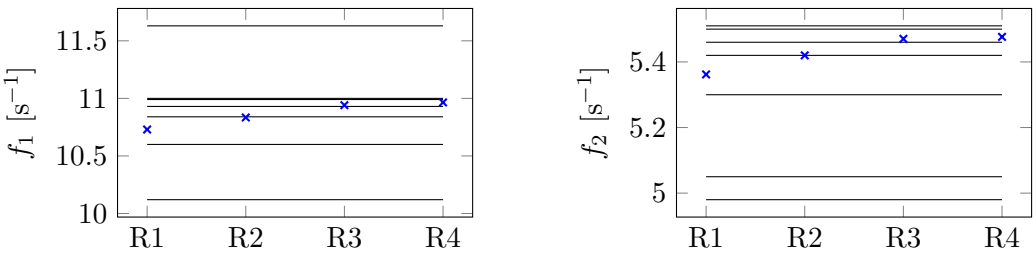

(a) Frequency of horizontal displacement.

(b) Frequency of vertical displacement.

Figure 5.4: Benchmark results for the displacement frequencies with respect to different mesh refinements. The values computed in this work are marked with blue crosses. The various reference values from [137] are delineated with black lines.

All benchmark values are computed as averages over 10 periods of vertical flapping of the elastic bar. The resulting values are given in Table 5.3 with respect to several mesh refinement levels.

The figures 5.3, 5.4 and 5.5 compare the results in Table 5.3 with the reference values given in [137]. Each of the reference values is delineated by a black line. The specific values and the

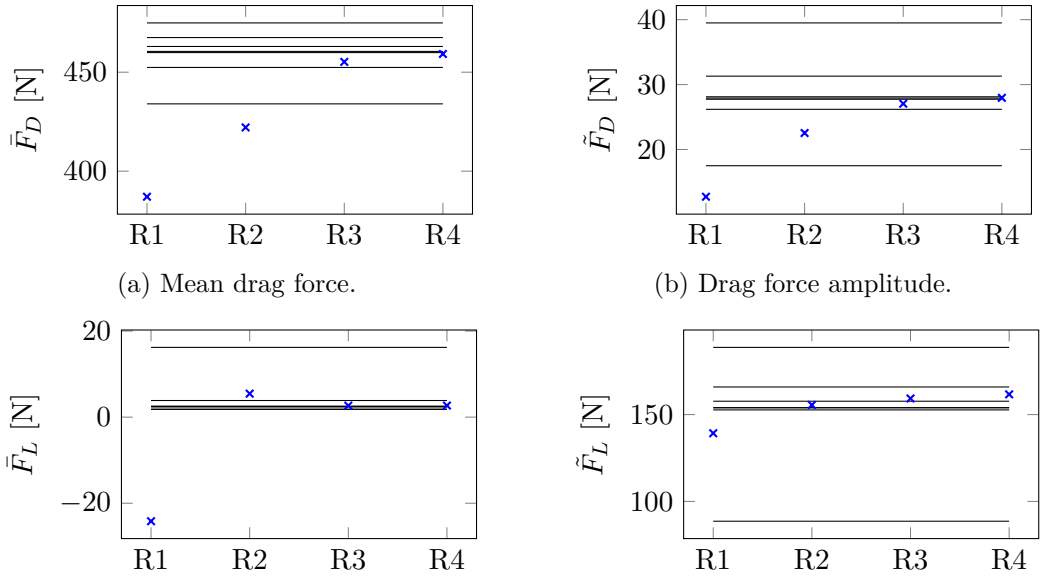

(a) Mean drag force.

(b) Drag force amplitude.

(c) Mean lift force.

(d) Lift force amplitude.

Figure 5.5: Benchmark results for the drag and lift forces with respect to different mesh refinements. The values computed in this work are marked with blue crosses. The various reference values from [137] are delineated with black lines.

respectively applied numerical method are described in [137]. In the plot's y-axis labels, a bar denotes the mean values and the amplitudes are denoted by a tilde. For the refinement levels R1 and R2, the discretisation error is relatively high, but a clear experimental convergence is visible for the plotted values. The results for the mesh refinement levels R3 and R4 are in very well accordance with most of the reference values.

5.1.3 Parallel scalability for the 2D problem

This section evaluates the parallel scalability of the problem-specific linear solver presented in section 4.2.5 by means of the FSI benchmark. In introduction to parallel computing with the definitions of scalability used in this section is given in [96, 1]. This scalability study was carried out on the standard nodes of the *BwForCluster MLS&WISO Production*. Each standard node had two *Intel Xeon E5-2630v3* processors on a *Haswell* architecture with 16 CPU cores at 2.4 GHz and 64 GB working memory. The network for MPI communication between the nodes was an *Infiniband* interconnect of *Quad Data Rate* (QDR).

For this scalability study, the model parameters are chosen as described in the previous section 5.1.1. The configuration of the subroutines of the linear solver is summarised in Table 5.4. It also shows the values for the preconditioner BoomerAMG (cf. section 4.2.5), that differ from the default configuration provided by HYPRE. The tolerance of the Newton method is chosen such that it takes approximately 3 to 4 Newton iterations to compute a time step. Independently of the respective Newton iteration, the linear solver is set to decrease the residual of the linear system of equations with 3 orders of magnitude. This allows for the investigation of the scalability of the average number of iterations the linear solver requires

to reach the relative tolerance. The number of iterations as well as the computational costs are computed as averages over the physical time period from 0.1 to 0.2.

Operator	Method	Parameter	Value
$\mathcal{M}^{-1}$	FGMRES	Relative tolerance	0.001
$\mathcal{M}^{-1}$	FGMRES	Maximal iterations	100
J^{uu-1}, J^{vv-1}, $\tilde{\mathcal{S}}^v$	AMG	Cycle type	V-cycle
J^{uu-1}, J^{vv-1}, $\tilde{\mathcal{S}}^v$	AMG	Aggressive coarsening	On all levels
J^{uu-1}, J^{vv-1}, $\tilde{\mathcal{S}}^v$	AMG	Interpolation type	Multipass interpolation
J^{uu-1}, J^{vv-1}, $\tilde{\mathcal{S}}^v$	AMG	Coarsening type	HMIS-coarsening
J^{uu-1}, J^{vv-1}, $\tilde{\mathcal{S}}^v$	AMG	Relax weight	1
J^{uu-1}, J^{vv-1}, $\tilde{\mathcal{S}}^v$	AMG	Strong threshold	0.7
$\mathcal{S}^{u-1}$	FGMRES	Relative tolerance	0.25
$\mathcal{S}^{u-1}$	FGMRES	Maximal iterations	50
J^{uu-1}	CG	Relative tolerance	0.001
J^{uu-1}	CG	Maximal iterations	10
J^{uu-1}	AMG	Number of iterations	1
J^{uu-1}	AMG	Relax type	hybrid sym. Gauss-Seidel
J^{uu-1}	AMG	Number of sweeps	2
$\mathcal{S}^{v-1}$	FGMRES	Relative tolerance	0.05
$\mathcal{S}^{v-1}$	FGMRES	Maximal iterations	50
J^{vv-1}	GMRES	Relative tolerance	0.03
J^{vv-1}	GMRES	Maximal iterations	10
J^{vv-1}	AMG	Number of iterations	1
J^{vv-1}	AMG	Relax type	hybrid Gauss-Seidel, forward
J^{vv-1}	AMG	Number of sweeps	3
$\tilde{\mathcal{S}}^v$	AMG	Maximal iterations	10
$\tilde{\mathcal{S}}^v$	AMG	Relative tolerance	0.03
$\tilde{\mathcal{S}}^v$	AMG	Relax type	hybrid sym. Gauss-Seidel
$\tilde{\mathcal{S}}^v$	AMG	Number of sweeps	3

Table 5.4: Configuration of the solver subroutines (cf. Figure 4.5) for the FSI benchmark.

The number of the degrees of freedom and the utilised time step length for this scalability study is shown in Table 5.5. The edge length of a mesh cell is approximately halved from one refinement level to the next. Accordingly, the time step length is halved from one level to the next.

Strong scaling results

The number of iterations of the linear solver averaged over all Newton iterations in the physical time period from 0.1 to 0.2 is shown in Figure 5.6.

Firstly, the average number of iterations of the linear solver is below 5 iterations in all cases. Hence, it can be said, that the problem-specific preconditioner presented in this work, suitably addresses the complex structure of the FSI benchmark problem.

Mesh refinement	# dofs	k
R2	32,507	0.001
R3	126,574	0.0005
R4	502,962	0.00025
R5	1,992,429	0.000125

Table 5.5: The number of degrees of freedom (dofs) of the respective mesh refinement level and the respectively utilised discrete time step length k for the scalability study.

Secondly, the number of iterations for each of the mesh refinement levels R2, R3 and R4 is almost independent from the degree of parallelisation. Though varying more compared to the other refinement levels, the number of iterations for R5 also does not show an upward trend. Thereby one can conclude, that the presented preconditioning method is well scalable in the investigated range of mesh refinement levels and CPU cores with respect to the number of iterations of the linear solver.

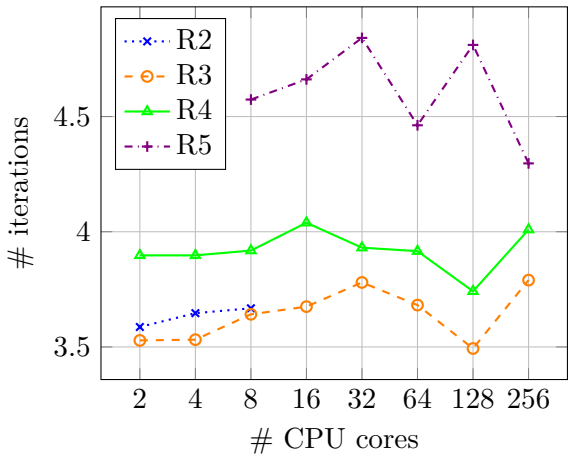

Figure 5.6: Average number of iterations of the linear solver for a relative decrease of the residual of 3 orders of magnitude. The results for the respective refinement levels are plotted over the number of utilised CPU cores.

For the respective sub-solvers of the preconditioner (cf. Figure 4.5), the pre-defined maximal number of iterations is given in Table 5.4. This limit is not reached in the benchmark simulations, such that the sub-solvers always reduce the residual by the respectively defined relative tolerance.

The computational costs of the presented linear solver are evaluated by means of the average wall time to compute one Newton step. The results for the considered mesh refinement levels are shown in Figure 5.7a. For the highest resolution R5, the problem size was too big to be computed on 2 or 4 CPU cores. For the mesh refinement R2 and a number of 16 CPU cores and higher, the computations gave erroneous results on the utilised computing cluster, which did not occur on other cluster systems.

The wall time for the computations with the smallest number of CPU cores ranges from 58.8 s for the mesh refinemenet level R4 to 0.174 s for R2. Initially, an approximatly log-log

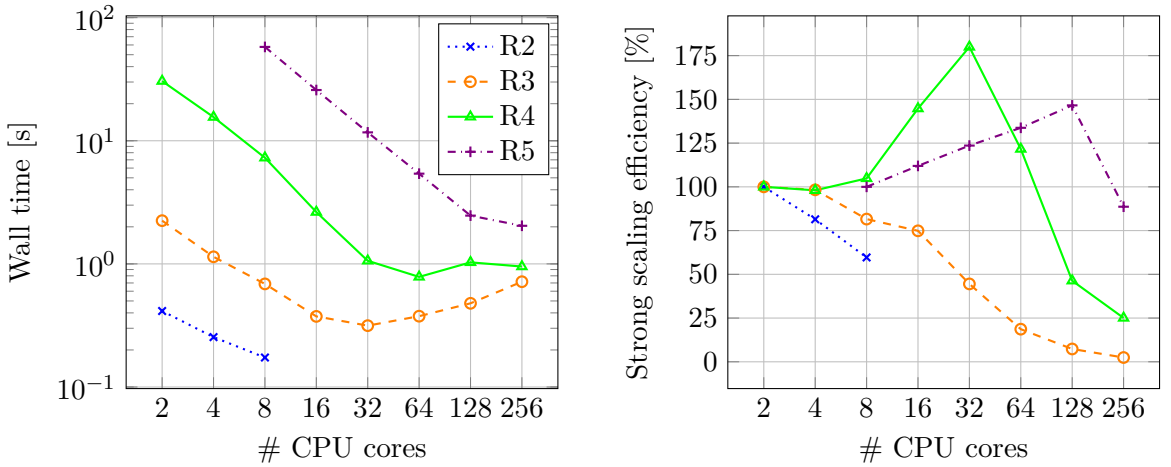

(a) Average wall time of the linear solver for a relative decrease of the residual at 3 orders of magnitude.

(b) Strong scaling efficiency of the linear solver based on the average wall time.

Figure 5.7: Evaluation of the computational costs and scalability of the problem-specific linear solver for FSI problems by means of the wall time. The results for the respective refinement levels are plotted over the number of utilised CPU cores.

linear decrease of the wall time is observed when increasing the parallelity. The refinement levels R3 and R4 show a minimum at 32 and 64 CPU cores, respectively. For R5, the wall time monotonously decreases up to 256 CPU cores.

Figure 5.7b shows the strong scaling efficiency with respect to the wall time. The strong scaling efficiency is given by

$$\frac{nT_n}{NT_N}100\%, \tag{5.4}$$

where n denotes the smallest utilised number of CPU cores and T_n is the corresponding wall time. N is the respectively considered number of CPU cores and T_N denotes the wall time for the execution on N cores.

Relative to $n = 2$, the solver shows a parallel efficiency of over 50 % for up to 8 and 16 CPU cores for the mesh refinement levels R2 and R3, respectively. For the refinement levels R4 ($n = 2$) and R5 ($n = 8$), the solver shows a significant parallel efficiency of over 100 % with a peak at 32 cores for R4 and at 128 cores for R5.

A more detailed parallel performance evaluation for the refinement level R4 and R5 is given in Figures 5.8 and 5.9, respectively. The wall time is highest for the inversion of the Schur complement matrices. The computational costs for the AMG-preconditioned inversion of J^{uu} and J^{vv} are approximately the same and one order of magnitude lower than for the Schur complement matrices. The multiple inversion of J^{uu} and J^{vv} is part of the inversion of the Schur complement matrices. Hence, the performance of the latter partly depends on the AMG-preconditioned sub-solvers. The application of AMG on $\tilde{\mathcal{S}}^v$ is fastest. One main reason for this lies in the approximately four times smaller number of the pressure degrees of freedom, $\tilde{\mathcal{S}}^v$ acts on, compared to the displacement degrees of freedom of J^{uu} and the velocity degrees of freedom of J^{vv}.

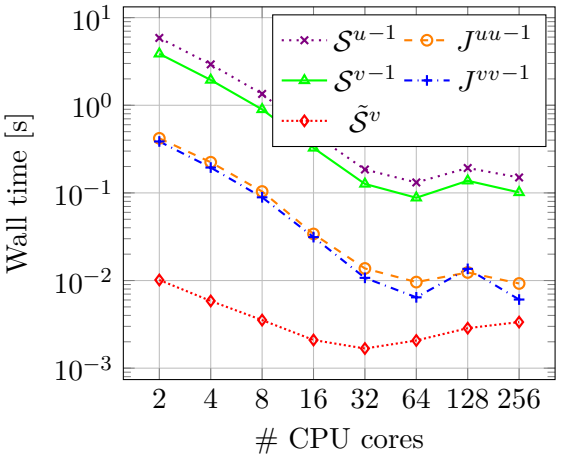

(a) Average wall time of the linear sub-solvers. The respective values for the relative decrease of the residuals are given in Table 5.4.

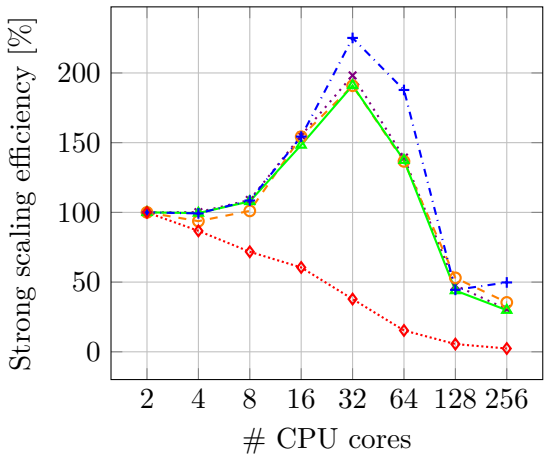

(b) Strong scaling efficiency of the linear sub-solvers based on the average wall time.

Figure 5.8: Refinement level R4: Detailed evaluation of the computational costs and scalability of the sub-solvers of the problem-specific preconditioner (cf. Figure 4.5).The results for the refinement level R4 are plotted over the number of utilised CPU cores.

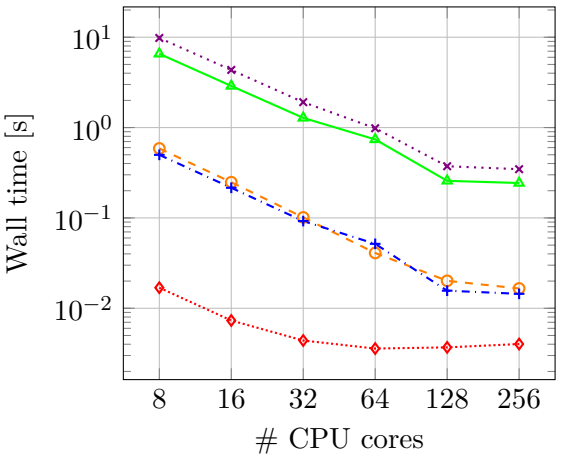

(a) Average wall time of the linear sub-solvers. The respective values for the relative decrease of the residual are given in Table 5.4.

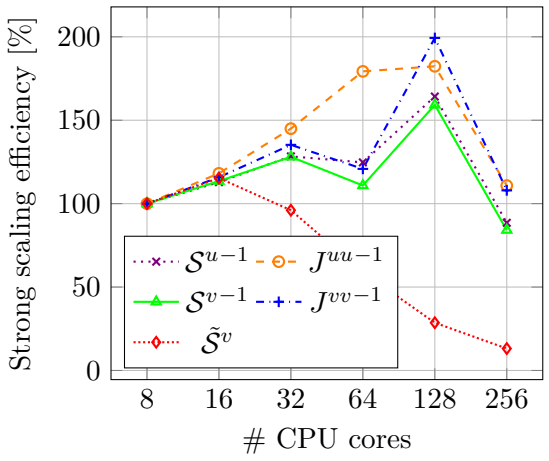

(b) Strong scaling efficiency of the linear sub-solvers based on the average wall time.

Figure 5.9: Refinement level R5: Detailed evaluation of the computational costs and scalability of the sub-solvers of the problem-specific preconditioner (cf. Figure 4.5).The results for the refinement level R5 are plotted over the number of utilised CPU cores.

With regard to the strong scaling efficiency in Figures 5.8b and 5.9b, all sub-solvers except for the sub-solver for $\tilde{\mathcal{S}}^v$ show almost the same behaviour as the overall efficiency of the linear solver in Figure 5.7b. An explanation for the scaling efficiency peaks being

significantly higher than 100 % could be given by the access to the different memory-layers of the employed hardware resources. As the amount of data each processor has to compute on gets smaller with increasing parallelisation, the ratio of data that can be kept in the fast processor cache increases. Less data has be read from the relatively slow main memory until the respective problem size is small enough to fully fit in the cache memory. After this threshold, the parallel efficiency usually drops again.

Weak scaling results

The weak scaling efficiency is calculated by fixing the number of degrees of freedom per CPU core (dpc) and dividing the wall time of a low reference refinement level T_n by the wall time of the respective execution on a higher refinement level T_N with a corresponding parallelisation:

$$\frac{T_n}{T_N} 100\%.$$

The degrees of freedom for the respective next higher mesh refinement level are almost four times more than for the lower level (cf. Table 5.5). Hence, to keep the problem size per core approximately constant, the wall time for the lower refinement level can be compared to the computation of the next higher level with a four times higher number of CPU cores.

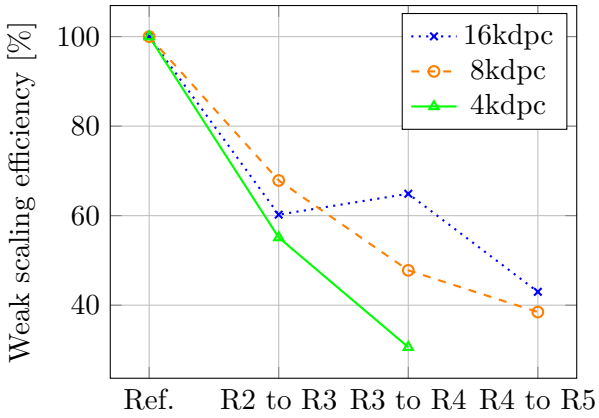

Figure 5.10: Weak scaling efficiency of the problem-specific linear solver based on the average wall time. The efficiency for the respective per core problem size (dpc) is plotted over the weak scaling steps.

For the weak scaling efficiency, as shown in Figure 5.10, the wall time data from Figure 5.7a is used. For the second step from R3 to R4 the weak scaling efficiency ranges from 30.6 % for the smallest problem size per core to 64.9 % for the largest problem size per core. For the step from R4 to R5 all values are below 50 %. For the weak scalability, not only the problem size can have a significant effect on the efficiency results, but also the condition number of the matrix with its sub-matrices. In return, the condition number of the FSI system matrix typically increases with the mesh refinement level and the time step size. This effect is sought to be counteracted by halving the time step size from one mesh refinement level to the next (cf. Table 5.5). However, the impact of the condition number on the weak scalability results remains an open question of this work and should be content of future ongoing research endeavour.

5.2 An analytically solvable UQ-FSI benchmark

Benchmark problems with an analytical solution allow for the verification of numerical simulation methods by means of the discretisation error with respect to the exact solution of the problem. A benchmark scenario for the three-dimensional incompressible Navier-Stokes equations with an analytical solution is presented for example in [39]. The addition of a second phase of a solid material substantially increases the complexity of the model equations. Hence, on the one side, the setup of the benchmark problem for the FSI equations has to be simple enough in order to enable the derivation of an analytical solution. On the other side, the analytical solution should be of a non-trivial structure and ideally contain all features which the model equations are able to describe.

This section is structured as follows: At first, a new FSI benchmark problem with uncertain parameters is presented in 5.2.1. To the best of the authors knowledge, such a benchmark has not been presented by others before. In section 5.2.2, the analytical solution of the problem is derived. Finally, numerical results are given in section 5.2.3.

A summary of the work on and the results for this benchmark problem has already been published as a preprint by the author in [81].

5.2.1 Benchmark description

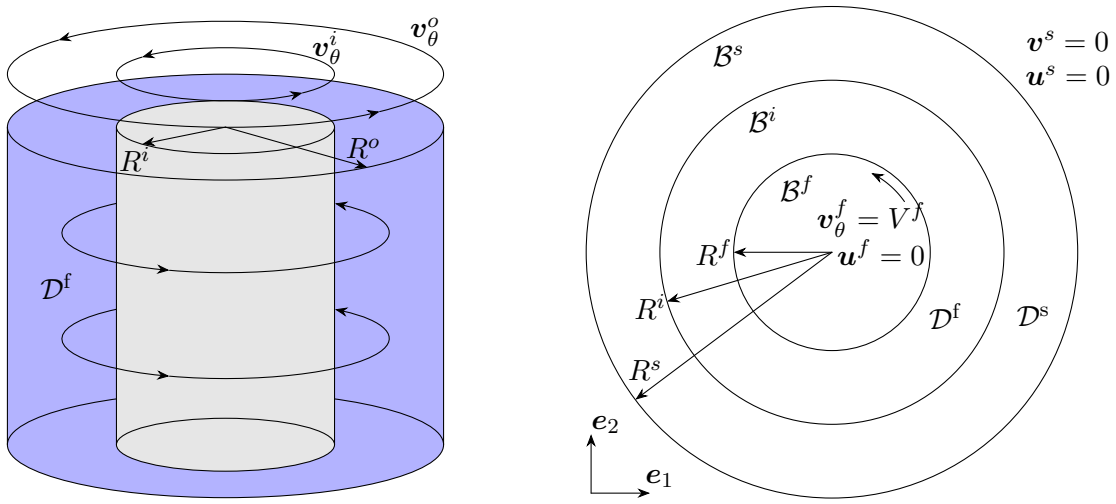

(a) A three-dimensional Taylor-Couette flow system. The fluid is contained in a double-walled cylinder. The inner and the outer wall with radius R^i and R^o rotate at two different speeds $\boldsymbol{v}_\theta^i$ and $\boldsymbol{v}_\theta^o$, respectively.

(b) A two-dimensional cut-plane of the Taylor-Couette flow system with a solid domain layer $\mathcal{D}^{\mathrm{s}}$ surrounding the fluid domain $\mathcal{D}^{\mathrm{f}}$. The illustration indicates the geometry and boundary conditions of the benchmark problem.

Figure 5.11: The geometry and boundary conditions for the considered Taylor-Couette flow.

The benchmark problem presented in this work for the FSI equations with uncertain parameters (UFSI) is inspired by the Taylor-Couette flow. As shown in Figure 5.11a, a Taylor-Coutte flow system consists of two concentrically arranged cylinders. The space in-between this double-walled cylinder is filled with a fluid. With a rotation of the inner and

the outer cylinder wall at different angular speeds, the development of a fluid flow field is induced depending on these boundary velocities. At a moderate to a high difference of the angular speed, the flow field develops a number of local circular revolutions. At a lower speed, a laminar velocity field develops. On a cut plane in two dimensions, this laminar velocity field can explicitly be described in polar coordinates. In other words, the emerging velocity field and the corresponding pressure field can be written as an analytical solution of the incompressible Navier-Stokes equations.

This scenario can be extended with a solid domain of an elastic material which is layered around the fluid domain as shown in Figure 5.11b. In this two-dimensional circular geometry, the inner and intermediate circle give the boundaries $\mathcal{B}^f$ and $\mathcal{B}^i$, respectively, of the fluid domain $\mathcal{D}^{\mathrm{f}}$. The surrounding solid domain $\mathcal{D}^{\mathrm{s}}$ is bounded by the interface to the fluid domain, given by $\mathcal{B}^i$, and the outer circle $\mathcal{B}^s$. The corresponding radii are denoted by R^f, R^i and R^s.

The figure also indicates the boundary conditions of the UFSI benchmark problem. As in the standard Taylor-Couette flow scenario, the angular velocity at the inner boundary is set to a certain speed $\boldsymbol{v}_\theta^f = V^f$. The radial velocity $\boldsymbol{v}_r^f$ at the inner boundary is zero. The displacement field at the inner $\boldsymbol{u}^f$ as well as at the outer boundary $\boldsymbol{u}^s$ is set to be zero. Accordingly, the velocity $\boldsymbol{v}^s$ of the material displacement on the outer boundary is zero.

In accordance with the modelling of the uncertain parametric influence as described in section 3.5.2, the Young's modulus Y and the boundary velocity V_f are considered as uncertain parameters of the UFSI problem with a uniform distribution:

$$V^f(\omega) := \bar{V}^f + \omega_1 \tilde{V}^f, \quad \omega_1 \sim U(-1,1), \tag{5.5}$$

$$Y(\omega) := \bar{Y} + \omega_2 \tilde{Y}, \qquad \omega_2 \sim U(-1,1). \tag{5.6}$$

The fluid flow is modelled by the stationary version of the NSE (3.25). In the Eulerian frame of reference they are given by

$$\rho(\boldsymbol{v}\cdot\nabla)\boldsymbol{v} - \rho\nu\Delta\boldsymbol{v} + \nabla p = 0, \quad \text{in } \mathcal{D}^{\mathrm{f}} \times \Omega, \tag{5.7}$$

$$\nabla \cdot \boldsymbol{v} = 0, \quad \text{in } \mathcal{D}^{\mathrm{f}} \times \Omega, \tag{5.8}$$

where Ω denotes the two-dimensional stochastical domain from the modelling of the two uncertain parameters.

For modelling the stationary elastic deformation of the solid domain, we simplify the STVK elasticity equation (3.42) under the assumption of small deformations. In this case, the deformation can be measured with the infinitesimal strain tensor (3.35). The resulting elasticity equation is linear in the displacement field:

$$-\nabla\cdot\boldsymbol{\sigma} = 0, \quad \text{in } \mathcal{D}^{\mathrm{s}} \times \Omega, \tag{5.9}$$

with

$$\begin{aligned}\boldsymbol{\sigma} &= \lambda_1 \mathrm{tr}(\boldsymbol{\epsilon})\boldsymbol{I} + 2\lambda_2\boldsymbol{\epsilon} \\ &= \lambda_1(\nabla\cdot\boldsymbol{u})\boldsymbol{I} + \lambda_2(\nabla\boldsymbol{u} + \nabla\boldsymbol{u}^T).\end{aligned} \tag{5.10}$$

The Lamé coefficients λ_1 and λ_2 depend on the Young's modulus Y and on the Poisson's ratio γ as defined in equation (3.41).

The boundary conditions of the UFSI benchmark problem are stated in the following.

$$(\boldsymbol{v}_\theta, \boldsymbol{v}_r) = (V^f, 0), \quad \text{on } \mathcal{B}^f \times \Omega, \tag{5.11}$$

$$\boldsymbol{u} = \boldsymbol{v} = 0, \quad \text{on } \mathcal{B}^s \times \Omega, \tag{5.12}$$

$$\left(\rho\nu(\nabla\boldsymbol{v} + \nabla\boldsymbol{v}^T) - p\boldsymbol{I}\right)\boldsymbol{\eta}_f - \boldsymbol{\sigma}\boldsymbol{\eta}_s = 0, \quad \text{on } \mathcal{B}^i \times \Omega. \tag{5.13}$$

The latter condition (5.13) describes the balance of forces on the fluid-solid interface $\mathcal{B}^i$. Through this condition, the shear stress of the flow field induces a displacement force on the solid material in angular direction.

5.2.2 Derivation of an analytical solution

In a Cartesian system of coordinates, the boundary value problem given by the partial differential equations (5.7), (5.8) and (5.9) and the boundary conditions (5.11), (5.12) and (5.13) is non-trivial to solve. However, the Cartesian coordinate system can be transformed to polar coordinates, following [26], which yields an equivalent system of ordinary differential equations (ODEs).

Denoting a unit vector in the respective coordinate system by $\boldsymbol{e}$, the gradient operator becomes

$$\begin{aligned}\nabla p &= \frac{\partial}{\partial \boldsymbol{x}_1} p\boldsymbol{e}_1 + \frac{\partial}{\partial \boldsymbol{x}_2} p\boldsymbol{e}_2 \\ &= \frac{\partial}{\partial r} p\boldsymbol{e}_r + \frac{1}{r}\frac{\partial}{\partial \theta} p\boldsymbol{e}_\theta\end{aligned} \tag{5.14}$$

The convection term in polar coordinates is hence given by

$$\begin{aligned}(\boldsymbol{v}\cdot\nabla)\boldsymbol{v} &= \boldsymbol{v}\cdot\nabla\boldsymbol{v}_1\boldsymbol{e}_1 + \boldsymbol{v}\cdot\nabla\boldsymbol{v}_2\boldsymbol{e}_2 \\ &= \left(\boldsymbol{v}_r\frac{\partial}{\partial r}\boldsymbol{v}_r + \frac{\boldsymbol{v}_\theta}{r}\frac{\partial}{\partial\theta}\boldsymbol{v}_r - \frac{\boldsymbol{v}_\theta\boldsymbol{v}_\theta}{r}\right)\boldsymbol{e}_r \\ &\quad + \left(\boldsymbol{v}_r\frac{\partial}{\partial r}\boldsymbol{v}_\theta + \frac{\boldsymbol{v}_\theta}{r}\frac{\partial}{\partial\theta}\boldsymbol{v}_\theta + \frac{\boldsymbol{v}_\theta\boldsymbol{v}_r}{r}\right)\boldsymbol{e}_\theta.\end{aligned} \tag{5.15}$$

For the Laplace operator we find

$$\begin{aligned}\Delta\boldsymbol{v} &= \Delta\boldsymbol{v}_1\boldsymbol{e}_1 + \Delta\boldsymbol{v}_2\boldsymbol{e}_2 \\ &= \left(\frac{1}{r}\frac{\partial}{\partial r}(r\frac{\partial}{\partial r}\boldsymbol{v}_r) + \frac{1}{r^2}\frac{\partial^2}{\partial\theta^2}\boldsymbol{v}_r - \frac{\boldsymbol{v}_r}{r^2} - \frac{2}{r^2}\frac{\partial}{\partial\theta}\boldsymbol{v}_\theta\right)\boldsymbol{e}_r \\ &\quad + \left(\frac{1}{r}\frac{\partial}{\partial r}(r\frac{\partial}{\partial r}\boldsymbol{v}_\theta) + \frac{1}{r^2}\frac{\partial^2}{\partial\theta^2}\boldsymbol{v}_\theta - \frac{\boldsymbol{v}_\theta}{r^2} + \frac{2}{r^2}\frac{\partial}{\partial\theta}\boldsymbol{v}_r\right)\boldsymbol{e}_\theta.\end{aligned} \tag{5.16}$$

The divergence operator of the velocity field transforms to

$$\begin{aligned}\nabla\cdot\boldsymbol{v} &= \frac{\partial}{\partial\boldsymbol{x}_1}\boldsymbol{v}_1 + \frac{\partial}{\partial\boldsymbol{x}_2}\boldsymbol{v}_2 \\ &= \frac{1}{r}\frac{\partial}{\partial r}(r\boldsymbol{v}_r) + \frac{1}{r}\frac{\partial}{\partial\theta}\boldsymbol{v}_\theta.\end{aligned} \tag{5.17}$$

The divergence of the stress tensor is written in polar coordinates as

$$\begin{aligned}\nabla \cdot \boldsymbol{\sigma} = & \left(\frac{\partial}{\partial \boldsymbol{x}_1}\boldsymbol{\sigma}_{11} + \frac{\partial}{\partial \boldsymbol{x}_2}\boldsymbol{\sigma}_{21}\right)\boldsymbol{e}_1 + \left(\frac{\partial}{\partial \boldsymbol{x}_1}\boldsymbol{\sigma}_{12} + \frac{\partial}{\partial \boldsymbol{x}_2}\boldsymbol{\sigma}_{22}\right)\boldsymbol{e}_2 \\ = & \left(\frac{\partial}{\partial r}\boldsymbol{\sigma}_{rr} + \frac{1}{r}\frac{\partial}{\partial \theta}\boldsymbol{\sigma}_{\theta r} + \frac{1}{r}(\boldsymbol{\sigma}_{rr} - \boldsymbol{\sigma}_{\theta\theta})\right)\boldsymbol{e}_r \\ & + \left(\frac{\partial}{\partial r}\boldsymbol{\sigma}_{r\theta} + \frac{1}{r}\frac{\partial}{\partial \theta}\boldsymbol{\sigma}_{\theta\theta} + \frac{1}{r}(\boldsymbol{\sigma}_{r\theta} + \boldsymbol{\sigma}_{\theta r})\right)\boldsymbol{e}_\theta.\end{aligned} \tag{5.18}$$

Inserting (5.10) yields

$$\begin{aligned}\nabla \cdot \boldsymbol{\sigma} = & \left(\frac{\partial}{\partial r}(\lambda_1(\boldsymbol{\epsilon}_{rr} + \boldsymbol{\epsilon}_{\theta\theta}) + 2\lambda_2\boldsymbol{\epsilon}_{rr}) + \frac{2\lambda_2}{r}\frac{\partial}{\partial \theta}\boldsymbol{\epsilon}_{\theta r} + \frac{2\lambda_2}{r}(\boldsymbol{\epsilon}_{rr} - \boldsymbol{\epsilon}_{\theta\theta})\right)\boldsymbol{e}_r \\ & + \left(2\lambda_2\frac{\partial}{\partial r}\boldsymbol{\epsilon}_{r\theta} + \frac{1}{r}\frac{\partial}{\partial \theta}(\lambda_1(\boldsymbol{\epsilon}_{rr} + \boldsymbol{\epsilon}_{\theta\theta}) + 2\lambda_2\boldsymbol{\epsilon}_{\theta\theta}) + \frac{2\lambda_2}{r}(\boldsymbol{\epsilon}_{r\theta} + \boldsymbol{\epsilon}_{\theta r})\right)\boldsymbol{e}_\theta.\end{aligned} \tag{5.19}$$

As shown in [128], the infinitesimal strain tensor (3.35) has the following form in polar coordinates.

$$\begin{aligned}\boldsymbol{\epsilon} &= \frac{1}{2}\left((\nabla \boldsymbol{u})^T + \nabla \boldsymbol{u}\right) \\ &= \begin{pmatrix} \frac{\partial}{\partial r}\boldsymbol{u}_r & \frac{1}{2}\left(\frac{1}{r}\frac{\partial}{\partial \theta}\boldsymbol{u}_r + \frac{\partial}{\partial r}\boldsymbol{u}_\theta - \frac{\boldsymbol{u}_\theta}{r}\right) \\ \frac{1}{2}\left(\frac{1}{r}\frac{\partial}{\partial \theta}\boldsymbol{u}_r + \frac{\partial}{\partial r}\boldsymbol{u}_\theta - \frac{\boldsymbol{u}_\theta}{r}\right) & \frac{1}{r}\left(\frac{\partial}{\partial \theta}\boldsymbol{u}_\theta + \boldsymbol{u}_r\right) \end{pmatrix}\end{aligned} \tag{5.20}$$

The geometry as well as the boundary conditions for the UFSI benchmark problem are rotationally symmetric to the centre point of the geometry. Hence, if the flow develops laminarly, it can be assumed, that it develops in a rotationally symmetric form. Then, the radial displacement and velocity are zero, $\boldsymbol{u}_r = \boldsymbol{v}_r = 0$, on the full domain. Analogously to the velocity boundary condition at the inner circle, it can be assumed that the angular displacement and velocity are constant, $\frac{\partial}{\partial \theta}\boldsymbol{u}_\theta = \frac{\partial}{\partial \theta}\boldsymbol{v}_\theta = 0$. With these assumptions, the coordinate transformation of (5.7), (5.8), (5.9) and (5.13) leads to the following system of stochastic ODEs on the centre line which is given by the radial interval $[R^f, R^s]$ and for all $\omega \in \Omega$.

Using (5.14), (5.15) and (5.16), equation (5.7) becomes in radial direction

$$-\frac{\rho}{r}\boldsymbol{v}_\theta(r,\omega)^2 + \frac{\partial}{\partial r}p(r,\omega) = 0, \quad r \in [R^f, R^i]. \tag{5.21}$$

In angular direction, equation (5.7) takes the form

$$\frac{\partial^2}{\partial r^2}\boldsymbol{v}_\theta(r,\omega) + \frac{1}{r}\frac{\partial}{\partial r}\boldsymbol{v}_\theta(r,\omega) - \frac{1}{r^2}\boldsymbol{v}_\theta(r,\omega) = 0, \quad r \in [R^f, R^i]. \tag{5.22}$$

The continuity equation (5.8) in polar coordinates (5.17) is trivially zero under the above mentioned assumptions.

For the elasticity equation (5.9), the insertion of the strain tensor (5.20) in (5.19) simplifies a lot under the point symmetry assumptions:

$$\lambda_2(\omega)\left(\frac{\partial^2}{\partial r^2}\boldsymbol{u}_\theta(r,\omega) + \frac{1}{r}\frac{\partial}{\partial r}\boldsymbol{u}_\theta(r,\omega) - \frac{1}{r^2}\boldsymbol{u}_\theta(r,\omega)\right) = 0, \quad r \in [R^i, R^s]. \tag{5.23}$$

Analogously and under the assumption, that the fluid pressure is zero at the fluid-solid interface, the coupling conditions (5.13) become

$$\rho\nu\frac{\partial}{\partial r}\boldsymbol{v}_\theta(R^i,\omega)+\lambda_2(\omega)\left(\frac{\partial}{\partial r}\boldsymbol{u}_\theta(R^i,\omega)-\frac{1}{R^i}\boldsymbol{u}_\theta(R^i,\omega)\right)=0. \tag{5.24}$$

Now, the equations (5.21), (5.22), (5.23) and (5.24) form a system of stochastical ODEs in the radius of the geometry. To decouple the geometric from the stochastic dimensions in the state variables $\boldsymbol{v}_\theta$, p and $\boldsymbol{u}_\theta$, the generalised PC expansion, as introduced in section 4.2.4, can be used. For the variables $\boldsymbol{v}_\theta$, p and $\boldsymbol{u}_\theta$ and $r\in[R^f,R^s]$, $\omega\in\Omega$, the PC expansion (4.23) is given by

$$[\boldsymbol{v}_\theta(r,\omega),p(r,\omega),\boldsymbol{u}_\theta(r,\omega)]=\left[\sum_{k=0}^{\infty}\boldsymbol{v}_{\theta,k}(r)\psi_k(\omega),\sum_{k=0}^{\infty}p_k(r)\psi_k(\omega),\sum_{k=0}^{\infty}\boldsymbol{u}_{\theta,k}(r)\psi_k(\omega)\right], \tag{5.25}$$

where ψ_k are multivariate Legendre polynomials. The PC expansion of the random input parameters (5.5) and (5.6) can be written as

$$\left[V^f(\omega),\lambda_2(\omega)\right]=\left[\sum_{k=0}^{\infty}V_k^f\psi_k(\omega),\sum_{k=0}^{\infty}\lambda_{2k}\psi_k(\omega)\right]. \tag{5.26}$$

In correspondence to (4.35) and (4.36), the coefficients for the expansion of the input parameters in (5.26) are given by

$$V_0^f=\bar{V}^f,\quad V_1^f=\tilde{V}^f,\qquad V_k^f=0,\quad \text{for } k>1, \tag{5.27}$$

$$\lambda_{20}=\bar{\lambda_2},\quad \lambda_{22}=\tilde{\lambda_2},\quad \lambda_{21}=\lambda_{2k}=0,\quad \text{for } k>2. \tag{5.28}$$

The PC expansions (5.25) and (5.26) can be inserted in the system of stochastical ODEs (5.21), (5.22), (5.23) and (5.24). Performing a Galerkin projection, the equations are multiplied with each of the chaos polynomials ψ_k, $k\in\mathbb{N}_0$, respectively and integrated over the stochastical domain Ω. This method is further described in [87]. As the chaos polynomials given by the multivariate Legendre polynomials form an orthogonal basis with respect to the L^2-norm on Ω, only the non-zero terms of the orthogonal projection remain to be noted in the following.

Equation (5.21) is projected to

$$\frac{\rho}{r}\sum_{j,l=0}^{\infty}\boldsymbol{v}_{\theta,j}(r)\boldsymbol{v}_{\theta,l}(r)c_{jlk}-\frac{\partial}{\partial r}p_k(r)=0,\quad r\in[R^f,R^i],\ k\in\mathbb{N}_0, \tag{5.29}$$

where the stochastic Galerkin tensor of third order c_{jlk} is defined in (4.40).

Equation (5.22) becomes

$$\frac{\partial^2}{\partial r^2}\boldsymbol{v}_{\theta,k}(r)+\frac{1}{r}\frac{\partial}{\partial r}\boldsymbol{v}_{\theta,k}(r)-\frac{1}{r^2}\boldsymbol{v}_{\theta,k}(r)=0,\quad r\in[R^f,R^i],\ k\in\mathbb{N}_0. \tag{5.30}$$

The projection of equation (5.23) is written as

$$\sum_{j,l=0}^{\infty}\lambda_{2j}\left(\frac{\partial^2}{\partial r^2}\boldsymbol{u}_{\theta,l}(r)+\frac{1}{r}\frac{\partial}{\partial r}\boldsymbol{u}_{\theta,l}(r)-\frac{1}{r^2}\boldsymbol{u}_{\theta,l}(r)\right)c_{jlk}=0,\quad r\in[R^i,R^s],\ k\in\mathbb{N}_0. \tag{5.31}$$

The interface coupling condition (5.24) becomes

$$\rho\nu\frac{\partial}{\partial r}\boldsymbol{v}_{\theta,k}(R^i)+\sum_{j,l=0}^{\infty}\lambda_{2j}\left(\frac{\partial}{\partial r}\boldsymbol{u}_{\theta,l}(R^i)-\frac{1}{r}\boldsymbol{u}_{\theta,l}(R^i)\right)c_{jlk}=0,\ k\in\mathbb{N}_0. \tag{5.32}$$

The equations defining the velocity and the displacement fields, (5.30) and (5.31), respectively, are Euler second order ODEs, for which analytical solutions are given in [111]. Thereupon, the solution for the pressure distribution can be calculated from the first order ODEs (5.29). The parameters of the general solutions of the system of ODEs can be fully determined by the boundary conditions (5.11) and (5.12) and the equations for the coupling conditions (5.32). Furthermore, it is to be taken into account, that the pressure and the velocity of the stationary solution at the fluid-solid interface are zero.

The analytical solutions for the velocity and the pressure field for every PC mode $k\in\mathbb{N}_0$ then denote as

$$\boldsymbol{v}_{\theta,k}(r)=\frac{V_k^f R^f}{R^{i2}-R^{f2}}\left(\frac{R^{i2}}{r}-r\right), \tag{5.33}$$

$$p_k(r)=\frac{\rho R^{f2}}{(R^{i2}-R^{f2})^2}\left(\frac{r^2}{2}+2R^{i2}(ln(R^i)-ln(r))-\frac{R^{i4}}{2r^2}\right)\sum_{j,l=0}^{\infty}V_j^f V_l^f c_{jlk}. \tag{5.34}$$

The calculation of the coefficients of the displacement field a_k and b_k involves the evaluation of an infinite number of linear equations:

$$\boldsymbol{u}_{\theta,k}(r)=\frac{b_k}{r}-a_k r, \tag{5.35}$$

$$\text{with } a_k=\frac{b_k}{R^{s2}},$$

$$\sum_{j,l=0}^{\infty}\lambda_{2j}c_{jlk}b_l=\rho\nu\frac{R^f R^{i2}V_k^f}{R^{i2}-R^{f2}}. \tag{5.36}$$

The PC modes of the angular velocity $\boldsymbol{v}_{\theta,k}$ (5.33) in the fluid domain and the angular displacement $\boldsymbol{u}_{\theta,k}$ (5.35) of the solid domain have the same dependency on the radius r apart from the coefficients. The coefficients of all three state variables depend on the radii of the geometry and the uncertain input parameters. To calculate the coefficients b_k, the sum in (5.36) is truncated at a very high mode index of 190 to obtain a finite, but accurate system of linear equations. It can be solved via Gaussian elimination. As the values for b_k exponentially converge to zero, a truncation of the infinite system of linear equations even at a much lower mode index would be sufficient.

5.2.3 Experimental convergence results

With the UFSI problem stated in section 5.2.1 and its analytical solution derived in section 5.2.2 a benchmark scenario can be set up. By means of this scenario the intrusive UQ solver presented in section 4.2.4 is verified in this section. The intrusive UQ solver is based on a Cartesian coordinate system in the geometric dimensions. Hence, the UFSI benchmark problem is non-trivial for the solver.

Parameter	Symbol	Value
Radii	R^f, R^i, R^s	0.2, 0.35, 0.5
Density	ρ	1×10^3
Kinematic viscosity	ν	1.5×10^{-3}
Boundary velocity	$\bar{V}^f \pm \tilde{V}^f$	1.0 ± 0.5
Reynolds number	Re	100 ± 50
Young's modulus	$\bar{Y} \pm \tilde{Y}$	$(5.6 \pm 2.8) \times 10^3$
Poisson's ratio	γ	0.4

Table 5.6: List of geometrical and model parameters for the utilised UFSI benchmark scenario.

The geometrical and model parameters for the verification scenario are given in Table 5.6. The Reynolds number (cf. (5.1.1)) for this scenario can be defined by

$$\mathrm{Re} = \frac{V^f(R^i - R^f)}{\nu}.$$

To numerically solve the stationary equations of the UFSI problem, the instationary version of the solver is used. Therefore, a simulation run is started with an initial condition of zero values for all variables. Then, the boundary velocity V^f is smoothly increased to the final value by the scheme (5.2). The time stepping is realised with the one-step-θ scheme as described in section 4.2.1. Using the numerical damping from the implicit Euler scheme with $\theta = 1$ leads to a faster convergence to a stationary state of the variables. The time step size is set to $k = 0.1$. The boundary velocity V^f is smoothly increased in the time range $0 \leq t < 1$. The results are evaluated at $t = 50$, where changes in the variable values are not apparent any more.

In principle, the linearisation of the UFSI problem differs from the presented linearisation in section 4.2.2 only in the elasticity equations on the solid domain. The elasticity equation of the UFSI problem already has a linear dependency on the displacement variable $\boldsymbol{u}$. This simplifies the directional derivatives for the elasticity equation, correspondingly.

As for the deterministic FSI benchmark, the software gmsh has been used to create discrete FEM meshes of the geometry with different refinement levels (cf. section 5.1.2) here, too. The spatial discretisation with the FEM is described in section 4.2.3.

Mesh refinement	# dofs P1	# dofs P2	# dofs P3	# dofs P4
R1	5820	11,640	19,400	29,100
R2	19,596	39,192	65,320	97,980
R3	70,581	141,162	235,270	352,905
R4	289,008	578,016	963,360	1,445,040

Table 5.7: The number of degrees of freedom (dofs) of the respective mesh refinement level and PC degree.

The stochastic dimensions of the UFSI problem are discretised using a PC expansion as described in section 4.2.4 in the version of the intrusive Galerkin projection. This approach

leads to a discrete monolithic problem for the geometric and stochastic dimensions. Table 5.7 gives the resulting numbers of degrees of freedom for a PC degree $P = 1, \ldots, 4$ and the utilised mesh refinement levels. From one mesh refinement level to the next, the edge length of a mesh cell is approximately halved.

In section 4.2.5, the FSI solver for the intrusive UQ approach is described. This solver is used to compute numerical solutions for each of the discretisation combinations given in Table 5.7. The simulations were carried out on the BwForCluster MLS&WISO Production (see section 5.1.2 and 5.1.3 for details). The computational costs ranged from half an hour wall time on 16 CPU cores for the smallest problem size R1-P1 and up to 48 hours wall time on 64 CPU cores on the largest problem size R4-P4.

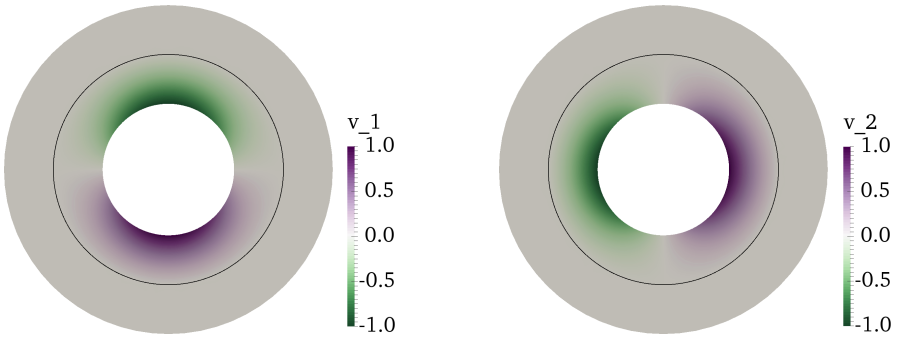

(a) Expected value of the velocity in horizontal (left image) and vertical (right image) direction.

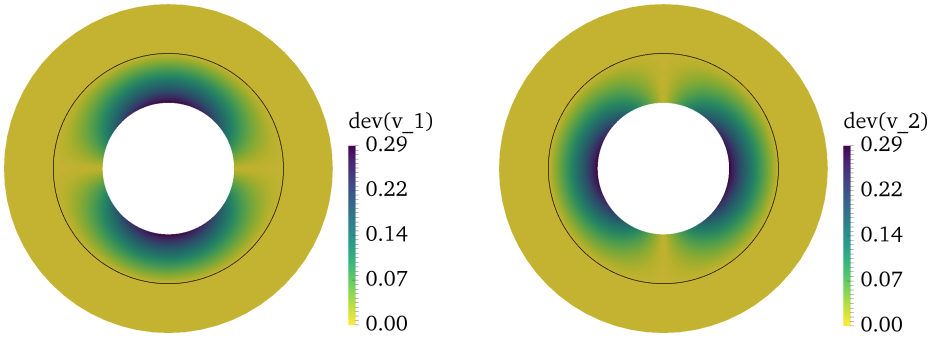

(b) Standard deviation of the velocity in horizontal (left image) and vertical (right image) direction.

Figure 5.12: Visualisation of the velocity field of the UFSI problem. The fluid-structure interface is indicated by a black circle.

A visualisation of the computed velocity field of the UFSI problem is given in Figure 5.12. In accordance with the analytical solution, the expected velocity (Figure 5.12a) declines from the boundary velocity V_f to zero at the fluid-structure interface. The solid domain is at rest in the stationary solution. The standard deviation of the velocity field (Figure 5.12b) shows that the solid domain is certainly at rest. The standard deviation is highest at the inner boundary with the prescribed standard deviation of the boundary velocity V_f.

Figure 5.13 shows the resulting pressure field. Naturally, the centrifugal forces of the circular fluid flow lead to a positive expected pressure gradient (Figure 5.13a) from the inner boundary to the fluid-structure interface. On the solid domain, the pressure variable is undefined and artificially set to zero. Together with the velocity field, the standard deviation

of the pressure (Figure 5.13b) is zero at the fluid-structure interface and highest at the inner boundary.

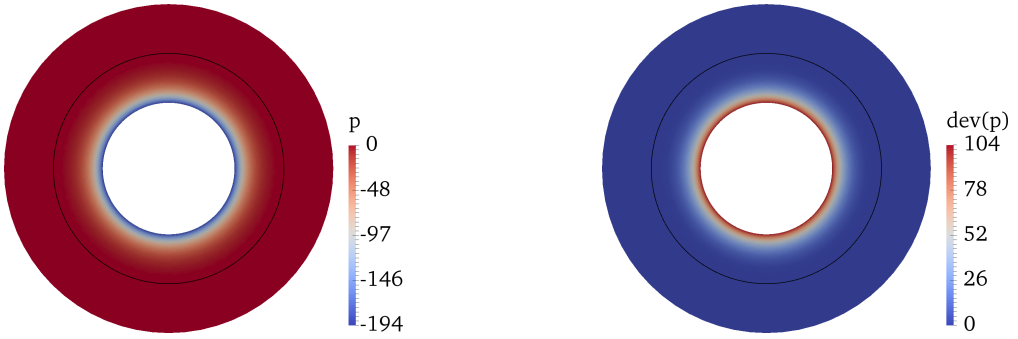

(a) Expected value of the pressure.

(b) Standard deviation of the pressure.

Figure 5.13: Visualisation of the pressure field of the UFSI problem. The fluid-structure interface is indicated by a black circle.

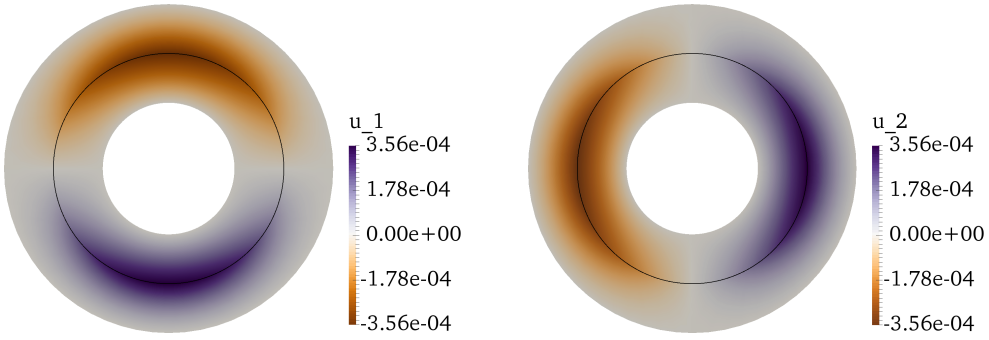

(a) Expected values of the displacement in horizontal (left image) and vertical (right image) direction.

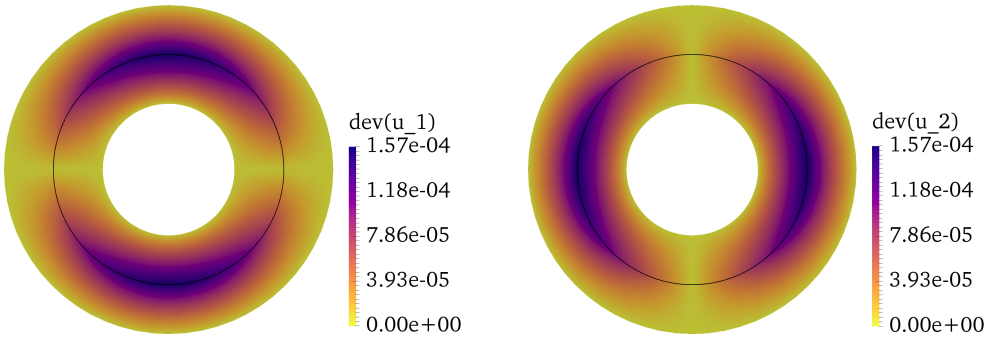

(b) Standard deviation of the displacement in horizontal (left image) and vertical (right image) direction.

Figure 5.14: Visualisation of the displacement field of the UFSI problem. The fluid-structure interface is indicated by a black circle.

The displacement field is visualised in Figure 5.14. Via the boundary conditions, the displacement field is set to be certainly zero at the inner and the outer boundary of the

geometry. On the solid domain, the displacement is governed by the elasticity equation and on the fluid domain it is governed by the ALE mesh deformation model (3.54). The shear forces of the fluid flow lead to a deformation of the solid domain in angular direction. The highest value of the expected displacement (Figure 5.14a) is at the fluid-structure interface with a decline to zero towards the outer and inner boundary. Again at the interface, the standard deviation of the displacement field (Figure 5.14b) takes its highest value.

The difference of the computed solution of the UFSI benchmark problem to the analytical solution can be evaluated by the relative error measure defined in the following. The error measure uses the L^2-norm over both, the geometric and stochastic dimensions.

$$\begin{aligned} \mathrm{err}_{\mathcal{D}}(\chi) &:= \frac{\|\chi_h - \chi\|_{L^2(\mathcal{D},\Omega)}}{\|\chi\|_{L^2(\mathcal{D},\Omega)}}, \\ \|\chi\|^2_{L^2(\mathcal{D},\Omega)} &:= \int_\Omega \int_{\mathcal{D}} |\chi(\boldsymbol{x},\omega)|^2 \mathrm{d}\boldsymbol{x} P(\mathrm{d}\omega), \end{aligned} \tag{5.37}$$

where χ represents the respective variable.

This relative L^2-error was computed for the geometrical and stochastical discretisation combinations given in Table 5.7. The results are shown in Figure 5.15 for the velocity field and in Figure 5.16 for the pressure field on the fluid domain. The error in the displacement field on the solid domain is shown in Figure 5.17.

As can be seen in Figure 5.15a, the numerically computed velocity field converges quadratically with the mesh refinement. This is in accordance with the theoretically expected order of convergence for the utilised FEM [59]. Figure 5.15b shows that the error in the velocity field has hardly any dependency on the PC degree. This can be explained with dependency of the velocity solution (5.33) on the PC expansion coefficients of the boundary velocity (5.27). The coefficients are zero for $P > 1$. Hence, the highest accuracy with respect to the stochastical dimensions is already reached for $P = 1$.

The pressure field (Figure 5.16a) shows a quadratic convergence with respect to the mesh refinement for $P > 1$ in accordance with the theory [59]. Due to the dependency of the pressure solution (5.34) on the the boundary velocity (5.27), the PC expansion coefficients of the pressure are zero for $P > 2$. Accordingly, the highest accuracy with respect to the stochastical dimensions is reached at $P = 2$ (cf. Figure 5.16b).

From Figures 5.17a and 5.17b, it can be seen, that the error in the displacement field widely depends on both, the mesh resolution and the PC degree. A quadratic order of convergence with respect to the mesh refinement can only be observed for $P = 4$. For the sufficiently high mesh resolution R4, the error in the displacement field shows an exponential convergence with respect to the PC degree. As it is shown theoretically in [145], exponential convergence is expected for the utilised PC discretisation of the stochastic dimensions.

The local distribution of the relative L^2-error is exemplarily shown in Figure 5.18 for the mesh refinement level R3 and a PC degree of $P = 3$. The error measure (5.37) can as well be computed for each cell of the FEM mesh $K \in \mathcal{T}_h$. At this, the error is again computed relative to the full domain $\mathcal{D}$:

$$\mathrm{err}_{K,\mathcal{D}}(\chi) := \frac{\|\chi_h - \chi\|_{L^2(K,\Omega)}}{\|\chi\|_{L^2(\mathcal{D},\Omega)}}. \tag{5.38}$$

Figure 5.18a illustrates that the relative L^2-error in the velocity field increases from the inner boundary to the fluid-structure interface. Similarly, the error in the displacement field

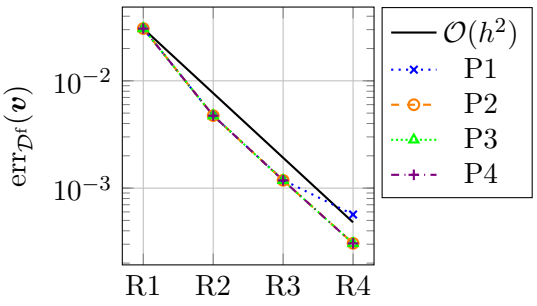

(a) By mesh resolution.

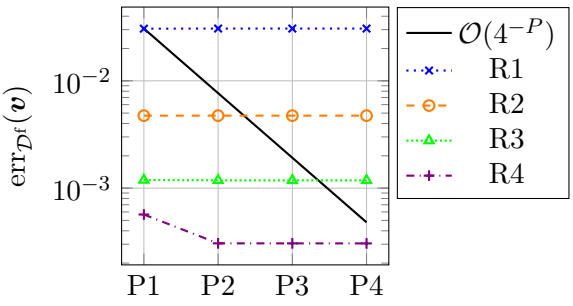

(b) By PC degree.

Figure 5.15: Error analysis of the velocity field on the fluid domain of the UFSI benchmark. The difference between the computed and the analytical solution is measured by the relative L^2-error (5.37). The results are plotted for the discretisation parameters given in Table 5.7. The ideal quadratic order convergence is indicated through the black line for comparison.

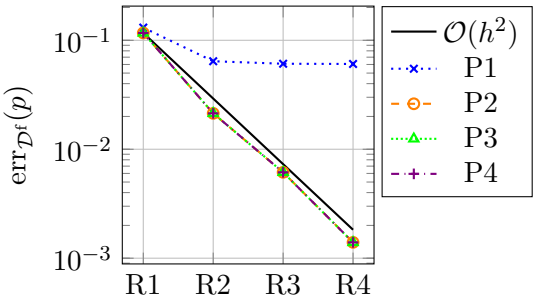

(a) By mesh resolution.

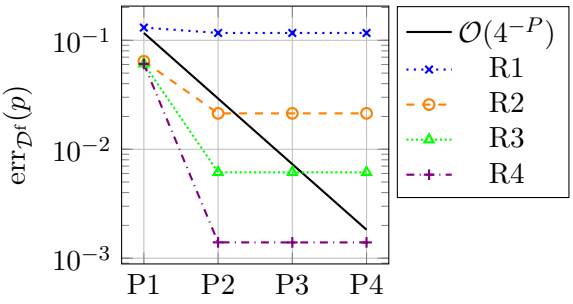

(b) By PC degree.

Figure 5.16: Error analysis of the pressure field on the fluid domain of the UFSI benchmark. The difference between the computed and the analytical solution is measured by the relative L^2-error (5.37). The results are plotted for the discretisation parameters given in Table 5.7. The ideal quadratic order convergence is indicated through the black line for comparison.

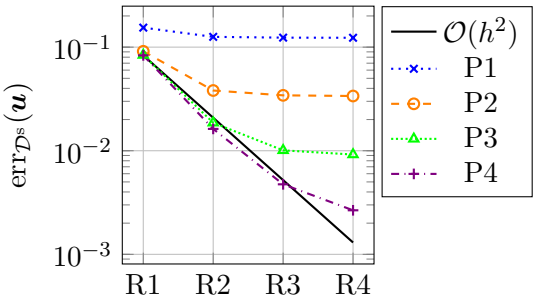

(a) By mesh resolution.

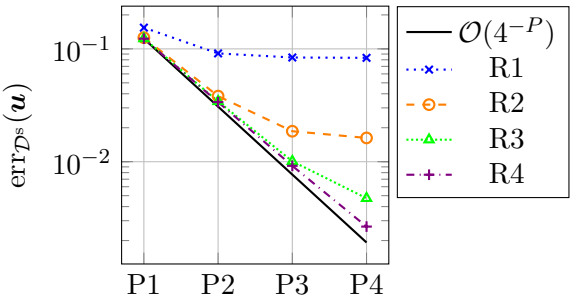

(b) By PC degree.

Figure 5.17: Error analysis of the displacement field on the solid domain of the UFSI benchmark. The difference between the computed and the analytical solution is measured by the relative L^2-error (5.37). The results are plotted for the discretisation parameters given in Table 5.7. The ideal quadratic order convergence is indicated through the black line for comparison.

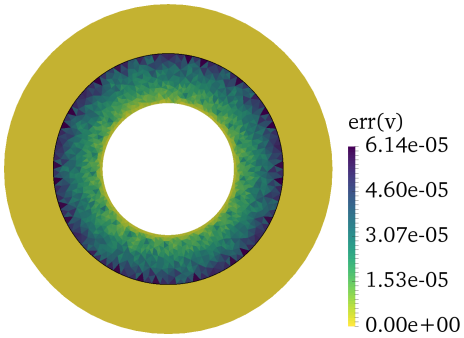

(a) The local error of the velocity field $\mathrm{err}_{K,\mathcal{D}^{\mathrm{f}}}(\boldsymbol{v})$ in the fluid domain.

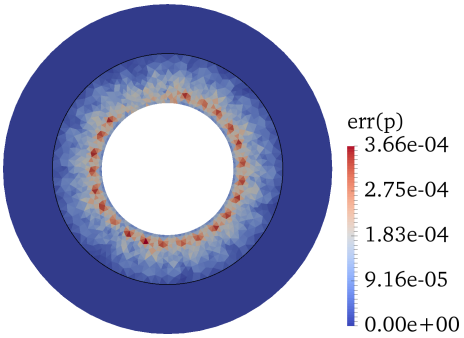

(b) The local error of the pressure field $\mathrm{err}_{K,\mathcal{D}^{\mathrm{f}}}(p)$ in the fluid domain.

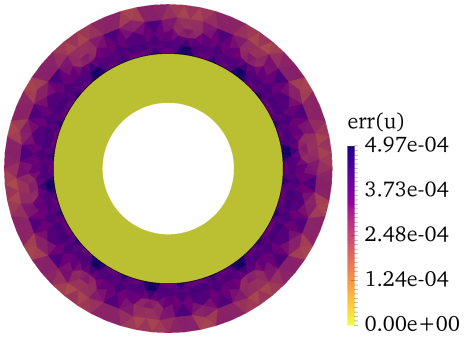

(c) The local error of the displacement field $\mathrm{err}_{K,\mathcal{D}^{\mathrm{s}}}(\boldsymbol{u})$ in the solid domain.

Figure 5.18: Visualisation of the local relative error (5.38) of the computed solution of the UFSI problem for the mesh refinement level R3 and PC degree $P = 3$.

has its highest values at the fluid-structure interface as it is shown in Figure 5.18c. The error of the computed pressure field (Figure 5.18b) shows peak values approximately in the area of the steep gradient of the solution near to the inner boundary (cf. Figure 5.13). Overall, all three local error visualisations show an approximately rotationally symmetric distribution. This is in accordance with the rotationally symmetric formulation and solution of the UFSI problem.

6 Aortic biomechanics simulation assuming uncertainties

A review of numerical simulations for the evaluation and treatment planning of aneurysms is given in [18]. According to the authors, further developments are needed for incorporating fluid-structure interaction simulations to better understand the factors of aneurysm growth. Additionally, further validation studies should increase the reliability of numerical simulation outcomes.

The stochastical dimensions of a hemodynamical problem are considered for arterial networks in [17] using uncertainty quantification. Aortic phantom experiments have been used to test and validate various flow imaging and pressure measuring techniques [31, 15]. In [138] a realistic phantom is presented and calibrated to emulate patient-specific aortic blood flow. Phantom experiments can also be used to validate numerical blood flow simulations [86]. Another validation study for a numerical framework is given in [109] by means of the flow through a medical device with rigid walls in the shape of a nozzle and by means of a fluid flow in a compliant vessel.

This chapter goes beyond the state of the art by the validation of the aortic blood flow simulation under uncertainties by means of an aortic phantom (section 6.1). Subsequently, as a proof of concept, the numerical framework presented in this work is applied to a patient-specific aortic bow of a healthy proband (section 6.2). Parts of the results described in this chapter have been published before by the author in [83, 84, 82]. In [83] a computational fluid dynamics simulation with rigid vessel walls has been compared to a fluid-structure interaction simulation of a prototypic aortic phantom. A solver for collocation-based UQ of an FSI-problem with an idealized phantom geometry is described in [84]. Aspects of the application of the numerical framework to an aortic bow are presented in [82].

6.1 Validation by means of an aortic phantom experiment

In this section, the numerical framework presented in this thesis is applied to the prototypical aortic phantom described in section 2.3. The authors of [31] are acknowledged for sharing the necessary data for realizing this numerical experiment. The data includes 2D and 4D MRI flow measurements and a 3D image of the geometry of the elastic vessel segment. Furthermore, the data comprises catheter-based measurements of the pressure difference between several measurement plane levels. The 2D flow data used for the numerical experiment in this work covers 128 time points of a flow period at a spatial resolution of $1.25\,\mathrm{mm}\times1.25\,\mathrm{mm}$. The voxel size of the 3D image for geometrical segmentation is $1.56\,\mathrm{mm}\times2.1\,\mathrm{mm}\times1.56\,\mathrm{mm}$.

The pressure values were measured at 31 points in time.

The details on the configuration of the model and the numerical workflow are given in the following subsection 6.1.1. Section 6.1.2 then evaluates the results of the simulation and gives a comparison to MRI measurements of the phantom.

6.1.1 Numerical experiment setup

In order to simulate the flow mechanics of the aortic phantom experiment, the subject-specific workflow presented in section 4.1 is used for the configuration and realisation of the simulation.

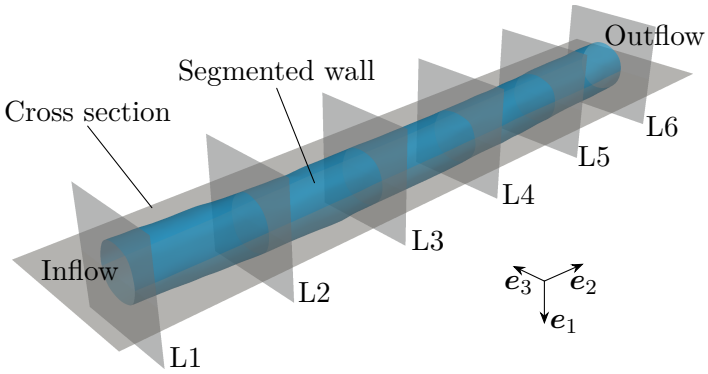

Figure 6.1: Segmentation of the prototypic aortic phantom. The illustration includes a denotation of the plane levels, where the flow was measured based on 2D flow MRI and the pressure was measured with a catheter. The levels L1 and L6 are taken as inflow and outflow boundaries. Additionally a cross section is delineated at which the simulation is visualised in section 6.1.2.

Firstly, a segmentation is generated from the 3D geometry image of the phantom's elastic tube (cf. section 4.1.1). The segmented surface together with the measurement plane levels and evaluation cross-sections is shown in Figure 6.1. The inflow and outflow boundaries are clipped in a way such that they coincide with the first and the last measurement planes, respectively. The measurement planes L1 to L6 are located every 5 cm. The total length of the clipped segmentation is 25 cm. The diameter of the tube is about $R = 1.5\,\text{cm}$. The resulting finite element mesh consists of 2.01×10^5 tetrahedral cells.

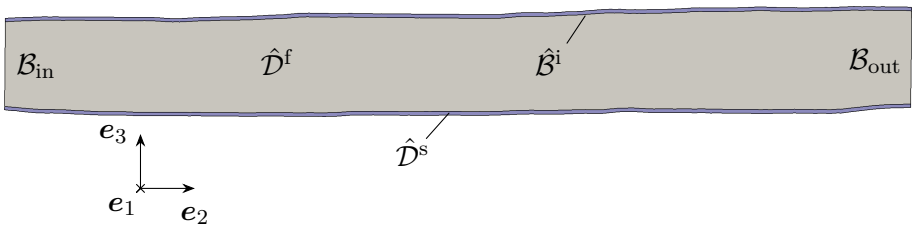

Figure 6.2: Illustration of the fluid and structure domains, $\hat{\mathcal{D}}^{\text{f}}$, $\hat{\mathcal{D}}^{\text{s}}$ by means of the cross section delineated in Figure 6.1. Furthermore, the inflow boundary $\mathcal{B}_{\text{in}}$, the outflow boundary $\mathcal{B}_{\text{out}}$ and the fluid-structure interface $\hat{\mathcal{B}}^{\text{i}}$ are assigned.

The longitudinal cross section indicated in Figure 6.1 is shown in detail in Figure 6.2. It is also used for the visualisation in the evaluation section 6.1.2. Figure 6.2 shows the location of the fluid and the solid domain.

The corresponding mathematical modelling of the blood-like flow through the phantom was presented section 3.2. The utilised model for the elastic deformation of the phantom's vessel wall was described in section 3.3. Details on the coupling between the fluid and the solid phase were given in section 3.4.

Additionally the location of the boundaries with specific boundary conditions is given in Figure 6.2. For the velocity and pressure field the boundary conditions were described in section 3.2.2. The boundary conditions of the displacement field were given in section 3.3.2. The parameter values for the various parts of the mathematical model are listed in Table 6.1. The values lead to a Reynolds number of about

$$\mathrm{Re} = \frac{v^{\mathrm{in}} 2R}{\nu} \approx 5000.$$

Due to the value of the Reynolds number, the fluid flow dynamics become convection dominated and require stabilisation in the numerical solving routine. This is done by a residual-based streamline diffusion scheme [14].

Parameter	Symbol	Value
Density	ρ	$1101.45\,\mathrm{kg\,m^{-3}}$
Kinematic viscosity	ν	$4.545 \times 10^{-6}\,\mathrm{m^2\,s^{-1}}$
Poisson's ratio	γ	0.45
Young's modulus	Y	$642 \pm 193\,\mathrm{kPa}$
Uncertain inflow factor	q	1.00 ± 0.15
Poisseuille exponent	β	8
Period of a heart cycle	T	$1.024\,\mathrm{s}$
Wall thickness	h	$1 \times 10^{-3}\,\mathrm{m}$

Table 6.1: Model parameters of the aortic phantom.

The workflow results in a subject-specific configuration of the abstract mathematical problem formulated in problem (2) with an uncertain vessel wall stiffness (Young's modulus) and inflow velocity. The discretisation for the given problem is presented in section 4.2. The discretisation parameters are listed in Table 6.2.

Parameter	Symbol	Value
Degrees of freedom	# dofs	1,606,464
time step length	k	$0.0005\,\mathrm{s}$
theta	θ	0.5005
smooth start duration	T_{start}	$0.02\,\mathrm{s}$
PC degree	P	4
Collocation points	$\#\mathcal{Q}$	36

Table 6.2: Discretisation parameters for the aortic phantom simulation.

As with the deterministic FSI benchmark (cf. (5.2)), the simulation of the phantom is initialised with zero values for the variables and smoothly run up to the first flowrate value of velocity boundary conditions. As opposed to the deterministic benchmark, the spline interpolation stated in equation (3.2.2) is used to implement the smooth start within the starting time T_{start}.

The maximal degree of the chaos polynomials $P = 4$ leads with equation (4.31) to a number of modes of $M = 14$. With that, a sufficient level of convergence is achieved with respect to the stochastical dimensions of the problem.

Operator	Method	Parameter	Value
$\mathcal{M}^{-1}$	FGMRES	Relative tolerance	0.01
$\mathcal{M}^{-1}$	FGMRES	Maximal iterations	100
J^{uu-1}, J^{vv-1}, $\tilde{\mathcal{S}}^v$	AMG	Cycle type	V-cycle
J^{uu-1}	AMG	Aggressive coarsening	On all levels
J^{vv-1}, $\tilde{\mathcal{S}}^v$	AMG	Aggressive coarsening	None
J^{uu-1}, $\tilde{\mathcal{S}}^v$	AMG	Interpolation type	Multipass interpolation
J^{vv-1}	AMG	Interpolation type	Extended+i interpolation
J^{uu-1}, J^{vv-1}, $\tilde{\mathcal{S}}^v$	AMG	Coarsening type	HMIS-coarsening
J^{uu-1}, J^{vv-1}, $\tilde{\mathcal{S}}^v$	AMG	Relax weight	1
J^{uu-1}, J^{vv-1}, $\tilde{\mathcal{S}}^v$	AMG	Strong threshold	0.9
$\mathcal{S}^{u-1}$	FGMRES	Maximal iterations	1
J^{uu-1}	CG	Relative tolerance	0.00001
J^{uu-1}	CG	Maximal iterations	100
J^{uu-1}	AMG	Number of iterations	1
J^{uu-1}	AMG	Relax type	hybrid sym. Gauss-Seidel
J^{uu-1}	AMG	Number of sweeps	1
$\mathcal{S}^{v-1}$	FGMRES	Relative tolerance	0.1
$\mathcal{S}^{v-1}$	FGMRES	Maximal iterations	20
J^{vv-1}	GMRES	Relative tolerance	0.001
J^{vv-1}	GMRES	Maximal iterations	100
J^{vv-1}	AMG	Number of iterations	1
J^{vv-1}	AMG	Relax type	hybrid Gauss-Seidel, forward
J^{vv-1}	AMG	Number of sweeps	1
$\tilde{\mathcal{S}}^v$	AMG	Maximal iterations	100
$\tilde{\mathcal{S}}^v$	AMG	Relative tolerance	0.01
$\tilde{\mathcal{S}}^v$	AMG	Relax type	hybrid sym. Gauss-Seidel
$\tilde{\mathcal{S}}^v$	AMG	Number of sweeps	1

Table 6.3: Configuration of the linear solver subroutines (cf. Figure 4.5) for the three-dimensional aortic phantom and the aortic bow simulations.

The problem-specific solver for the collocation points, presented in section 4.2.5, is configured for the three-dimensional problem as specified in Table 6.3. For the preconditioner BoomerAMG (cf. section 4.2.5), only values that differ from the default configuration provided by HYPRE are given. The absolute tolerance of the Newton method, namely 10^{-8}, is

chosen such that it takes approximately 1 to 3 Newton iterations to compute a time step. The configuration differs from the values for the two-dimensional version of the deterministic FSI problem given in Table 5.4, as the third spatial dimension and the different geometrical setup alters the structure and condition number of the discrete problem. The configuration was determined by several test runs to find an acceptable numerical convergence behaviour of the solver.

6.1.2 Simulation results

As for the benchmark problems, the BwForCluster MLS&WISO Production (see section 5.1.2) was used for the simulation of the aortic phantom. The computing time for one of the 36 collocation points was about 42 hours on 256 CPUs, resulting in a total amount of computational costs for the UQ-simulation of 2 time periods of 3.87×10^5 core hours. The first time period is seen as start-up phase and for the second period, the evaluation and results are shown in the following. Firstly, visualisations of the solution variables by means of the cross section as indicated in Figure 6.1 are given. Then, the flowrate profiles in the marker plane levels of the simulation are compared to the MRI measurements. Finally, the simulated flowrates and pressure differences over the time are compared to the respective measurements.

Visualisation in the longitudinal cross section

To illustrate the results of the aortic phantom simulation, Figure 6.3 to 6.9 show visualisations of the direct solution variables in the longitudinal cross section delineated in Figure 6.1 at the point in time with the highest systolic inflow $t = 0.1\,\mathrm{s}$. The data of the inflow flowrates contains a second and smaller peak at $t = 0.22\,\mathrm{s}$. To give an illustration of the time course of the dynamics, all visualisations are also given for this second point in time in the appendix in Figure 8.2 to 8.8. The velocity and pressure field visualisations are shown with respect to the deformed domain $\mathcal{D}_t$ at the respective point in time. The displacement field visualisations are given with respect to the reference domain $\hat{\mathcal{D}}$.

The first three figures, Figures 6.3, 6.4 and 6.5, show the displacement variable in all three spatial directions in the form of the expected value and the standard deviation. The orientation of the spatial directions can be seen in Figure 6.1 and Figure 6.2. Accordingly, Figure 6.3 shows the displacement values directed into the image plane. For this displacement component, the standard deviation is highest in the middle of the length of the geometry. A reason for this is that the displacement at the inflow and outflow boundary is fixed to zero without uncertainties.

Figure 6.4 shows the expected value and standard deviation of the displacement in the longitudinal direction of the tube from the inflow to the outflow. Whereas the inflow and outflow boundary of the vessel is fixed with zero values in the displacement, the middle section shows a deformation from the outflow to the inflow. Physically, this can be explained with Figure 6.5. Here, an expansion in the transversal direction can be observed after the inflow boundary in the first half of the geometry. The transversal expansion in the beginning of the vessel leads to a backward pulling force in the rest of the solid structure. The standard deviation of the longitudinal displacement $\sigma(\boldsymbol{u}_2)$ is qualitatively similar to $\sigma(\boldsymbol{u}_1)$. However, the standard deviation of the transversal displacement $\sigma(\boldsymbol{u}_3)$ in Figure 6.5 is higher at the vessel wall than in the inner lumen. The highest expected transversal expansion of the vessel

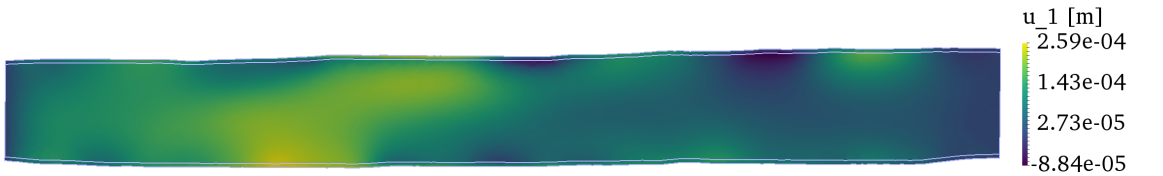

(a) Expected value $E(\boldsymbol{u}_1)$.

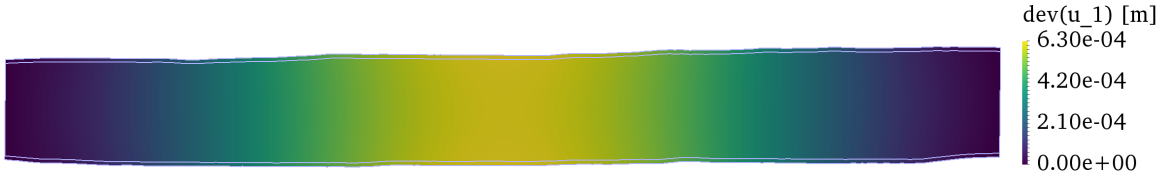

(b) Standard deviation $\sigma(\boldsymbol{u}_1)$.

Figure 6.3: Visualisation of the displacement into the shown cross section $\boldsymbol{u}_1$ (cf. Figure 6.1) at mid-systole, $t = 0.1\,\mathrm{s}$.

(a) Expected value $E(\boldsymbol{u}_2)$.

(b) Standard deviation $\sigma(\boldsymbol{u}_2)$.

Figure 6.4: Visualisation of the displacement along the cross section $\boldsymbol{u}_2$ (cf. Figure 6.1) at mid-systole, $t = 0.1\,\mathrm{s}$.

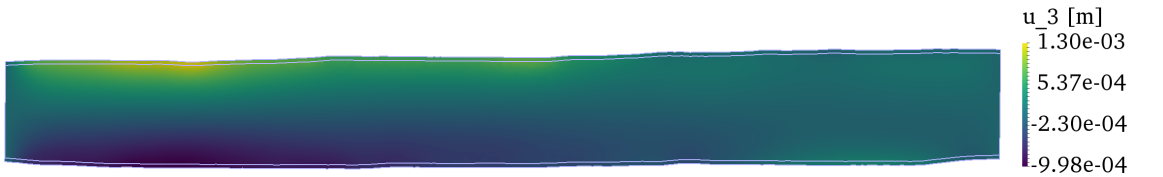

(a) Expected value $E(\boldsymbol{u}_3)$.

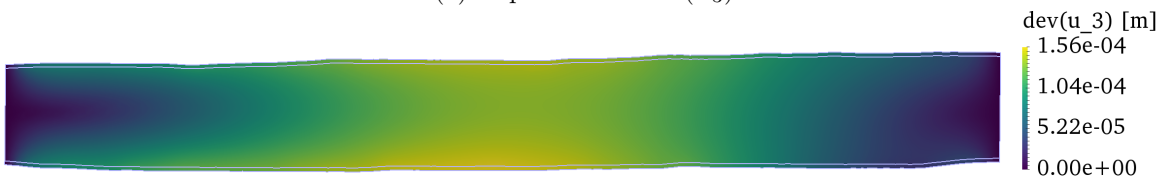

(b) Standard deviation $\sigma(\boldsymbol{u}_3)$.

Figure 6.5: Visualisation of the vertical displacement in the cross section $\boldsymbol{u}_3$ (cf. Figure 6.1) at mid-systole, $t = 0.1\,\mathrm{s}$.

is 1.3 mm (see Figure 6.4). In absolute values, the standard deviation of $\boldsymbol{u}_1$ exceeds the expected value. However, the standard deviation of all three spatial displacement directions keeps below the expected value of the transversal component $\boldsymbol{u}_3$.

The three spatial directions of the velocity field are shown in Figures 6.6 to 6.8. Figure 6.6 shows the expected value and standard deviation of the velocity component directed into the image plane. For this flow direction, $\boldsymbol{v}_1$, the boundary values at the inflow are set to be certainly almost zero. At the outflow boundary, there are no direct conditions on the velocity field and its uncertainty. Nevertheless, the standard deviation $\sigma(\boldsymbol{v}_1)$ is vanishingly small at the outflow boundary. The highest standard deviation is apparent on halfway in the vessel.

(a) Expected value $E(\boldsymbol{v}_1)$.

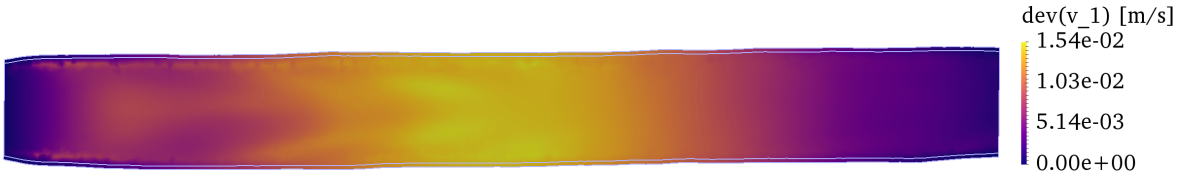

(b) Standard deviation $\sigma(\boldsymbol{v}_1)$.

Figure 6.6: Visualisation of the velocity into the shown cross section $\boldsymbol{v}_1$ (cf. Figure 6.1) at mid-systole, $t = 0.1$ s.

(a) Expected value $E(\boldsymbol{v}_2)$.

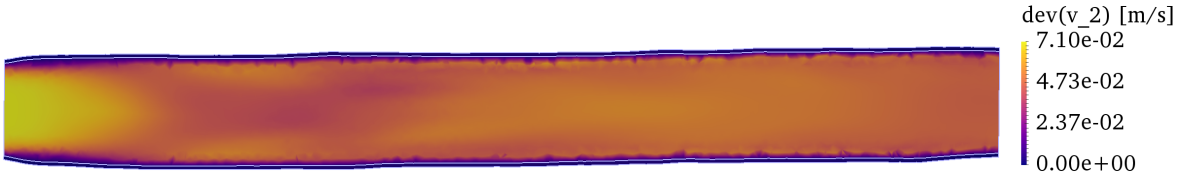

(b) Standard deviation $\sigma(\boldsymbol{v}_2)$.

Figure 6.7: Visualisation of the velocity along the cross section $\boldsymbol{v}_2$ (cf. Figure 6.1) at mid-systole, $t = 0.1$ s.

The expected value and standard deviation of the second velocity component along the vessel direction is shown in Figure 6.7. At the time of the first inflow peak, the velocity at the inflow is naturally highest. In the appendix, it can be seen, how the peak velocity progresses in an attenuated way in Figure 8.6. Along with the high values for the expected value of $\boldsymbol{v}_2$

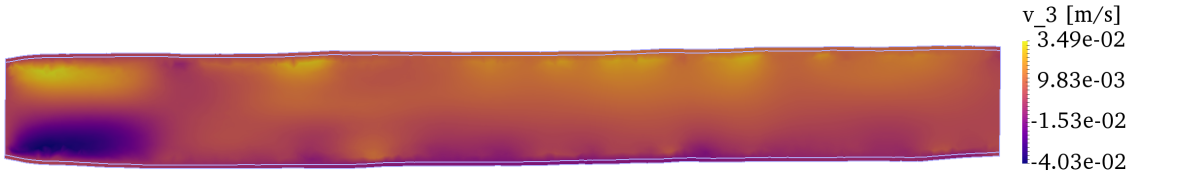

(a) Expected value $E(\boldsymbol{v}_3)$.

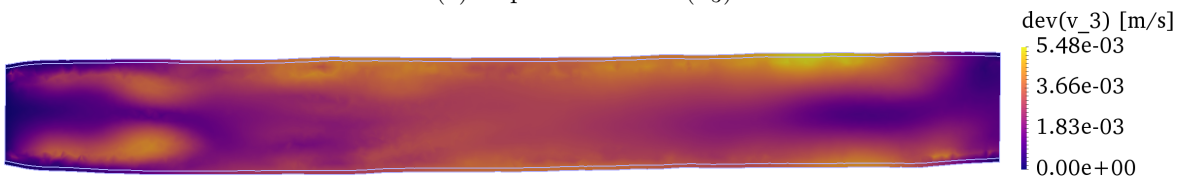

(b) Standard deviation $\sigma(\boldsymbol{v}_3)$.

Figure 6.8: Visualisation of the vertical velocity in the cross section $\boldsymbol{v}_3$ (cf. Figure 6.1) at mid-systole, $t = 0.1\,\mathrm{s}$.

goes an increased uncertainty visible in the standard deviation $\sigma(\boldsymbol{v}_2)$.

Also, the expected value of the velocity in transversal direction $\boldsymbol{v}_3$ correlates with its standard deviation, as can be seen in Figure 6.8. In the illustrated phase in time, the expected value of $\boldsymbol{v}_3$ indicates a slight transversal flow, pushing the vessel wall outwards.

(a) Expected value $E(p)$.

(b) Standard deviation $\sigma(p)$.

Figure 6.9: Visualisation of the pressure p in the cross-sectional plane (cf. Figure 6.1) at mid-systole, $t = 0.1\,\mathrm{s}$.

The dilatation of the vessel (Figure 6.5) is driven by the fluid flow dynamics, which can be seen in the transversal velocity (Figure 6.8), but also in the pressure field (Figure 6.9). The expected value of the pressure is highest at the inflow boundary and correspondingly acts highest on the vessel wall in the beginning of the vessel. However, relative to the pressure reference value of zero, there is an overpressure in all of the vessel. The absolute pressure value in the vessel follows the pressure value of the pressure boundary condition at the outflow boundary. Considering the values of the standard deviation of the pressure, the uncertainty is relatively evenly distributed over the whole cross section with a slight peak at two-thirds of the vessel length.

Visualisation of the plane levels

In Table 6.4, the simulated flow values are visually compared to the measured 2D flow MRI values. The velocity component in the main flow direction along the vessel $\boldsymbol{v}_2$ is shown for the marker plane levels L2, L3, L4 and L5, which are denoted in Figure 6.1. The visualisations show the fluid domain without the solid domain, in which the longitudinal velocity is almost zero. The simulated velocity is given on the one hand by its expected value. On the other hand, the addition and subtraction of the standard deviation to the expected value aims to illustrate the range of values, the velocity can take by means of the UQ simulation. This range of simulated velocity values is compared to the respective 2D flow MRI measurement. Hereby, it is to be stressed, that only a single measurement point is available, which is also subject to uncertainty.

$t = 0.1\,\mathrm{s}$	L2	L3	L4	L5	
2D flow MRI: $\boldsymbol{v}_2$				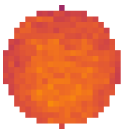	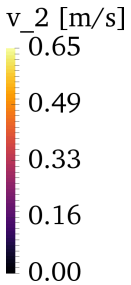
$E(\boldsymbol{v}_2) - \sigma(\boldsymbol{v}_2)$	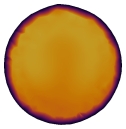	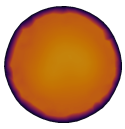	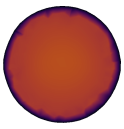	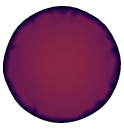	
$E(\boldsymbol{v}_2)$	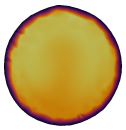	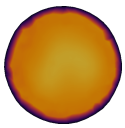	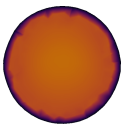	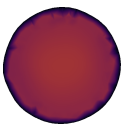	
$E(\boldsymbol{v}_2) + \sigma(\boldsymbol{v}_2)$	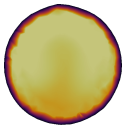	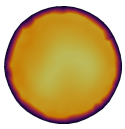	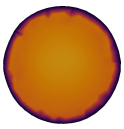	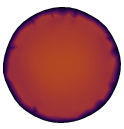	

Table 6.4: Visualisation of the velocity field $\boldsymbol{v}_2$ in the cross-sectional plane levels L2, L3, L4 and L5 (cf. Figure 6.1) at mid-systole, $t = 0.1\,\mathrm{s}$. The first row shows the velocity data measured by 2D flow MRI. The second to the last row shows the simulated velocity field. Hereby, the expected value $E(\boldsymbol{v}_2)$ is shown in the third row. The second row shows the standard deviation $\sigma(\boldsymbol{v}_2)$ substracted from the expected value. The standard deviation added to the expected value is shown in the fourth row.

The simulation well captures the decline of the flow strength from one marker plane level to the next, respectively. This damping of the flow would not be obtained by the simulation, if the vessel wall was modelled to be rigid, as a comparison to a sole CFD simulation clarified in [83]. Regarding the respective marker plane levels, it can be seen, that the MRI measurement does not exactly match the expected value but lies within the range of values spanned by the addition and subtraction of the standard deviation.

The results in Table 6.4 are given for the point in time of the highest inflow flowrate $t = 0.1\,\mathrm{s}$ in mid-systole. For a secondly considered point in time $t = 0.22\,\mathrm{s}$, the results are given in the appendix in Table 8.2. The flowrate values integrated over the respective marker

planes are considered over a full time period in the following section.

Simulated and measured flowrate and pressure difference values

The value of the flowrate is obtained by integrating the longitudinal velocity component over the respective marker plane. Figures 6.10 to 6.13 show the flowrate results plotted over one time period for the inner marker plane levels L2 to L5 (cf. Figure 6.1). The simulated flowrates are shown by means of their expected value and the range obtained by adding and subtracting the standard deviation. The results of the simulation are directly compared to the values of the corresponding 2D flow MRI measurement.

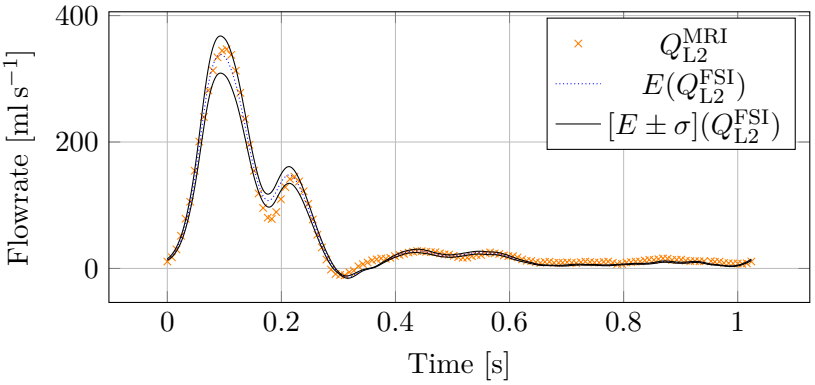

Figure 6.10: The measured (MRI) and simulated (FSI) flowrate at the plane level L2 (see Figure 6.1). The simulated flowrate is shown by its expected value and the expected value plus/minus its standard deviation.

It can be seen in the first plot, Figure 6.10, that the simulated values for the plane level L2 well coincide with the MRI measurement. For the plane level L3 (Figure 6.11), the MRI-measured values at the systolic peaks are at the lower border of the simulated standard deviation range. In the first half of the diastole at $t \approx 0.53\,\mathrm{s}$ the measured data shows a flow peak, which is not reflected in the simulation results. As can be seen in Figure 6.12 and Figure 6.13, the measured flowrate values in the marker planes L4 and L5 are overestimated by the simulation in the systole and slightly underestimated in the diastole.

In the aortic phantom experiment the pressure difference δp between two marker planes was measured over a time period by a catheter. Hereby, the plane level L2 was taken as the reference and the pressure difference to the plane levels L3, L4 and L5 was measured, respectively. For the computation of the pressure difference values from the simulation, the average pressure value over the respective marker plane is used. As the pressure in the transversal planes shows a very homogeneous distribution with almost no deviation from the average, this average value can be used for comparison to the point-based pressure measurement at the tip of the catheter, for which the exact position is not included in the data.

Analogously to the flowrate plots, the simulated pressure difference values are compared to the catheter-measured values in Figures 6.14, 6.15 and 6.16. As can be seen in all of the three plots, the simulation results coincide only partially with the catheter measurements. The amplitude of the first maximum is well captured, whereas the first minimum is significantly

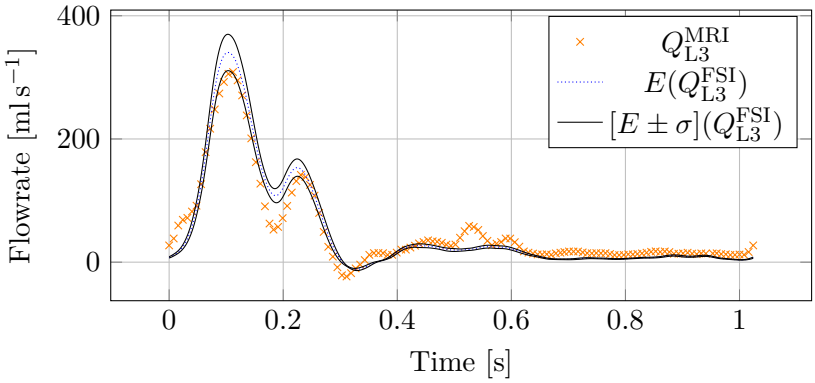

Figure 6.11: The measured (MRI) and simulated (FSI) flowrate at the plane level L3 (see Figure 6.1). The simulated flowrate is shown by its expected value and the expected value plus/minus its standard deviation.

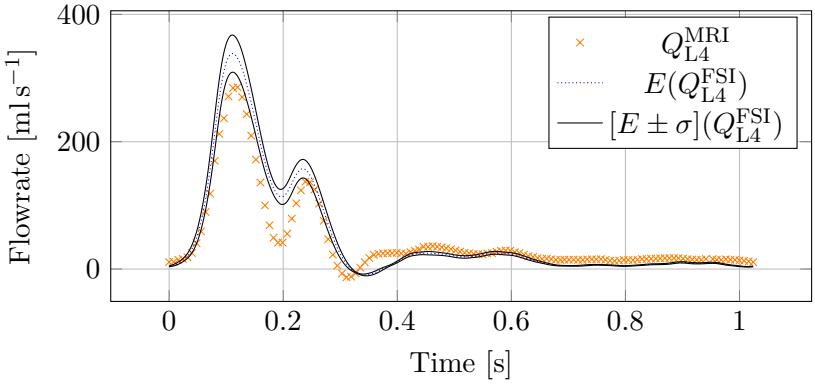

Figure 6.12: The measured (MRI) and simulated (FSI) flowrate at the plane level L4 (see Figure 6.1). The simulated flowrate is shown by its expected value and the expected value plus/minus its standard deviation.

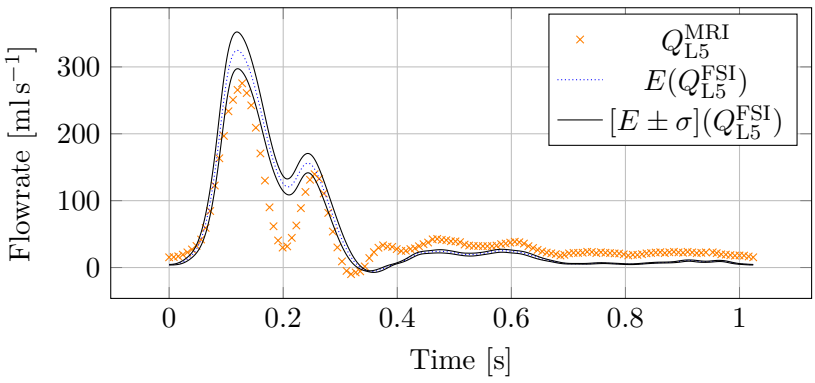

Figure 6.13: The measured (MRI) and simulated (FSI) flowrate at the plane level L5 (see Figure 6.1). The simulated flowrate is shown by its expected value and the expected value plus/minus its standard deviation.

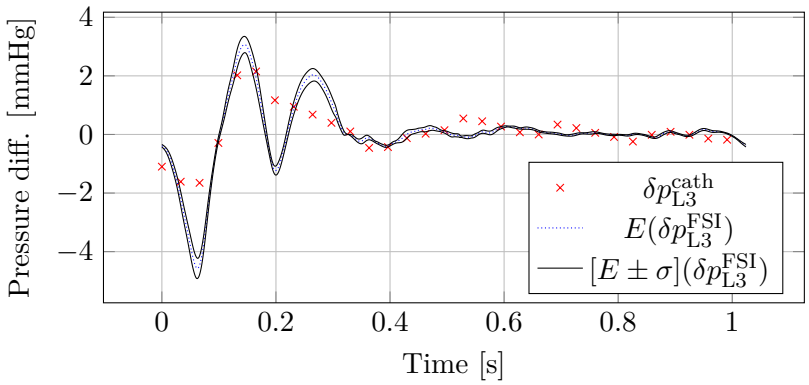

Figure 6.14: The measured (cath) and simulated (FSI) pressure difference from plane level L2 to L3 (see Figure 6.1). The simulated pressure difference is shown by its expected value and the expected value plus/minus its standard deviation.

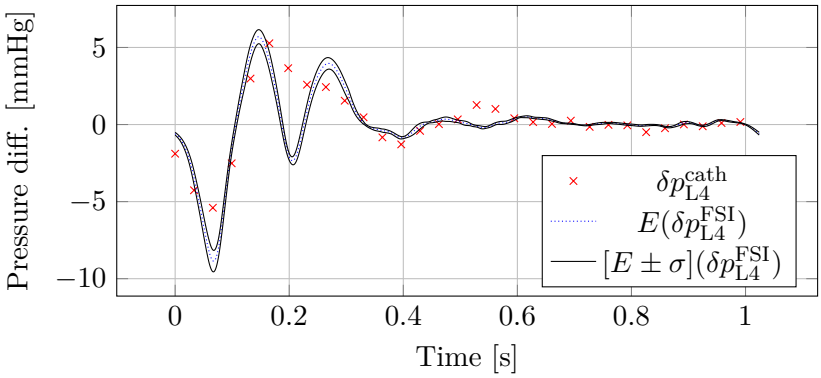

Figure 6.15: The measured (cath) and simulated (FSI) pressure difference from plane level L2 to L4 (see Figure 6.1). The simulated pressure difference is shown by its expected value and the expected value plus/minus its standard deviation.

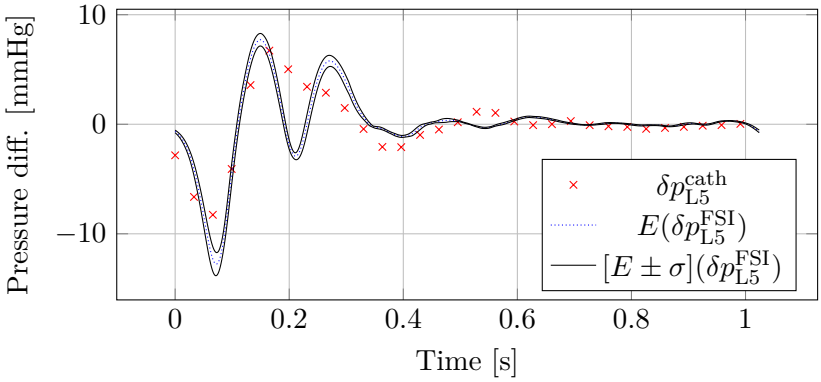

Figure 6.16: The measured (cath) and simulated (FSI) pressure difference from plane level L2 to L5 (see Figure 6.1). The simulated pressure difference is shown by its expected value and the expected value plus/minus its standard deviation.

lower than the measurement. The second minimum of the simulated values is not reflected in the measurements at all. The zero value in the beginning of the diastole again coincides in the simulation and the measurement.

In the interpretation of the obtained results, it is to be remarked, that initially, the aortic phantom experiment was carried out to evaluate the capabilities of the 2D and 4D flow MRI technology for flow measurements and not to validate a numerical simulation framework. For the modelling and the setup of the simulation only the retrospectively available information and data could be used. This left high uncertainties in the details of the configuration and setup of the experiment. For example, the geometrical information is only known from the MRI measurement and not in full detail from the real construction of the experiment. Furthermore, it would have been useful to configure the outflow boundary condition of the simulation with the measurement of the absolute pressure values. Overall, the used measurement data only contains singular measurement values without any information on a possible variance of the measurement values. In this light, a reasonably good coincidence of the simulation results to the measured data can be stated.

6.2 Simulation of an aortic bow

In the previous section 6.1, the subject-specific simulation framework presented in this thesis is tested by means of a prototypic aortic phantom. This section addresses the application of the simulation framework to a healthy human proband. As a showcase, the application is meant to demonstrate the subject-specific workflow and to show the potential of including uncertainty quantification in the simulation framework. Hereby, the model equations and material properties for the phantom simulation are also used for the human proband. As pointed out in the description of the physiology and the mathematical modelling in chapters 2 and 3, the details of the biomechanics for a human aorta are far more complex than for the aortic phantom. Nevertheless, the results of the UQ-analysis can be exemplified.

UQ methods have already been used in other works, for example in [120], to obtain a data-driven statistical model for the wall shear stress in intracranial aneurysms. Furthermore, the UQ-study in [11] investigated the von Mises stress in the vessel wall of abdominal aneurysms under uncertainties.

This work considers illustration possibilities of the expected value and standard deviation of simulation results to gain an information on the reliability of the simulation. Additionally, the parameter for the probability of overstress proposed in this work is visualised by means of the considered human aorta.

This section begins with the description of the numerical experiment for the human proband in section 6.2.1. Subsequently, in section 6.2.2, the problem-specific linear solver is investigated with respect to its parallel scalability for the three-dimensional problem. Finally, the UQ-simulation of the human aorta is analysed and evaluated in section 6.2.3.

6.2.1 Numerical experiment setup

Like for the aortic phantom, the subject-specific workflow is used for the human proband to set up and carry out the simulation of the biomechanics.

The author acknowledges Matthias Müller-Eschner and Christian Weis from the Department of Radiology at the Heidelberg University Hospital for providing the MRI data for this work. The MRI data includes the morphology and 2D flow MRI data of a male human proband aged between 20 and 30. The spatial resolution of the time-averaged morphology image is $1.77\,\text{mm} \times 1.77\,\text{mm} \times 2.2\,\text{mm}$. The flow MRI values are measured at 24 points in time.

Figure 6.17 shows the segmented morphology with a smoothed surface and clipped boundaries for the inflow and outflow boundary conditions. The segmentation comprises the aortic bow beginning with the ascending aorta, the bifurcation to the brachiocephalic artery, the common bifurcation to the left common carotid artery and the left subclavian artery and the beginning of the descending aorta (cf. Figure 2.4). The flowrate values for the boundaries are extracted from the 2D flow MRI data. They are utilized for the velocity boundary conditions as defined in section 3.2.2 at the inflow and the outflow B and C. In the same section, the outflow pressure boundary condition for outflow D is described. The parameters for the model equations are set to the same as for the phantom and given in Table 6.1. Only the time period of one heart beat differs with $T = 1.02\,\text{s}$. Just like for the phantom, the Young's modulus and the flowrate for the velocity boundary conditions are modelled to be uncertain with a uniform distribution. Hereby, the three velocity boundary conditions are scaled with a single random variable and not independently from each other. The Reynolds number for

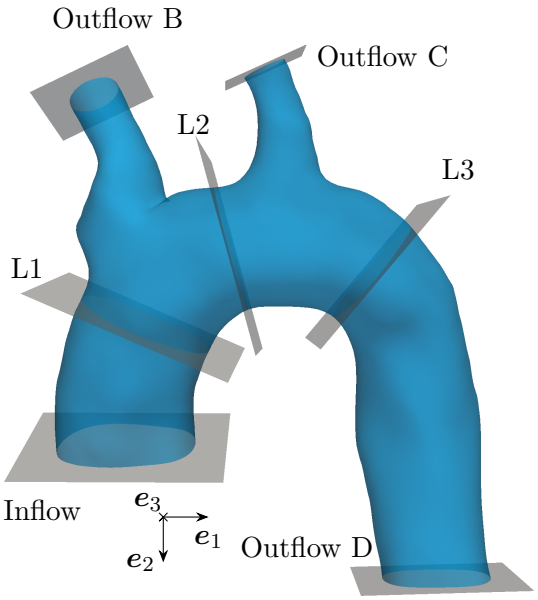

(a) Denotation of the inflow and outflow boundaries as well as of cross sectional planes for the visualisation.

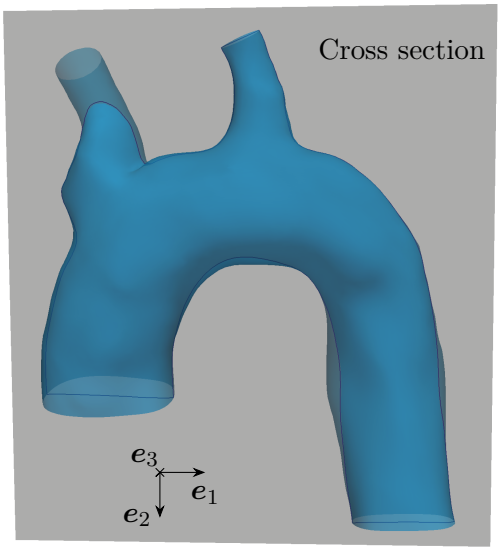

(b) Denotation of a frontal cross sectional plane for the visualisation. The plane is aligned with the centre points of the inflow and outflow C2 and D.

Figure 6.17: Segmentation of the aortic bow with an indication of several cross sectional planes for the definition of boundary conditions and for the visualisation in section 6.2.3.

this scenario with a vessel radius at the inflow $R \approx 1\,\mathrm{cm}$ is about

$$\mathrm{Re} = \frac{v^{\mathrm{in}} 2R}{\nu} \approx 4400.$$

The generated FEM mesh counts 2.30×10^5 tetrahedral cells, which leads to 1,830,975 # dofs. The discretisation parameters other than the number of degrees of freedom coincide with the values in Table 6.2. The problem-specific linear solver is configured with the parameters in Table 6.3. For the Newton method, the absolute tolerance is set to 10^{-8} and the absolute tolerance of the linear solver for $\mathcal{M}^{-1}$ is set to the slightly lower value of 5×10^{-9}. This way, it is ensured, that the absolute tolerance of the Newton method is undercut.

Figure 6.17 also shows the cross sectional planes, that are used for the visualisation.

6.2.2 Parallel scalability for the 3D problem

In section 5.1.3, the parallel scalability properties of the problem-specific solver proposed in this work are investigated by means of the two-dimensional deterministic benchmark problem. For the simulation of the three-dimensional problem considered in this chapter, the solver and its sub-routines had to be slightly reconfigured. The parameters for the linear solver, that lead to a satisfying numerical convergence in the case of the three-dimensional problem are summarised in Table 6.3.

To examine the parallel scalability properties also for the 3D case, the results of another scalability test are shown in this section. The test was carried out by means of a single deter-

ministic simulation run of the aortic bow simulation. The scalability test was carried out on the same hardware as the scalability study for the 2D benchmark, namely the BwForCluster MLS&WISO Production. See section 5.1.3 for details on the utilised hardware.

The values that are presented in the following are again average values over a range of time steps from the simulation start to $t = 0.28\,\mathrm{s}$, which is the longest time range, that could be obtained using the smallest number of 16 CPU cores.

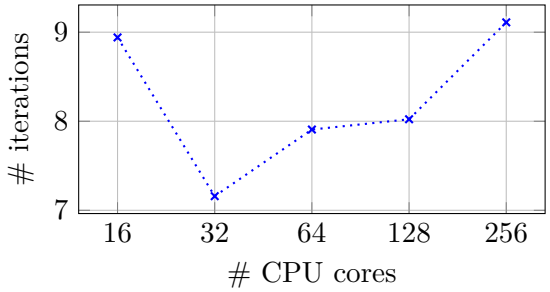

Figure 6.18: Average number of iterations of the linear solver in the Newton method for the aortic bow simulation. The result is plotted over the number of utilised CPU cores.

Figure 6.18 shows the average number of the linear solver until the necessary accuracy is gained for the respective step of the Newton method. As with the 2D case, there is only a marginal dependency of the number of iterations on the number of utilised CPU cores. With respect to the number of iterations of the linear solver a good parallel scalability can be concluded.

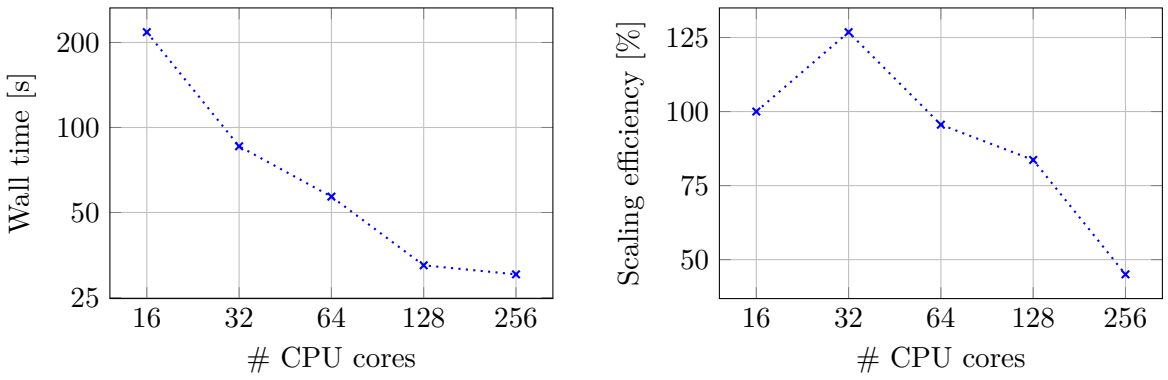

(a) Average wall time of the linear solver.

(b) Strong scaling efficiency of the linear solver based on the average wall time.

Figure 6.19: Evaluation of the computational costs and scalability of the problem-specific linear solver for FSI problems by means of the wall time. The results are plotted over the number of utilised CPU cores.

The computational costs in terms of wall time are shown for several numbers of utilised CPU cores in Figure 6.19a. Up to a number of 256 CPU cores, the wall time decreases with every duplication of the utilised CPUs. Figure 6.19b shows the strong scaling efficiency defined in equation (5.4). With respect to 16 cores, the efficiency using 256 cores is almost at

50 %, still. Like for the 2D case, the efficiency curve shows an exaggerated increase, in this case for 32 CPU cores. This can be explained likewise with the access time to the different memory-layers. With a higher parallelisation, the data per process, that has to be kept in the memory, gets less and it can be fully stored in the faster memory layers.

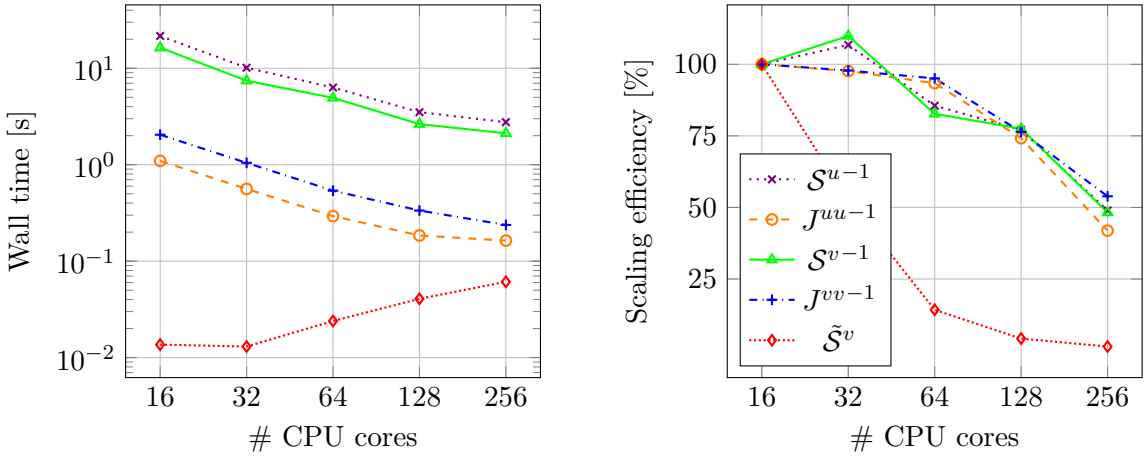

(a) Average wall time of the linear sub-solvers of the problem-specific preconditioner. The respective specified values for the relative decrease of the residual are given in Table 6.3.

(b) Strong scaling efficiency of the linear sub-solvers based on the average wall time.

Figure 6.20: Detailed evaluation of the computational costs and scalability of the sub-solvers of the problem-specific preconditioner (cf. Figure 4.5). The results are plotted over the number of utilised CPU cores.

The parallel scalability of the sub-solvers of the linear solver routine are shown in Figure 6.20. Up to 128 CPU cores, all of the sub-solvers except for $\tilde{\mathcal{S}}^v$ show a strong efficiency of over 75 %. The sub-solver for $\tilde{\mathcal{S}}^v$ carries no weight due to its small absolute time consumption. At a number of 256 cores, the first four sub-solvers have an efficiency of 50 % similarly to the full linear solver routine (cf. Figure 6.19b). The almost non-existent parallel scalability of the sub-solver for $\tilde{\mathcal{S}}^v$ is also comparable to the results of the 2D case.

6.2.3 Parameter evaluation

The computing time on the BwForCluster MLS&WISO Production for one of the 36 collocation points was about 48 hours on 256 CPUs, resulting in a total amount of computational costs for the UQ-simulation of two time periods of 4.42×10^5 core hours. The first time period is seen as start-up phase and for the second period, the evaluation and results are shown in the following. Firstly, the flowrate and pressure values are evaluated at the inflow and outflow boundaries. Then visualisations of the solution variables by means of the cross section as indicated in Figure 6.17 are given. Finally, the simulated stress parameters are shown.

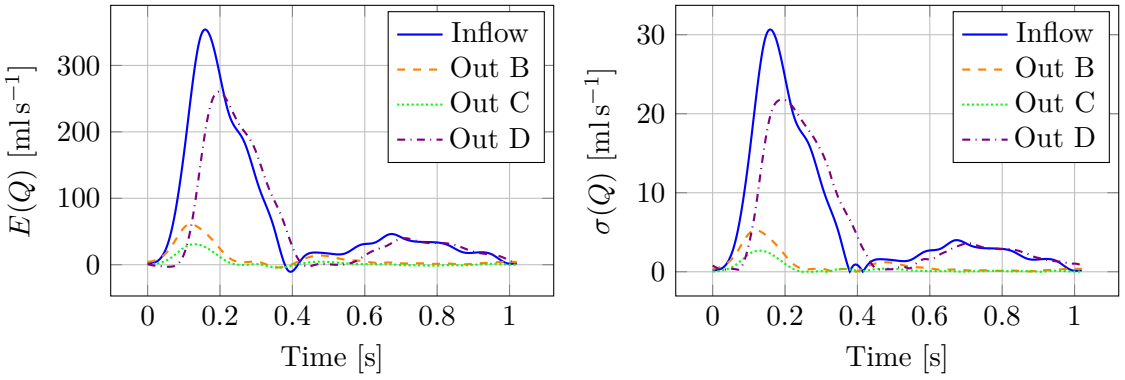

(a) Expected value of the flowrates.

(b) Standard deviation of the flowrates.

Figure 6.21: Evaluation of the flowrate at the inflow and outflow boundaries over one time period.

Flowrates and pressure at the inflow and outflow boundaries

The flowrate values $Q(t)$ shown in Figure 6.21 are computed by integration of the velocity directed through the inflow and outflow boundaries. The resulting expected values are shown in Figure 6.21a and the standard deviation is given in Figure 6.21b. For the inflow boundary, as well as the outflow boundaries B and C the mean value and the stochastical distribution are prescribed by the velocity boundary conditions. Only for the outflow D the values result from the dynamics of the simulation. In correspondence to the range of values for the uncertain flowrate factor (see Table 6.1), the standard deviation follows the expected value up to a constant scaling factor for the values fixed by the boundary condition. This is also roughly the case for the flowrate through the outflow D.

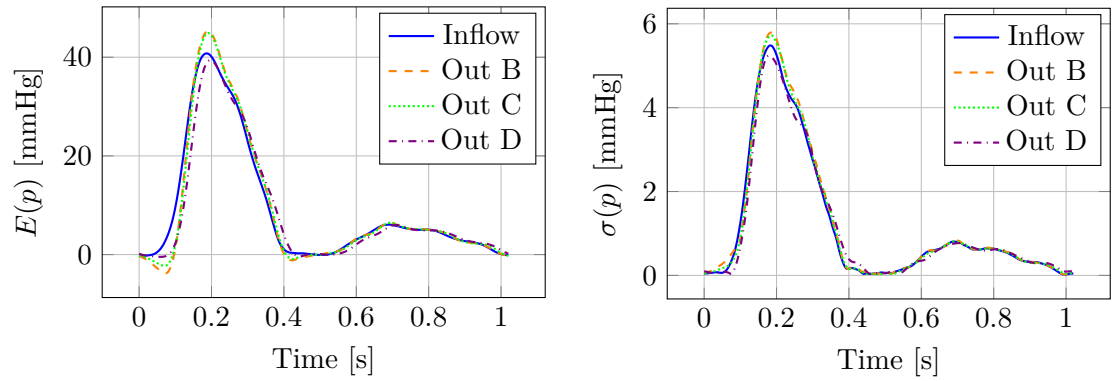

(a) Expected value of the pressure.

(b) Standard deviation of the pressure.

Figure 6.22: Evaluation of the pressure at the inflow and outflow boundaries over one time period.

Figure 6.22 shows pressure values $p(t)$ averaged over the inflow and outflow boundaries by means of the expected value and the standard deviation. The pressure is prescribed only

at the outflow D via the pressure boundary condition (3.30). For the other boundaries, the values result from the simulated dynamics over the whole domain. In the considered mathematical model, the pressure represents a relative value and has a reference level of $p = 0$. As opposed to that, the blood pressure level in the human cardiovascular system is about 80 mmHg higher on average. Much more important than the absolute pressure value is the difference between minimal and maximal pressure. In the simulation, the difference amounts to approximately 40 mmHg, which represents a physiologically very realistic value. As with the flowrates (Figure 6.21b), the standard deviation of the pressure also follows the expected value up to an almost constant scaling factor.

Visualisation by means of the cross sections

For the visualisations of the solution variables, the displacement, the velocity and the pressure fields, firstly, the mid-systolic point in time $t = 0.16\,\mathrm{s}$ with the highest flow at the inflow boundary is chosen. For another point in time $t = 0.66\,\mathrm{s}$ in the mid-diastole, further visualisations are given in the appendix in section 8.4.

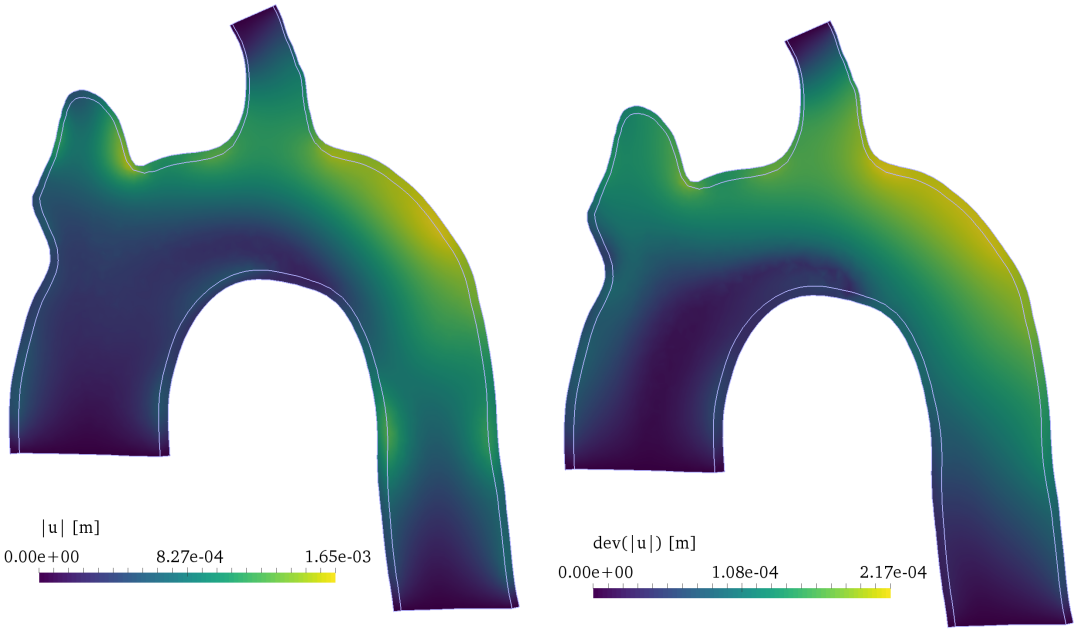

(a) Expected value of the displacement $E(|\boldsymbol{u}|)$.

(b) Standard deviation $\sigma(|\boldsymbol{u}|)$.

Figure 6.23: Visualisation of the displacement magnitude by means of the frontal cross sectional plane defined in Figure 6.17b in mid-systole at $t = 0.16\,\mathrm{s}$.

Figure 6.23 shows the magnitude of the displacement field by means of its expected value and the standard deviation. At the inflow and outflow boundaries, it can be seen, that the geometrical movement is fixed with a value of certainly zero for the displacement. This is one of the points at which the simulation can be further developed in the future by transferring the movement of the vessel visible in the MRI data to the displacement boundary conditions of the simulation. At the considered point in time, the displacement of the outer vessel wall

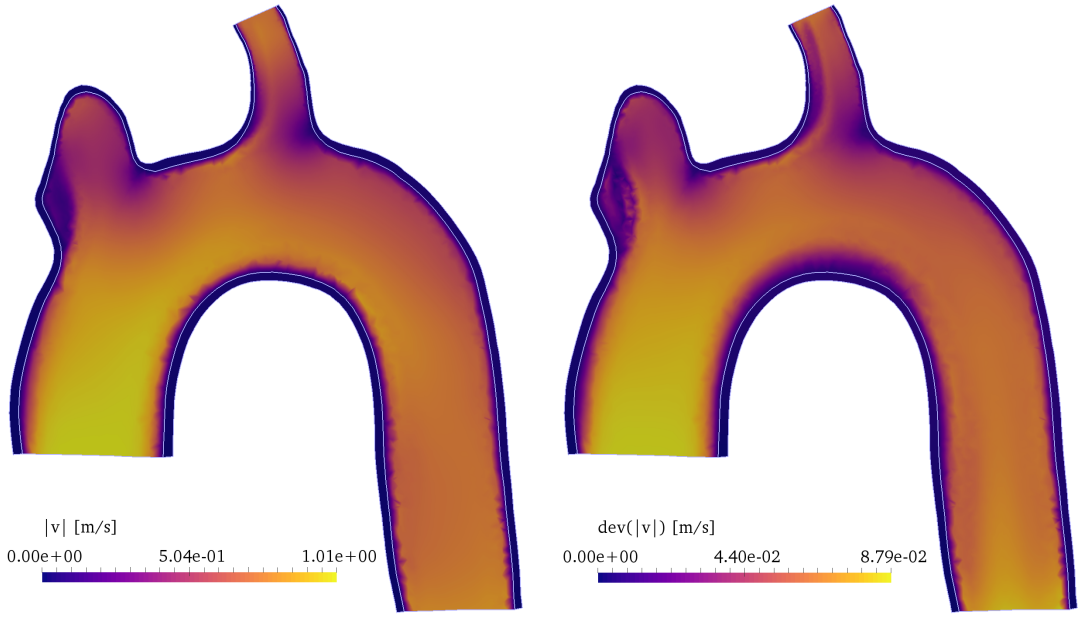

(a) Expected value of the velocity $E(|\boldsymbol{v}|)$. (b) Standard deviation $\sigma(|\boldsymbol{v}|)$.

Figure 6.24: Visualisation of the velocity magnitude by means of the frontal cross sectional plane defined in Figure 6.17b in mid-systole at $t = 0.16\,\mathrm{s}$.

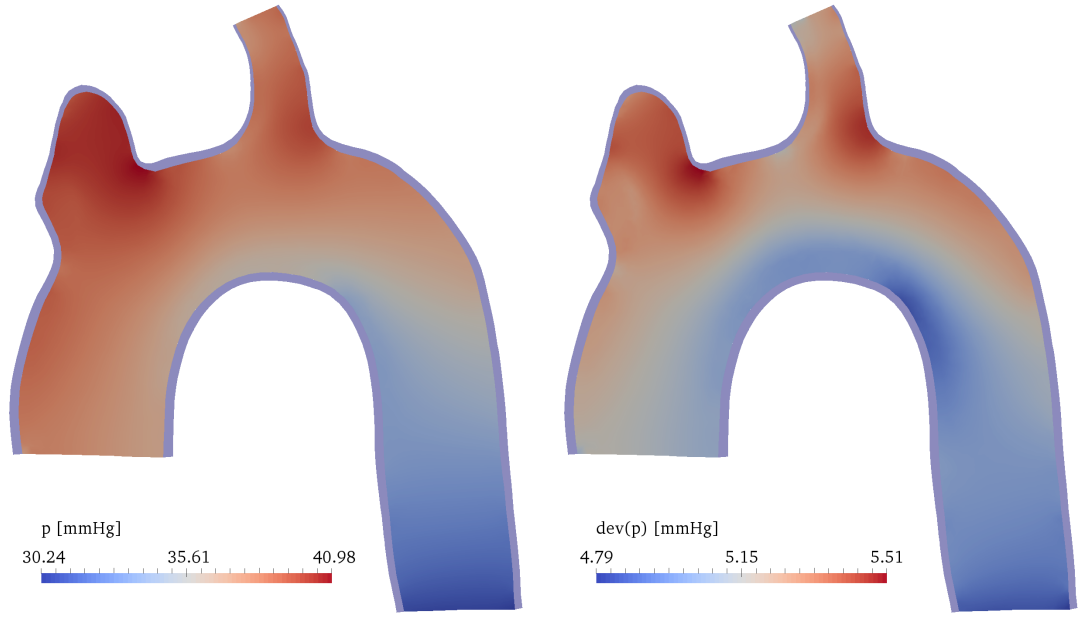

(a) Expected value of the pressure $E(p)$. (b) Standard deviation $\sigma(p)$.

Figure 6.25: Visualisation of the pressure by means of the frontal cross sectional plane defined in Figure 6.17b in mid-systole at $t = 0.16\,\mathrm{s}$.

is highest after the second bifurcation. In this region, also the standard deviation indicates a relatively high uncertainty.

The magnitude of the velocity field is shown in Figure 6.24. The expected value and the standard deviation is prescribed at the inflow and outflow B and C by the velocity boundary conditions. In the simulation, a mostly laminar flow develops from the inflow to the three outflow boundaries. At the illustrated point in time, the flow is strongest along the bow down to the descending aorta. The standard deviation is widely similar to the expected value up to a constant scaling factor, except for an increasing value towards the outflow D.

$t = 0.16\,\mathrm{s}$	L1	L2	L3	
$E(\lvert\boldsymbol{u}\rvert)$	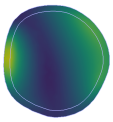	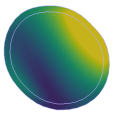	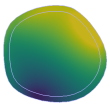	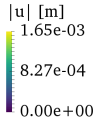
$\sigma(\lvert\boldsymbol{u}\rvert)$	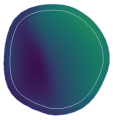	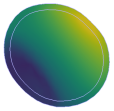		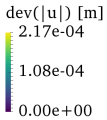
$E(\lvert\boldsymbol{v}\rvert)$	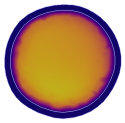	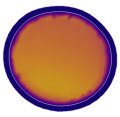	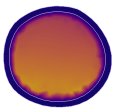	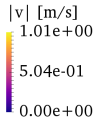
$\sigma(\lvert\boldsymbol{v}\rvert)$	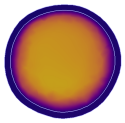	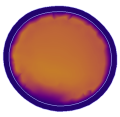	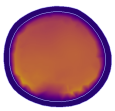	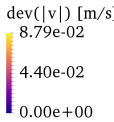
$E(p)$	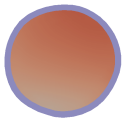	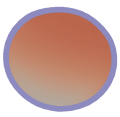		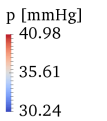
$\sigma(p)$		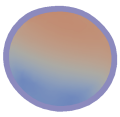		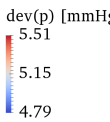

Table 6.5: Visualisation of the aortic bow simulation by means of the cross sectional levels defined in Figure 6.17 in mid-systole at $t = 0.16\,\mathrm{s}$. The orientation is such, that the bottom of the cross sections is oriented towards the arc center of the bow. The left side is in the back of Figure 6.17 and the right side of the cross sections is directed to the front.

Figure 6.25 shows the pressure field by means of its expected value and standard deviation. At the considered point in time, a pressure drop is visible from the inflow to the outflow D. The bifurcations develop pressure points at the backside of their entries. The standard deviation of the pressure shows only little variation over the frontal cross section. Nevertheless, the highest uncertainty by means of the standard deviation can be observed at the pressure points of the bifurcations.

Table 6.5 shows the development of the solution variables by means of the cross sectional levels L1, L2, and L3 indicated in Figure 6.17.

Visualisation of the stress measures

The wall shear stress as defined in equation (3.70) represents a measure for the force that the blood flow dynamics exert on the vessel wall. As described in section 3.6.1, the wall shear stress can have an effect on the structural development of the vessel wall. In Figure 6.26, a visualisation of the wall shear stress magnitude τ_{W} is given at the considered mid-systolic point in time $t = 0.16\,\mathrm{s}$. As the considered subject is a healthy human being, the absence of anomalies is expected. The figure shows a possibility to visualise the expected value and the standard deviation. It can be seen, that the expected value of the wall shear stress in the narrower branches is higher compared to the aorta. This comes from a steeper velocity gradient towards the vessel wall in the narrow parts of the branches. The standard deviation gives a measure of certainty of the expected value over the vessel's geometry. In this case, the standard deviation is widely similar to the expected value up to a constant scaling factor.

The second stress measure considered in this work is the von Mises stress τ_{M} within the vessel wall as it is defined in equation 3.71. The full volumetric FSI simulation considered in this work allows for an evaluation not only of the fluid stresses but also of the stress distribution within the vessel wall. Hereby, the von Mises stress for a non-complex solid material model, as it is described in section 3.3, can not serve as an absolute measure for the stress distribution in the complex human vessel wall structure. Nevertheless, it can serve as a comparative value between various subjects, for example groups of healthy and pathological cases. In Figure 6.27, the von Mises stress is shown over the fluid-structure interface from the inside of the aortic bow. In the appendix, another visualisation showing the outer surface is given in Figure 8.13. It can be seen, that the expected value of the von Mises stress has peak values at the first bifurcation. In this area, also a point of high pressure is observed (cf. Figure 6.25a) with a considerable displacement (cf. Figure 6.23a). The standard deviation is widely similar to the expected value up to a constant scaling factor.

For the considered stress measures of the wall shear stress and the von Mises stress, overload thresholds can possibly be determined in future clinical studies. Given a range of uncertainties in the input data for a simulation-based computation of the stress values, UQ enables the evaluation of the probability that a threshold value is exceeded for a specific subject. This overload probability, as it is introduced in this work in equation (3.72), is considered in the following for artificially chosen threshold values.

Figure 6.28 shows the probability, that the wall shear stress magnitude exceeds a value of 7 Pa at any point in the full time period. This threshold is surely exceeded in the narrow branches of the geometry, which is only naturally as explained in the description for Figure 6.26. In diseased cases, such as aortic stenosis or aortic aneurysms, a different result would possibly be obtained. For aneurysms, also a probability measure can be defined giving an information on whether all parts of the vessel wall undergo a minimal wall shear stress level, because a too low wall shear stress can also have an adverse effect. Both aspects are worthwhile to be considered in future work.

Figure 6.29 shows the probability, that the von Mises stress exceeds a value of $1 \times 10^5\,\mathrm{Pa}$ at any point in the full time period. This threshold is surely exceeded at the entrance areas of the bifurcating branches of the geometry. Comparing the visualisation to Figure 6.27c, these

areas coincide with the areas of high expected von Mises stress only for the first bifurcation. The benefit of the representation by the proposed probability definition (3.72) lies in the consideration of all time steps. With that, the overload probability over the full time period can be shown in a single image. It would be worthwhile to investigate the possibilities applying the overload probability evaluation to a range of diseased cases in a future work and to compare the differences between groups of pathological cases.

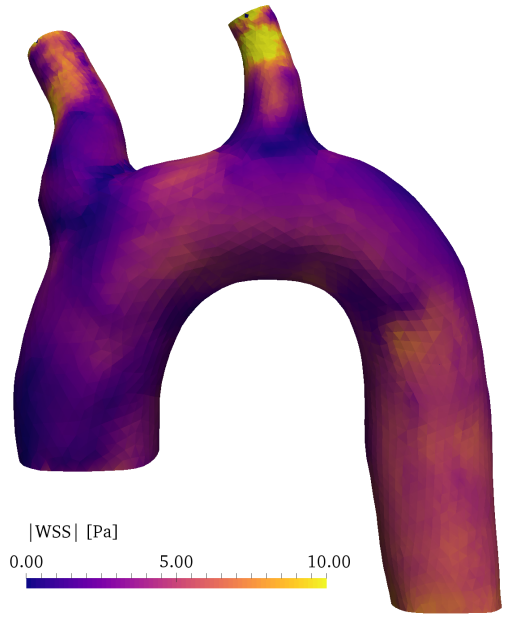

(a) Expected value $E(\tau_W)$, front view.

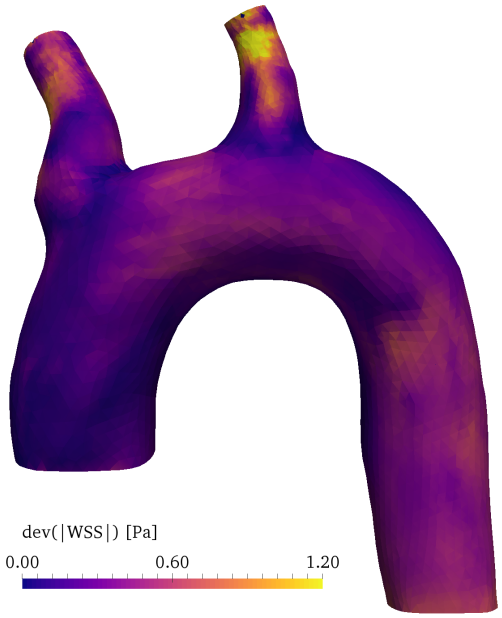

(b) Standard deviation $\sigma(\tau_W)$, front view.

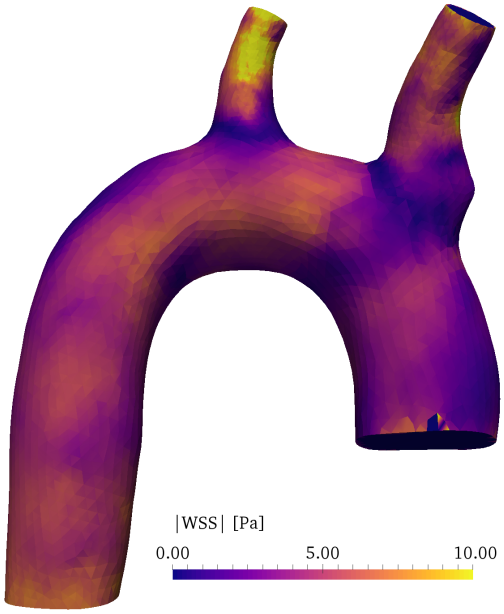

(c) Expected value $E(\tau_W)$, back view.

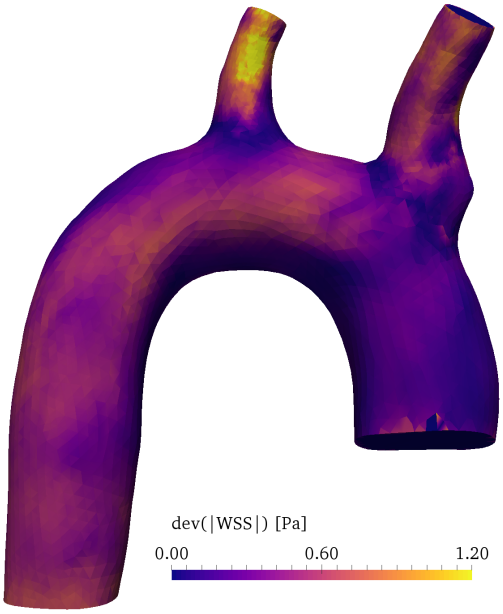

(d) Standard deviation $\sigma(\tau_W)$, back view.

Figure 6.26: Visualisation of the wall shear stress magnitude on the outside of the fluid-structure interface in mid-systole at $t = 0.16\,\mathrm{s}$.

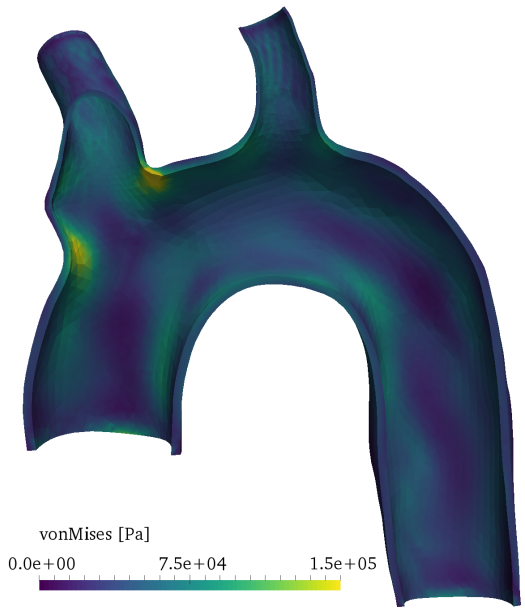

(a) Expected value $E(\tau_{\mathrm{M}})$, front view.

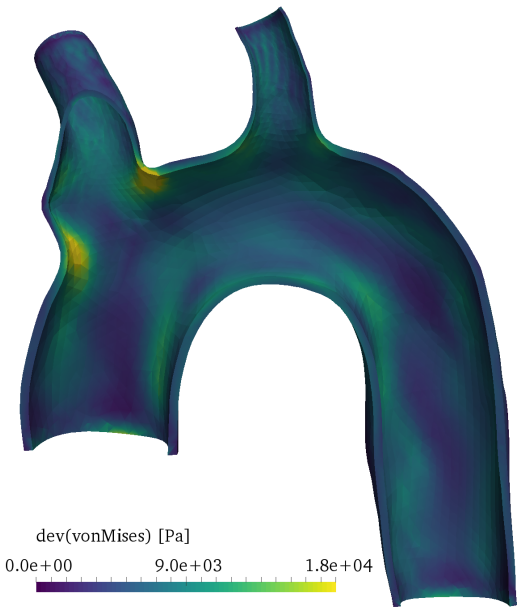

(b) Standard deviation $\sigma(\tau_{\mathrm{M}})$, front view.

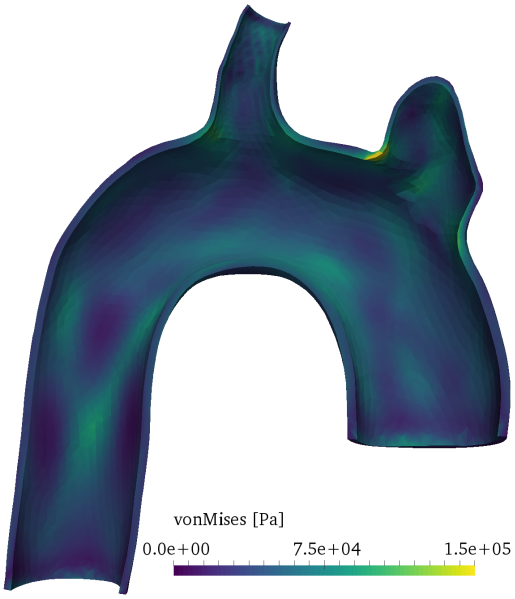

(c) Expected value $E(\tau_{\mathrm{M}})$, back view.

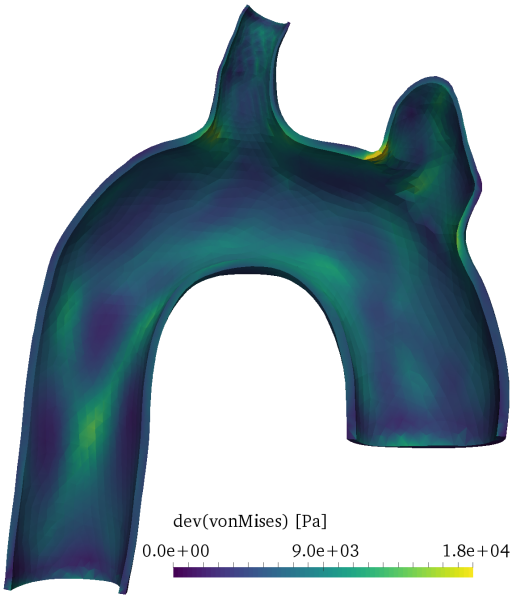

(d) Standard deviation $\sigma(\tau_{\mathrm{M}})$, back view.

Figure 6.27: Visualisation of the von Mises stress on the inside of the fluid-structure interface in mid-systole at $t = 0.16\,\mathrm{s}$.

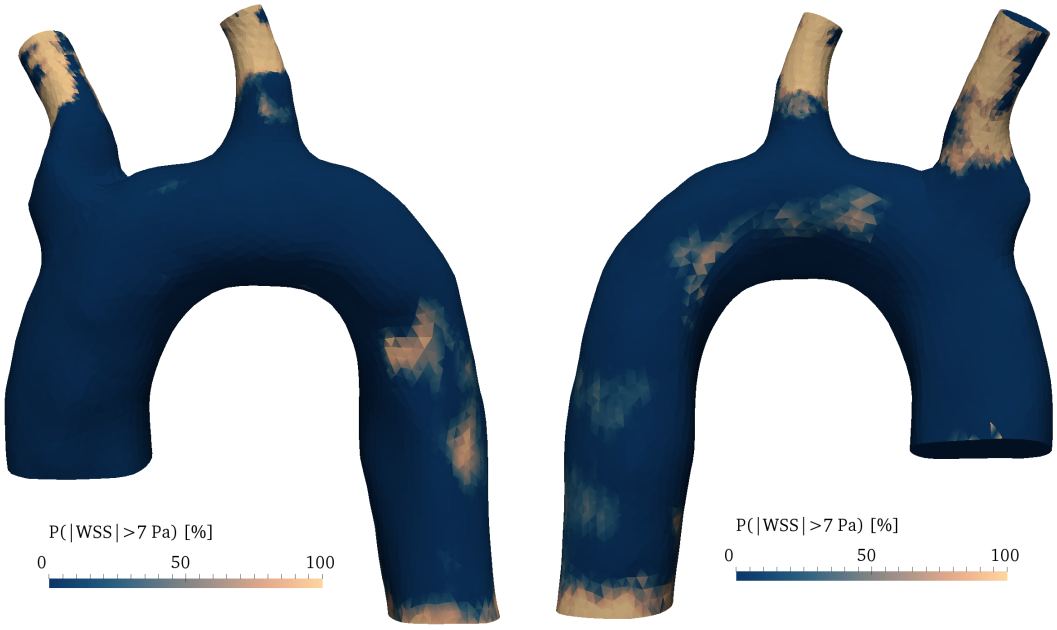

(a) Front view. (b) Back view.

Figure 6.28: Visualisation of the wall shear stress overload probability $P^{\tau_{\mathrm{W}},\max}$ on the outside of the fluid-structure interface.

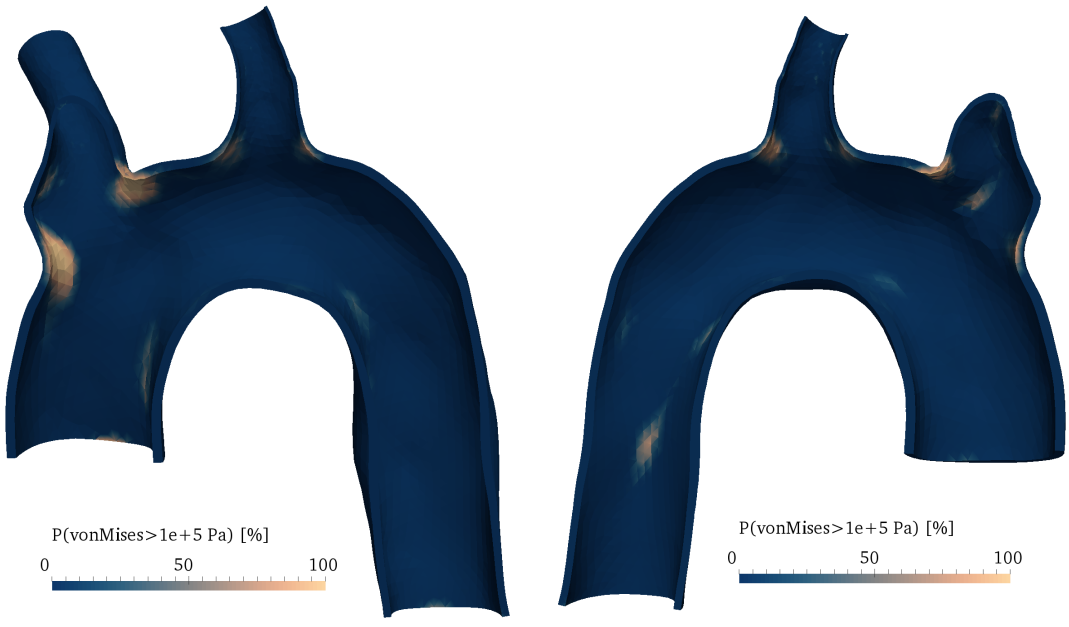

(a) Front view. (b) Back view.

Figure 6.29: Visualisation of the von Mises stress overload probability $P^{\tau_{\mathrm{M}},\max}$ on the inside of the fluid-structure interface.

7 Conclusion

The present work investigates and develops UQ methods for the further development of the simulation of fluid-structure interaction problems. The biomechanics of aortic blood flow are considered as a motivation and application field.

This work begins with an overview on the cardiovascular system in general and on the physiology and pathology of the aorta in particular. There are a number of open questions related to the understanding of the physiology and the development of diseases of the aorta. Even though advanced technology is available for the investigation of the aortic physiology, the possibilities of non-invasive examination methods of a living patient, in vivo, remain limited. In microscopic detail, soft tissue structures can usually be examined post mortem, only. These samples then already have an altered, non-living state. For a better understanding of the biomechanical dynamics, artificial (in vitro) experiments can emulate the physiology up to a certain level of the reality. With the capabilities of mathematical modelling and numerical simulation of the biomechanical dynamics, in silico, a third column of investigation possibilities can be considered. For this, the foundations of the mathematical modelling of blood flow and deformation of the aortic wall are described in this work. They lead to the definition of the complex class of fluid-structure interaction problems.

To date, for numerical simulations of the physiologic and biomechanical dynamics in the cardiovascular system mainly deterministic models have been used. However, the dynamics are often subject to not to be underestimated uncertainties. As an example, the elastic structure of the aortic vessel wall is highly uncertain for each individual patient. This applies all the more for diseased soft tissue. But also measurable quantities, such as the blood flow speed in a considered vessel underlie measurement inaccuracies. This work illustrates how these uncertainties can be incorporated and propagated in a numerical simulation with methods of uncertainty quantification. The simulation results can then be stochastically evaluated. An information on the stochastical distribution of the results is especially important if potential risk parameters are considered, such as stress values at and within the vessel wall.

Furthermore, this work presents a workflow for the application of the simulation specifically to an individual patient. The workflow starts with MRI and flow MRI data. It generates an individually adapted FEM mesh with specifically configured boundary conditions for the simulation. This work continuous with the description of a problem-specific solver with appropriate discretisation schemes for a numerical solvability of the complex mathematical problem. In particular, two different UQ methods based on the polynomial chaos expansion are described for the application to the FSI problem. On the one hand, for a simplified formulation of the FSI equations, an intrusive UQ method can be used, which allows for the usage of efficient monolithical solvers for the UQ problem. On the other hand, a collocation

method is described, for which an existing solver for the deterministic FSI problem can be used. Furthermore, a novel linear solver specifically for FSI problems is proposed based on the Schur complement method.

For the testing and verification of the developed methods, a range of numerical benchmarking experiments is carried out. At first, the results of a standard deterministic benchmark for fluid-structure interaction are reproduced by the simulation framework implemented in this work. Also, by means of the 2D benchmark, the parallel scalability of the novel problem specific linear solver is examined. Additionally, this work presents a novel definition of an analytically solvable benchmark problem for FSI problems with uncertain parameters. The analytical solution is derived for the 2D problem and the numerical convergence behaviour of the considered intrusive solver is evaluated.

Finally, the framework developed in this work for the subject-specific numerical simulation of aortic biomechanics is applied to a prototypic aortic phantom experiment and a human aortic bow. Hereby, the mathematical modelling is geared for the phantom experiment with a configuration for the fluid and vessel wall material employed in the artificial phantom vessel. The validation of the numerical simulation by means of the phantom experiment shows very good results. By means of the application of the framework to the human aortic bow, the linear solver is tested again in 3D with respect to its parallel scalability. Several visualisation possibilities are presented for the results of the UQ simulation of the aortic bow. Last but not least, the overstress probability parameters newly presented in this work for the assessment of the aortic biomechanics are evaluated.

For possible future work in this highly interesting field of research, there are a range of open research questions.

There is vivid ongoing research in refining the mathematical modelling towards a more and more realistic imitation of the biomechanics of human soft tissue and the physiology of blood flow. A particular challenge is given by the connection of cellular models on a microscopic scale to the macroscopic continuum mechanics. The presented numerical simulation framework is open for extensions towards more complex and realistic material models.

Along with the consideration of detailed material models, the modelling of the uncertainty influence factors can also be refined. Particularly, an inhomogeneous geometrical distribution of the uncertainty can be considered in many cases, which increases both the complexity and the dimension of the UQ problem. Since the computational costs can rapidly increase in the quantification of uncertainties, it is worthwhile to investigate the possibilities of model reduction for both the deterministic counterpart of a model as well as the stochastic formulation.

The possibilities of the configuration of the simulation by means of the flow MRI measurements have not yet been fully exhausted. The flow field measurements are used for the respective boundary conditions. But future work can include the entanglement of the simulation and the velocity data from a 4D flow MRI on the full domain by means of data assimilation. This way, the simulation can be seen as a direct enhancement of the MRI measurement with additional information coming from the simulation model. Conversely, the simulation results become more realistically aligned to the measurements.

In the application to a range of pathological cases, the potential of the presented framework can be investigated. The proposed parameters of the overstress probabilities can be evaluated with respect to their significance and eventually new risk parameters can be defined in the assessment of diseased aortic geometries.

Bibliography

[1] Götz Alefeld, Ingrid Lenhardt, and Holger Obermaier. *Parallele numerische Verfahren*. Springer-Verlag Berlin Heidelberg, 2002.

[2] Luca Antiga, Joaquim Peiró, and David A. Steinman. From image data to computational domains. *Cardiovascular Mathematics*, pages 123–175, 2009.

[3] Luca Antiga, Marina Piccinelli, Lorenzo Botti, Bogdan Ene-Iordache, Andrea Remuzzi, and David A Steinman. An image-based modeling framework for patient-specific computational hemodynamics. *Medical & biological engineering & computing*, 46(11):1097, 2008.

[4] Pedro Aparício, Mark S. Thompson, and Paul N. Watton. A novel chemo-mechano-biological model of arterial tissue growth and remodelling. *Journal of biomechanics*, 49(12):2321–2330, 2016.

[5] Richard Askey and James Wilson. *Some basic hypergeometric orthogonal polynomials that generalize Jacobi polynomials*. Number 319 in Memoirs of the American Mathematical Society. American Mathematical Society, 1985.

[6] Utkarsh Ayachit. *The ParaView Guide: A Parallel Visualization Application*. Kitware, Inc., USA, 2015.

[7] Andrew T. Barker and Xiao-Chuan Cai. Scalable parallel methods for monolithic coupling in fluid–structure interaction with application to blood flow modeling. *Journal of computational physics*, 229(3):642–659, 2010.

[8] Klaus-Jürgen Bathe. The inf–sup condition and its evaluation for mixed finite element methods. *Computers & Structures*, 79(2):243–252, 2001.

[9] Klaus-Jürgen Bathe. *Finite element procedures*. Klaus-Jürgen Bathe, 2006.

[10] Klaus-Jürgen Bathe and Gustavo A. Ledezma. Benchmark problems for incompressible fluid flows with structural interactions. *Computers & structures*, 85(11):628–644, 2007.

[11] Jonas Biehler, Michael W. Gee, and Wolfgang A. Wall. Towards efficient uncertainty quantification in complex and large-scale biomechanical problems based on a bayesian multi-fidelity scheme. *Biomechanics and modeling in mechanobiology*, 14(3):489–513, 2015.

[12] P.J. Blanco, R.A. Feijóo, and E.A. Dari. A variational framework for fluid–solid interaction problems based on immersed domains: Theoretical bases. *Computer Methods in Applied Mechanics and Engineering*, 197(25):2353–2371, 2008.

[13] Dietrich Braess. *Finite Elemente: Theorie, schnelle Löser und Anwendungen in der Elastizitätstheorie*. Springer-Verlag, 5th edition, 2013.

[14] Alexander N. Brooks and Thomas J. R. Hughes. Streamline upwind/petrov-galerkin formulations for convection dominated flows with particular emphasis on the incompressible navier-stokes equations. *Computer methods in applied mechanics and engineering*, 32(1):199–259, 1982.

[15] Martin Büsen, Tim A. S. Kaufmann, Michael Neidlin, Ulrich Steinseifer, and Simon J. Sonntag. In vitro flow investigations in the aortic arch during cardiopulmonary bypass with stereo-piv. *Journal of biomechanics*, 48(10):2005–2011, 2015.

[16] C. G. Caro, T. J. Pedley, R. C. Schroter, and W. A. Seed. *The mechanics of the circulation*. Cambridge University Press, 2nd edition, 2012.

[17] Peng Chen, Alfio Quarteroni, and Gianluigi Rozza. Simulation-based uncertainty quantification of human arterial network hemodynamics. *International journal for numerical methods in biomedical engineering*, 29(6):698–721, 2013.

[18] Bongjae Chung and Juan Raul Cebral. Cfd for evaluation and treatment planning of aneurysms: review of proposed clinical uses and their challenges. *Annals of biomedical engineering*, 43(1):122–138, 2015.

[19] K. Andrew Cliffe, Mike B. Giles, Robert Scheichl, and Aretha L. Teckentrup. Multilevel monte carlo methods and applications to elliptic pdes with random coefficients. *Computing and Visualization in Science*, 14(1):3, 2011.

[20] Wikimedia Commons. File:aorta scheme en.svg — wikimedia commons, the free media repository, 2016. `https://commons.wikimedia.org/w/index.php?title=File:Aorta_scheme_en.svg&oldid=215165373` [Online; accessed 3-April-2018].

[21] Wikimedia Commons. File:diagram of the human heart (cropped).svg — wikimedia commons, the free media repository, 2016. `https://commons.wikimedia.org/w/index.php?title=File:Diagram_of_the_human_heart_(cropped).svg&oldid=194599161` [Online; accessed 3-April-2018].

[22] Wikimedia Commons. File:gray506.svg — wikimedia commons, the free media repository, 2017. `https://commons.wikimedia.org/w/index.php?title=File:Gray506.svg&oldid=259192911` [Online; accessed 3-April-2018].

[23] Wikimedia Commons. File:wiggers diagram 2.svg — wikimedia commons, the free media repository, 2017. `https://commons.wikimedia.org/w/index.php?title=File:Wiggers_Diagram_2.svg&oldid=262202428` [Online; accessed 3-April-2018].

[24] Wikimedia Commons. File:blausen 0055 arterywallstructure.png — wikimedia commons, the free media repository, 2018. `https://commons.wikimedia.org/w/index.php?title=File:Blausen_0055_ArteryWallStructure.png&oldid=284404447` [Online; accessed 3-April-2018].

[25] Wikimedia Commons. File:circulatory system en.svg — wikimedia commons, the free media repository, 2018. `https://commons.wikimedia.org/w/index.php?title=File:Circulatory_System_en.svg&oldid=288998459` [Online; accessed 3-April-2018].

[26] Wikipedia contributors. Del in cylindrical and spherical coordinates — wikipedia, the free encyclopedia, 2018. `https://en.wikipedia.org/w/index.php?title=Del_in_cylindrical_and_spherical_coordinates&oldid=827585607` [Online; accessed 23-March-2018].

[27] Daniel Coutand and Steve Shkoller. Motion of an elastic solid inside an incompressible viscous fluid. *Archive for rational mechanics and analysis*, 176(1):25–102, 2005.

[28] Daniel Coutand and Steve Shkoller. The interaction between quasilinear elastodynamics and the navier-stokes equations. *Archive for rational mechanics and analysis*, 179(3):303–352, 2006.

[29] Paolo Crosetto, Simone Deparis, Gilles Fourestey, and Alfio Quarteroni. Parallel algorithms for fluid-structure interaction problems in haemodynamics. *SIAM Journal on Scientific Computing*, 33(4):1598–1622, 2011.

[30] Anirudh R. Damughatla, Brian Raterman, Travis Sharkey-Toppen, Ning Jin, Orlando P. Simonetti, Richard D. White, and Arunark Kolipaka. Quantification of aortic stiffness using mr elastography and its comparison to mri-based pulse wave velocity. *Journal of Magnetic Resonance Imaging*, 41(1):44–51, 2015.

[31] Michael Delles, Fabian Rengier, Sebastian Ley, Hendrik von Tengg-Kobligk, Hans-Ulrich Kauczor, Roland Unterhinninghofen, and Rüdiger Dillmann. Influence of imaging quality on magnetic resonance-based pressure gradient measurements. In *Proc. SPIE 7626, Medical Imaging 2010: Biomedical Applications in Molecular, Structural, and Functional Imaging*, page 762624. Society of Photo-Optical Instrumentation Engineers, 2010.

[32] Simone Deparis, Davide Forti, Gwenol Grandperrin, and Alfio Quarteroni. Facsi: A block parallel preconditioner for fluid–structure interaction in hemodynamics. *Journal of Computational Physics*, 327:700–718, 2016.

[33] Simone Deparis, Gwenol Grandperrin, and Alfio Quarteroni. Parallel preconditioners for the unsteady navier–stokes equations and applications to hemodynamics simulations. *Computers & Fluids*, 92:253–273, 2014.

[34] Peter Deuflhard and Folkmar Bornemann. *Numerische Mathematik 2: Gewöhnlicher Differentialgleichungen*. De Gruyter Studium. Walter de Gruyter, Berlin/Boston, 4th edition, 2013.

[35] Andrea Ducci, Francesco Pirisi, Spyridon Tzamtzis, and Gaetano Burriesci. Transcatheter aortic valves produce unphysiological flows which may contribute to thromboembolic events: An in-vitro study. *Journal of Biomechanics*, 49(16):4080–4089, 2016.

[36] Thomas Dunne and Rolf Rannacher. Adaptive finite element approximation of fluid-structure interaction based on an eulerian variational formulation. In *Fluid-structure interaction*, pages 110–145. Springer, 2006.

[37] Petter Dyverfeldt, Malenka Bissell, Alex J. Barker, Ann F. Bolger, Carl-Johan Carlhäll, Tino Ebbers, Christopher J. Francios, Alex Frydrychowicz, Julia Geiger, Daniel Giese, Michael D. Hope, Philip J. Kilner, Sebastian Kozerke, Saul Myerson, Stefan Neubauer, Oliver Wieben, and Michael Markl. 4d flow cardiovascular magnetic resonance consensus statement. *Journal of Cardiovascular Magnetic Resonance*, 17(1):72, 2015.

[38] Raimund Erbel, Victor Aboyans, Catherine Boileau, Eduardo Bossone, Roberto Di Bartolomeo, Holger Eggebrecht, Arturo Evangelista, Volkmar Falk, Herbert Frank, Oliver Gaemperli, Martin Grabenwöger, Axel Haverich, Bernard Iung, Athanasios John Manolis, Folkert Meijboom, Christoph A. Nienaber, Marco Roffi, Hervé Rousseau, Udo Sechtem, Per Anton Sirnes, Regula S. von Allmen, Christiaan J.M. Vrints, and ESC Committee for Practice Guidelines. 2014 esc guidelines on the diagnosis and treatment of aortic diseases. *European heart journal*, 35(41):2873–2926, 2014.

[39] C. Ross Ethier and D. A. Steinman. Exact fully 3d navier–stokes solutions for benchmarking. *International Journal for Numerical Methods in Fluids*, 19(5):369–375, 1994.

[40] Lawrence C. Evans. *Partial differential equations*, volume 19 of *Graduate Studies in Mathematics*. American Mathematical Society, 2nd edition, 2010.

[41] Robert D. Falgout and Ulrike Meier Yang. hypre: A library of high performance preconditioners. In Peter M. A. Sloot, Alfons G. Hoekstra, C. J. Kenneth Tan, and Jack J. Dongarra, editors, *Computational Science — ICCS 2002*, pages 632–641. Springer Berlin Heidelberg, 2002.

[42] Jonathan Feinberg and Hans Petter Langtangen. Chaospy: An open source tool for designing methods of uncertainty quantification. *Journal of Computational Science*, 11:46–57, 2015.

[43] Miguel Ángel Fernández and Marwan Moubachir. A newton method using exact jacobians for solving fluid–structure coupling. *Computers & Structures*, 83(2-3):127–142, 2005.

[44] Institute for Health Metrics and Evaluation (IHME). Gbd compare data visualization, 2016. Seattle, WA: IHME, University of Washington. `https://vizhub.healthdata.org/gbd-compare/` [Online; accessed 6-June-2018].

[45] Luca Formaggia, Alfio Quarteroni, and Alessandro Veneziani, editors. *Cardiovascular Mathematics: Modeling and simulation of the circulatory system*. Springer-Verlag Italia, Milano, 2009.

[46] Message Passing Interface Forum. *MPI: A Message-Passing Interface Standard, Version 3.0*. University of Tennessee, Knoxville, TN, USA, 2012.

[47] Jonathan B. Freund. Numerical simulation of flowing blood cells. *Annual review of fluid mechanics*, 46:67–95, 2014.

[48] Roland W. Freund and Ronald H.W. Hoppe. *Stoer/Bulirsch: Numerische Mathematik 1*. Springer-Verlag Berlin Heidelberg, 10th edition, 2007.

[49] Yuan-Cheng Fung. *Biomechanics: mechanical properties of living tissues*. Springer Science & Business Media New York, 2nd edition, 1993.

[50] Yuan-Cheng Fung. *Biomechanics: circulation*. Springer Science & Business Media New York, 2nd edition, 1997.

[51] Giovanni P. Galdi and Rolf Rannacher, editors. *Fundamental Trends in Fluid-structure Interaction*, volume 1 of *Contemporary Challenges in Mathematical Fluid Dynamics and Its Applications*. World Scientific Publishing, 2010.

[52] Giovanni P. Galdi, Rolf Rannacher, Anne M. Robertson, and Stefan Turek, editors. *Hemodynamical Flows : Modeling, Analysis and Simulation*, volume 37 of *Oberwolfach Seminars*. Birkhäuser Basel, 2008.

[53] T. Christian Gasser, Ray W. Ogden, and Gerhard A. Holzapfel. Hyperelastic modelling of arterial layers with distributed collagen fibre orientations. *Journal of the royal society interface*, 3(6):15–35, 2006.

[54] Simon Gawlok, Philipp Gerstner, Saskia Haupt, Vincent Heuveline, Jonas Kratzke, Philipp Lösel, Katrin Mang, Mareike Schmidtobreick, Nicolai Schoch, Nils Schween, Jonathan Schwegler, Chen Song, and Martin Wlotzka. Hiflow3 – technical report on release 2.0. *Preprint Series of the Engineering Mathematics and Computing Lab*, (06), 2017.

[55] Michael W. Gee, Ulrich Küttler, and Wolfgang A. Wall. Truly monolithic algebraic multigrid for fluid–structure interaction. *International Journal for Numerical Methods in Engineering*, 85(8):987–1016, 2011.

[56] Christophe Geuzaine and Jean-François Remacle. Gmsh: A 3-d finite element mesh generator with built-in pre-and post-processing facilities. *International journal for numerical methods in engineering*, 79(11):1309–1331, 2009.

[57] Roger G. Ghanem and Pol D. Spanos. *Stochastic finite elements: a spectral approach*. Dover Publications, Mineola, New York, revised edition, 2003.

[58] Daniel T. Ginat and Rajiv Gupta. Advances in computed tomography imaging technology. *Annual review of biomedical engineering*, 16:431–453, 2014.

[59] Vivette Girault and Pierre-Arnaud Raviart. *Finite element methods for Navier-Stokes equations: Theory and Algorithms*, volume 5 of *Springer series in computational mathematics*. Springer-Verlag Berlin Heidelberg, 1986.

[60] Roland Glowinski, Tsorng-Whay Pan, and Jacques Periaux. A lagrange multiplier/fictitious domain method for the dirichlet problem — generalization to some flow problems. *Japan Journal of Industrial and Applied Mathematics*, 12(1):87–108, 1995.

[61] Gene H. Golub and Charles F. Van Loan. *Matrix computations*. Johns Hopkins University Press, Baltimore, 4th edition, 2013.

[62] J. De Hart, G. W. M. Peters, P. J. G. Schreurs, and F. P. T. Baaijens. A two-dimensional fluid–structure interaction model of the aortic value. *Journal of Biomechanics*, 33(9):1079–1088, 2000.

[63] J. De Hart, G. W. M. Peters, P. J. G. Schreurs, and F. P. T. Baaijens. A three-dimensional computational analysis of fluid–structure interaction in the aortic valve. *Journal of Biomechanics*, 36(1):103–112, 2003.

[64] Van Emden Henson and Ulrike Meier Yang. Boomeramg: a parallel algebraic multigrid solver and preconditioner. *Applied Numerical Mathematics*, 41(1):155–177, 2002.

[65] John G. Heywood and Rolf Rannacher. Finite-element approximation of the nonstationary navier–stokes problem. part iv: Error analysis for second-order time discretization. *SIAM Journal on Numerical Analysis*, 27(2):353–384, 1990.

[66] Loren F. Hiratzka, George L. Bakris, Joshua A. Beckman, Robert M. Bersin, Vincent F. Carr, Donald E. Casey Jr, Kim A. Eagle, Luke K. Hermann, Eric M. Isselbacher, Ella A. Kazerooni, Nicholas T. Kouchoukos, Bruce W. Lytle, Dianna M. Milewicz, David L. Reich, Souvik Sen, Julie A. Shinn, Lars G. Svensson, and David M. Williams. 2010 accf/aha/aats/acr/asa/sca/scai/sir/sts/svm guidelines for the diagnosis and management of patients with thoracic aortic disease. *Journal of the American College of Cardiology*, 55(14):e27–e129, 2010.

[67] Gerhard A. Holzapfel. *Nonlinear Solid Mechanics: A Continuum Approach for Engineering*. John Wiley & Sons, 2000.

[68] Gerhard A. Holzapfel. Determination of material models for arterial walls from uniaxial extension tests and histological structure. *Journal of Theoretical Biology*, 238(2):290–302, 2006.

[69] Gerhard A. Holzapfel. Microstructure and mechanics of human aortas in health and disease. In *Biomechanics: Trends in Modeling and Simulation*, pages 157–192. Springer International Publishing, 2017.

[70] Gerhard A. Holzapfel, Thomas C. Gasser, and Ray W. Ogden. A new constitutive framework for arterial wall mechanics and a comparative study of material models. *Journal of elasticity and the physical science of solids*, 61:1–48, 2000.

[71] Gerhard A. Holzapfel and Ray W. Ogden, editors. *Biomechanics of soft tissue in cardiovascular systems*. Number 441 in CISM courses and lectures. Springer-Verlag Wien New York, 2003.

[72] Gene Hou, Jin Wang, and Anita Layton. Numerical methods for fluid-structure interaction—a review. *Communications in Computational Physics*, 12(2):337–377, 2012.

[73] Jaroslav Hron and Stefan Turek. A monolithic fem/multigrid solver for an ale formulation of fluid-structure interaction with applications in biomechanics. In Hans-Joachim Bungartz and Michael Schäfer, editors, *Fluid-structure interaction*, pages 146–170. Springer Berlin Heidelberg, 2006.

[74] Jay D. Humphrey. Mechanics of the arterial wall: review and directions. *Critical reviews in biomedical engineering*, 23(1-2):1–162, 1994.

[75] Yohsuke Imai, Toshihiro Omori, Yuji Shimogonya, Takami Yamaguchi, and Takuji Ishikawa. Numerical methods for simulating blood flow at macro, micro, and multi scales. *Journal of biomechanics*, 49(11):2221–2228, 2016.

[76] Fabio Inzoli, Federica Boschetti, Mario Zappa, Tito Longo, and Roberto Fumero. Biomechanical factors in abdominal aortic aneurysm rupture. *European journal of vascular surgery*, 7(6):667–674, 1993.

[77] F. James. Monte carlo theory and practice. *Reports on Progress in Physics*, 43(9):1145, 1980.

[78] João Janela, Alexandra Moura, and Adélia Sequeira. Absorbing boundary conditions for a 3d non-newtonian fluid–structure interaction model for blood flow in arteries. *International Journal of Engineering Science*, 48(11):1332–1349, 2010.

[79] Bärbel Janssen and Thomas Wick. Block preconditioning with schur complements for monolithic fluid-structure interactions. In *ECCOMAS CFD*, 2010.

[80] Peter Knabner and Lutz Angermann. *Numerik partieller Differentialgleichungen: Eine anwendungsorientierte Einführung*. Springer-Verlag Berlin Heidelberg, 2000.

[81] Jonas Kratzke and Vincent Heuveline. An analytically solvable benchmark problem for fluid-structure interaction with uncertain parameters. *Preprint Series of the Engineering Mathematics and Computing Lab*, (2), 2016.

[82] Jonas Kratzke and Vincent Heuveline. Hpc-based uncertainty quantification for fluid-structure coupling in medical engineering. In *Proceedings of the 4th bwHPC Symposium*. Eberhard Karls Universität Tübingen, Germany, 2017. [in print].

[83] Jonas Kratzke, Fabian Rengier, Christian Weis, Carsten J. Beller, and Vincent Heuveline. In vitro flow assessment: From pc-mri to computational fluid dynamics including fluid-structure interaction. In *Proc. SPIE 9783, Medical Imaging 2016: Physics of Medical Imaging*, page 97835C. Society of Photo-Optical Instrumentation Engineers, 2016.

[84] Jonas Kratzke, Michael Schick, and Vincent Heuveline. Fluid-structure interaction simulation of an aortic phantom with uncertain young's modulus using the polynomial chaos expansion. In Peter F. Pelz and Peter Groche, editors, *Applied Mechanics and Materials*, volume 807, pages 34–44. Trans Tech Publications, 2015.

[85] Timm Krüger, Halim Kusumaatmaja, Alexandr Kuzmin, Orest Shardt, Goncalo Silva, and Erlend Magnus Viggen. *The Lattice Boltzmann Method: Principles and Practice*. Springer International Publishing, 2017.

[86] Ethan O. Kung, Andrea S. Les, C. Alberto Figueroa, Francisco Medina, Karina Arcaute, Ryan B. Wicker, Michael V. McConnell, and Charles A. Taylor. In vitro validation of finite element analysis of blood flow in deformable models. *Annals of biomedical engineering*, 39(7):1947–1960, 2011.

[87] Olivier P. Le Maître and Omar M. Knio. *Spectral methods for uncertainty quantification: with applications to computational fluid dynamics*. Springer Dordrecht Heidelberg London New York, 2010.

[88] Randall J. LeVeque. *Finite Difference Methods for Ordinary and Partial Differential Equations*. Society for Industrial and Applied Mathematics, 2007.

[89] Jörg Liesen and Zdenek Strakos. *Krylov subspace methods: principles and analysis*. Oxford University Press, 2013.

[90] Biyue Liu and Dalin Tang. Influence of non-newtonian properties of blood on the wall shear stress in human atherosclerotic right coronary arteries. *Molecular & cellular biomechanics: MCB*, 8(1):73, 2011.

[91] A. M. Maceira, S. K. Prasad, M. Khan, and D. J. Pennell. Normalized left ventricular systolic and diastolic function by steady state free precession cardiovascular magnetic resonance. *Journal of Cardiovascular Magnetic Resonance*, 8(3):417–426, 2006.

[92] A. Maier, M. W. Gee, C. Reeps, J. Pongratz, H.-H. Eckstein, and W. A. Wall. A comparison of diameter, wall stress, and rupture potential index for abdominal aortic aneurysm rupture risk prediction. *Annals of biomedical engineering*, 38(10):3124–3134, 2010.

[93] Giuseppe Mancia, Robert Fagard, Krzysztof Narkiewicz, Josep Redon, Alberto Zanchetti, Michael Böhm, Thierry Christiaens, Renata Cifkova, Guy De Backer, Anna Dominiczak, Maurizio Galderisi, Diederick E. Grobbee, Tiny Jaarsma, Paulus Kirchhof, Sverre E. Kjeldsen, Stéphane Laurent, Athanasios J. Manolis, Peter M. Nilsson, Luis Miguel Ruilope, Roland E. Schmieder, Per Anton Sirnes, Peter Sleight, Margus Viigimaa, Bernard Waeber, and Faiez Zannad. 2013 esh/esc guidelines for the management of arterial hypertension. *Blood Pressure*, 22(4):193–278, 2013.

[94] Emilie Marchandise, Christophe Geuzaine, and Jean-Francois Remacle. Cardiovascular and lung mesh generation based on centerlines. *International journal for numerical methods in biomedical engineering*, 29(6):665–682, 2013.

[95] Michael Markl, Alex Frydrychowicz, Sebastian Kozerke, Mike Hope, and Oliver Wieben. 4d flow mri. *Journal of Magnetic Resonance Imaging*, 36(5):1015–1036, 2012.

[96] Timothy G. Mattson, Beverly Sanders, and Berna Massingill. *Patterns for parallel programming*. Addison-Wesley Professional, 2004.

[97] Jan Mayer. Ilu++: A new software package for solving sparse linear systems with iterative methods. *PAMM*, 7(1):2020123–2020124, 2007.

[98] Jan Mayer. A multilevel crout ilu preconditioner with pivoting and row permutation. *Numerical Linear Algebra with Applications*, 14(10):771–789, 2007.

[99] Jamie R. Mitchell and Jiun-Jr Wang. Expanding application of the wiggers diagram to teach cardiovascular physiology. *Advances in physiology education*, 38(2):170–175, 2014.

[100] Umberto Morbiducci, Raffaele Ponzini, Giovanna Rizzo, Marcello Cadioli, Antonio Esposito, Franco Maria Montevecchi, and Alberto Redaelli. Mechanistic insight into the physiological relevance of helical blood flow in the human aorta: an in vivo study. *Biomechanics and modeling in mechanobiology*, 10(3):339–355, 2011.

[101] Paul D. Morris, Andrew Narracott, Hendrik von Tengg-Kobligk, Daniel Alejandro Silva Soto, Sarah Hsiao, Angela Lungu, Paul Evans, Neil W. Bressloff, Patricia V. Lawford, D. Rodney Hose, and Julian P. Gunn. Computational fluid dynamics modelling in cardiovascular medicine. *Heart*, 102(1):18–28, 2016.

[102] F. Moukalled, L. Mangani, and M. Darwish. *The finite volume method in computational fluid dynamics*. Springer International Publishing, 2015.

[103] Habib N. Najm. Uncertainty quantification and polynomial chaos techniques in computational fluid dynamics. *Annual review of fluid mechanics*, 41:35–52, 2009.

[104] Wilmer Nichols, Michael O'Rourke, and Charalambos Vlachopoulos. *McDonald's blood flow in arteries: theoretical, experimental and clinical principles*. CRC Press, 6th edition, 2011.

[105] Fabio Nobile, Raúl Tempone, and Clayton G. Webster. A sparse grid stochastic collocation method for partial differential equations with random input data. *SIAM Journal on Numerical Analysis*, 46(5):2309–2345, 2008.

[106] Christopher Noble, Nicole Smulders, Roger Lewis, Matt J. Carré, Steve E. Franklin, Sheila MacNeil, and Zeike A. Taylor. Controlled peel testing of a model tissue for diseased aorta. *Journal of Biomechanics*, 49(15):3667–3675, 2016.

[107] Toshiro Ohashi and Masaaki Sato. Remodeling of vascular endothelial cells exposed to fluid shear stress: experimental and numerical approach. *Fluid dynamics research*, 37(1):40–59, 2005.

[108] Linda A. Pape, Thomas T. Tsai, Eric M. Isselbacher, Jae K. Oh, Patrick T. O'Gara, Arturo Evangelista, Rossella Fattori, Gabriel Meinhardt, Santi Trimarchi, Eduardo Bossone, Toru Suzuki, Jeanna V. Cooper, James B. Froehlich, Christoph A. Nienaber, and Kim A. Eagle. Aortic diameter$\geq$ 5.5 cm is not a good predictor of type a aortic dissection. *Circulation*, 116(10):1120–1127, 2007.

[109] Tiziano Passerini, Annalisa Quaini, Umberto Villa, Alessandro Veneziani, and Suncica Canic. Validation of an open source framework for the simulation of blood flow in rigid and deformable vessels. *International journal for numerical methods in biomedical engineering*, 29(11):1192–1213, 2013.

[110] Charles S. Peskin. The immersed boundary method. *Acta numerica*, 11:479–517, 2002.

[111] Andrei D. Polyanin and Valentin F. Zaitsev. Handbook of exact solutions for ordinary differential equations. *Campman & Hall/CRC*, 2003.

[112] Catherine E. Powell and Elisabeth Ullmann. Preconditioning stochastic galerkin saddle point systems. *SIAM Journal on Matrix Analysis and Applications*, 31(5):2813–2840, 2010.

[113] Alfio Quarteroni, Massimiliano Tuveri, and Alessandro Veneziani. Computational vascular fluid dynamics: problems, models and methods. *Computing and Visualization in Science*, 2(4):163–197, 2000.

[114] Alfio Quarteroni and Alberto Valli. *Domain decomposition methods for partial differential equations*. Numerical mathematics and scientific computation. Clarendon Press, Oxford, 1999.

[115] Mudassar Razzaq, Hogenrich Damanik, Jaroslav Hron, Abderrahim Ouazzi, and Stefan Turek. Fem multigrid techniques for fluid–structure interaction with application to hemodynamics. *Applied Numerical Mathematics*, 62(9):1156–1170, 2012.

[116] Thomas Richter. A monolithic geometric multigrid solver for fluid-structure interactions in ale formulation. *International Journal for Numerical Methods in Engineering*, 104(5):372–390, 2015.

[117] Charles S. Roy. The elastic properties of the arterial wall. *The Journal of physiology*, 3(2):125–159, 1881.

[118] Sethuraman Sankaran and Alison L. Marsden. A stochastic collocation method for uncertainty quantification and propagation in cardiovascular simulations. *Journal of biomechanical engineering*, 133(3):031001, 2011.

[119] Sunetra Sarkar and Jeroen A. S. Witteveen, editors. *Uncertainty Quantification in Computational Science: Theory and Application in Fluids and Structural Mechanics*. World Scientific Publishing, 2017.

[120] Ali Sarrami-Foroushani, Toni Lassila, Ali Gooya, Arjan J. Geers, and Alejandro F. Frangi. Uncertainty quantification of wall shear stress in intracranial aneurysms using a data-driven statistical model of systemic blood flow variability. *Journal of Biomechanics*, 49(16):3815–3823, 2016.

[121] Michael Schäfer, Stefan Turek, Franz Durst, Egon Krause, and Rolf Rannacher. Benchmark computations of laminar flow around a cylinder. In *Flow simulation with high-performance computers II*, pages 547–566. Springer, 1996.

[122] Nicolai Schoch, Fabian Kißler, Markus Stoll, Sandy Engelhardt, Raffaele De Simone, Ivo Wolf, Rolf Bendl, and Vincent Heuveline. Comprehensive patient-specific information preprocessing for cardiac surgery simulations. *International journal of computer assisted radiology and surgery*, 11(6):1051–1059, 2016.

[123] Will Schroeder, Ken Martin, and Bill Lorensen. *The Visualization Toolkit, An Object-Oriented Approach To 3D Graphics*. Kitware, Inc., 4th edition, 2006.

[124] Adélia Sequeira and João Janela. An overview of some mathematical models of blood rheology. In ManuelSeabra Pereira, editor, *A Portrait of State-of-the-Art Research at the Technical University of Lisbon*, pages 65–87. Springer Netherlands, 2007.

[125] James A. Sethian. *Level set methods and fast marching methods: evolving interfaces in computational geometry, fluid mechanics, computer vision, and materials science*. Cambridge University Press, 2nd edition, 1999.

[126] Hang Si. Tetgen, a delaunay-based quality tetrahedral mesh generator. *ACM Transactions on Mathematical Software (TOMS)*, 41(2):11, 2015.

[127] David Silvester, Howard Elman, David Kay, and Andrew Wathen. Efficient preconditioning of the linearized navier—stokes equations for incompressible flow. In *Partial Differential Equations*, pages 261–279. Elsevier, 2001.

[128] William S. Slaughter. *The linearized theory of elasticity*. Birkhäuser Basel, 2002.

[129] Ralph C. Smith. *Uncertainty quantification: theory, implementation, and applications*. Society for Industrial and Applied Mathematics, 2014.

[130] Keith Stein, Tayfun E. Tezduyar, and Richard Benney. Mesh moving techniques for fluid-structure interactions with large displacements: Flow simulation and modeling. *Journal of Applied Mechanics*, 70(1):58–63, 2003.

[131] Timothy J. Sullivan. *Introduction to uncertainty quantification*, volume 63 of *Texts in Applied Mathematics*. Springer International Publishing, 2015.

[132] Stefan Suwelack, Markus Stoll, Sebastian Schalck, Nicolai Schoch, Rüdiger Dillmann, Rolf Bendl, Vincent Heuveline, and Stefanie Speidel. The medical simulation markup language-simplifying the biomechanical modeling workflow. In *MMVR*, pages 394–400, 2014.

[133] Roger Temam. *Navier-stokes equations: Theory and numerical analysis*. North-Holland Amsterdam, 3rd edition, 1984.

[134] Tayfun E. Tezduyar and Sunil Sathe. Modelling of fluid–structure interactions with the space–time finite elements: Solution techniques. *International Journal for Numerical Methods in Fluids*, 54(6-8):855–900, 2007.

[135] Justin S. Tran, Daniele E. Schiavazzi, Abhay B. Ramachandra, Andrew M. Kahn, and Alison L. Marsden. Automated tuning for parameter identification and uncertainty quantification in multi-scale coronary simulations. *Computers & Fluids*, 142:128–138, 2017.

[136] Stefan Turek and Jaroslav Hron. Proposal for numerical benchmarking of fluid-structure interaction between an elastic object and laminar incompressible flow. *Lecture notes in computational science and engineering*, 53:371, 2006.

[137] Stefan Turek, Jaroslav Hron, Mudassar Razzaq, Hilmar Wobker, and Michael Schäfer. Numerical benchmarking of fluid-structure interaction: A comparison of different discretization and solution approaches. In *Fluid Structure Interaction II*, pages 413–424. Springer, 2011.

[138] Jesús Urbina, Julio A. Sotelo, Daniel Springmüller, Cristian Montalba, Karis Letelier, Cristián Tejos, Pablo Irarrázaval, Marcelo E. Andia, Reza Razavi, Israel Valverde, and Sergio A. Uribe. Realistic aortic phantom to study hemodynamics using mri and cardiac catheterization in normal and aortic coarctation conditions. *Journal of Magnetic Resonance Imaging*, 44(3):683–697, 2016.

[139] Alvaro Valencia, Patricio Burdiles, Miguel Ignat, Jorge Mura, Eduardo Bravo, Rodrigo Rivera, and Juan Sordo. Fluid structural analysis of human cerebral aneurysm using their own wall mechanical properties. *Computational and mathematical methods in medicine*, 2013:293128, 2013.

[140] Tullio Valent. *Boundary value problems of finite elasticity: local theorems on existence, uniqueness, and analytic dependence on data*, volume 31 of *Springer Tracts in Natural Philosophy*. Springer-Verlag New York, 1988.

[141] T. Washio, T. Hisada, H. Watanabe, and T. E. Tezduyar. A robust preconditioner for fluid–structure interaction problems. *Computer Methods in Applied Mechanics and Engineering*, 194(39):4027–4047, 2005.

[142] Thomas Wick. *Adaptive Finite Element Simulation of Fluid-Structure Interaction with Application to Heart-Valve Dynamics*. PhD thesis, Universität Heidelberg, Nov 2011.

[143] Thomas Wick. Fully eulerian fluid-structure interaction for time-dependent problems. *Computer Methods in Applied Mechanics and Engineering*, 255:14–26, 2013.

[144] Norbert Wiener. The homogeneous chaos. *American Journal of Mathematics*, 60(4):897–936, 1938.

[145] Dongbin Xiu and George Em Karniadakis. The wiener–askey polynomial chaos for stochastic differential equations. *SIAM journal on scientific computing*, 24(2):619–644, 2002.

8 Appendix

8.1 Definition of the Jacobian system matrix

In the following the definition is given for the Jacobian system matrix J and the right-hand side $L^{h,k}$ of the linear system of equations (4.21). The variables and the strain tensors are used in their form as discrete finite element functions at the respective Newton iteration n. Variables of the previous time step are indicated with $l-1$. Since the quadrature rule is chosen to be exact for the polynomial ansatz and test functions of the finite element discretisation, we keep the notation of the scalar product.

The Jacobian matrix has the following entries.

$$
\begin{aligned}
J_{ij}^{uu} &= \frac{1}{k}\left(\psi_j, \psi_i\right)_s \\
&\quad - \left(J^{-1}\mathrm{tr}(\boldsymbol{F}^{-1}\nabla\psi_j)\nabla\boldsymbol{u}^{h,n}, \nabla\psi_i\right)_f \\
&\quad + \left(J^{-1}\nabla\psi_j, \nabla\psi_i\right)_f, \\
J_{ij}^{uv} &= -\theta\left(\psi_j, \psi_i\right)_s, \\
J_{ij}^{up} &= 0,
\end{aligned}
$$

$$
\begin{aligned}
J_{ij}^{pu} &= \left(J\mathrm{tr}(\boldsymbol{F}^{-1}\nabla\psi_j)\mathrm{tr}(\nabla\boldsymbol{v}^{h,n}\boldsymbol{F}^{-1}), \psi_i\right)_f \\
&\quad - \left(J\mathrm{tr}(\nabla\boldsymbol{v}^{h,n}\boldsymbol{F}^{-1}\nabla\psi_j\boldsymbol{F}^{-1}), \psi_i\right)_f, \\
J_{ij}^{pv} &= \left(J\mathrm{tr}(\nabla\psi_j\boldsymbol{F}^{-1}), \psi_i\right)_f, \\
J_{ij}^{pp} &= 0,
\end{aligned}
$$

$$
\begin{aligned}
J_{ij}^{vu} = & \frac{\theta}{\rho}\left(\nabla\psi_j(\lambda_1 \mathrm{tr}(\boldsymbol{E})\boldsymbol{I} + 2\lambda_2\boldsymbol{E}), \nabla\psi_i\right)_s \\
& + \frac{\theta}{\rho}\left(\boldsymbol{F}(\lambda_1\frac{1}{2}\mathrm{tr}(\nabla\psi_j^T\boldsymbol{F} + \boldsymbol{F}^T\nabla\psi_j)\boldsymbol{I} + \lambda_2(\nabla\psi_j^T\boldsymbol{F} + \boldsymbol{F}^T\nabla\psi_j)), \nabla\psi_i\right)_s \\
& + \frac{\theta}{k}\left(J\mathrm{tr}(\boldsymbol{F}^{-1}\nabla\psi_j)(\boldsymbol{v}^{h,n} - \boldsymbol{v}^{h,l-1}), \psi_i\right)_f \\
& - \frac{1}{k}\left(J\mathrm{tr}(\boldsymbol{F}^{-1}\nabla\psi_j)\boldsymbol{F}^{-1}(\boldsymbol{u}^{h,n} - \boldsymbol{u}^{h,l-1})\cdot\nabla\boldsymbol{v}^{h,n}, \psi_i\right)_f \\
& + \frac{1}{k}\left(J\boldsymbol{F}^{-1}\nabla\psi_j\boldsymbol{F}^{-1}(\boldsymbol{u}^{h,n} - \boldsymbol{u}^{h,l-1})\cdot\nabla\boldsymbol{v}^{h,n}, \psi_i\right)_f \\
& - \frac{1}{k}\left(J\boldsymbol{F}^{-1}\psi_j\cdot\nabla\boldsymbol{v}^{h,n}, \psi_i\right)_f \\
& + \theta\left(J\mathrm{tr}(\boldsymbol{F}^{-1}\nabla\psi_j)\boldsymbol{F}^{-1}\boldsymbol{v}^{h,n}\cdot\nabla\boldsymbol{v}^{h,n}, \psi_i\right)_f \\
& - \theta\left(J\boldsymbol{F}^{-1}\nabla\psi_j\boldsymbol{F}^{-1}\boldsymbol{v}^{h,n}\cdot\nabla\boldsymbol{v}^{h,n}, \psi_i\right)_f \\
& + \theta\nu\left(J\mathrm{tr}(\boldsymbol{F}^{-1}\nabla\psi_j)(\nabla\boldsymbol{v}^{h,n}\boldsymbol{F}^{-1} + \boldsymbol{F}^{-T}\nabla\boldsymbol{v}^{h,n^T})\boldsymbol{F}^{-T}, \nabla\psi_i\right)_f \\
& - \theta\nu\left(J(\nabla\boldsymbol{v}^{h,n}\boldsymbol{F}^{-1}\nabla\psi_j\boldsymbol{F}^{-1} + \boldsymbol{F}^{-T}\nabla\psi_j^T\boldsymbol{F}^{-T}\nabla\boldsymbol{v}^{h,n^T})\boldsymbol{F}^{-T}, \nabla\psi_i\right)_f \\
& - \theta\nu\left(J(\nabla\boldsymbol{v}^{h,n}\boldsymbol{F}^{-1} + \boldsymbol{F}^{-T}\nabla\boldsymbol{v}^{h,n^T})\boldsymbol{F}^{-T}\nabla\psi_j^T\boldsymbol{F}^{-T}, \nabla\psi_i\right)_f \\
& - \frac{1}{\rho}\left(J\mathrm{tr}(\boldsymbol{F}^{-1}\nabla\psi_j)p^{h,n}\boldsymbol{F}^{-T}, \nabla\psi_i\right)_f \\
& + \frac{1}{\rho}\left(Jp^{h,n}\boldsymbol{F}^{-T}\nabla\psi_j^T\boldsymbol{F}^{-T}, \nabla\psi_i\right)_f \\
& - \theta\nu\left(J\mathrm{tr}(\boldsymbol{F}^{-1}\nabla\psi_j)\boldsymbol{F}^{-T}\nabla\boldsymbol{v}^{h,n^T}\boldsymbol{F}^{-T}\boldsymbol{\eta}, \psi_i\right)_{\mathrm{out}} \\
& + \theta\nu\left(J\boldsymbol{F}^{-T}\nabla\psi_j^T\boldsymbol{F}^{-T}\nabla\boldsymbol{v}^{h,n^T}\boldsymbol{F}^{-T}\boldsymbol{\eta}, \psi_i\right)_{\mathrm{out}} \\
& + \theta\nu\left(J\boldsymbol{F}^{-T}\nabla\boldsymbol{v}^{h,n^T}\boldsymbol{F}^{-T}\nabla\psi_j^T\boldsymbol{F}^{-T}\boldsymbol{\eta}, \psi_i\right)_{\mathrm{out}} \\
& + \frac{1}{\rho}\left(J\mathrm{tr}(\boldsymbol{F}^{-1}\nabla\psi_j)p^{\mathrm{out}}\boldsymbol{F}^{-T}\boldsymbol{\eta}, \psi_i\right)_{\mathrm{out}} \\
& - \frac{1}{\rho}\left(Jp^{\mathrm{out}}\boldsymbol{F}^{-T}\nabla\psi_j^T\boldsymbol{F}^{-T}\boldsymbol{\eta}, \psi_i\right)_{\mathrm{out}}, \\
J_{ij}^{vv} = & \frac{1}{k}\left(\psi_j, \psi_i\right)_s + \frac{1}{k}\left(J^{l,\theta}\psi_j, \psi_i\right)_f \\
& - \frac{1}{k}\left(J\boldsymbol{F}^{-1}(\boldsymbol{u}^{h,n} - \boldsymbol{u}^{h,l-1})\cdot\nabla\psi_j, \psi_i\right)_f \\
& + \theta\left(J\boldsymbol{F}^{-1}\psi_j\cdot\nabla\boldsymbol{v}^{h,n}, \psi_i\right)_f + \theta\left(J\boldsymbol{F}^{-1}\boldsymbol{v}^{h,n}\cdot\nabla\psi_j, \psi_i\right)_f \\
& + \theta\nu\left(J(\nabla\psi_j\boldsymbol{F}^{-1} + \boldsymbol{F}^{-T}\nabla\psi_j^T)\boldsymbol{F}^{-T}, \nabla\psi_i\right)_f \\
& - \theta\nu\left(J\boldsymbol{F}^{-T}\nabla\psi_j^T\boldsymbol{F}^{-T}\boldsymbol{\eta}, \psi_i\right)_{\mathrm{out}}, \\
J_{ij}^{vp} = & -\frac{1}{\rho}\left(J\psi_j\boldsymbol{F}^{-T}, \nabla\psi_i\right)_f.
\end{aligned}
$$

The right-hand side reads as follows.

$$
\begin{aligned}
L_i^{h,k}(\psi_u^h) = &\left(\frac{1}{k}(\boldsymbol{u}^{h,n} - \boldsymbol{u}^{h,l-1}), \psi_i\right)_s \\
&- \theta \left(\boldsymbol{v}^{h,n}, \psi_i\right)_s \\
&- (1-\theta) \left(\boldsymbol{v}^{h,l-1}, \psi_i\right)_s \\
&+ \left(J^{-1}\nabla \boldsymbol{u}^{h,n}, \nabla\psi_i\right)_f,
\end{aligned}
$$

$$
\begin{aligned}
L_i^{h,k}(\psi_v^h) = &\left(\frac{1}{k}(\boldsymbol{v}^{h,n} - \boldsymbol{v}^{h,l-1}), \psi_i\right)_s \\
&+ \theta \left(\frac{1}{\rho}\boldsymbol{F}\left(\lambda_1 \mathrm{tr}(\boldsymbol{E})\boldsymbol{I} + 2\lambda_2 \boldsymbol{E}\right), \nabla\psi_i\right)_s \\
&+ (1-\theta) \left(\frac{1}{\rho}\boldsymbol{F}^{l-1}\left(\lambda_1 \mathrm{tr}(\boldsymbol{E}^{l-1})\boldsymbol{I} + 2\lambda_2 \boldsymbol{E}^{l-1}\right), \nabla\psi_i\right)_s \\
&+ \left(J^{l,\theta}\frac{1}{k}(\boldsymbol{v}^{h,n} - \boldsymbol{v}^{h,l-1}), \psi_i\right)_f \\
&- \left(J\boldsymbol{F}^{-1}\frac{1}{k}(\boldsymbol{u}^{h,n} - \boldsymbol{u}^{h,l-1})\cdot\nabla\boldsymbol{v}, \psi_i\right)_f \\
&+ \theta \left(J\boldsymbol{F}^{-1}\boldsymbol{v}^{h,n}\cdot\nabla\boldsymbol{v}^{h,n}, \psi_i\right)_f \\
&+ (1-\theta) \left(J^{l-1}\boldsymbol{F}^{l-1^{-1}}\boldsymbol{v}^{h,l-1}\cdot\nabla\boldsymbol{v}^{h,l-1}, \psi_i\right)_f \\
&+ \theta \left(\nu J\left(\nabla\boldsymbol{v}^{h,n}\boldsymbol{F}^{-1} + \boldsymbol{F}^{-T}\nabla\boldsymbol{v}^{h,n^T}\right)\boldsymbol{F}^{-T}, \nabla\psi_i\right)_f \\
&+ (1-\theta) \left(\nu J^{l-1}\left(\nabla\boldsymbol{v}^{h,l-1}\boldsymbol{F}^{l-1^{-1}} + \boldsymbol{F}^{l-1^{-T}}\nabla\boldsymbol{v}^{h,l-1^T}\right)\boldsymbol{F}^{l-1^{-T}}, \nabla\psi_i\right)_f \\
&- \left(\frac{1}{\rho}\left(Jp^{h,n}\boldsymbol{F}^{-T}\right), \nabla\psi_i\right)_f \\
&- \theta \left(\nu J\boldsymbol{F}^{-T}\nabla\boldsymbol{v}^{h,n^T}\boldsymbol{F}^{-T}\boldsymbol{\eta}, \psi_i\right)_{\mathrm{out}} \\
&- (1-\theta) \left(\nu J^{l-1}\boldsymbol{F}^{l-1^{-T}}\nabla\boldsymbol{v}^{h,l-1^T}\boldsymbol{F}^{l-1^{-T}}\boldsymbol{\eta}, \psi_i\right)_{\mathrm{out}} \\
&+ \left(\frac{1}{\rho}Jp^{\mathrm{out}}\boldsymbol{F}^{-T}\boldsymbol{\eta}, \psi_i\right)_{\mathrm{out}},
\end{aligned}
$$

$$
L_i^{h,k}(\psi_p^h) = \left(J\mathrm{tr}(\nabla\boldsymbol{v}^{h,n}\boldsymbol{F}^{-1}), \psi_i\right)_f.
$$

8.2 Implementation and software issues

The workflow for preparing subject-specific simulations, described in section 4.1, together with the numerical discretisation, as described in section 4.2, leads to a complex numerical simulation algorithm. The proposed scheme aims at solving a resulting large system of linear equations in each time and Newton iteration. In all of the numerical experiments considered in chapter 5 and 6 the solution variables for the displacement, velocity and pressure are represented by high-dimensional finite element vectors. The complexity and size of the discrete problems requires an efficient implementation of the numerical algorithms comprising the usage of high performance computing (HPC).

In order to cope with these requirements, the open source software framework *HiFlow*[3][1] [54] is choosen for the implementation of the simulations considered in this work. Hereby, the programming language *C++* and the parallelisation standard *MPI*[46] is used. C++ allows for a hardware-aware realisation of the numerical algorithms and MPI enables an efficient paralellisation on HPC clusters with distributed memory. HiFlow[3] natively works with a domain decomposition, distributing equally sized subdomains of the geometry to the CPUs. Figure 8.1 illustrates the decomposition of a domain by means of the deterministic FSI benchmark that is considered in section 5.1. After the distribution, each of the CPUs holds the discrete variable values defined on its subdomain in its corresponding memory. For the decomposition of the domain, the open source graph partitioner *metis*[2] is used.

Figure 8.1: Illustration of the decomposition of a domain in a number of subdomains. The figure exemplarily shows the decomposition of the domain of the deterministic FSI benchmark considered in section 5.1 when using 40 CPUs.

All simulations presented in this work were computed on the standard nodes of the *BwForCluster MLS&WISO Production*[3] located at Heidelberg University. Each standard node had two *Intel Xeon E5-2630v3* processors on a *Haswell* architecture with 16 CPU cores at 2.4 GHz and 64 GB working memory. The network for MPI communication between the nodes was an *Infiniband* interconnect of *Quad Data Rate* (QDR). As C++ and MPI compilers, the *Intel* compilers *icpc* and *impi*, both version 17.0 were used. The discretisation parameters and computational costs from the sections about the respective simulations are summarised in table 8.1.

[1] hiflow3.org
[2] glaros.dtc.umn.edu/gkhome/metis/metis/overview
[3] www.bwhpc-c5.de/wiki/index.php/Category:BwForCluster_MLS%26WISO_Production

Parameter	Det. benchmark	UQ benchmark	Phantom	Aortic bow
Degrees of freedom	5.0×10^5	1.4×10^6	1.6×10^6	1.8×10^6
Timesteps	1.0×10^4	5.0×10^2	4.1×10^3	4.1×10^3
PC degree	deterministic	4	4	4
Collocation points	deterministic	intrusive UQ	36	36
CPU cores	64	64	256	256
Wall time	30 h	48 h	42 h	48 h
Total core hours	1.9×10^3 h	3.1×10^3 h	3.9×10^5 h	4.4×10^5 h

Table 8.1: Discretisation parameters and computational costs for the four considered numerical experiments: Deterministic FSI benchmark (section 5.1), UQ-FSI benchmark (section 5.2), aortic phantom experiment (section 6.1), aortic bow simulation (section 6.2). The numbers are given for the highest simulated resolution, respectively.

Implementation of the collocation method

In the following, the Python script is given which implements the essential functions for the UQ collocation method described in section 4.2.4.

```
import numpy as np
import scipy.special
# chaospy, version of Sept. 27, 2017, obtained via
# git clone git@github.com:jonathf/chaospy.git
import chaospy as cp

# construct basic collocation rule
# for uniformly distributed random variables
# input:
# - dimension of the stochastic space
# - maximal polynomial degree of the chaos polynomials
# output:
# - collocation points
# - weights of the quadrature rule
def construct_collocation_rule ( N, poly_degree ):
  # order of Gauss-Legendre quadrature for an exact integration
  # of the scalar product of the chaos polynomials
  quadrature_order = poly_degree + 1

  # creating a multidimensional uniform distribution
  uniform_dists = [ cp.Uniform ( -1, 1 ) for n in range ( N ) ]
  joint_dist = cp.J ( *uniform_dists )

  # generate the quadrature, rule="E" -> Gauss-Legendre
  nodes, weights = cp.generate_quadrature \
                   ( quadrature_order, joint_dist, rule="E" )
  return nodes, weights

# generate collocation points in physical units
# for uniformly distributed random variables
```

```
# input:
# - maximal polynomial degree of the chaos polynomials
# - list of mean values of the input random variables
# - list of deviation values from the means of the random variables
# output:
# - collocation points in physical units
# - weights of the quadrature rule
def generate_collocation ( poly_degree, means, deviations ):
  # get dimension of stochastic space
  N = len ( means )
  assert N == len ( deviations )

  # construct the quadrature
  nodes, weights = construct_collocation_rule ( N, poly_degree )
  num_quad_nodes = len ( weights )

  # map the collocation points to the physical values
  for n in range( N ):
    assert num_quad_nodes == len ( nodes[n] )
    for i in range( num_quad_nodes ):
      nodes[n][i] = means[n] + deviations[n] * nodes[n][i]
  return nodes, weights

# faculty of a number
def faculty ( num ):
  fac = 1
  for n in range ( num ):
    fac = fac * ( n + 1 )
  return fac

# multiindex for the chaos polynomial basis
def compute_multiindex ( num_modes, poly_degree, N ):
  multii = np.zeros ( shape = ( num_modes + 1, N ) )
  if poly_degree > 0:
    for i in range ( 1, N + 1 ):
      multii[i][i-1] = 1
  if poly_degree > 1:
    R = N
    mat = np.zeros ( shape = ( N, poly_degree ) )
    for i in range ( N ):
      mat[i][0] = 1
    for k in range ( 1, poly_degree ):
      L = R
      for i in range ( N ):
        s = 0
        for l in range ( i, N ):
          s = s + mat[l][k-1]
        mat[i][k] = s
      for j in range ( N ):
        for l in range ( L - int ( mat[j][k] ) + 1, L + 1 ):
          R = R + 1
```

```
            for i in range ( N ):
              multii[R][i] = multii[l][i]
            multii[R][j] = multii[R][j] + 1
  return multii

# evaluation of a 1D Legendre polynomial
def legendre ( degree, x ):
  return scipy.special.eval_legendre ( degree, x )

# evaluation of a multivariate Legendre polynomial
def legendre_multi ( degree, multiindex, x_vec ):
  degrees = multiindex[degree]
  assert len ( degrees ) == len ( x_vec )
  val = 1.
  for i in range ( len ( degrees ) ):
    val = val * legendre ( degrees[i], x_vec[i] )
  return val

# calculate the squared norm of a 1D Legendre polynomial
def legendre_norm_sq ( degree ):
  return 2. / ( 2. * degree + 1. )

# calculate the squared norm of a multivariate Legendre polynomial
def legendre_multi_norm_sq ( degree, multiindex ):
  degrees = multiindex[degree]
  val = 1.
  for i in range ( len ( degrees ) ):
    val = val * legendre_norm_sq ( degrees[i] )
  return val

# compute quadrature factors
# for uniformly distributed random variables
# input:
# - dimension of the stochastic space
# - maximal polynomial degree of the chaos polynomials
# output:
# - factors for the multiplication with the results computed
#   for each collocation point
#   summation then yields the respective stochastic mode
def compute_quadrature_factors ( N, poly_degree ):
  # construct the quadrature
  nodes, weights = construct_collocation_rule ( N, poly_degree )
  nodes = nodes.T
  num_quad_nodes = len ( weights )

  # calculate number of modes
  num_modes = ( faculty ( poly_degree + N ) \
              / ( faculty ( poly_degree ) * faculty ( N ) ) ) - 1

  # calculate multiindices
  alpha = compute_multiindex ( num_modes, poly_degree, N )
```

```
# calculate the size of the stochastical domain
stoch_dom_size = 2**N

# calculate quadrature factors for each mode and collocation point
factors = []
for mode in range( num_modes + 1 ):
  leg_norm_sq_inv = stoch_dom_size \
                    / legendre_multi_norm_sq ( mode, alpha )
  factors.append ( [ leg_norm_sq_inv * weights[i] \
                     * legendre_multi ( mode, alpha, nodes[i] ) \
                     for i in range ( num_quad_nodes ) ] )
return factors
```

8.3 Additional visualisation of the aortic phantom simulation

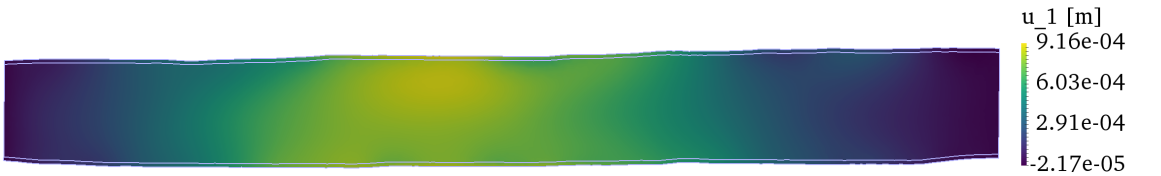

(a) Expected value $E(\boldsymbol{u}_1)$.

(b) Standard deviation $\sigma(\boldsymbol{u}_1)$.

Figure 8.2: Visualisation of the displacement into the shown cross section $\boldsymbol{u}_1$ (cf. Figure 6.1) at the second systolic peak, $t = 0.22\,\mathrm{s}$.

(a) Expected value $E(\boldsymbol{u}_2)$.

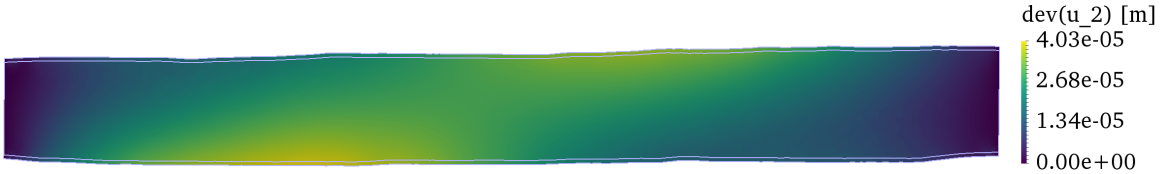

(b) Standard deviation $\sigma(\boldsymbol{u}_2)$.

Figure 8.3: Visualisation of the displacement along the cross section $\boldsymbol{u}_2$ (cf. Figure 6.1) at the second systolic peak, $t = 0.22\,\mathrm{s}$.

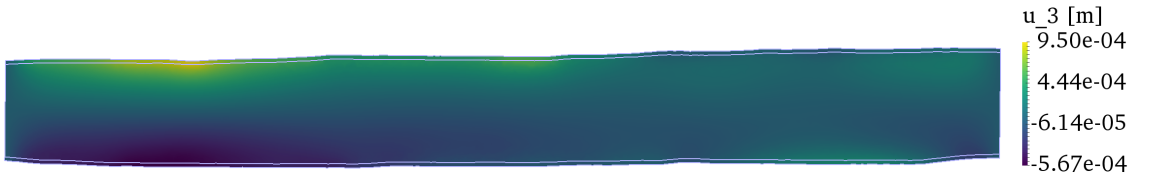

(a) Expected value $E(\boldsymbol{u}_3)$.

(b) Standard deviation $\sigma(\boldsymbol{u}_3)$.

Figure 8.4: Visualisation of the vertical displacement in the cross section $\boldsymbol{u}_3$ (cf. Figure 6.1) at the second systolic peak, $t = 0.22\,\mathrm{s}$.

(a) Expected value $E(\boldsymbol{v}_1)$.

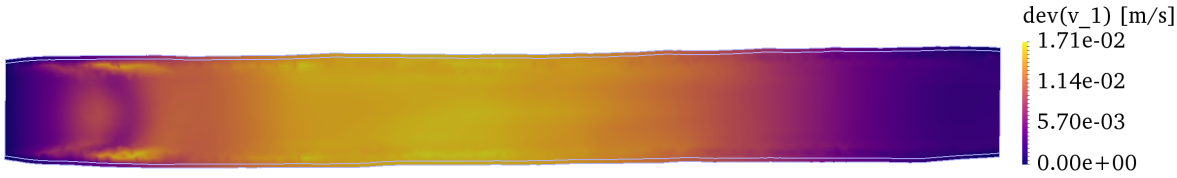

(b) Standard deviation $\sigma(\boldsymbol{v}_1)$.

Figure 8.5: Visualisation of the velocity into the shown cross section $\boldsymbol{v}_1$ (cf. Figure 6.1) at the second systolic peak, $t = 0.22\,\mathrm{s}$.

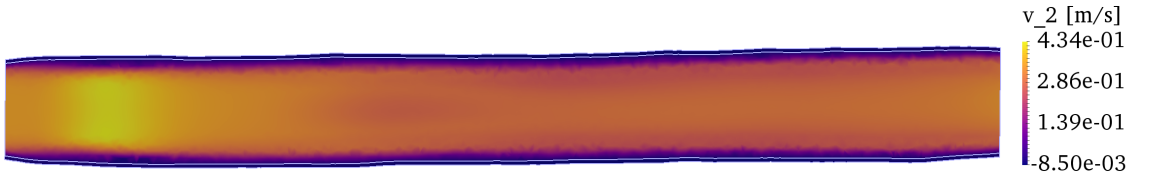

(a) Expected value $E(\boldsymbol{v}_2)$.

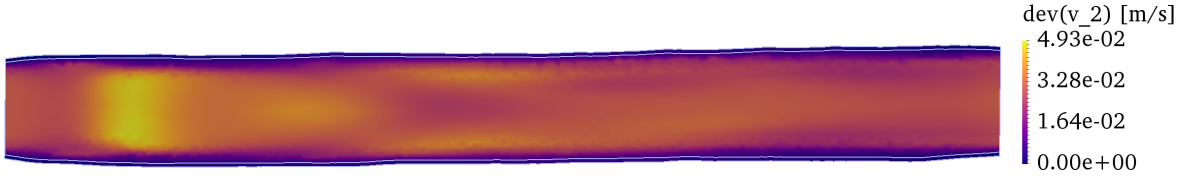

(b) Standard deviation $\sigma(\boldsymbol{v}_2)$.

Figure 8.6: Visualisation of the velocity along the cross section $\boldsymbol{v}_2$ (cf. Figure 6.1) at the second systolic peak, $t = 0.22\,\mathrm{s}$.

(a) Expected value $E(\boldsymbol{v}_3)$.

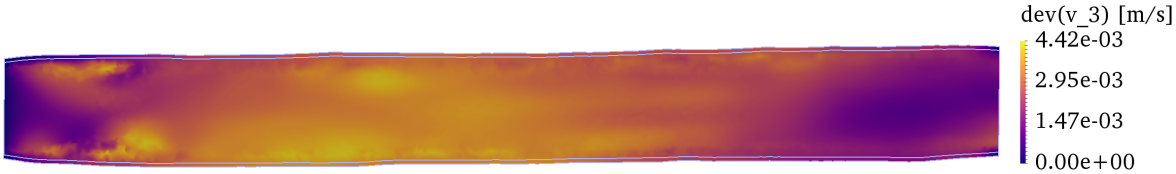

(b) Standard deviation $\sigma(\boldsymbol{v}_3)$.

Figure 8.7: Visualisation of the vertical velocity in the cross section $\boldsymbol{v}_3$ (cf. Figure 6.1) at the second systolic peak, $t = 0.22\,\mathrm{s}$.

(a) Expected value $E(p)$.

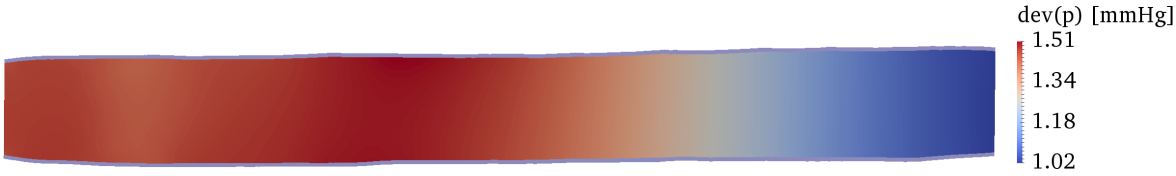

(b) Standard deviation $\sigma(p)$.

Figure 8.8: Visualisation of the pressure p in the cross-sectional plane (cf. Figure 6.1) at the second systolic peak, $t = 0.22\,\mathrm{s}$.

$t = 0.22\,\mathrm{s}$	L2	L3	L4	L5	
2D flow MRI: $\boldsymbol{v}_2$	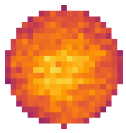	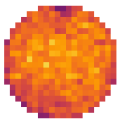		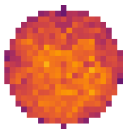	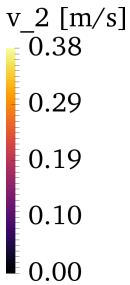
$E(\boldsymbol{v}_2) - \sigma(\boldsymbol{v}_2)$	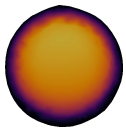	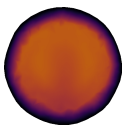	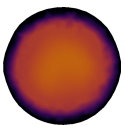	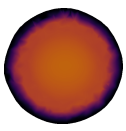	
$E(\boldsymbol{v}_2)$	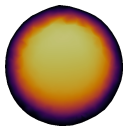	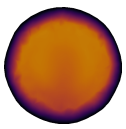	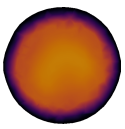	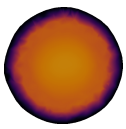	
$E(\boldsymbol{v}_2) + \sigma(\boldsymbol{v}_2)$	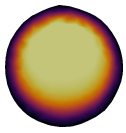	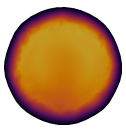	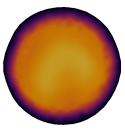	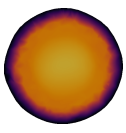	

Table 8.2: Visualisation of the velocity field $\boldsymbol{v}_2$ in the cross-sectional plane levels L2, L3, L4 and L5 (cf. Figure 6.1) at the second systolic peak, $t = 0.22\,\mathrm{s}$. The first row shows the velocity data measured by 2D flow MRI. The second to the last row show the simulated velocity field. Hereby, the expected value $E(\boldsymbol{v}_2)$, shown in the third row is subtracted by the standard deviation $\sigma(\boldsymbol{v}_2)$ in the second row. The standard deviation added to the expected value is shown in the fourth row.

8.4 Additional visualisation of the aortic bow simulation

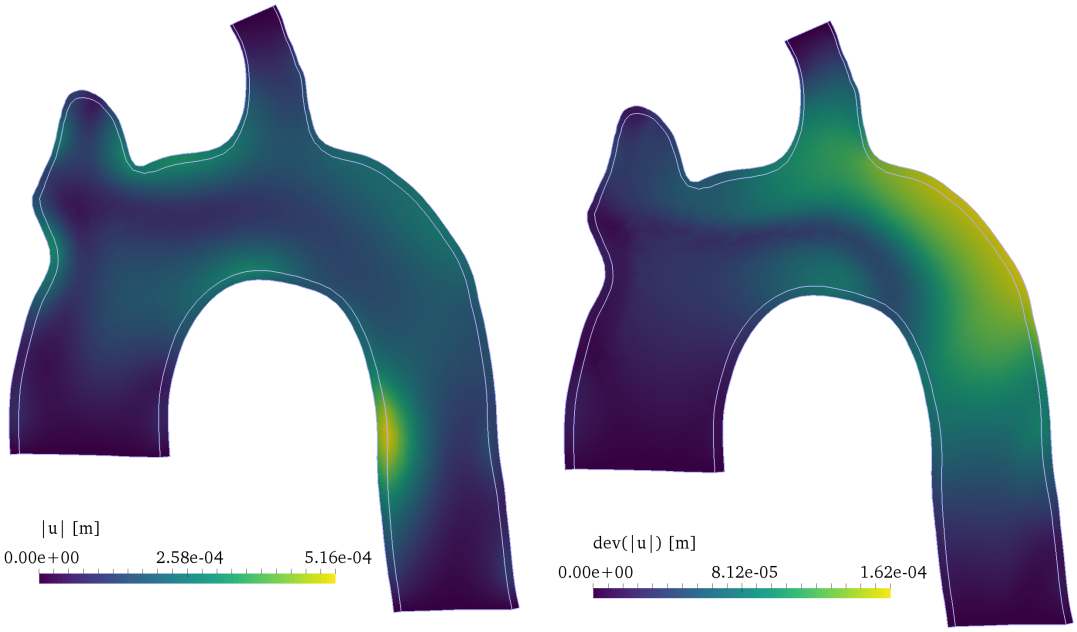

(a) Expected value of the displacement $E(|\boldsymbol{u}|)$.

(b) Standard deviation $\sigma(|\boldsymbol{u}|)$.

Figure 8.9: Visualisation of the displacement magnitude by means of the frontal cross sectional plane defined in Figure 6.17b in mid-diastole at $t = 0.66\,\mathrm{s}$.

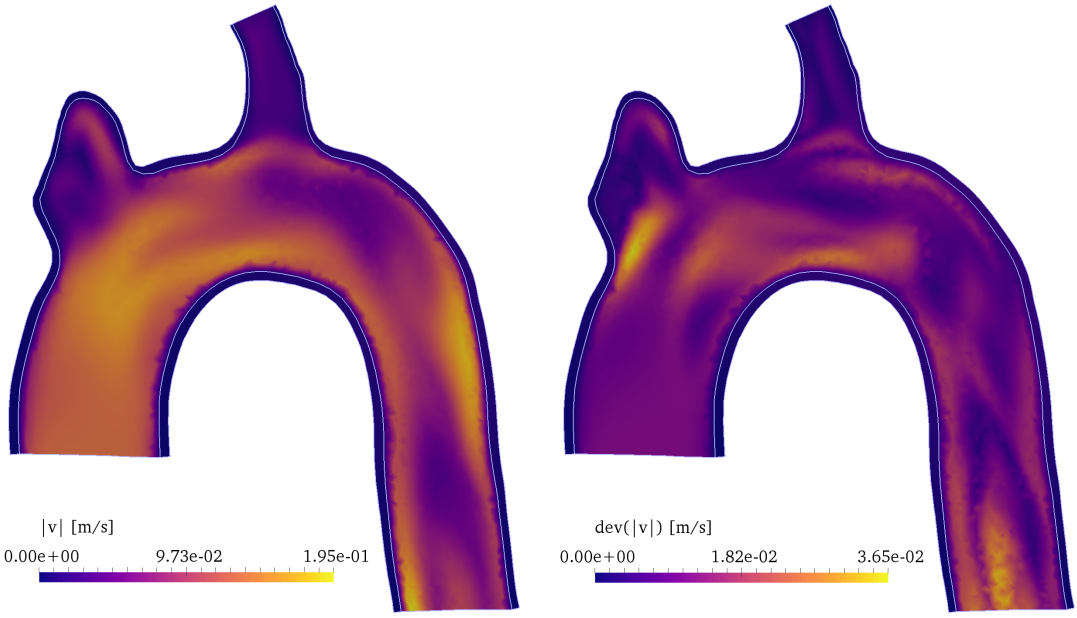

(a) Expected value of the velocity $E(|\boldsymbol{v}|)$. (b) Standard deviation $\sigma(|\boldsymbol{v}|)$.

Figure 8.10: Visualisation of the velocity magnitude by means of the frontal cross sectional plane defined in Figure 6.17b in mid-diastole at $t = 0.66\,\mathrm{s}$.

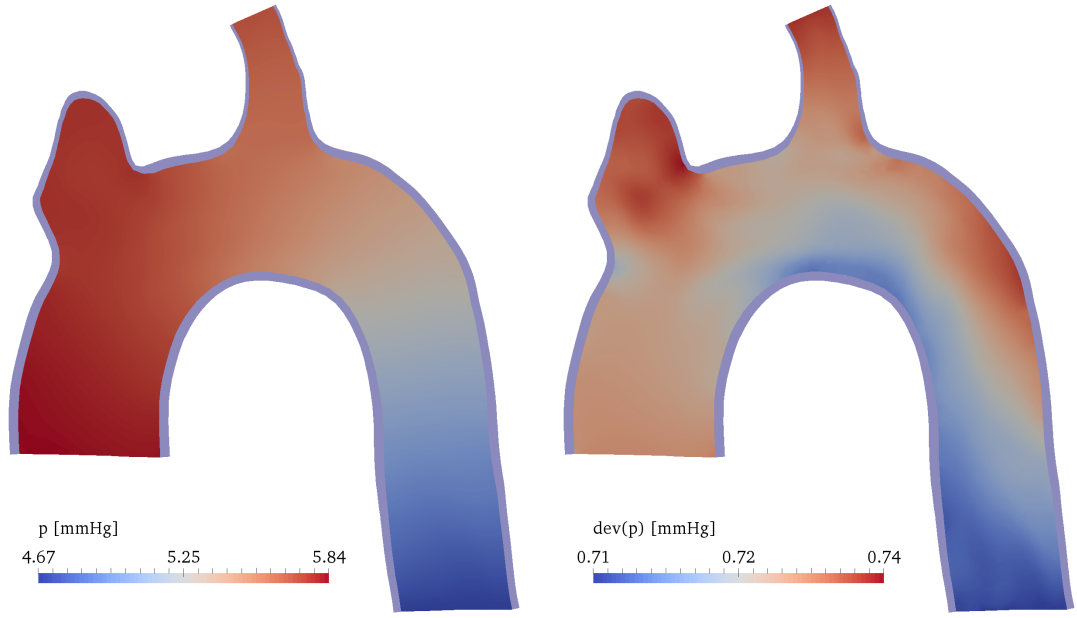

(a) Expected value of the pressure $E(p)$. (b) Standard deviation $\sigma(p)$.

Figure 8.11: Visualisation of the pressure by means of the frontal cross sectional plane defined in Figure 6.17b in mid-diastole at $t = 0.66\,\mathrm{s}$.

$t = 0.66\,\mathrm{s}$	L1	L2	L3	
$E(\lvert\boldsymbol{u}\rvert)$	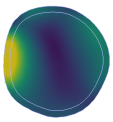	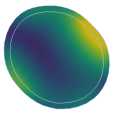		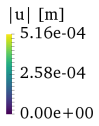
$\sigma(\lvert\boldsymbol{u}\rvert)$		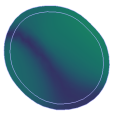	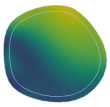	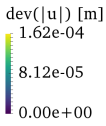
$E(\lvert\boldsymbol{v}\rvert)$	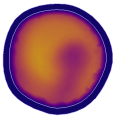	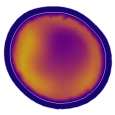	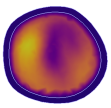	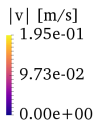
$\sigma(\lvert\boldsymbol{v}\rvert)$	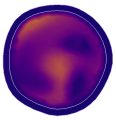	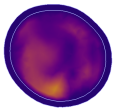	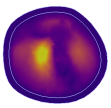	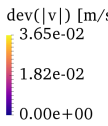
$E(p)$				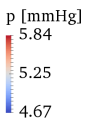
$\sigma(p)$	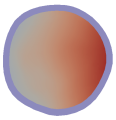		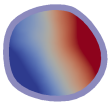	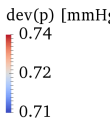

Table 8.3: Visualisation of the aortic bow simulation by means of the cross sectional levels defined in Figure 6.17 in mid-diastole at $t = 0.66\,\mathrm{s}$. The orientation is such, that the bottom of the cross sections is oriented towards the arc center of the bow. The left side is in the back of Figure 6.17 and the right side of the cross sections is directed to the front.

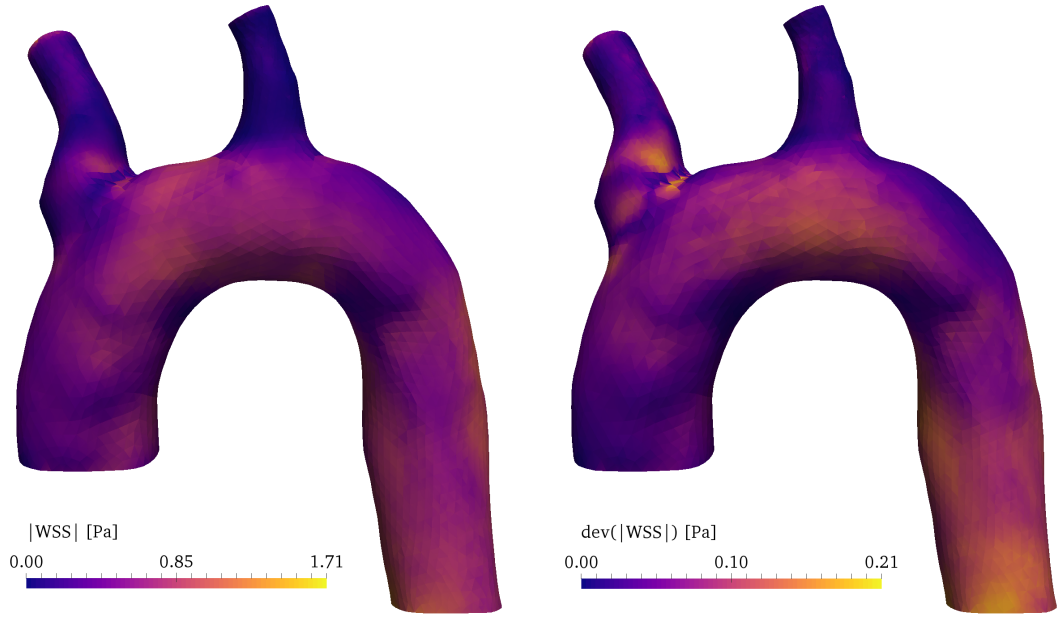

(a) Expected value $E(\tau_W)$, front view.

(b) Standard deviation $\sigma(\tau_W)$, front view.

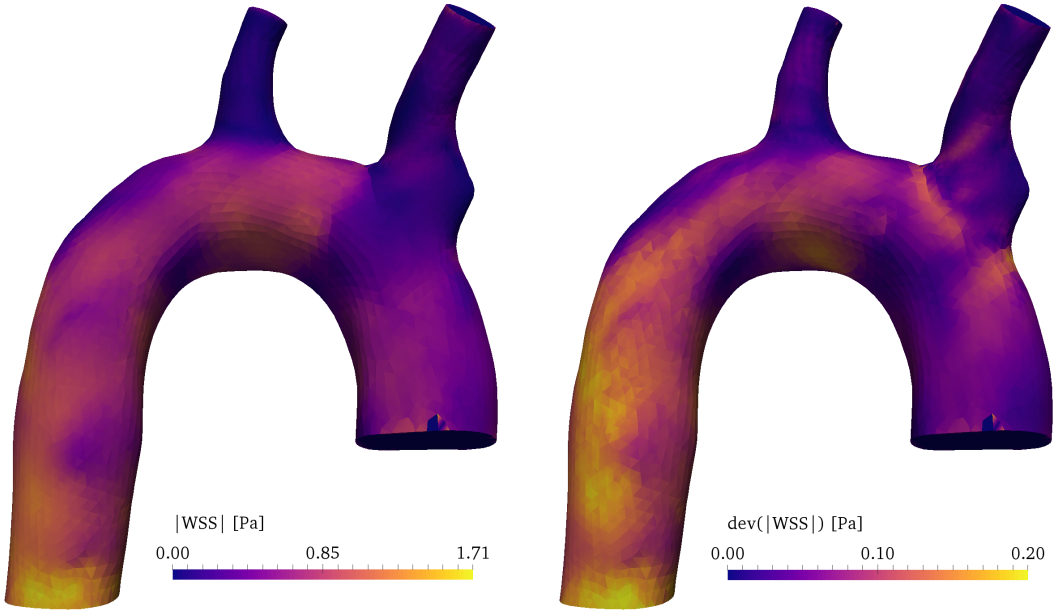

(c) Expected value $E(\tau_W)$, back view.

(d) Standard deviation $\sigma(\tau_W)$, back view.

Figure 8.12: Visualisation of the wall shear stress magnitude on the outside of the fluid-structure interface in mid-diastole at $t = 0.66\,\mathrm{s}$.

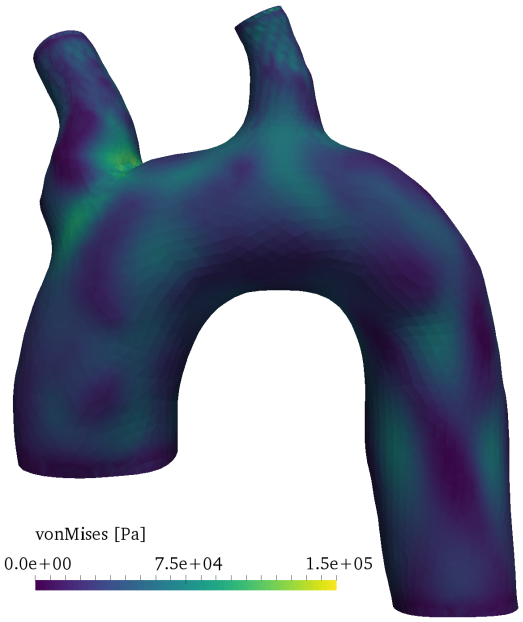

(a) Expected value $E(\tau_{\mathrm{M}})$, front view.

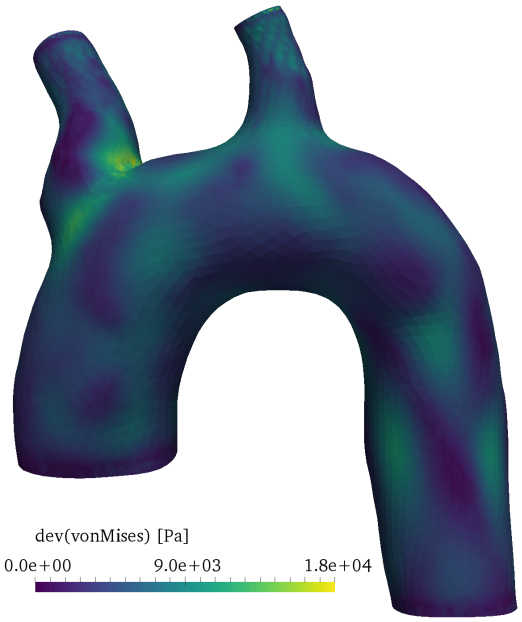

(b) Standard deviation $\sigma(\tau_{\mathrm{M}})$, front view.

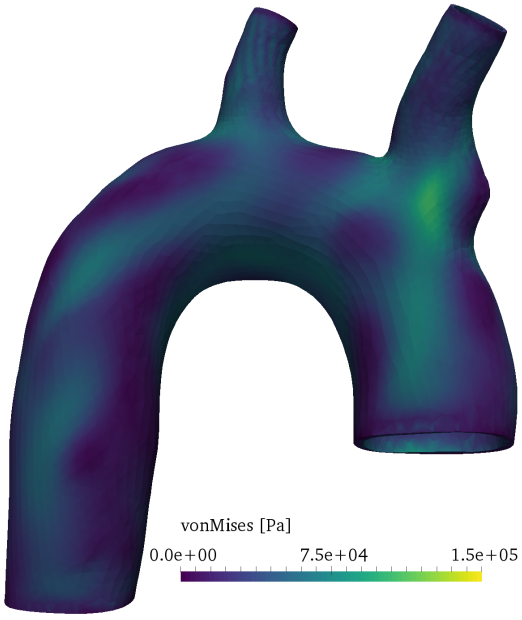

(c) Expected value $E(\tau_{\mathrm{M}})$, back view.

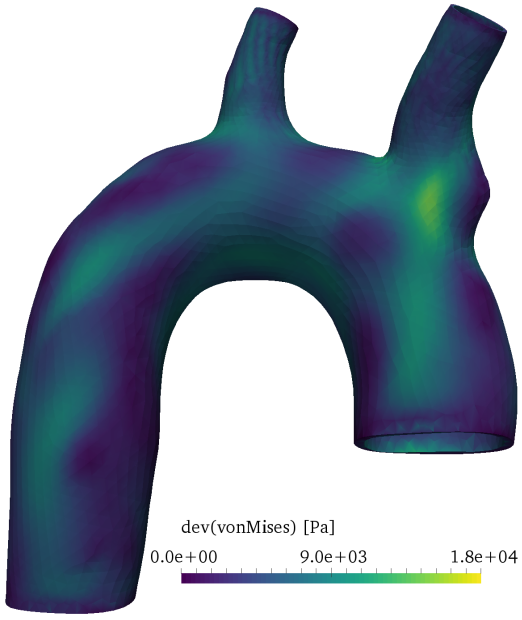

(d) Standard deviation $\sigma(\tau_{\mathrm{M}})$, back view.

Figure 8.13: Visualisation of the von Mises stress on the outside of the geometry in mid-systole at $t = 0.16\,\mathrm{s}$.

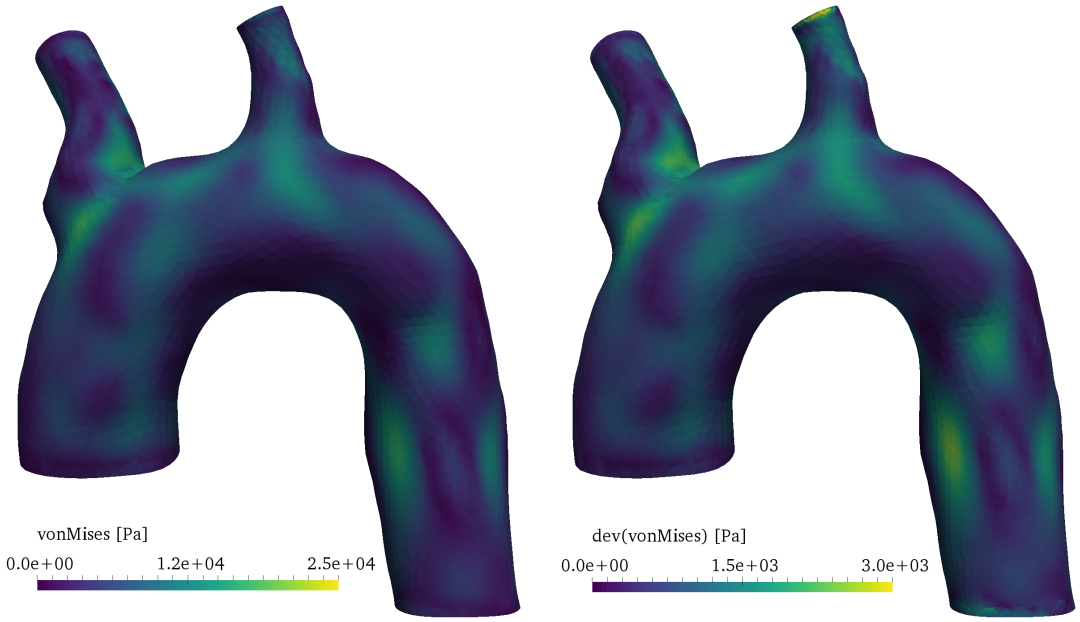

(a) Expected value $E(\tau_{\mathrm{M}})$, front view.

(b) Standard deviation $\sigma(\tau_{\mathrm{M}})$, front view.

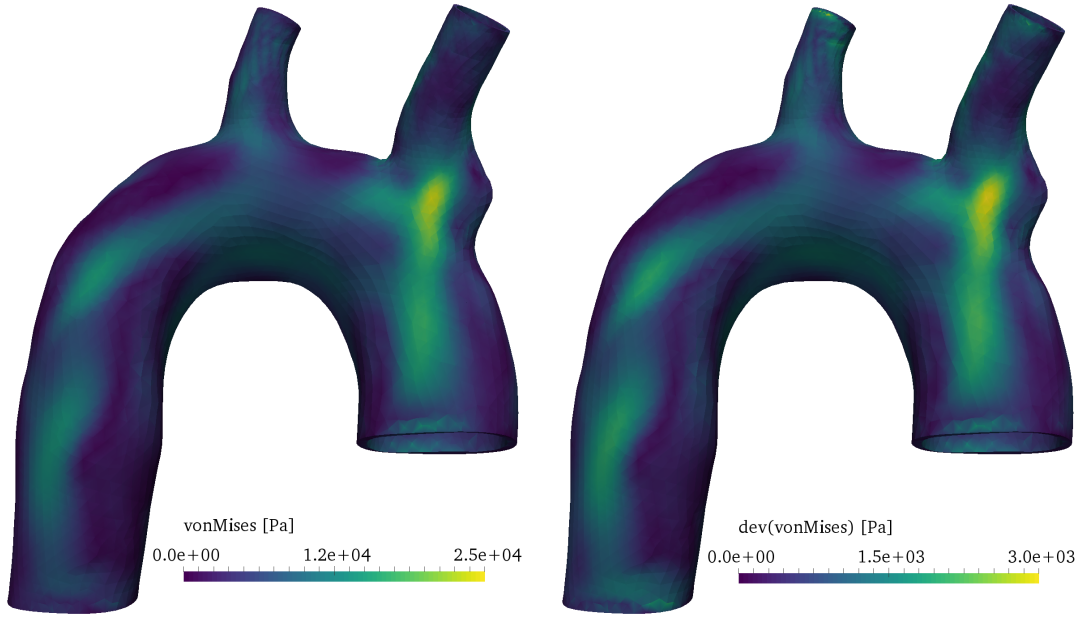

(c) Expected value $E(\tau_{\mathrm{M}})$, back view.

(d) Standard deviation $\sigma(\tau_{\mathrm{M}})$, back view.

Figure 8.14: Visualisation of the von Mises stress on the outside of the geometry in mid-diastole at $t = 0.66\,\mathrm{s}$.

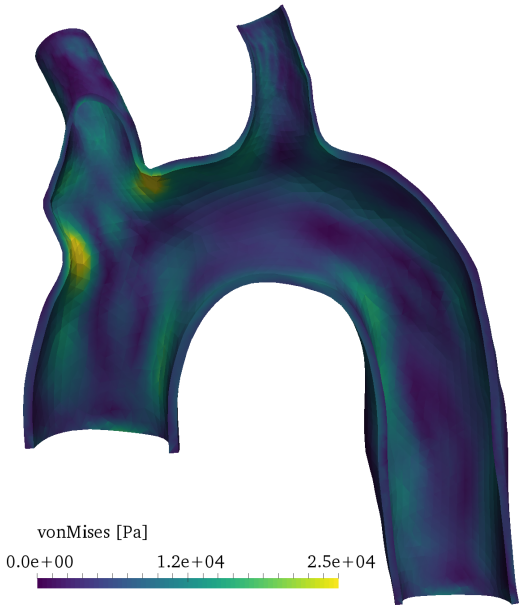

(a) Expected value $E(\tau_{\mathrm{M}})$, front view.

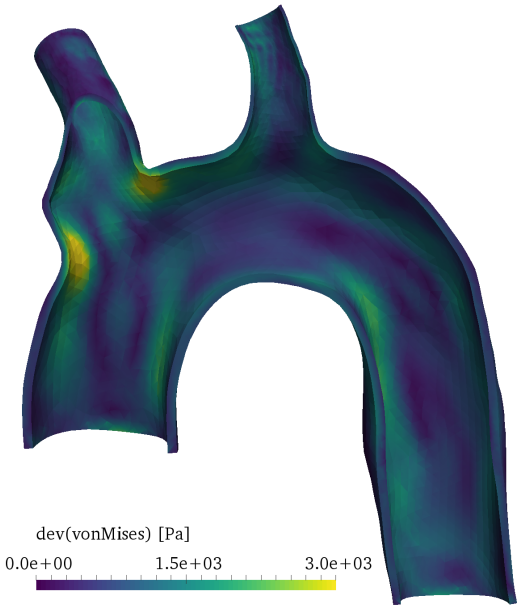

(b) Standard deviation $\sigma(\tau_{\mathrm{M}})$, front view.

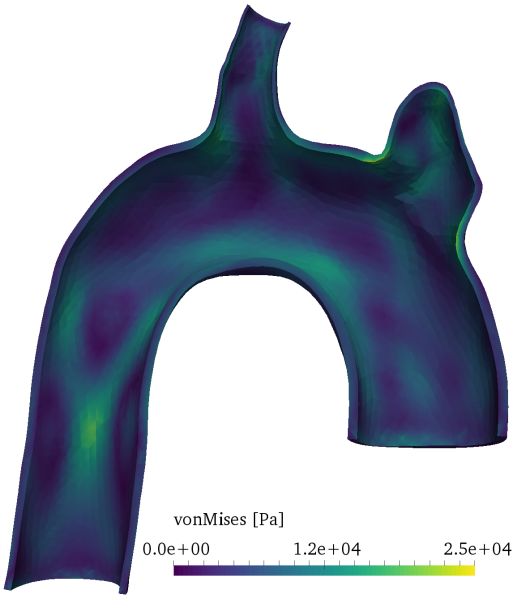

(c) Expected value $E(\tau_{\mathrm{M}})$, back view.

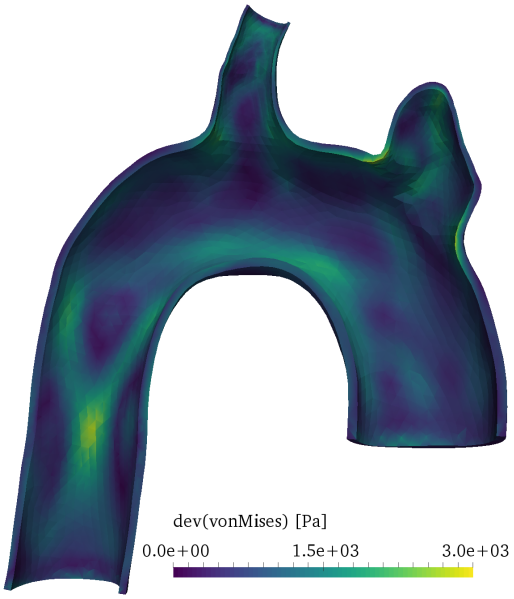

(d) Standard deviation $\sigma(\tau_{\mathrm{M}})$, back view.

Figure 8.15: Visualisation of the von Mises stress on the inside of the fluid-structure interface in mid-diastole at $t = 0.66\,\mathrm{s}$.